Matériaux pour la Géologie de la Suisse

GEOPHYSIQUE
N° 35

Publiés par la Commission Suisse de Géophysique
Organe de l'Académie Suisse des Sciences Naturelles,
Subventionnée par la Confédération

ON THE DISTRIBUTION OF THE ELECTRICAL CONDUCTIVITY IN THE CENTRAL ALPS

Marcus GURK

ISSN 0253-1186

Imprimeries Centrales Neuchâtel S.A. - CH-2001 Neuchâtel
2000

Author's address:

M. Gurk

Groupe de Géomagnétisme
Institut de Géologie
Université de Neuchâtel
Rue Emile-Argand 11
CH-2007 Neuchâtel
Switzerland
marcus.gurk@unine.ch

Editor's Preface

The present publication entitled "On the distribution of the electrical conductivity in the central Alps" is Report Nr. 35 of the "Contribution to the Geology of Switzerland - Geophysical Series", published by the Swiss Geophysical Commission.
This report contains an interesting study of the electrical conductivity of the central alps deduced from magneto-telluric and geomagnetic deep soundings. The authors gives in the first part the necessary theoretical background for the understanding of the method, followed by a short description of the data acquisition procedures.
The second part describes the analysis of the transfer functions of GDS and MT and the structural and geological consequences of the results. An interesting chapter is dedicated to the study of the structural discontinuities of the Tschera nappe and to the separation of local and regional conductive structures. Finally the method of the Hypothetical Event Analysis is applied to the data and the conclusions put in the geological frame of the region.
The Swiss Geophysical Commission is very grateful to Mr Marcus Gurk for having produced this monograph which is an important contribution to the knowledge of the distribution of the electrical conductivity in the central Alps.
Special thanks are due to the Swiss National Academy of Natural Sciences for its financial support of this publication.

Zurich, December 2000

In the name of the Swiss
Geophysical Commission
The President:

Prof. Emile Klingelé

Acknowledgments

This survey was carried out as a joint project of the Swiss Geophysical Commission and the Institute of Geology of the University of Neuchâtel, with the support of the Swiss National Science Foundation, grants # 20-47135.96 and 20-53924.98.

Résumé

A l'est des Alpes centrales et dans les Alpes orientales, la distribution de l'induction géomagnétique se caractérise à grande échelle par une région dans laquelle les flèches d'induction réelles présentent une anomalie d'orientation. Cette région s'étend du domaine pennique de Suisse orientale (Grisons) probablement jusqu'aux Carpathes. Un réseau de mesures magnétotelluriques (MT) et d'induction magnétique profonde (GDS) réalisées dans les cantons des Grisons et du Valais indique que cette anomalie de variations électromagnétiques se limite aux sédiments mésozoïques des schistes lustrés (Bündnerschiefer) du domaine nord pennique. Ce faciès commence en Suisse orientale et s'étend vers l'est sous les unités Austro-alpine, Sud-Pennique et Sud-alpine. Cette zone présente des ressemblances frappantes de position, d'arrangement, et de signature magnétique par rapport aux Alpes orientales. L'analyse des données GDS au moyen de la méthode de l'Analyse d'Evénement Hypothétique (HEA) montre que la canalisation de courants affecte les champs électromagnétiques dans cette zone, et produit des anomalies d'orientation des flèches d'induction. Nous considérons les courants électriques induits dans diverses structures conductrices locales et régionales et fuyant dans les schistes lustrés, comme la cause probable des effets observés sur les flèches d'induction. Nous basant sur une interprétation combinée des données GDS des Alpes orientales et de l'ouest de la Hongrie avec nos récentes données des Alpes centrales et de leur partie orientale, nous déduisons les implications suivantes:

i) un découplage spatial des processus d'induction de la croûte supérieure et inférieure
ii) une structure conductrice de la croûte inférieure causée par l'indentation du promontoire ou région géologique adriatique
iii) un empilement lithosphérique dans la partie orientale des Alpes centrales et dans les Alpes orientales
iv) le prolongement vers l'est du faciès des schistes lustrés, au moins jusqu'à la fenêtre tectonique de Rechnitz.

Zusammenfassung

Das Muster der elektromagnetischen Induktionsparameter ist in den östlichen Zentralalpen und in den Ostalpen durch eine (kontinuierliche) langerstreckte Zone gekennzeichnet, auf denen die Realteile der Induktionspfeile ein anomales Richtungsverhalten zeigen. Diese Zone erstreckt sich vermutlich vom Penninikum der Ostschweiz (Graubünden) bis in die Karpaten hinein.
Magnetotellurische (MT) und Erdmagnetische Tiefensondierungen (ETS) auf einem dichten Messpunktraster in den Graubündener und Waliser Alpen (Westschweiz) zeigen, dass diese beobachtete elektromagnetische Variationsanomalie auf Messpunkte, die auf den mezozoischen Sedimenten der Bündnerschieferfazies errichtet wurden, beschränkt ist. Die Fazies beginnt in der Ostschweiz und erstreckt sich unterhalb Südpenninischer, Austroalpiner und Südalpiner Einheiten nach Osten. Hinsichtlich ihrer Position und ihrem Arrangement zeigt die Anomalie eine auffällige Gemeinsamkeit zur magnetischen Signatur in den Ostalplen. Die Analyse der ETS Daten mit Hilfe der sogenannten „Hypothetical Event Analysis" lässt vermuten, dass kanalisierte Stromsysteme im Untergrund die elektromagnetischen Felder auf den Bündnerschiefer verzerren und das anomale Richtungsverhalten der Induktionspfeile verursacht. Wir nehmen an, dass diese Stromsysteme in verschiedenen lokalen und regionalen leitfähigen Strukturen in- und ausserhalb des Messgebietes induziert werden und dann anschliessend in die Bündnerschiefer hineinfliessen.
Basierend auf der gemeinsamen Analyse bereits vorhandener ETS Daten aus den Ostalpen und Westungarn zusammen mit unseren aktuellen Daten aus den Zentralalpen können untenstehende geologische Folgerungen abgeleitet werden:

i) Eine räumliche Entkopplung der Induktionsprozesse von der oberen zur unteren Kruste.
ii) Eine leitfähige Struktur in der Unterkruste entstanden durch die Indentation des Adriatischen Vorgebirges oder Krustenfragments.
iii) Eine Lithosphärenverdopplung in den östlichen Zentral- und Ostalpen.
iv) Die Erstreckung der Bündnerschieferfazies mindestens bis zum tektonischen Fenster von Rechnitz.

Abstract

The electromagnetic induction pattern in the eastern Central and Eastern Alps is characterised by a (continuous) large-scale zone on which the real parts of the induction arrows show anomalous directional behaviour. This zone extends from the Penninic Domain of eastern Switzerland (Graubünden) into the Carpathian ranges. A coarse mesh of Magnetotelluric (MT) and Geomagnetic Deep Soundings (GDS) in the Alps of Graubünden and Valais (western Switzerland) indicates that this electromagnetic variation anomaly is restricted to the Mesozoic sediments of the North Penninic Bündnerschiefer-facies. The facies begins in eastern Switzerland and extends towards the East beneath Austroalpine, South Penninic and Southalpine units. Striking similarities in position and arrangement between this zone and the magnetic signature in the Eastern Alps are found. The analysis of the GDS data with the method of the Hypothetical Event Analysis (HEA) shows implications that current channelling affects the electromagnetic fields in this zone and causes the anomalous direction of induction arrows. We consider electric currents induced in various local and regional conductive structures and leaking into the Bündnerschiefer as possible causes for the observed effect upon the induction arrows. Based on the combined interpretation of GDS data from the Eastern Alps and West Hungary together with our recent data from the Central and eastern Central Alps, the following geological implications are deduced:

i) A spatial decoupling of induction processes from the upper to the lower crust
ii) A lower crustal conductive structure caused by the indentation of the northern Adriatic promontory or terrane
iii) A stacked lithosphere in the eastern Central and Eastern Alps
iv) The eastward continuation of the Bündnerschiefer-facies at least to the tectonic window of Rechnitz.

Contents

List of Figures

number *description*

List of Tables

List of Symbols

symbol	*description*
x, y, z	Cartesian coordinates, z positive downwards
x', y', z'	Regional strike coordinates
x'', y'', z''	Local strike coordinates
$\hat{\mathbf{x}}, \hat{\mathbf{y}}, \hat{\mathbf{z}}$	Unit vector
θ_r, θ_l	regional, local strike azimuth (pos. from north), respectively: $\theta_l - \theta_r = \alpha$
$s(t)$	signal in time domain, probing signal, incoming signal
$g(t)$	signal in time domain, response
LTI	Linear Time Invariant system: $s(t)$ LTI $g(t)$
$\delta(t)$	Dirac impulse function
$h(t)$	Transfer function of a LTI system in time domain
$*$	convolution operator
$Tr\{...\}$	Transformation
$\Im\{...\}$	Fourier transformation
$S(f)$	Fourier transformed probing signal, spectrum of $s(t)$
$G(f)$	Fourier transformed response, spectrum of $g(t)$
$H(f)$	Transfer-function of a LTI system in frequency domain, spectrum of $h(t)$

i	Imaginary number $\sqrt{-1} := i$
Re, Im	Real, imaginary part of a complex number: C = Re + iIm
C^*	Complex conjugate of C ; C^* = Re - iIm
B	Magnetic induction vector; $\mathbf{B}^0$ regional field, $\mathbf{B}^a$ anomalous local field; [Tesla]= [Vs/m^2]
E	Electric field vector; $\mathbf{E}^0$ regional field, $\mathbf{E}^a$ local electrostatic field; [V/m]
j	Electric current density [A/m^2]
D	Electric displacement [As/m^2]
$\dot{\mathbf{D}}$	Displacement current
r	Field vector to observation point
$\mathbf{r}'$	Field vector to source point
t	Time [s]
T	Period [s]; $T^{-1} = f$ frequency [s^{-1}]
T_0	Period of sign change of the magnetic phase
ω	Angular frequency $\omega = \frac{2\pi}{T}$; [s^{-1}]
k	Wavenumber [m^{-1}]; $k_0 = \sqrt{i\omega\mu_0\sigma_0}$
σ	Electrical conductivity $\sigma = \rho^{-1}$; [S/m]
τ	Electrical conductance [S] = [Ω^{-1}]; [A/V]
q	Volume density of charge [As/m^3] = [C/m^3]
μ_0	Magnetic permeability $\mu_0 = 4\pi 10^{-7} \frac{Vs}{Am}$; [H/m]
	μ_r : relative permeability; $\mu = \mu_r \mu_0$
ε	Dielectric constant (electrical permittivity) $\varepsilon_0 = \frac{1}{36\pi} 10^{-9} \frac{As}{Vm}$;[F/m]
	ε_r =: relative permittivity; $\varepsilon = \varepsilon_r \varepsilon_0$
ρ	Electrical resistivity $\rho = \sigma^{-1}$; [Ωm]
ρ_a	Apparent resistivity; [Ωm]
δ_{skin}	Skin-depth at which the electromagnetic wave is attenuated by a factor
	$1/e$; $\delta_{skin} = \sqrt{\frac{2}{\omega\mu\sigma}} \approx 0.5\sqrt{T\rho}$; [km]
$\underline{\mathbf{I}}$	Unity matrix
$\underline{\mathbf{Z}}$	Magnetotelluric impedance tensor with complex components (transfer functions) $Z_{xx}, Z_{xy}, Z_{yx}, Z_{yy}$; [m/s]
$\underline{\mathbf{Z}}^0$	Regional impedance tensor in strike coordinates (x', y') with
Z_E, Z_B	Principal impedances; $Z_{\tilde{E}}, Z_{\tilde{B}}$, distorted principal impedances
φ_E, φ_B	Phases of the principal impedances
$\underline{\mathbf{C}}$	Electrical distortion tensor with real components
	$C_{xx}, C_{xy}, C_{yx}, C_{yy}$

$\underline{\mathbf{D}}$ Magnetic distortion tensor with real components $D_{xx}, D_{xy}, D_{yx}, D_{yy}$; [s/m]

(A,B) Magnetic transfer functions: A,B in x, y directions, respectively; (A^0,B^0) regional; $(\tilde{A}^0,\tilde{B}^0)$ distorted regional; (A^l,B^l) local

φ_m Magnetic phase: phase of the magnetic transfer function B^l in strike coordinates x′

$\mathbf{P,Q}$ Real and imaginary induction arrow; L_P, L_Q: lengths, θ_P, θ_Q: directions

$\mathbf{B}^*$ Hypothetical horizontal magnetic field

ϑ^* Polarisation azimuth of the hypothetical event

B_z^P Predicted vertical magnetic field

$\underline{\mathbf{R}}_\theta$ Rotation matrix for anti-clockwise rotation ($\theta > 0$) with:

$$\underline{\mathbf{R}}_\theta = \begin{pmatrix} cos\theta & -sin\theta & 0 \\ sin\theta & cos\theta & 0 \\ 0 & 0 & 1 \end{pmatrix} \text{ or only } \underline{\mathbf{R}}_\theta = \begin{pmatrix} cos\theta & -sin\theta \\ sin\theta & cos\theta \end{pmatrix}$$

$\underline{\mathbf{R}}$ Rotation matrix for clockwise rotation ($\theta < 0$) with:

$$\underline{\mathbf{R}} = \begin{pmatrix} cos\theta & sin\theta & 0 \\ -sin\theta & cos\theta & 0 \\ 0 & 0 & 1 \end{pmatrix} \text{ or only } \underline{\mathbf{R}} = \begin{pmatrix} cos\theta & sin\theta \\ -sin\theta & cos\theta \end{pmatrix}$$

∇ Nabla operator; $\nabla A = grad\, A$, $\nabla \cdot \mathbf{A} = div\mathbf{A}$, $\nabla \times \mathbf{A} = curl\mathbf{A}$, $\nabla^2\mathbf{A}$ = Laplacian of $\mathbf{A}$, $\nabla^2\mathbf{A} := \nabla(\nabla \cdot \mathbf{A}) - \nabla \times (\nabla \times \mathbf{A})$.

$[XY^*] = \frac{1}{N}\sum_{i=1}^{N} X_i Y_i^*$, N = total number of measurements, X_i, Y_i^* = single measuremet, (* indicates here the complex conjugate).

$[C_1, C_2]$ Commutator, C_1, C_2 complex numbers:
$[C_1, C_2] = Im(C_2 C_1^*) = Re\,C_1\, Im\,C_2 - Re\,C_2\, Im\,C_1$ and
$\{C_1, C_2\} = \mathrm{Re}(C_2 C_1^*) = \mathrm{Re}\,C_1\,\mathrm{Re}\,C_2 + \mathrm{Im}\,C_2\,\mathrm{Im}\,C_1$,
(* indicates here the complex conjugate).

1 Introduction

Based on the available seismic, gravimetric, magnetic and geologic data from the recent years, our understanding of the Central Alps has been revised. This part of the alpine mountain belt (Fig. 1.1) was formed during the Late Cretaceous (Fig. 1.2) and Pliocene (Schmid et al., 1996) by the collision of the European and Adriatic continents and (several) supposed intermediate terranes. Various long and short seismic profiles, together with information from geological field and laboratory studies, have been projected on three major traverses across the Western and Central Alps (Pfiffner & Hitz, 1997). The E1 (Eastern Traverse) profile is part of the European Geotraverse conducted from the active Mediterranean margin to the Precambrian shield in Scandinavia (Blundell et al., 1992). The aim of the combined interpretation of geophysical and geological information (Schmid et al, 1996) was to elucidate the regional mechanisms involved in the building of the Alps. Close to this line, sixty-four MT and GDS sites with a spacing of about 5 km measured the natural magnetic and telluric variations in a period range T= 1-300 s. We suggested to search for structural and geometrical correlations of well defined series within the Bündnerschiefer to provide additional information about the three-dimensional structure of the upper and lower crust, as well as to reveal similarities or differences between the electrical conductivity distribution in the western and eastern Penninic Alps. However, the initial results show anomalous directional behaviour of the real parts of the induction arrows derived from the GDS data. Similar observations have been documented in several field examples over elongated conductive structures (Arora & Adam, 1992).

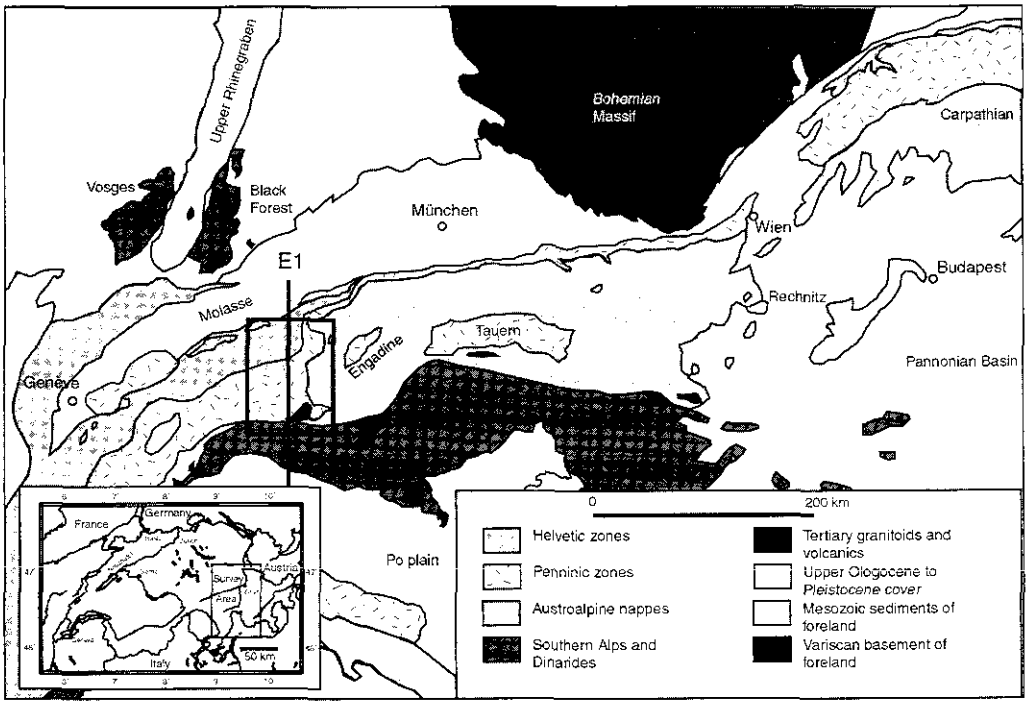

Fig.1.1: Sketch map of the Alps and surrounding areas. Box and Line indicate the position of the survey area and the Eastern Traverse (E1). Redrawn from Trümpy (1988).

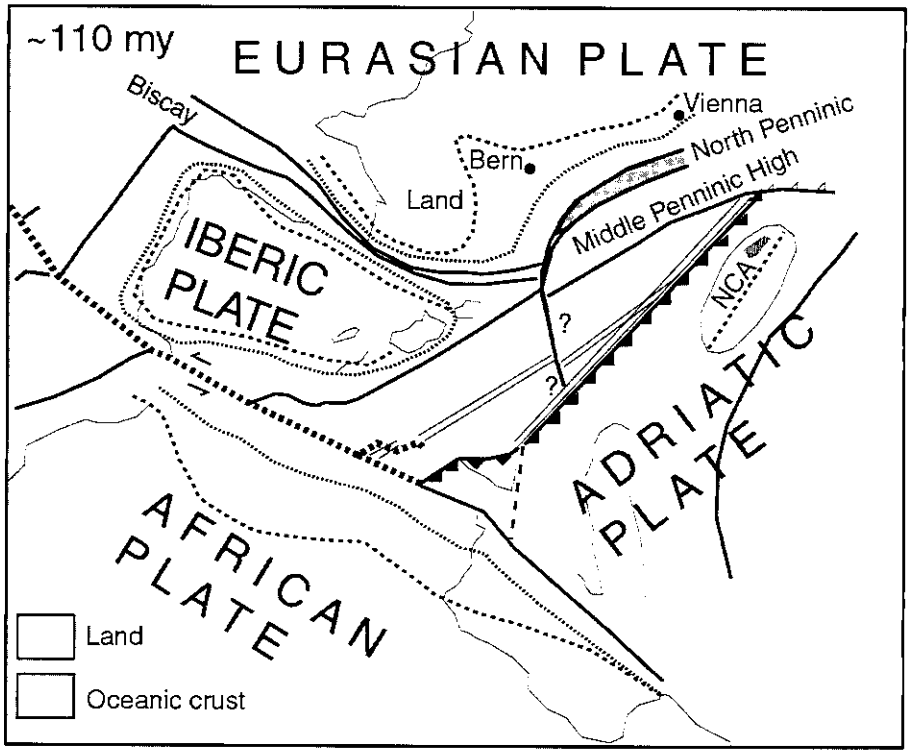

mid-oceanic ridge; NCA: Northern Calcareous Alps;
Continental masses; important transform fault;
lines of future rifting;
separates area of land against shallow water sedimentation;
separates area of shallow water against deep see water sedimentation.

Fig. 1.2: Palaeogeographic reconstruction of the western Mediterranean in late Lower Cretaceous time. Redrawn from Frisch (1979)

Since the real parts of the induction arrows are pointing towards a region of lower electrical conductivity, they are a powerful tool for mapping lateral changes in the conductivity distribution. The pioneer of this investigation method is H. Wiese. His publications where the first to present the data in the form of induction arrows on regional maps (Wiese, 1962).

Two predominant anomalies are present in Central Europe: The North German anomaly (Untiedt, 1970) that roughly extends East-West and a conductivity anomaly that assumes the arc of the Carpathian Ranges. The North German anomaly is the largest one in extent and is the most extensively investigated of the two. On the other hand, the electromagnetic induction pattern in the Central Alps remains almost unknown. Besides two long period (T> 1000 s) induction studies in the Western and Eastern Alps (Bahr, 1992) and the MT/GDS survey in the western Swiss Alps (Schnegg, 1998), no further modern studies have been conducted in the Central Alps so far.

Even at locations quite far from the influence of the North German anomaly, the characteristic South direction of the real part of the induction arrow is preserved, whereas one would have expected it to change towards and within (Schnegg, 1998) the Western Central Alps. This general observation is at present not well understood. It may result from a gradual decrease of the subsurface conductivity toward the South or result from a more complex structure of the external field (Schmucker, 1999). In

southern Germany a predominant southeast direction of the real part induction arrows can be observed. Berktold (pers. comm.) suspects an additional conductivity anomaly (900-9000 S) within the northern phyllite zone of the post Variscan cover in front of the Mid-German Crystalline High (Blundell et al., 1992) superimposed on the North German anomaly to cause the southeast direction of the induction arrows. Real part induction arrows that exhibit this general direction north of the Central Alps are well documented by several MT and GDS studies (Richards et al., 1980b; Tezkan, 1988; Berktold, 1978, Berktold et. al, 1976).

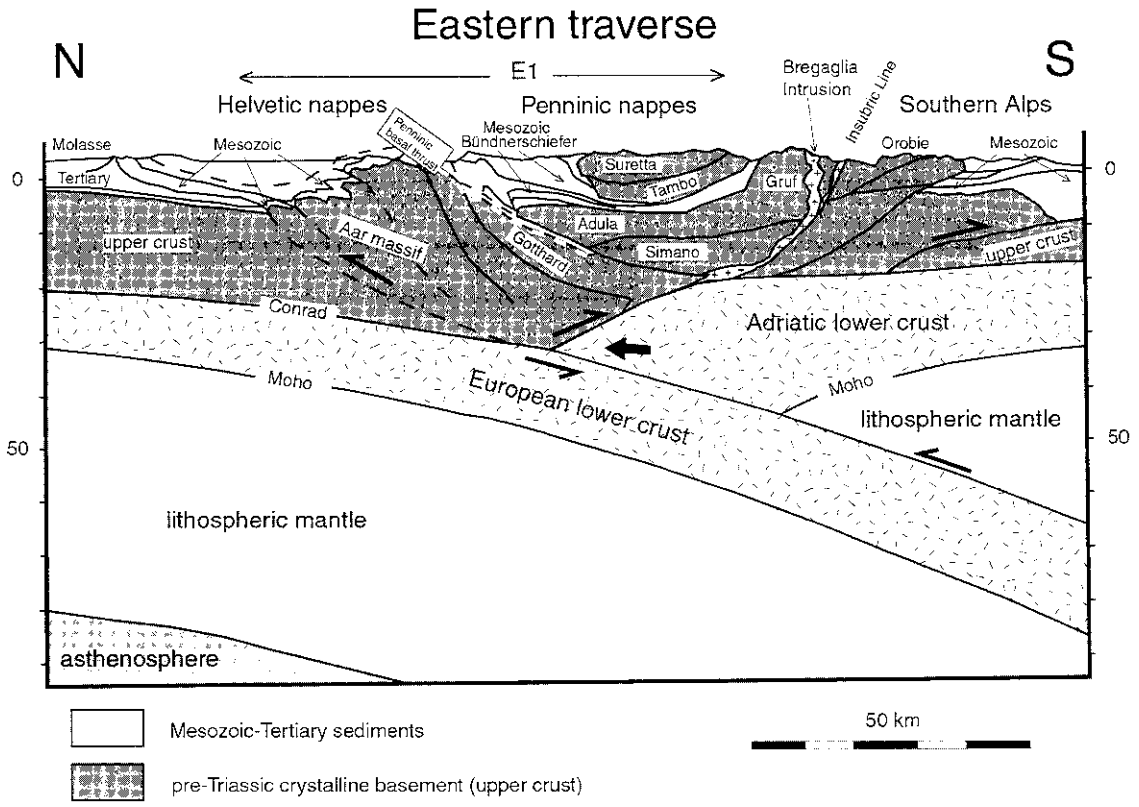

Fig. 1.3: General geological profile across the alpine orogen drawn along the trace of the Eastern Traverse but expanded to the Molasse basin and the Po basin (Pfiffner et al., 1997). Line E1 is part of the European Geotraverse.

1.1 Geological outlines

Fig. 1.1 shows a tectonic map of the Alps containing the surveyed area (box) and the location of the E1 profile (Eastern traverse). Fig. 1.3 shows a simplified north-south profile along the E1 line across the eastern Central Alps from the Molasse foredeep to the South Alpine thrust belt cross-cut the three main domains (Coward & Dietrich, 1989, Pfiffner et al., 1997). From north to south we find (Fig. 1.4):

i) an external part (Helvetic Aar and Gotthard Massives)
ii) the Penninic Zone and
iii) South Alpine Units.

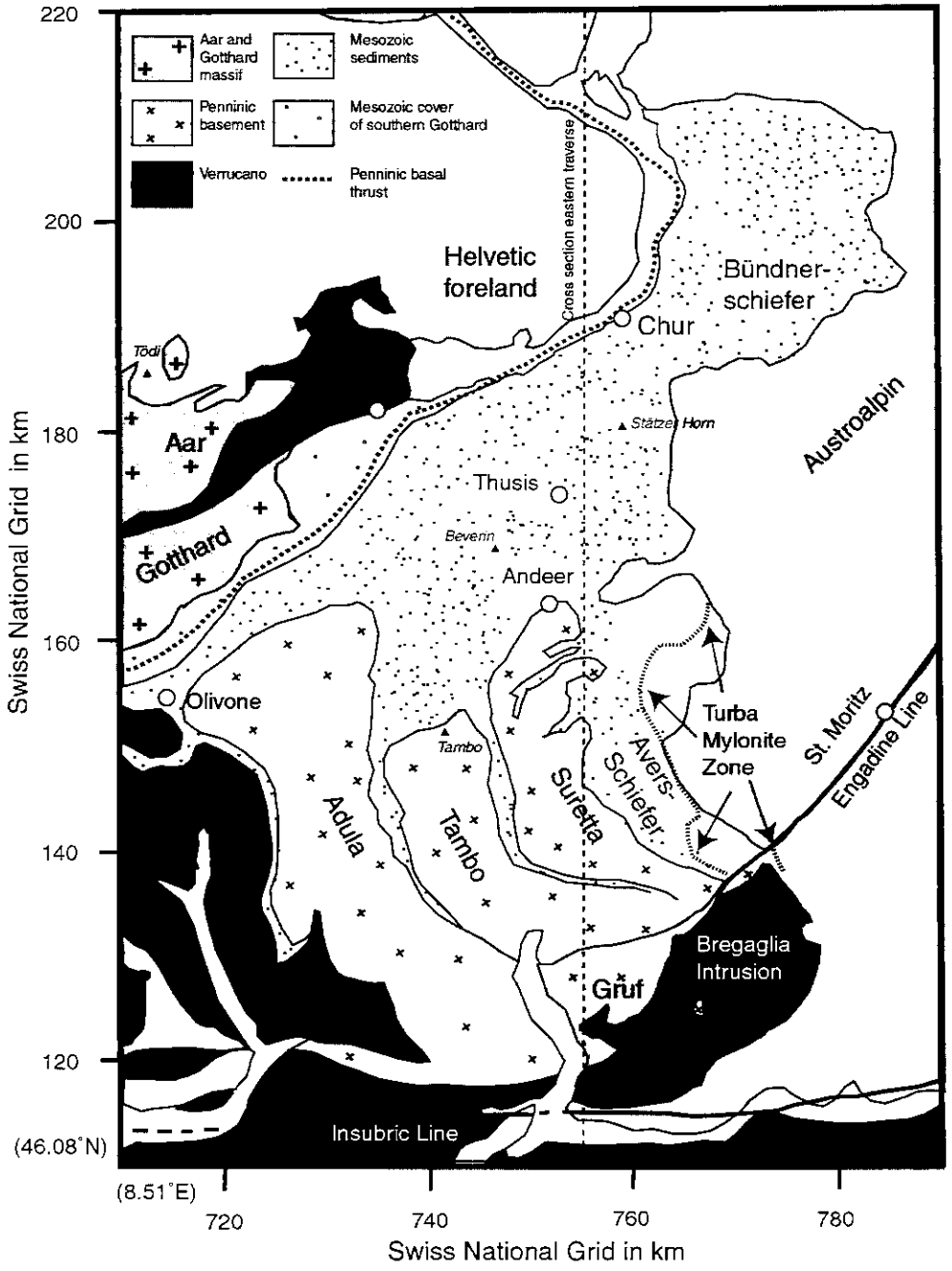

Fig. 1.4: Simplified tectonic map of the Graubünden area.

The Penninic Zone consists of imbricate stacks of sedimentary and basement slices, including the Mesozoic Bündnerschiefer facies, Avers-Schiefer, Schams, and the crystalline micro-continents Adula, Tambo and Suretta. Together with ophiolithic rocks they form the remnant of the alpine Thetys, which has been divided by deep-sea swells into different pull-part basins. In one of these basins, the Bündnerschiefer was deposited by turbidity currents. During Tertiary period the intrusion of the Bregaglia massive (30 Ma) took place along the Insubric Line forming the southermost border of the investigation area. To the East we find the remnants of a rift-related, low angle detachment system (Manatschal et al., 2000) of a passive margin that delineates the transition zone between the Eastern and Central/Western Alps. In this context, the Avers-Schiefer is considered to be either part of an ancient mélange zone or an accretion prism. Within the orogenic zone, all major tectonic units have a pronounced easterly axial dip. Consequently, the crustal structure in eastern Switzerland can be described as a triple junction.

1.2 Palaeogeographical outlines

The North Penninic basin (Fig. 1.2) is a sub-basin in the northern part of the Mesozoic Thetys ocean. Remnants of the eastern North Penninic basin are preserved in the Alps of eastern Switzerland as low metamorphic Mesozoic Bündnerschiefer sediments and associated basaltic rocks which formed approximately 140-170 Ma ago (Steinmann & Stille, 1999). The Bünderschiefer are situated between the Helvetic units below and the Middle Penninic, South Penninic and Austroalpine units above (Fig. 1.1, Fig. 1.3, Fig. 1.4). It is controversially discussed whether the North Penninic basin can be interpreted as an isolated marginal basin which was completely underlain by thinned continental crust (Weissert & Bernoulli, 1985), or as a partial oceanic basin which was replaced toward the east by the South Penninic ocean in a large "en–echelon" structure (Trümpy, 1988). A third solution is proposed by Stämpfli in which the oceanization of the North Penninic basin was already complete (Stämpfli & Marchant, 1997).
Geochemical data (Steinmann & Stille, 1999) show that the North Penninic basalts are directly derived from a depleted mantle source and are overlain by 2.5 km thick series of siliclastic-turbiditic Bündnerschiefer sediments. Compared to the South Penninic oceanic basalts, which were covered by a reduced series of pelagic sediments, the North Penninic realm was not so far evolved in oceanization.
Toward the east, the Bünderschiefer-facies become covered by Middle Penninic, South Penninic and Austroalpine units. They are thought to reappear (Fig. 1.1) in the tectonic windows of Engadine, Tauern and Rechnitz, although they cannot directly be correlated in the field with the Bündnerschiefer-facies (Trümpy, 1988). A modern analogue for the North Penninic basin may be seen in the pull-apart basins of the southernmost Gulf of California (Robinson, et al., 1983).

1.3 The Bündnerschiefer facies in Graubünden

The Bündnerschiefer facies in eastern Switzerland is mainly represented by series of the Misox-Bündnerschiefer, showing a monotonous lithology. Its major mineral phase bears quartz, calcite, chlorite, and illite, whereas the minor phase consists of paragonite, dolomite, pyrite, pyrrhotite, rutile, zircon, turmaline and garnet. They

form series of low-grade metamorphic, shaly-calcareous-terrigenous sediments. Relics of Fe-Mg-carpholite from the Lugnez valley (south-east of Ilanz, Fig. 1.4) and of carpholite pseudomorphs found near Thusis (Fig. 1.4) indicate an early high pressure – low temperature path (ca. 350°C, >7 kbar) for the Bündnerschiefer (Goffe & Oberhänsli, 1992). In the northern part of the investigation area, the metamorphism in the Prättigau-Schiefer (denoted as Bündnerschiefer in the upper right corner of Fig. 1.4) increases from West towards the East from greenschist facies to anchizonal grade (Weh et al., 1996; Mählmann, 1995).

2 Theoretical background

This study mainly deals with a two-dimensional interpretation of the magnetic transfer function in the Graubünden and adjacent areas, which is based on a simplified decomposition model. Therefore, all conclusions should be understood as an approximation to the actual three-dimensional conductivity distribution. Our research benefits from closely spaced sites arranged in an array to show an alternative way of presenting and determining the electrical strike when three-dimensionality affects the magnetic transfer functions. To do so, we assume that regional currents, originated in remote areas, are distorted and generate a local anomalous magnetic field in the investigation area that is superimposed on the regional magnetic field. Hence the phase of the anomalous magnetic field equals the phase of the regional electric field. From the observed anomalous magnetic field caused by current channelling at a near surface inhomogeneity we can then derive, from the phase, information about the strike of a regional (hidden) conductive structure.

2.1 The inducing (external) electromagnetic fields

Whereas the VLF method relies entirely on fields of artificial origin, the external fields used in the electromagnetic induction technique are of natural origin. The natural electromagnetic spectrum (Fig 2.1) is caused by fluctuations of the expanding solar corona producing the solar wind. The sun emits protons and towards the earth's magnetosphere with a velocity of some 100 km/s. This deforms the magnetosphere and creates its typical shape with a tail at the side opposite of the sun. The ionised particles are trapped in different regions of the magnetosphere (plasmasphere, VanAllen belt, tail) and in the ionosphere, creating terrestrial ring current systems, e.g. the equatorial electrojet.

The magnetic variations shown in Fig. 2.1 due to these fluctuating current systems are superimposed to the total magnetic field and can be observed as magnetic storms, sub-storms, and geomagnetic pulsations at the earth's surface. These effects caused by the solar wind are quite irregular and are strongly enhanced in periods of intensive sun spot activity in general once or twice a month and may last several days. Compared to the background strength of the magnetic field, a pulsation can enhance the spectral energy 10-100 times and will also enhance the quality of the measurement. The geomagnetic pulsations are classified into two groups: continuous pulsations (pc), with a stable pattern of oscillation exhibiting a fairly regular quasi-sinusoidal character, and irregular pulsations (pi), appearing as trains of damped oscillations. Pulsations of type pc3, pc4 and pc5 occur almost every day in daytime and are used

for MT and GDS studies (Rokityansky, 1982). Their abundance, shown in Tab. 2.1, is strongly dependent on the dynamics of the ionosphere between night and day (Beniof, 1960).

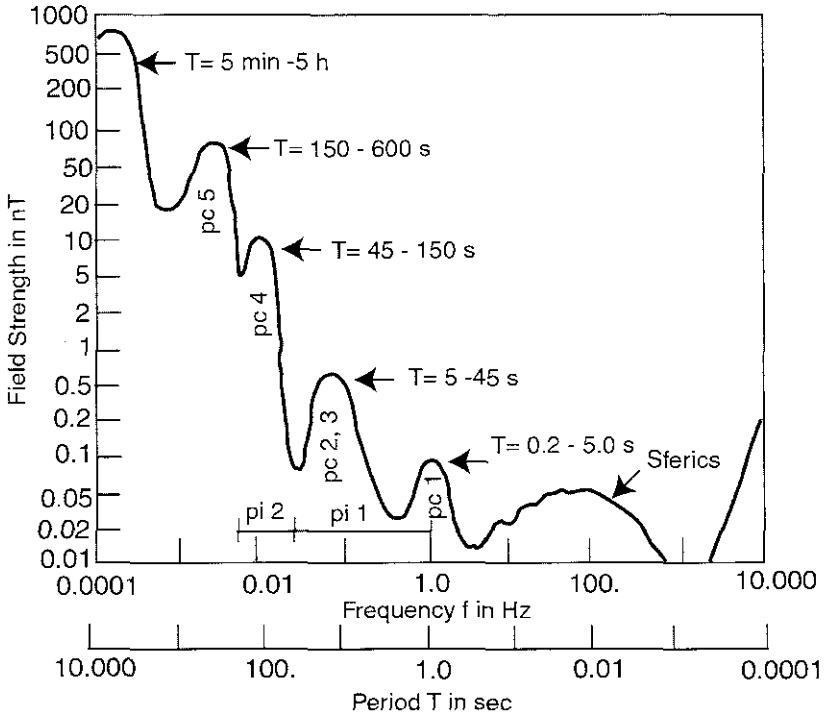

Fig. 2.1: The electromagnetic spectrum. Redrawn from Campbell et al. (1967)

period T in s	Time of most frequent occurrence
0.3 - 2.5	Night
3 - 8	Synchronous with polar lights
7 – 30	Day
40 – 120	24.00 (local time)

Tab. 2.1: Abundance of pulsations (Beniof, 1960).

Sferics (f= 1Hz – 1 GHz) are electromagnetic impulses that are created by lightning strokes and are therefore associated with the global thunderstorm activity in the equatorial region. They propagate around the world, trapped in the wave-guide formed by the surface and the lowermost ionised layer (D-layer) of the ionosphere. This D-layer vanishes at night and in day-time it is created by interactions with photons and ionised gas. Variation in the height of the wave-guide during night and day also leads to diurnal variations in the spectra of the sferics. The propagation of the signal in the wave-guide generates Schumann resonances with local maxima at the frequencies f= 8, 14, 20, 26 and 31 Hz (Fig. 2.2).

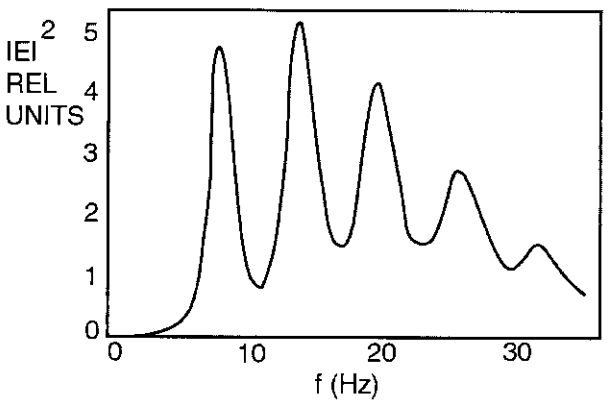

Fig. 2.2: The spectrum of the Schumann resonance. Redrawn from Volland (1984)

Man-made noise produced e.g. by power lines, electric fences and radio transmitters are part of the background spectra. Their influence on the data quality depends not only on the abundance of the source and its field strength but also on the conductivity of the subsurface. In a subsurface of low resistivity, noise will be soon attenuated (Lange, 1985), whereas in highly resistive regions the influence of e.g. a DC train (Schnegg & Fischer, 1986) in the data will still be visible at a distance of about 30 km.
Artificial noise can be used when the distance between the survey area and the source is greater than a few of skin-depths.

2.2 The transfer function in some electromagnetic induction techniques

We have used different geophysical methods that use natural and artificial time varying magnetic fields. Because of their physical principles the methods are closely related.

They are:
i) geomagnetic deep sounding (GDS)
ii) magnetotelluric sounding (MT)
iii) very low frequency technique (VLF)

In this chapter the author gives a simple introduction to these techniques on the basis of a signal analysis. This avoids sophisticated mathematical expressions and introduces the fundamental concept of a transfer function. Overviews of the basic aspects and applications of this analysis are given in several text-books (Lüke, 1991; Schwartz & Shaw, 1975; Gold & Rader, 1969). If not otherwise mentioned, the following paragraphs refer to the cited texts.
The general principle is as follow: to gain information about the subsurface, a time varying electromagnetic signal is applied to the surface and the response of this signal is recorded. The response will have the form of the initial signal transformed by the physical properties of the subsurface. In general it will also contain some distorting effects which may often come from outside the survey area. The study of these transformation mechanisms is the task of our investigation.

2.2.1 The earth as a Linear Time Invariant System (LTI)

The assumption is made that the subsurface consists of different isotropic media that create either a one-dimensional (1-D, $\sigma = \sigma(z)$) or two-dimensional (2-D, $\sigma = \sigma(y,z)$) conductivity distribution with a plane surface separating the conductive earth from the air, considered to be a perfect insulator. The x and y axes of the Cartesian coordinate system identify the earth's surface, the vertical axis z points downwards.

Let us consider the earth's substratum as a system or a "black box" probed by a known signal $s(t)$. To gain information on the system we must study the physics of the "black box":

$$s(t) \quad \overset{\text{black box}}{} \quad g(t)$$

The properties of the "black box" will be described by mathematically clear relations (transformations) between responses $g(t)$ and incoming signals $s(t)$:

$$g(t) = Tr\{s(t)\} \tag{1}$$

An important class of systems is the Linear Time Invariant system (LTI):

$$s(t) \quad \text{LTI} \quad g(t)$$

a) **Linear:** This means that any linear combination of incoming signals $s_i(t), (i = 1,2,3,...)$ results in the respective linear combination of responses $g_i(t)$. For any constant a_i the following superposition will be valid:

$$Tr\left\{\sum_i a_i s_i(t)\right\} = \sum_i a_i Tr\{s_i(t)\} = \sum_i a_i g_i(t) \tag{2}$$

We can therefore separate the system into several subsystems and solve the problem for each subsystem independently. The superposition of the individual solutions will contribute to the total solution. A bias in the transformation, or in the incoming signal, due to a particular constant a_i will therefore result in a biased response. Such a distorting effect, i.e. the "static shift" (Larsen, 1977), is a major problem in the magnetotelluric data analysis. The phase of the transfer function is less affected by bias effects. Thus, analysing the phase is more reliable and is especially applied in Bahr's decomposition method (Bahr, 1985).

b) **Time invariant:** Means that a time displacement t_o yields a time-shifted response:

$$Tr\{s(t - t_0)\} = g(t - t_0) \tag{3}$$

In other words, the physical properties of the subsurface do not change with time and the measurement is repeatable (we do not consider geological time scales!).

Every time varying signal $s(t)$ can be approximated by a series of Dirac impulses. With equation (2) and (3) this allows a calculation of the transfer function of the LTI system by a convolution in the time domain:

$s(t) \quad h(t) \quad g(t)$

$$\Rightarrow g(t) = s(t) * h(t) \tag{4}$$

We call $h(t)$ the **transfer function** of the LTI system.

A convolution in the time domain is equivalent to a multiplication of the respective Fourier transformed signals in the frequency domain:

$$g(t) = s(t) * h(t) \Leftrightarrow G(f) = S(f) \cdot H(f) \tag{5}$$

Hence, we find a general frequency and space dependent expression for the transfer function:

$$H(f,\mathbf{r}) = \left(\frac{G(f,\mathbf{r})}{S(f)} \right) \tag{6}$$

In general, the transfer function is complex:

$$H(f,\mathbf{r}) := Re\,H(f,\mathbf{r}) + i \cdot Im\,H(f,\mathbf{r}) \tag{7}$$

Note that the incoming or probing signal $\Im\{s(t)\} = S(f)$ is independent of the measuring point and can be obtained elsewhere, synchronously with the response signal. In combination with the linearity of the system this is used in the remote reference technique (Gamble et al., 1979). This technique often improves the evaluation of the transfer function as it permits to correct a bias from the transfer function (caused by a bias in the probing signal) by substituting the affected probing signals with the bias free signal of the remote site. When the probing signal and its response are measured at one site, the technique will be called "single site".
A typical example of time-series (from the Valais survey, Schnegg, 1998) recorded simultaneously at two remote sites is shown in Fig. 2.3. The sites are located 18 km apart and illustrate the laterally fairly homogenous horizontal magnetic fields (probing signal). The electrical field variations and the vertical magnetic field (i.e. the responses) strongly depend on the local geology.

Since we want to probe the subsurface with a time varying magnetic field of the form

$$s(t) = \mathbf{B} = \begin{pmatrix} |B_x| \\ |B_y| \\ B_z \end{pmatrix} \cdot e^{i\omega t} \quad , \tag{8}$$

the skin-effect will yield transfer functions that are related to different propagation depths of the wave. In the electromagnetic induction technique we often use the term skin-depth δ_{skin} at which the electromagnetic wave is attenuated by a factor $1/e$ from its surface amplitude:

$$\delta_{skin} = \sqrt{\frac{2}{\omega\mu\sigma}} \approx 0.5\sqrt{T\rho} \text{ in km.} \qquad (9)$$

The longer the period of the electromagnetic wave, the deeper it penetrates into a halfspace of uniform conductivity. Due to the linearity of the system it is possible to apply signals of different periods to calculate a series of depth dependent transfer functions at one measuring point. Tab. 2.2 shows a list of skin-depths for various periods and resistivities of host rocks, typical for EM studies.

	T= 1 s	**T =10 s**	**T =100 s**
ρ = 10 Ωm	1.6 km	5 km	16 km
ρ = 100 Ωm	5 km	16 km	50 km
ρ = 1000 Ωm	16 km	50 km	160 km
ρ = 10000 Ωm	50 km	160 km	500 km

Tab. 2.2: Skin-depths for various periods and resistivities of the host rock.

2.2.2 The transfer function in GDS

The GDS technique uses a primary time varying horizontal magnetic field of various polarisation azimuths that penetrates into the ground and induces eddy currents (or telluric currents) in the earth. If a lateral conductivity gradient is present (Fig. 2.4) this current system will be the source of a secondary magnetic field with a pronounced vertical component. The method is therefore sensitive to lateral changes of the electrical conductivity.
Since the secondary field strength in the horizontal component is much smaller than the corresponding primary field, $|\mathbf{B}_P| >> |\mathbf{B}_S|$ (Parasnis, 1986), we only use the vertical component as response to the inducing primary field:

$$(B_{Px}, B_{Py}, 0) \qquad A, B \qquad (0, 0, B_{Sz})$$

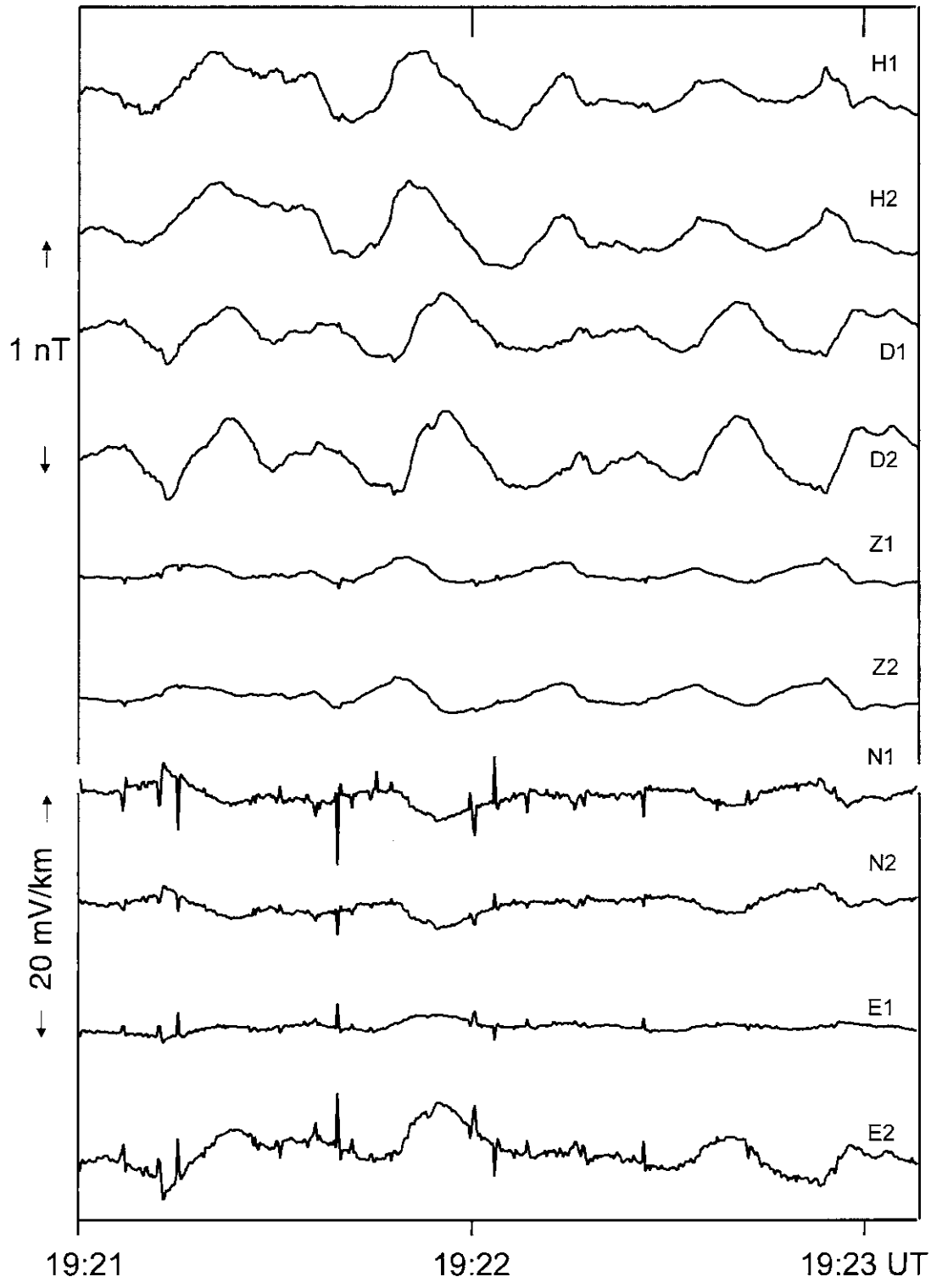

Fig. 2.3: Magnetic and electric signals, simultaneously recorded at sites TOU(1) and LUS(2) in the time interval 19:21-19:23 UT on 30 September 1992. H, D, Z components refer to magnetic north, east, and vertical. Components N and E refer to north and east electric fields, Schnegg (1998).

$$\Rightarrow \begin{pmatrix} 0 \\ 0 \\ B_{Sz}(f,\mathbf{r}) \end{pmatrix} = \begin{pmatrix} A(f,\mathbf{r}) \\ B(f,\mathbf{r}) \\ 0 \end{pmatrix} \cdot \begin{pmatrix} B_{Px}(f) \\ B_{Py}(f) \\ 0 \end{pmatrix} \tag{10}$$

$$\Rightarrow B_{Sz}(f,\mathbf{r}) = A(f,\mathbf{r}) \cdot B_{Px}(f) + B(f,\mathbf{r}) \cdot B_{Py}(f) \tag{11}$$

Thus, $A(f,\mathbf{r})$ and $B(f,\mathbf{r})$ are the complex transfer functions in GDS.

2.2.3 The transfer function in MT

Instead of measuring the secondary magnetic field, the magnetotelluric technique uses pairs of electrodes (Fig. 3.3) to measure the horizontal electrical field of the induced telluric currents. Magnetic and electric field components are linearly related via the impedance of the surface:

$$(B_{Px},B_{Py},0) \qquad \begin{matrix} Z_{xx} & Z_{xy} \\ Z_{yx} & Z_{yy} \end{matrix} \qquad (E_x,E_y,0)$$

$$\Rightarrow \begin{pmatrix} E_x(f,\mathbf{r}) \\ E_y(f,\mathbf{r}) \end{pmatrix} = \begin{pmatrix} Z_{xx}(f,\mathbf{r}) & Z_{xy}(f,\mathbf{r}) \\ Z_{yx}(f,\mathbf{r}) & Z_{yy}(f,\mathbf{r}) \end{pmatrix} \cdot \begin{pmatrix} B_{Px}(f) \\ B_{Py}(f) \end{pmatrix}. \tag{12}$$

The four complex elements of the impedance tensor

$$\underline{\mathbf{Z}} = \begin{pmatrix} Z_{xx}(f,\mathbf{r}) & Z_{xy}(f,\mathbf{r}) \\ Z_{yx}(f,\mathbf{r}) & Z_{yy}(f,\mathbf{r}) \end{pmatrix} \tag{13}$$

constitute the transfer function in MT. This method leads to apparent resistivities and their phases and in 1-D situations makes it possible, at least in principle, to derive the conductivity distribution with depth.

2.2.4 The transfer function in VLF

In the following paragraphs the frequency and spatial dependence will no longer always be written explicitly.
Figure 2.4 illustrates the principle of the VLF technique. It uses the magnetic fields induced in the earth by broadcasting stations. The method does not give a direct estimate of the electrical conductivity but is a most popular electromagnetic tool for mapping near-surface lateral conductivity contrasts. The transmitter is considered to be at a distance greater than several free space wave-lengths from the geological structure, which is represented here by an electrically conductive dyke of infinite extension embedded in a layered half-space. Note that here the strike of the dyke and the antenna are in line and delineate the x-axis of the Cartesian coordinate system. An

alternating current (AC) of a single frequency $f = 2\pi\omega = 1/T$ applied to the antenna causes a horizontal primary magnetic field:

$$\mathbf{B_P} = (B_{Px}, B_{Py}, 0). \tag{14}$$

At the survey point the primary electromagnetic wave-front can be considered as quasi-linear. This means that there is only one polarisation azimuth:

$$\mathbf{B_P} = (0, B_{Py}, 0). \tag{15}$$

This will induce eddy currents within the dyke:

$$\mathbf{E} = (E_x, 0, E_z), \tag{16}$$

which in turn generate secondary magnetic fields:

$$\mathbf{B_S} = (0, B_{Sy}, B_{Sz}). \tag{17}$$

With an orthogonal coil system (y- and z-axis), the superposition of primary and secondary magnetic field can then be measured:

$$\mathbf{B_R} = \mathbf{B_P} + \mathbf{B_S}. \tag{18}$$

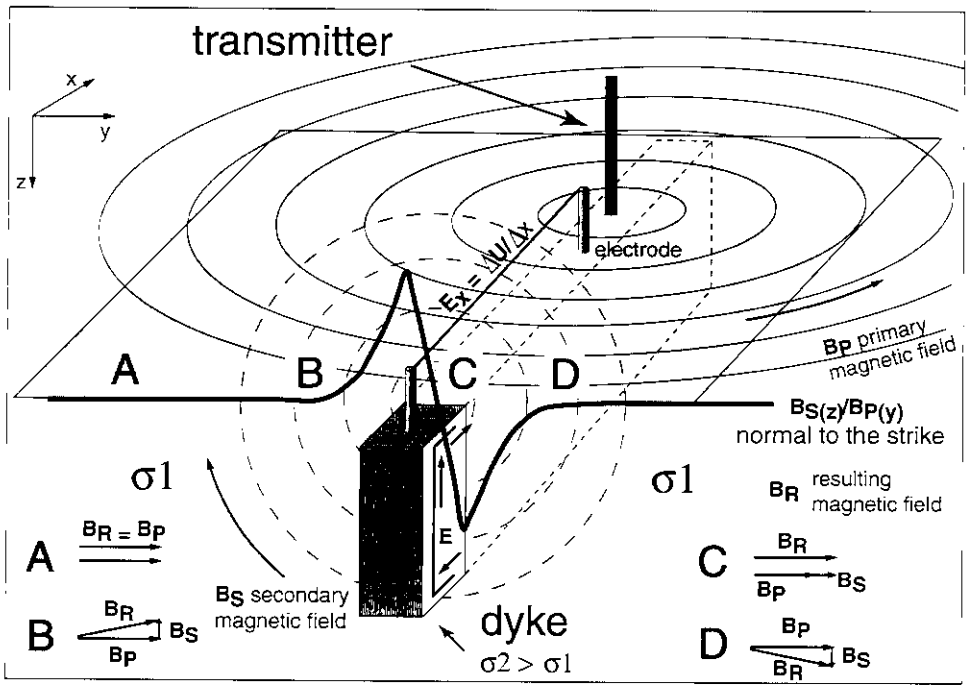

Fig. 2.4: The Electromagnetic Induction Method and the resulting out-of-phase curve over a conductive dyke. Superposition of the primary and secondary magnetic field at observation points A. B. C and D. $\mathbf{B_R}$ is along y-axis and $\mathbf{B_S}$ is along z-axis Modified fromr Turberg (1992).

The change in the "in-phase" and "out of-phase" (synonyms for real and imaginary) ratio of primary to secondary magnetic fields B_{Sz}/B_{Py} over a profile directly reflects geological features such as fractures, faults and lateral facies/permeability contrasts.

Obviously, this technique is similar to the GDS method, but is generally only used for a 2-D conductivity distribution with $\sigma = \sigma(y,z)$:

$$(0, B_{Py}, 0) \qquad B \qquad (0, 0, B_{Sz})$$

$$\Rightarrow B(f,\mathbf{r}) = \left(\frac{B_{Sz}(f,\mathbf{r})}{B_{Py}(f)} \right), \tag{19}$$

with $B(f,\mathbf{r})$ the complex transfer function in VLF.

2.2.5 The VLF technique as a special 2-D case of GDS

The VLF technique actually yields the transfer function $B_{Sz}/B_{Py} = B$ in the particular case of the measuring configuration in which x and the induced telluric current (and therefore the electric field) are in line with the strike of the structure. The transfer function $B_{Sz}/B_{Px} = A$ normal to the strike vanishes as no telluric currents are induced in this direction.
If we now assume, that the strike direction θ_r of the structure does not coincide with the coordinate system of observation the antenna will not be in line whith the strike and none of the components (A, B) in VLF will vanish. With only one transmitter of polarisation azimuth ϑ_1 the analysis is not possible. To compose the full set of transfer functions an additional independent polarisation azimuth ϑ_2 of the primary field is necessary. This means that another transmitter of the same (or nearly the same) frequency $f_1 \cong f_2$, but of different direction $|\alpha_1 - \alpha_2| > 30°$ must be found (Radic & Aschmann, 1998), to produce a phase lag.

$B_{z1} = A \cdot B_{x1} + B \cdot B_{y1}$ transmitter 1, frequency f_1, direction α_1
$B_{z2} = A \cdot B_{x2} + B \cdot B_{y2}$ transmitter 2, frequency f_2, direction α_2.

For an average frequency $\bar{f} = \sqrt{f_1 \cdot f_2}$ it can be shown (Radic & Aschmann, 1998) that:

$$A(\bar{f},\mathbf{r}) = \frac{\dfrac{B_{z2}}{B_{y2}} - \dfrac{B_{z1}}{B_{y1}}}{\dfrac{B_{z2}}{B_{y2}}\left(\dfrac{B_{z2}}{B_{x2}}\right)^{-1} - \dfrac{B_{z1}}{B_{y1}}\left(\dfrac{B_{z1}}{B_{x1}}\right)^{-1}} \quad \text{and}$$

$$B(\bar{f},\mathbf{r}) = \frac{\dfrac{B_{z2}}{B_{x2}} - \dfrac{B_{z1}}{B_{x1}}}{\dfrac{B_{z2}}{B_{x2}}\left(\dfrac{B_{z2}}{B_{y2}}\right)^{-1} - \dfrac{B_{z1}}{B_{x1}}\left(\dfrac{B_{z1}}{B_{y1}}\right)^{-1}}. \qquad (20)$$

2.2.6 Composition of the transfer function for a 2-D structure derived from E- and B-Polarisations

As seen in the previous paragraph, for a 2-D conductivity distribution with a (regional) strike direction chosen along the x-axis and therefore with $\sigma = \sigma(y,z)$, the transfer functions in VLF, GDS and MT are *composed* of two de-coupled principal components. They are determined by two linear and independent polarisation azimuths of the primary magnetic field:

- The component of the transfer function whose electrical field is along the strike of the structure is called the E-Polarisation of the transfer function.
- The component of the transfer function whose electrical field is normal to the strike of the structure is called the B-Polarisation of the transfer function.

For a 3-D conductivity distribution $(\sigma = \sigma(x,y,z))$, the distinction between E-Polarisation and B-Polarisation is no longer applicable.
Note that the linearity of the system provides to compose or decompose any 3-D conductivity distribution into several 1-D, 2-D subsystems plus a subsystem that represents the distorting effects due to small- scale inhomogeneities. Each subsystem can be treated separately.

2.2.7 Determining the transfer function in GDS and MT

The transformation of the recordings (timeseries of the magnetic and electric fields) into the frequency domain is generally accomplished by a Fast Fourier Transformation (FFT). The evaluation of the GDS and MT transfer function from the auto- and cross-spectral densities is done with the technique of the robust transfer function estimation, pioneered by Egbert (Egbert & Booker, 1986). Those techniques use a bivariate analysis of the linear system.
But the recordings and therefore the spectra of the probing signal $S(f)$ and of the response $G(f)$ of the system are not free of noise. With the assumption that only one of the channels is affected by noise, we obtain three sets of estimates for the transfer function. Over a large distance, the homogenous magnetic field is less disturbed. Hence in this study we consider that there is only noise in the response: The noise $\Delta G(f)$ is random, independent of the signal, and its variance is time dependent. The basic idea is to estimate the values of the transfer functions a and b from a series of stochastic measurements:

$$G(f) = aS_x(f) + bS_y(f) + \Delta G(f). \qquad (21)$$

This can be done by means of least square procedures, as shown in several publications (Swift, 1967; Vozoff, 1972; Hermance, 1973; Scheelke, 1972).

The estimates of $\bar{a}(f)$ and $\bar{b}(f)$, that minimise in the equation (21) the average sum of the least square mistakes $\overline{SF} = \left[\Delta G(f) \cdot \Delta G^*(f)\right]$, are given by
(Jenkins & Watts, 1968):

$$\bar{a}(f) = \frac{[GS_x^*]\cdot[S_yS_y^*] - [GS_y^*]\cdot[S_yS_x^*]}{[S_xS_x^*]\cdot[S_yS_y^*] - [S_xS_y^*]\cdot[S_yS_x^*]} \text{ and}$$

$$\bar{b}(f) = \frac{[GS_y^*]\cdot[S_xS_x^*] - [GS_x^*]\cdot[S_xS_y^*]}{[S_xS_x^*]\cdot[S_yS_y^*] - [S_xS_y^*]\cdot[S_yS_x^*]}. \qquad (22)$$

Note that the denominator of the equation will vanish if $S_x(f)$ and $S_y(f)$ are completely correlated, as is the case in the traditional VLF technique (see 2.2.5).

GDS:
Replacing equation (21) with:

$$B_{Sz}(f,\mathbf{r}) = A(f,\mathbf{r}) \cdot B_{Px}(f) + B(f,\mathbf{r}) \cdot B_{Py}(f) + \Delta B_{Sz}(f,\mathbf{r}) \qquad (23)$$

leads to the transfer function in GDS.

MT:
With the approach that the measured magnetic field is free of noise, we obtain four stable complex estimates for the components of the MT transfer function:

$$\underline{\mathbf{Z}}^{\mathrm{E}} = \begin{pmatrix} Z_{xx}^{E_x} & Z_{xy}^{E_x} \\ Z_{yx}^{E_x} & Z_{yy}^{E_x} \end{pmatrix} \text{ (noise, either in } E_x \text{ or } E_y\text{), with:}$$

$$Z_{xx}^{E_x} = \frac{[E_xB_x^*][B_yB_y^*] - [E_xB_y^*][B_yB_x^*]}{[B_xB_x^*][B_yB_y^*] - [B_xB_y^*][B_yB_x^*]},\quad Z_{xy}^{E_x} = \frac{[E_xB_y^*][B_xB_x^*] - [E_xB_x^*][B_xB_y^*]}{[B_xB_x^*][B_yB_y^*] - [B_xB_y^*][B_yB_x^*]},$$

$$Z_{yx}^{E_y} = \frac{[E_yB_x^*][B_yB_y^*] - [E_yB_y^*][B_yB_x^*]}{[B_xB_x^*][B_yB_y^*] - [B_xB_y^*][B_yB_x^*]},\quad Z_{yy}^{E_y} = \frac{[E_yB_y^*][B_xB_x^*] - [E_yB_x^*][B_xB_y^*]}{[B_xB_x^*][B_yB_y^*] - [B_xB_y^*][B_yB_x^*]} \qquad (24).$$

2.3 Parameters

2.3.1 Parameters in Geomagnetic Deep Soundings

The two magnetic transfer functions (A,B) bear information on the lateral conductivity distribution and can be expressed as real and imaginary induction arrows (Schmucker, 1970):

$$\mathbf{P}(f) = Re\,A(f)\hat{\mathbf{x}} + Re\,B(f)\hat{\mathbf{y}} \tag{25}$$

$$\mathbf{Q}(f) = Im\,A(f)\hat{\mathbf{x}} + Im\,B(f)\hat{\mathbf{y}} \tag{26}$$

The arrows are the projections of the magnetic field on the surface, their length is a measure of the lateral conductivity gradient. Since they are perpendicular to the direction of current flow (Schmucker, 1970), their direction permits to map the strike direction of the lateral conductivity distribution. The lengths and direction of the induction arrows are given by:

$$L_{\mathrm{P}} = \sqrt{ReA^2 + ReB^2}\,, \qquad \theta_{\mathrm{P}} = arctan\left(\frac{ReB}{ReA}\right), \tag{27}$$

$$L_{\mathrm{Q}} = \sqrt{ImA^2 + ImB^2}\,, \qquad \theta_{\mathrm{Q}} = arctan\left(\frac{ImB}{ImA}\right). \tag{28}$$

The maps displaying the induction arrows are often not easy to read (see Fig.1.2 as an example). This is probably the reason why in recent years the literature lacks relatively modern compilations. In a recent paper (Wybraniec et al., 1999; Wybraniec, 1997) a new method of presenting the arrow fields is introduced, using a 2-D Hilbert transformations (Nabighian, 1984). After transformation the maps contain the same information as the original ones, but the pattern of anomalies is clearer. Fig. 2.5 shows the transformed data from the European induction arrow distribution in Fig.1.2. This technique has recently been used to transform magnetic transfer functions obtained by the VLF/GDS technique into apparent resistivities and phases known from the MT method (Gharibi & Pedersen, 1999).
The Hypothetical Event Analysis (HEA) is another alternative technique to map conductivity contrasts based on the study of the magnetic transfer function. This technique will be introduced in a following section.

2.3.2 Parameters in Magnetotellurics

1-D:
The conductivity distribution is only dependent on the depth and for the MT impedance yields a symmetric relation:

$$\underline{\mathbf{Z}} = \begin{pmatrix} 0 & Z_{xy} \\ Z_{yx} & 0 \end{pmatrix}, \text{ with } Z_{xy} = -Z_{yx}\,. \tag{29}$$

2-D:
The conductivity distribution is a function of the depth and of one horizontal direction:

$$\underline{\mathbf{Z}} = \begin{pmatrix} 0 & Z_{xy} \\ Z_{yx} & 0 \end{pmatrix} = \begin{pmatrix} 0 & Z_E \\ Z_B & 0 \end{pmatrix}, \text{ with } Z_{xy} \neq -Z_{yx}, \quad (30)$$

But this is only true, if the orthogonal coordinates are aligned with the direction of the geological strike, as had for example been assumed for the VLF technique. Otherwise, the diagonal elements of the tensor will not vanish and we cannot immediately distinguish between a 3-D and a 2-D conductivity distribution. For this purpose, the skew is a useful parameter. By definition it vanishes for a 1-D and a true 2-D conductivity distribution.

Using:

$$\begin{aligned} S_1 &= Z_{xx} + Z_{yy}, \\ S_2 &= Z_{xy} + Z_{yx}, \\ D_1 &= Z_{xx} - Z_{yy}, \\ D_2 &= Z_{xy} - Z_{yx}, \end{aligned} \quad (31)$$

With the exception of S_2 the other parameters in equations (31) are for a 2-D conductivity distribution invariant against a rotation of the tensor (Fischer & Masero, 1994) we derive the skew after Swift (1967):

$$S_{Swift} = \left| \frac{S_1}{D_2} \right|, \quad (32)$$

valid only for a purely inductive transfer function. After Scheelke (1972) we can treat a general 3-D structure as a 1-D case for skew values of S<0.3, as a 2-D distribution for values S<0.6. But according to Bahr (1991), three-dimensionality and distorting effects already affect the transfer function when S> 0.1.

From the tensor elements we get the apparent resistivities and their phases:

$$\rho_{a_{ij}} = 0.2 \cdot T \left| Z_{ij} \right|^2 \quad (33)$$

$$\varphi_{ij} = arctan\left(\frac{ImZ_{ij}}{ReZ_{ij}} \right), \text{ with the indices } i = x, y \text{ and } j = y, x \ . \quad (34)$$

Plots of the phases and the logarithmic apparent resistivities against the logarithmus of the signal period are commonly used to present MT studies.

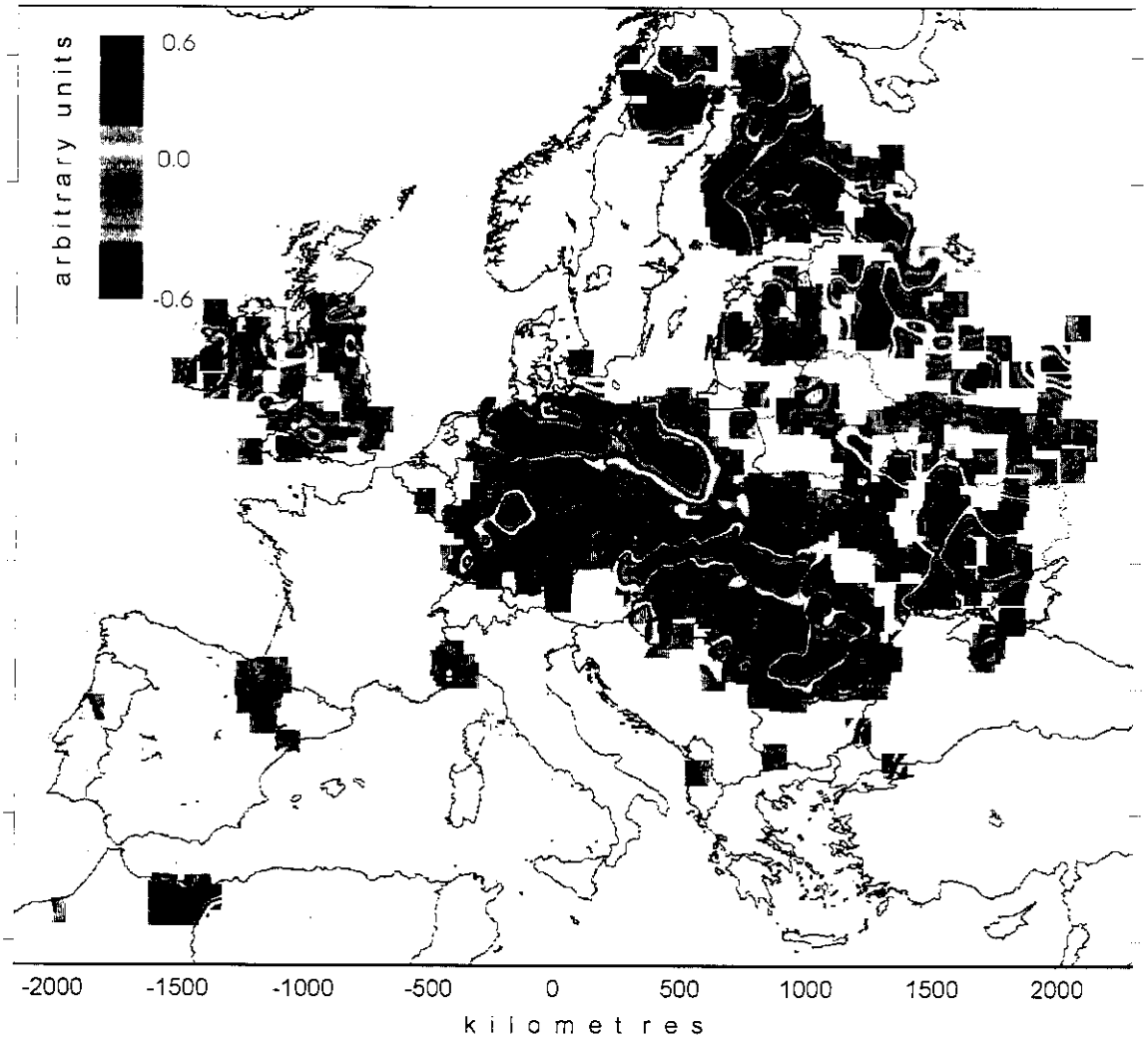

Fig. 2.5: The geomagnetic induction arrow field after 2-D Hilbert transformation. Scalar sum of the Hilbert transform parameters A and B. Conductivity anomalies appear in dark colours. (Wybraniec et al., 1999).

2.3.3 Simple decomposition of the 2-D MT transfer function into E- and B-Polarisations

Swift (1967) presented a decomposition of the transfer function into the principal impedances Z_E and Z_B by rotating the orthogonal measuring coordinate system into the direction of the geological strike. He minimised (or maximised) the norm of the diagonal elements

$$\left|Z'_{xx}\right|^2 + \left|Z'_{yy}\right|^2 = min, \qquad (35)$$

to calculate a rotation angle that, at a given period, determines the (local) strike of the structure:

$$\vartheta_{Swift} = \frac{1}{4} arctan\left(\frac{2\,Re\left(D_1^* S_2\right)}{|D_1|^2 - |S_2|^2}\right) \pm \frac{\pi}{2}. \qquad (36)$$

As for the skew after Swift, the strike obtained by this equation is only true for a non distorted transfer function.
As is clear from equation. (36), the rotation angles are indefinite to $\pm 90°$. To differentiate between E-and B-Polarisation cases, the induction arrows are a helpful parameter.
After $\underline{\mathbf{Z}}$ has been estimated, e.g. in the geographical coordinate system, it can be rotated (positive, clockwise) into the system of the geological strike:

$$\underline{\mathbf{Z}}^{\circ} = \underline{\mathbf{R}}\underline{\mathbf{Z}}\underline{\mathbf{R}}^{\mathrm{T}}, \text{ with } \underline{\mathbf{R}} = \begin{pmatrix} cos\theta & sin\theta \\ -sin\theta & cos\theta \end{pmatrix}. \qquad (37)$$

From the rotated impedances we can extract a parameter that contributes to the electrical anisotropy of the MT transfer function:

$$Anis = \max\left(\frac{|Z'_{xy}|}{|Z'_{yx}|}, \frac{|Z'_{yx}|}{|Z'_{xy}|}\right). \qquad (38)$$

2.4 Distortion of the GDS and MT transfer function

The study of near-surface lateral conductivity variations and of their static-shift effects on 2-D magnetotelluric transfer functions has intensified over the past decades. The linearity of the system provides the possibility to separate local distortion effects from regional information in the transfer function. Different decomposition techniques to overcome the telluric distortion effects in the MT transfer functions have been published (Groom & Bailey, 1989; Bahr, 1985, Poll et al., 1989; Chave & Smith, 1994; Lilley, 1993; Zhang et al., 1987; Zhang et al., 1993; Bahr, 1991; Groom & Bahr, 1991).

In some field examples it is found that on elongated conductive structures the real part of the induction arrows align with the strike of the conductor (Arora & Adam, 1992). These authors state that this distinctive anomalous behaviour of the induction arrows seems to be not only controlled by the superposition of several 2-D conductors creating a 3-D conductivity distribution, but also by the length of the conductive body relative to the period of the signal. Recent papers discuss the magnetic distortion of the GDS transfer function and show a technique for data arrays, e.g. the Hypothetical Event Technique, to recover the regional strike direction(s) from distorted data, even if a strong, spatially varying regional vertical field component is present in the data (Ritter, 1996; Ritter & Banks, 1998; Gurk, 1999).

2.4.1 Local and Regional conductive structures

Electromagnetic investigations are usually intended to examine regional structures where induction takes place at a given long period range. However, the regional information is often distorted by galvanic effects at local conductivity boundaries and/or by telluric currents that are injected into the investigation area. Conductive bodies causing this problem are typically too small or too shallow to be involved in the induction processes at the relevant period range, and thus produce no 2-D or 3-D inductive transfer functions. They are therefore referred to as *local* inhomogeneities, as opposed to *regional* structures, that do have an electromagnetic response originating from induction within the local perturbation (Ritter, 1996).

In general, we address our observations to the distortion effect caused by the three-dimensional tectonic setting of the conductive structures in the upper and lower crust. Locally, we suspect near-surface inhomogeneities to cause current channelling and/or deflection (Rokityansky, 1982; Jiracek, 1990), which are likely to affect the directions of the induction arrows and distort the MT transfer function. Moreover, telluric currents, that originate in remote regional structures can be injected into the investigation area and be concentrated or deflected by local structures. The currents may be related to local or regional induction processes. These currents can also be injected from structures elsewhere at the surface of the globe, outside the survey area (Fischer, 1984). Consequently, the investigation area may be too small to account for regional or global effects on the data. In those cases, the regional electrical strike determined from single site MT data for the computation of reliable E- and B-mode impedances for modelling the data might be misleading (Bahr, 1988; Jones & Groom, 1993). Hence, the observed induction arrows will not confirm the regional strike obtained by MT transfer function analysis. Such observations may result from a 3D tectonic setting of the structures (macro-anisotropy) and/or may be caused by strong electrical anisotropy of the subsurface. Many studies dealing these questions are well known, for instance, from the Rhine Graben (Tezkan, 1988; Tezkan et al., 1996) or from the KTB (Kontinentale Tiefenbohrung) in Bavaria (Eisel, 1995; Eisel & Haak, 1999). If GDS data are available, the Hypothetical Event technique provides a tool to visualise anomalous current concentrations.

2.4.2 Magnetic Distortion

The local superposition of an anomalous magnetic field $\mathbf{B}^a$ on a regional field $\mathbf{B}^r$ causes a magnetic distortion: the measured field $\mathbf{B}$ is then the sum of the regional and anomalous fields $\mathbf{B}^r + \mathbf{B}^a$. The anomalous field (B_x^a, B_y^a, B_z^a) is generated by the spatial deviation of uniform regional currents through or around a local anomaly, which is assumed to be much smaller than the skin-depth at the investigated period range (Groom & Bahr, 1991). In this case $\mathbf{B}^a$ can be seen to be in phase with the regional electric field $\mathbf{E}^r$ (Groom, 1988). Similarly to the galvanic distortion effect of the regional electric field (Bahr, 1985; Groom, 1988), magnetic distortions of the regional magnetic field can be expressed by a frequency independent real distortion matrix $\underline{\mathbf{D}}$:

$$\mathbf{B}^a = \underline{\mathbf{D}} \cdot \mathbf{E}^r. \qquad (39)$$

Replacing the regional field $\mathbf{E}^r$ by the product of the regional MT impedance $\underline{\mathbf{Z}}^r$ and the regional (horizontal) magnetic field $\mathbf{B}^r$, we obtain:

$$\mathbf{B}^a = \underline{\mathbf{D}} \cdot \underline{\mathbf{Z}}^r \cdot \mathbf{B}^r . \tag{40}$$

This replacement is only valid if the local anomaly is sufficiently removed, either horizontally or vertically from the regional lateral conductivity boundaries (Ritter, 1996). Explicitly, if the regional conductivity distribution is 2-D, the last equation can be expressed as follows:

$$\begin{pmatrix} B_x^a \\ B_y^a \\ B_z^a \end{pmatrix} = \begin{pmatrix} D_{xx} & D_{xy} \\ D_{yx} & D_{yy} \\ D_{zx} & D_{zy} \end{pmatrix} \cdot \begin{pmatrix} 0 & Z_E \\ Z_B & 0 \end{pmatrix} \cdot \begin{pmatrix} B_x^r \\ B_y^r \end{pmatrix} \tag{41}$$

with Z_E, Z_B the principal impedances in the coordinate system of regional strike θ_r (counter-clockwise). In the coordinates of the meassurement system we obtain for the vertical component:

$$B_z^a = \left(D_{zx}, D_{zy}\right) \cdot \underline{\mathbf{R}}_{\theta_r} \cdot \begin{pmatrix} 0 & Z_E \\ Z_B & 0 \end{pmatrix} \cdot \underline{\mathbf{R}}_{\theta_r}^T \cdot \begin{pmatrix} B_x^r \\ B_y^r \end{pmatrix} \tag{42}$$

$$\Rightarrow B_z^a = A^l \cdot B_x^r + B^l \cdot B_y^r . \tag{43}$$

The components A^l and B^l of the local transfer function depend on the regional impedances Z_E, Z_B, the strike of the local inhomogeneity θ_l, the strike of the regional structure θ_r, their difference $\alpha = \theta_l - \theta_r$, and on a real distortion parameter. In practice, if we measure the magnetic variation over a local inhomogeneity and if magnetic distortion is present, the last equation replaces the commonly used equation by Schmucker (1970):

$$B_z = A^l \cdot B_x + B^l \cdot B_y . \tag{44}$$

As a consequence, the real induction arrows may not indicate the local strike, nor the regional one, but a mixture of both.
Hence, we obtain the following expression for the components of the local transfer function (Ritter, 1996):

$$A^l = D_{zx}'' \cdot \left(-Z_E \cdot \sin\theta_r \cdot \cos\alpha + Z_B \cdot \cos\theta_r \cdot \sin\alpha\right) \tag{45}$$

$$B^l = D_{zx}'' \cdot \left(+Z_E \cdot \cos\theta_r \cdot \cos\alpha + Z_B \cdot \sin\theta_r \cdot \sin\alpha\right) \tag{46}$$

with D_{zx}'' as the magnetic distortion parameter in the measurement coordinates.

To sum up, magnetic distortion on a local conductive structure depends not only on the lateral conductivity contrast, but also on its dimension relative to the skin depth of the penetrating fields, and the shape and geometry of the inhomogeneity compared to the host rocks (Ritter, 1996). Therefore, in a small conductive body at shallow depth, short period induction processes will generate strong local magnetic fields. At longer periods the same structure can also deviate or concentrate telluric currents originating from a deep regional structure. This will create an additional anomalous static magnetic field on the local response of the inhomogeneity (Ritter, 1996). The previous effect has recently been discussed as the cause of distortions in the high-resolution aeromagnetic survey of Australia (Milligan, 1999). Most important, the information about the strike of a hidden or remote regional 2-D structure comes mainly from the phase of the remote telluric currents into the investigation area.

2.4.3 Telluric Distortion

In this chapter, we introduce the principal superposition model of a regional 2-D structure and a local 3-D structure as presented by Bahr (Bahr, 1988; Bahr, 1991) and by Groom & Bailey (1989) that distorts the MT transfer function. Bahr put a special emphasis on the phase of the observed MT transfer functions. Since only telluric distortion is assumed, which means distortion of the measured components $(E_x, E_y, 0)$ of the electrical field, both elements of the two columns of the impedance tensor must contain the same phase information.
The distortion effects on the regional electrical fields (Bahr, 1985; Groom, 1988) can be expressed by a real distortion matrix, which is independent of frequency:

$$\underline{\mathbf{C}} = \begin{pmatrix} C_{xx} & C_{xy} \\ C_{yx} & C_{yy} \end{pmatrix}. \tag{47}$$

In the coordinates of the regional strike of the 2-D structure we obtain for the measured impedance tensor:

$$\underline{\mathbf{Z}} = \underline{\mathbf{C}}\underline{\mathbf{Z}}^{0} = \begin{pmatrix} -C_{xy}Z_B & C_{xx}Z_E \\ -C_{yy}Z_B & C_{yx}Z_E \end{pmatrix}. \tag{48}$$

Bahr's decomposition methods extract several parameters, that are aimed to recover the two undistorted principal impedances, the undistorted strike direction and a trustworthy undistorted dimensionality parameter (skew). The skew after Bahr (1988) with S_i, D_i as from equation (31) is:

$$S_{Bahr} = \frac{\sqrt{Im(S_2 D_1^*) - Im(D_2 S_1^*)}}{|D_{2_1}} \quad (*: \text{complex conjugate}) \tag{49}$$

and the measure of the phase difference (Bahr, 1991) of the impedance tensor:

$$\mu = \frac{\sqrt{\left|Im\left(S_2 D_1^*\right)\right| + \left|Im\left(D_2 S_1^*\right)\right|}}{\left|D_2\right|} \qquad (50)$$

are based on the analysis of the phase and are therefore less affected by bias effects caused by galvanic distortion. Bahr also uses the phase to calculate a less distorted rotation angle to recover the regional strike. In several publications he extended his decomposition method to determine, for varying classes of distortion models of increasing complexity, more reliable rotation angles. They are referred to as:

Bahr 1: (Bahr, 1988)

$$\vartheta_{Bahr} = \frac{1}{2} arctan\left(\frac{Im(S_2 S_1^*) - Im\left(D_2 D_1^*\right)}{Im\left(D_1 S_1^*\right) - Im\left(D_2 S_2^*\right)}\right) \pm \frac{\pi}{2}. \qquad (51)$$

Bahr 11: (equation 11, Bahr, 1988)

$$tan(\vartheta_{Bahr11}) = \pm\left[(B+C)/(B-C) + \left(A/(B-C)\right)^2\right]^{\frac{1}{2}} - A/(B-C)), \qquad (52)$$

with:

$$A = [S_1, D_1] + [S_2, D_2],$$
$$B = [S_1, S_2] - [D_1, D_2]$$
$$C = [D_1, S_2] - [S_1, D_2]. \qquad (53)$$

Bahr 30: (equation 30 as given by Bahr (Bahr, 1991))

Groom & Bailey (1989) presented an equivalent approach for the decomposition of the MT transfer function. They used a factorisation of the distortion matrix related to different distorting effects on the impedance tensor:

$$\underline{\mathbf{C}} = g\underline{\mathbf{TSA}} = g\begin{pmatrix} 1 & -t \\ t & 1 \end{pmatrix}\begin{pmatrix} 1 & e \\ e & 1 \end{pmatrix}\begin{pmatrix} 1+s & 0 \\ 0 & 1-s \end{pmatrix}, \qquad (54)$$

with g the site gain, $\underline{\mathbf{T}}$ the twist tensor, $\underline{\mathbf{S}}$ the shear tensor and $\underline{\mathbf{A}}$ an anisotropy or splitting tensor. The decomposition method allows a determination of the regional strike angle. Plots of twist and shear tensor components are a measure for the dimensionality of the subsurface. For a proposed local 3-D structure over a regional 2-D structure they should show a frequency independent behaviour. Nevertheless, the frequency independent amplification of the electric field (static shift factor) remains unknown in both decomposition methods.

2.5 The self-potential method

A fraction of the field work was spent deploying the self-potential technique (SP) to investigate a major structural contact zone in the survey area in which we expected to find a graphite conductivity anomaly. The self-potential equipment consists of a pair of non-polarisable Cu-$CuSO_4$ electrodes arranged on spade sticks and a voltmeter to

measure the potential differences between the two electrodes. One electrode (the base) is kept fixed whereas the second electrode is used to sample the potential field over a profile.
SP-anomalies are nearly invariant in time and can have a magnitude of up to -1.8 V (Gay, 1967). The background values may be affected by natural induced telluric current systems. If this is the case, their electric fields are superimposed to the self-potential anomaly and cause rapid fluctuations or a slow trend in the data.
In the MT technique the measurements of the components of the horizontal electric field are, as in the SP method, obtained by recording the voltage variations between grounded electrodes (Fig. 3.3) and dividing by their separation. Poll et al. (1989) state that this procedure gives the true value of the electric field only if it is uniform between the electrodes. In regions with local inhomogeneities, as assumed for the Graubünden area, this condition is not often fulfilled and in extreme cases each electrode may be in contact with soil of different conductivity. This effect will produce a pure galvanic distorting effect (static shift) on the MT data. Hence, compared to the GDS technique, the magnetotelluric method is locally more affected by small-scale conductivity inhomogeneities.

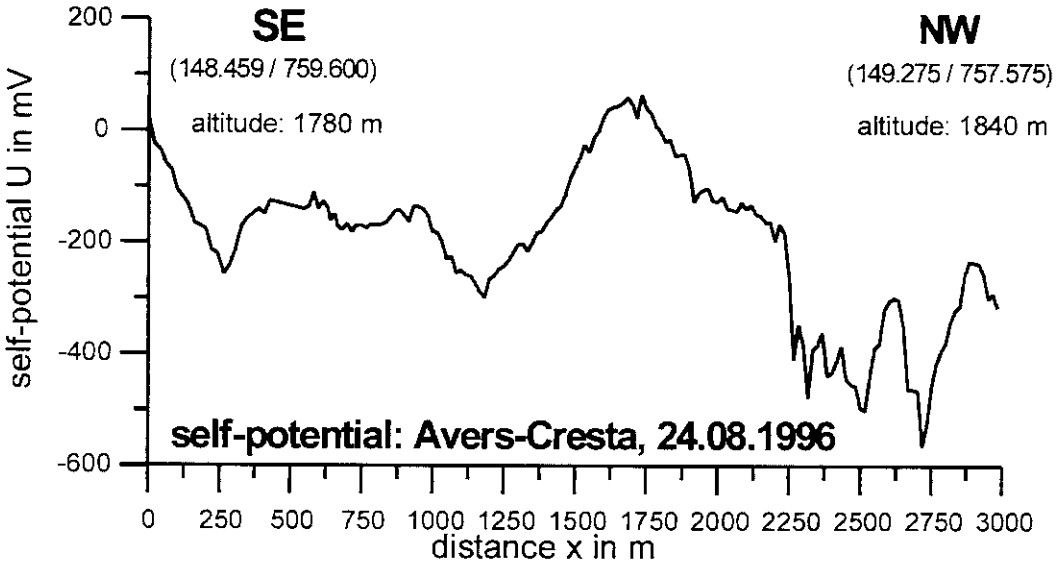

Fig 2.6: Example for a self-potential survey in the Alps of Graubünden along the contact zone Suretta nappe-Avers-Schiefer. The profile ends ca. 100 m before MT/GDS site CRE (Fig. 3.1).

A total number of 67 MT/GDS sites (Tab. 3.1 and Tab. 3.2) have been installed in the Alps of Graubünden (Fig. 3.1) during two stages. In the first field campaign, in the summer of 1996, we conducted an initial profile (I) normal to the alpine strike from the external part (Helvetic domain near the town of Ilanz) over the Penninic domain to the South Alpine units and into the Bregaglia valley (Engadine Line). The data obtained on this profile (**Grisons I**) proved the capability of the MT and GDS techniques to reveal changes in the conductivity distribution correlated with different tectonic units. The density of the projected measurements onto this ca. 60 km profile is about 4 km. It allows the detection of lateral changes in the conductivity distribution with a resolution down to about 2 km.

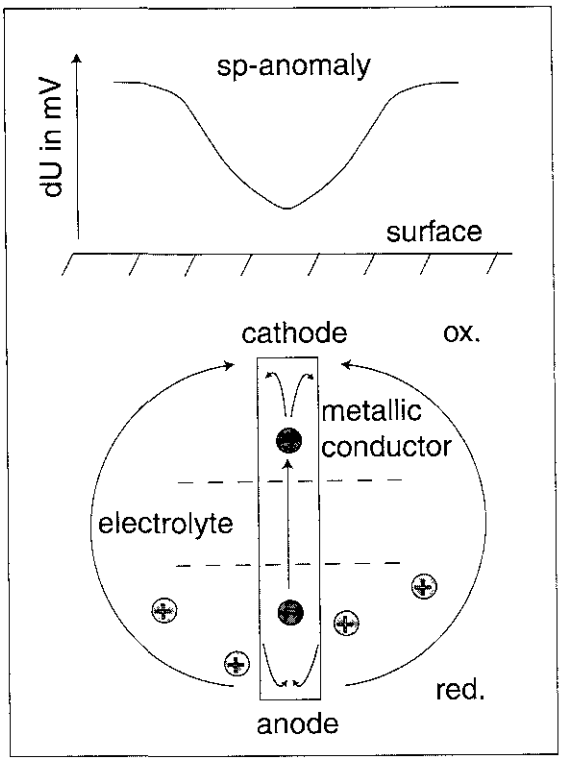

Fig. 2.7: A steeply inclined electronic conductor connects regions of different redox potentials (ox: oxidation zone, red: reduction zone) and forms a "geobattery". The redox potential difference corresponds to an electron flow from the formation into the lower end of electron conductor (anode). The electrons move to the upper end (cathode) and are transferred to the environment. (Sato & Mooney, 1960).

In hydrogeological and hydrothermal studies the self-potential caused by the streaming potential in porous media plays an important role and can be used to characterise the aquifer (Revil et al., 1999-a; Revil et al., 1999-b, Ishido et al., 1999; Michel & Zlotnicki, 1998)

Thermoelectric and/or electrokinetic coupling processes are known to generate SP anomalies (Fittermann, 1979), but they can also be produced by electrochemical processes similar to those in a galvanic cell. Geological structures showing such processes are called geobatteries (Sivenas & Beales, 1982). The conceptual model of a self-potential anomaly caused by a geobattery is shown in Fig. 2.7. According to Sato & Mooney (1960), a steeply inclined metallic conductor (graphite, pyrite, ores, etc.) connects the oxidising milieu in the subsurface and the reducing environment at depth. Due to the chemical energy of the gradient of the redox potential, electrons flow within the conductor from its lower end - the anode of the battery - upwards to the cathode. Charge conservation is insured through a simultaneous flow of ions in the formation and the voltage drop at the surface is measured as SP anomaly. Geobatteries may produce SP magnitudes of several hundreds of millivolts (Fig. 2.6) and are a strong indication for interconnected electronically conducting minerals (Bigalke & Grabner, 1997; Stoll et al., 1995).

3 MT/GDS Database

The real part induction arrows in particular, which could be evaluated in the fieldcamp, showed a change of direction over the transition zone between the Mesozoic Bündnerschiefer and the Penninic Suretta nappe. This general feature was therefore taken into account when the plan was made for the field campaign of summer 1997 (**Grisons II**). The aim was to be able to map the change of direction of the real part of the induction arrow in Graubünden, using a coarse mesh of measurements. The information derived from the calculated induction arrows of one day were helpful parameters when planning the next day's work.

site	X	Y	latitude	longitude	alt. (m)	map no.	date	location
BAM	177.125	726.175	46°44.079N	9°05.472E	1670	1214	17-21.07	Bamwald
MAR	179.3	726.75	46°45.247N	9°05.960E	1140	1214	17-19.07	Maracal
TER	172.875	734.5	46°41.688N	9°11.938E	1410	1214	20-23.07	Tersnaus
MUR	175.275	729.9	46°43.038N	9°08.367E	1690	1214	22-24.07	Murtens
SAF	165	740.875	46°37.359N	9°16.798E	1682	1234	24-28.07	Safien
BOD	162.75	741.35	46°36.139N	9°17.129E	1810	1234	24-28.07	Bodenaelpli
SUF	161.3	749.125	46°35.255N	9°23.195E	1990	1235	29-31.07	Sufer
ROS	158.65	748.6	46°33.832N	9°22.733E	1710	1235	29-31.07	Rosschopf
AUS	157.625	754.075	46°33.204N	9°27.001E	1565	1255	31-02.08	Ausserferrera
BLE	153.538	754.775	46°30.990N	9°27.467E	1762	1255	31-05.08	Bleis
PLA	152.675	756.225	46°30.504N	9°28.584E	1889	1255	02-05.08	Plan
CRE	149.3	757.8	46°28.660N	9°29.748E	1885	1255	05-08.08	Cresta
VOR	145.35	762.45	46°26.462N	9°33.302E	1990	1276	05-08.08	Vord.Bergalga
JUF	144.95	765.475	46°26.201N	9°35.658E	2150	1276	08-11.08	Juf/Plangga
CUR	165.3	746.075	46°37.454N	9°20.881E	2330	1235	09-11.08	Curtiginatschten
TEN	179	745.8	46°44.851N	9°20.927E	1415	1215	14-16.08	Tenna
CAM	168.725	741.125	46°39.366N	9°17.063E	1715	1234	14-16.08	Camana Wald
PAS	180.3	755.525	46°45.420N	9°28.598E	1635	1215	15-18.08	Trans/Pascus
OBE	172.275	746.55	46°41.212N	9°21.388E	1785	1215	16-18.08	Obergmeind
BIV	147.475	768.75	46°27.515N	9°38.273E	1950	1256	19-21.08	Bivio
SEP	144.875	769.9	46°26.095N	9°39.115E	2119	1276	19-21.08	Septimer Pass

Tab. 3.1: MT and GDS station locations on profile (I) **Grisons I (1996)**, listed in chronological order. **X**, **Y** are the metric coordinate in the Swiss system CH1903. The **map nos.** give the number of the "Landeskarte der Schweiz, 1:25 000", the period range covered is: T= 1-300 s.

3.1 MT/GDS data acquisition

With regard to the general practical aspects of the data acquisition, including the problems of finding convenient sites for the measurements and the cultural noise due to DC trains and hydroelectrical water power plants in this survey, these problems were found to be similar to those described by Schnegg (1998).
The three instruments used in this study were developed by the Group of Geomagnetism of the University of Neuchâtel. During the first stage of the field campaign data were obtained covering the period interval T= 1–300 s. To enhance the data quality of the MT transfer functions toward shorter periods, we extended the period range to T= 0.01–300 s during the second stage. For this purpose it was necessary to modify the systems. The new instruments make it possible to switch

between the overlapping short-period (AudioMagnetoTelluric=AMT) and long-period (MT) modes. A block diagram showing the actual version of the amplifier/filter arrangement of the apparatus is given in Fig. 3.2.

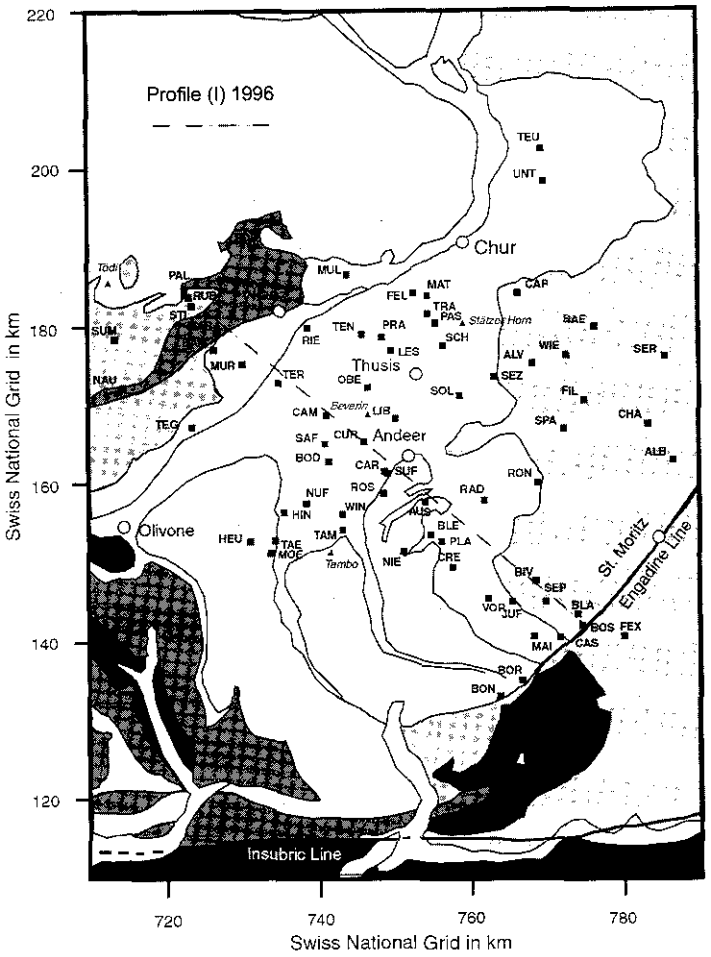

Fig. 3.1: MT/GDS site locations (filled squares) of the data-sets **Grisons I** and **Grisons II**.

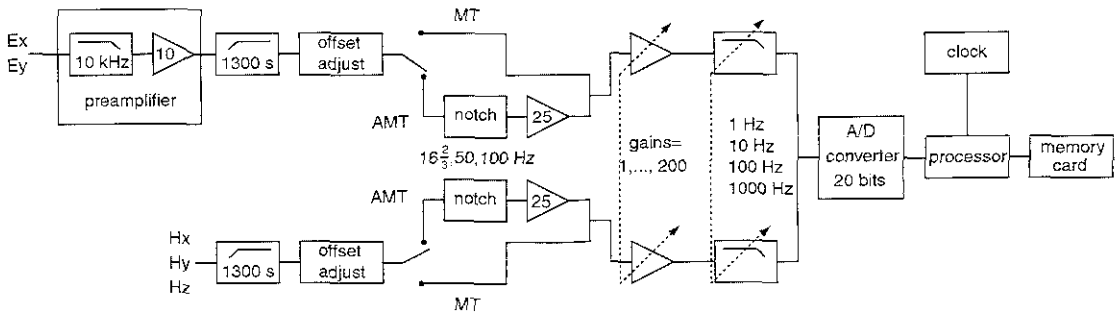

Fig. 3.2: Block diagram of the MT/GDS data acquisition system.

site	X	Y	latitude	longitude	alt. (m)	map no.	date	location
TRA	181.75	754.525	46°46.217N	9°27.841E	1540	1215	08-10.05	Trans
MAT	183.975	754.555	46°47.417N	9°27.910E	1793	1195	09-11.05	Plaun digls-Mats
FEL	184.125	752.7	46°47.523N	9°26.453E	1450	1195	10-11.05	Feldis
BOR	134.9	766.775	46°20.760N	9°36.457E	1085	1276	14-16.05	Borgonovo
FEX	140.425	780.125	46°23.533N	9°47.005E	1978	1277	15-17.05	Alp Suot/Val Fex
CAS	140.25	771.8	46°23.570N	9°40.498E	1600	1276	24-28.05	Casaccia
SCH	177.6	756.45	46°23.950N	9°29.270E	1885	1215	20-22.05	Scharans/Culm
STI	182.8	723.375	46°47.174N	9° 3.364E	1420	1193	22-24.05	Alp da Stiarls
PAL	184.6	722.45	46°48.155N	9° 2.666E	1620	1193	22-24.05	Paliu da Rubi
RUB	183.85	723.025	46°47.744N	9° 3.106E	1630	1193	22-24.05	Chischaradas
BLA	143.25	774.2	46°25.152N	9°42.440E	2030	1276	26-28.05	Blaunca
MAI	140.425	768.25	46°23.719N	9°37.729E	1910	1276	26-28.05	Maira/ Val Maroz
BON	132.875	763.8	46°19.711N	9°34.093E	1125	1296	27-28.05	Bondo
ALV	175.3	768.3	46°42.539N	9°38.532E	2220	1216	05-07.06	Alvaneu
WIE	176.275	772.675	46°42.991N	9°42.149E	1970	1216	05-07.06	Wiesner Alp
SEZ	173.65	763.175	46°41.722N	9°34.470E	1570	1216	06-08.06	Seznas/ Lenz
SOL	171.1	758.65	46°40.411N	9°30.864E	1508	1215	09-11.06	Colm da Solas
SER	176.2	785.538	46°42.747N	9°52.098E	2015	1217	09-11.06	Sertig Dörfli
BAE	179.9	776.3	46°44.894N	9°44.924E	1890	1216	10-12.06	Bärental/ Davos
PRA	178.55	748.5	46°44.572N	9°23.041E	1910	1215	12-14.06	Präzer Alp
LES	176.825	749.7	46°43.625N	9°23.950E	1463	1215	12-14.06	Lescha
MUL	186.626	743.875	46°48.990N	9°19.558E	970	1195	13-15.06	Mulin
LIB	168.325	750.15	46°39.032N	9°24.136E	2015	1235	16-18.06	Mathon
NUF	157.5	738.375	46°33.344N	9°14.703E	2049	1254	17-19.06	Nufenen
HIN	156.275	735.45	46°32.718N	9°12.390E	2151	1254	17-19.06	Hinterrhein
HEU	152.525	730.775	46°30.750N	9°08.666E	1700	1254	20-22.06	Heuberg
MOE	151.125	733.7	46°39.960N	9°10.931E	2010	1254	20-22.06	Laghetto Moesola
TAE	152.725	734.075	46°30.819N	9°11.252E	1940	1254	20-22.06	Tällialp
FIL	170.475	774.975	46°39.829N	9°43.666E	1833	1216	23-25.06	Filisur
SPA	166.8	772.4	46°37.889N	9°41.562E	2010	1236	23-25.06	Piz Spadlatsch
ALB	162.775	786.663	46°35.485N	9°52.655E	2280	1237	24-26.06	Albula Pass
CHA	167.5	783.35	46°38.089N	9°50.170E	2010	1237	25-27.06	Chants
CAP	184.225	766.413	46°47.380N	9°37.244E	1775	1196	03-05.07	Capätsch
TEU	202.45	769.4	46°57.168N	9°40.002E	1540	1176	03-05.07	Teufried
UNT	198.35	769.725	46°54.951N	9°40.166E	1555	1176	04-06.07	Untersäss
TAM	154.05	743.175	46°31.421N	9°18.397E	2040	1255	08-10.07	Tambo Alp
WIN	156.075	743.225	46°32.513N	9°18.474E	1760	1255	08-10.07	Windigstafel
CAR	161.525	748.775	46°35.881N	9°22.925E	2020	1235	09-11.07	Caritsch
NIE	151.3	751.163	46°29.831N	9°24.596E	1940	1255	11-13.07	Val Niemet
RON	159.95	768.888	46°34.244N	9°38.655E	1720	1236	16-18.07	Rona
RAD	157.75	761.925	46°33.160N	9°33.152E	1852	1256	16-18.07	Radons
SUM	178.45	713.325	46°44.933N	8°55.397E	2071	1213	20-22.07	Sumvitg
NAU	172.15	714.35	46°41.522N	8°56.108E	1910	1213	21-23.07	Naustgel Dado
FOP	190.05	731.3	46°50.995N	9°09.722E	2110	1194	22-24.07	Fops
RIE	179.9	738.575	46°45.429N	9°15.265E	1810	1214	23-25.07	Riesner Alp
TEG	167.363	723.45	46°38.842N	9°03.174E	1945	1233	24-26.07	Tegia Sut

Tab. 3.2: MT and GDS station locations **Grisons II (1997)**, listed in chronological order. **X**, **Y** are the metric coordinates in the Swiss system CH1903. The **map nos.** give the number of the "Landeskarte der Schweiz, 1:25 000", the period range covered is: T= 0.001-300 s.

For the chosen mode a total amount of 4MB of MT and GDS data can be recorded simultaneously. For statistical reason (Jenkins & Watts, 1968) the duration of recording must be 8-10 times longer than the longest period in the covered interval. To insure this, long period data were recorded continuously during 24 h at a sampleing-rate of 0.24 s, whereas short period data were sampled during 5 minutes at a sample-rate of 2 kHz.
We used two different sets of French ECA induction coils (Andrieux et al., 1974) mounted on stable aluminium spikes. Short period magnetic field variations were measured with ECA-CM16 coils, long period variations with ECA-CM11E coils. The coils have optimal operating performance in the period ranges T= 0.0025- 0.125 s, respectively T= 0.01- 1000 s. They have very low noise characteristics and the sensitivity of both types is 50mV/nT and 20 mV/nT.

The electrical field variations were measured by pairs of non-polarisable Ag-AgCl electrodes designed for ocean studies (Filloux, 1973). They were slightly modified for use in fieldwork on dry ground (Fig. 3.4). The electrodes are driven into the earth in 30 cm holes filled with salted bentonite. Compared to non-polarisable Cu-$CuSO_4$ electrodes used for the self-potential survey (see chapter 2.4) and in some MT studies, the Ag-AgCl electrodes are less affected by diurnal temperature variations. Systematic studies of different types of electrodes for long period measurements have been published by Petiau & Dupis (1980), Junge (1990) and Perrier at al. (1997). A general MT/GDS set-up is shown in Fig. 3.3.

Instead of the shown L-shaped electrode set-up in Fig. 3.3, during the second stage of fieldwork we generally used a five electrodes X-shaped set-up with a reference electrode in the centre. If possible the electrode spacing was extended up to a maximum of 100 m to enhance the signal-to-noise ratio.
To make use of the remote-reference technique, two instruments are started, whenever possible, time synchronously. With this technique, three sites (PAS, TEN and OBE) were corrected for distorted horizontal magnetic fields.

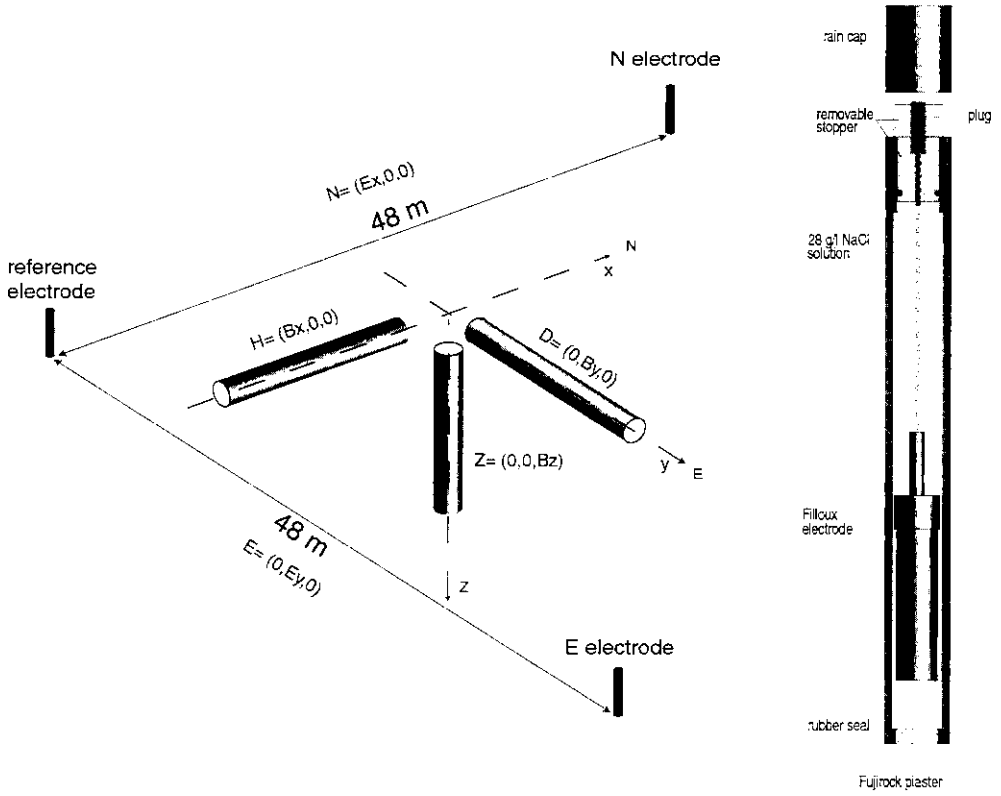

Fig. 3.3 (left): MT and GDS set-up showing three induction coils aligned towards North, East and downwards. The electric field is measured as potential difference between electrode pairs, using a single electrode as reference. Modified from Schnegg (1998).
Fig. 3.4 (right): Unpolarizable Ag-AgCl telluric electrode with plexiglas housing and porous tip. Overall length with weather cap: 32 cm (Schnegg, 1998).

3.2 GDS transfer functions

Fig. 3.5 shows the GDS transfer functions for the period range T= 1-300 s expressed as real and imaginary induction arrows versus signal period. The axes of the figure are orientated N-S (ordinate) and E-W (abscissa), the scale on the ordinate indicate amplitudes of the induction arrows from –2 to 2. Except for a few sites, they show a smoothly varying function over period, with a maximum inductive response at ca. T= 10 s, shifted toward the East at slightly longer periods.
Obviously, the chosen period range of T= 1-300 s adequatly covers this important feature. Most conspicuous are the high amplitudes of some real part induction arrows for several sites up to values of ± 2.
Furthermore, the real induction arrows show a directional dualism. They point either south-easterly or south-westerly. This particular behaviour is best illustrated in the plan views for various periods in Fig. 3.6.

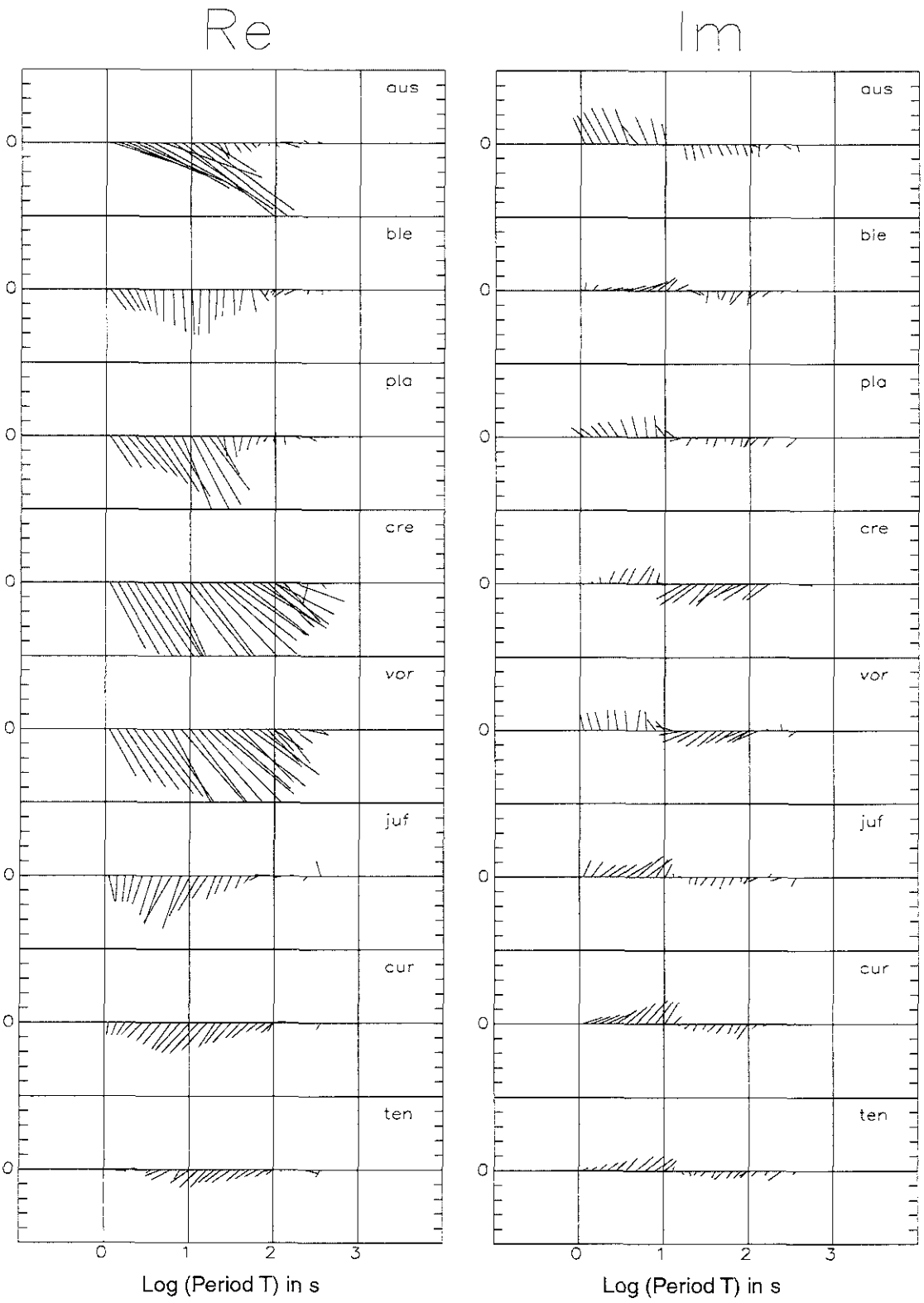

Fig. 3.5: Measured induction arrows vs. signal period

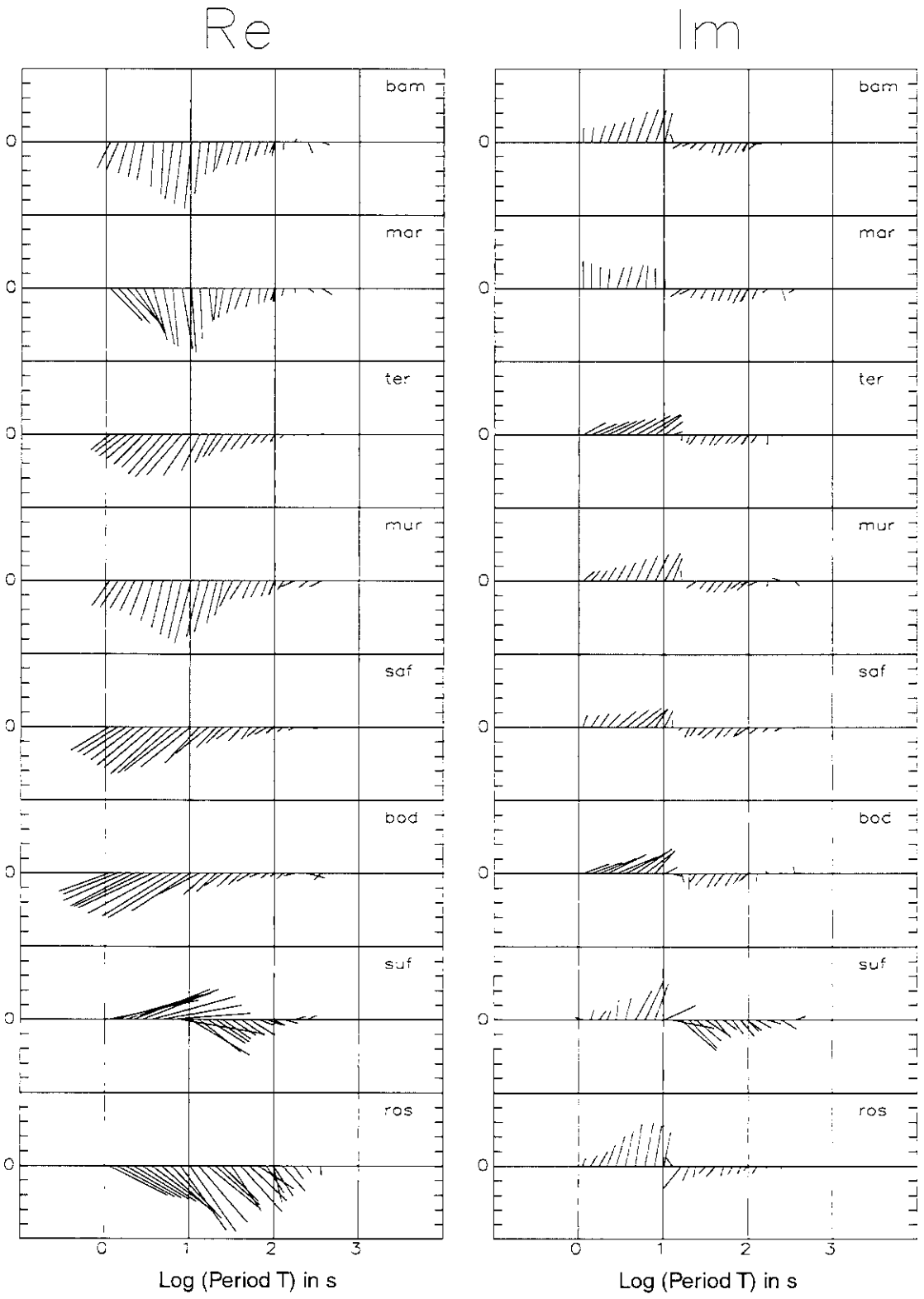

Fig. 3.5 (cont.): Measured induction arrows vs. signal period

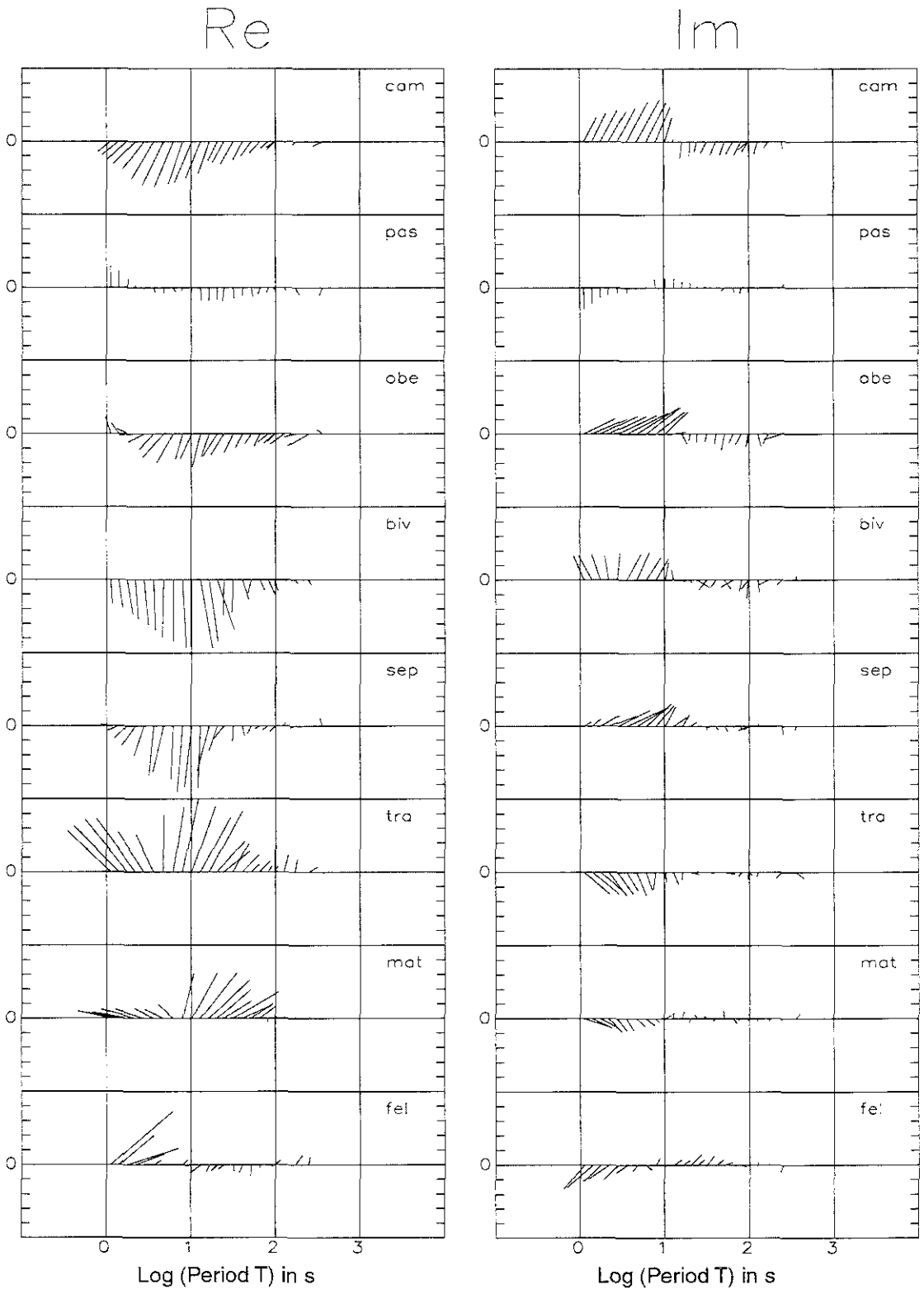

Fig. 3.5 (cont.): Measured induction arrows vs. signal period

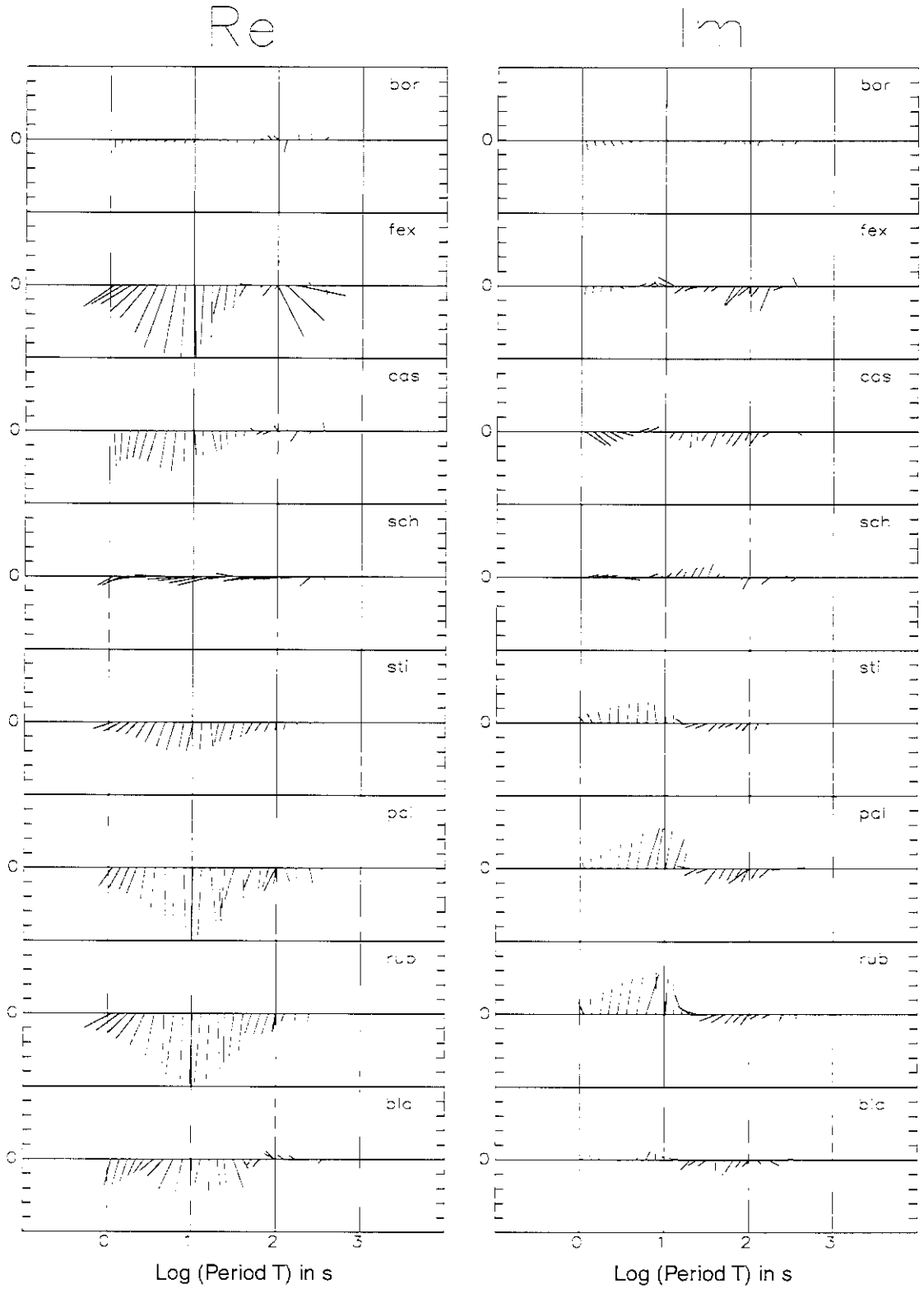

Fig. 3.5 (cont.): Measured induction arrows vs. signal period

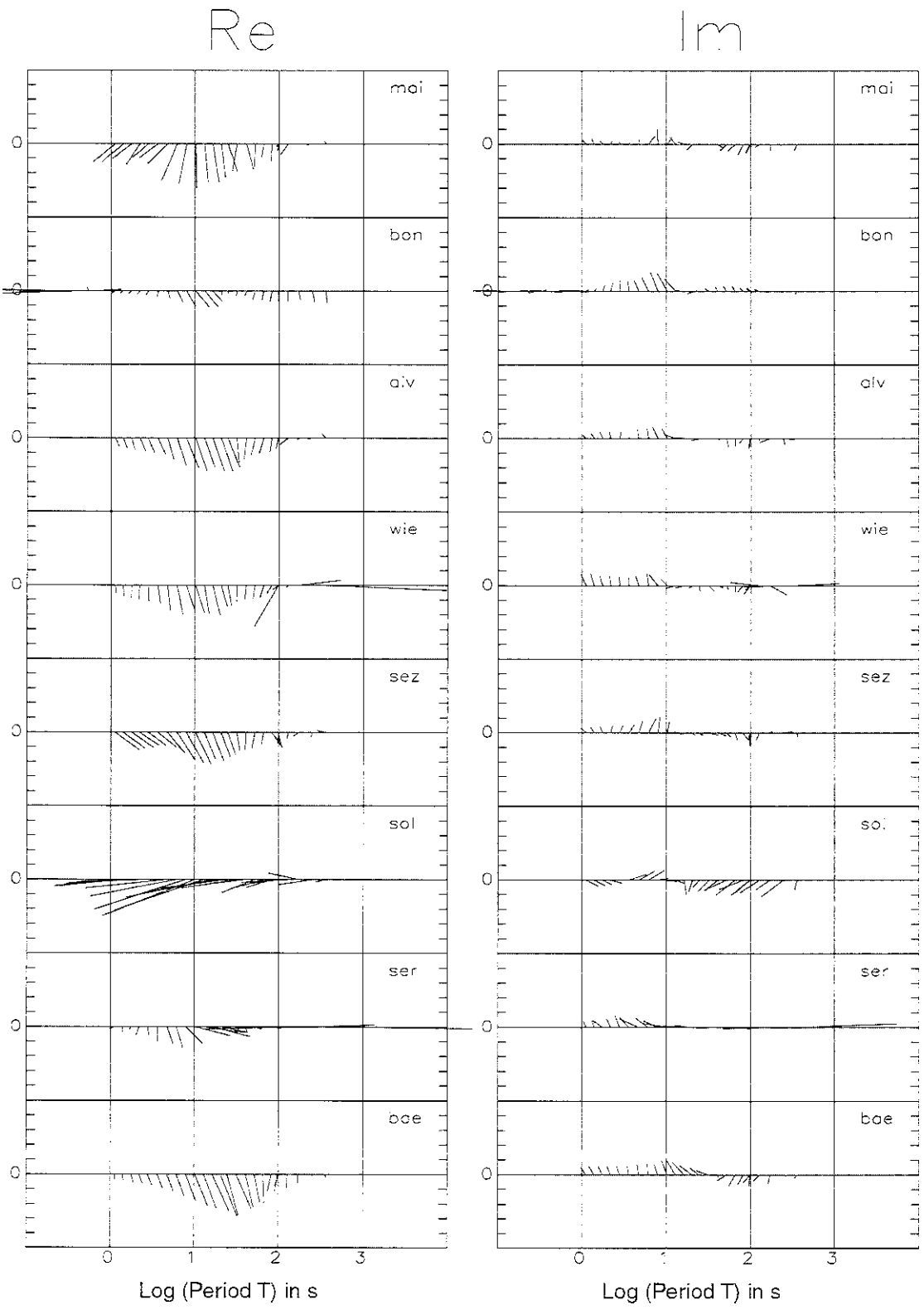

Fig. 3.5 (cont.): Measured induction arrows vs. signal period

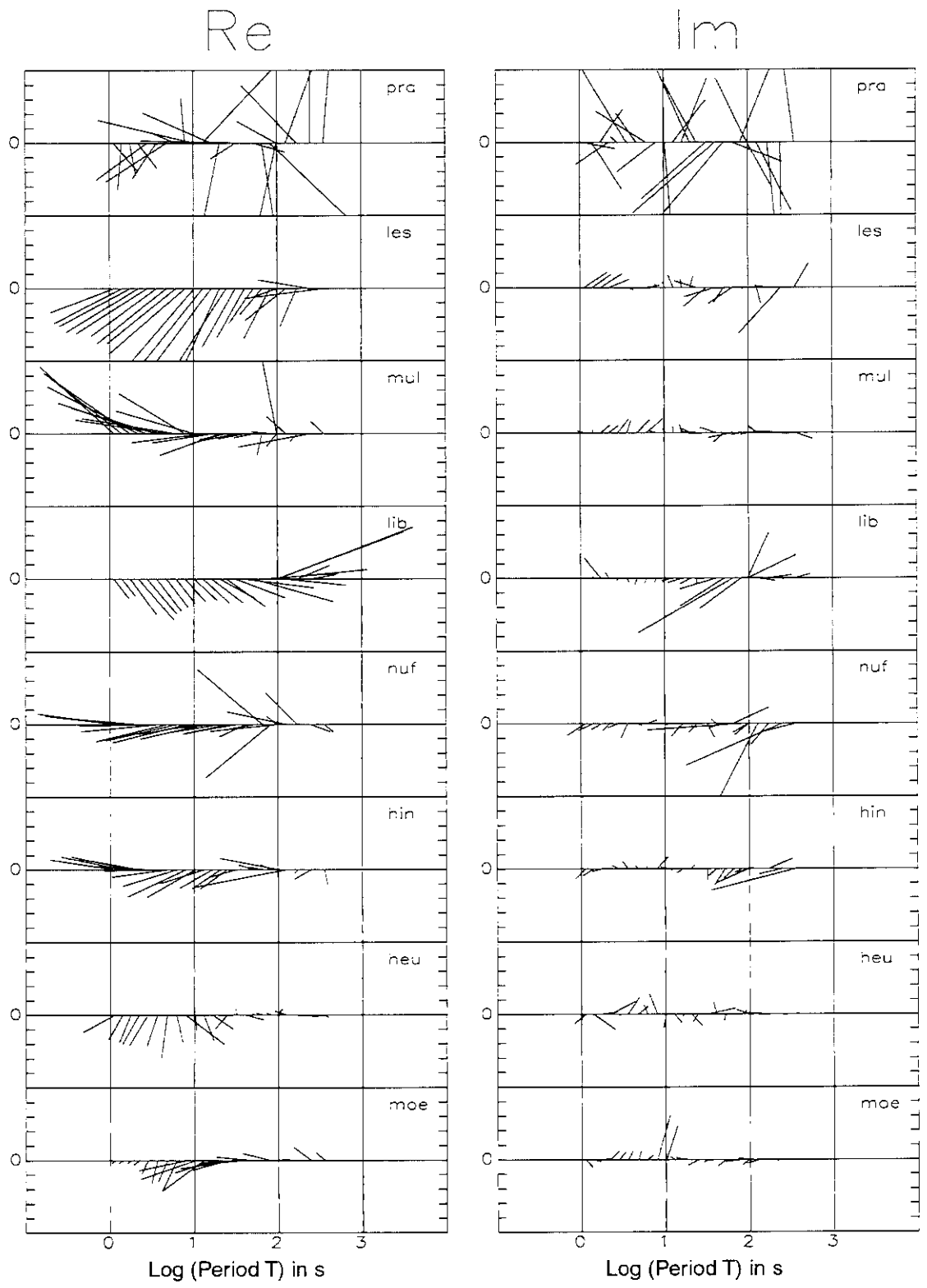

Fig. 3.5 (cont.): Measured induction arrows vs. signal period

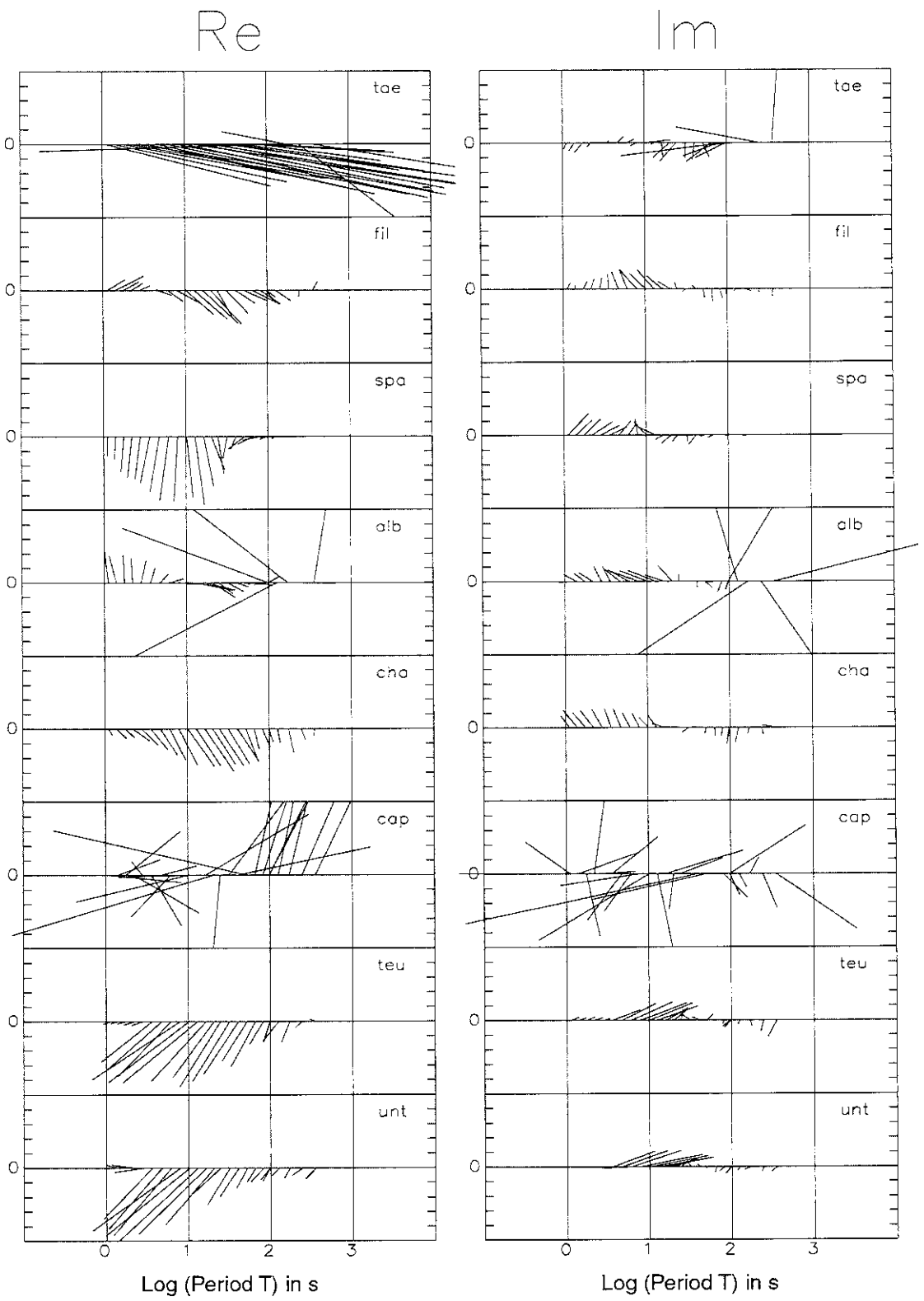

Fig. 3.5 (cont.): Measured induction arrows vs. signal period

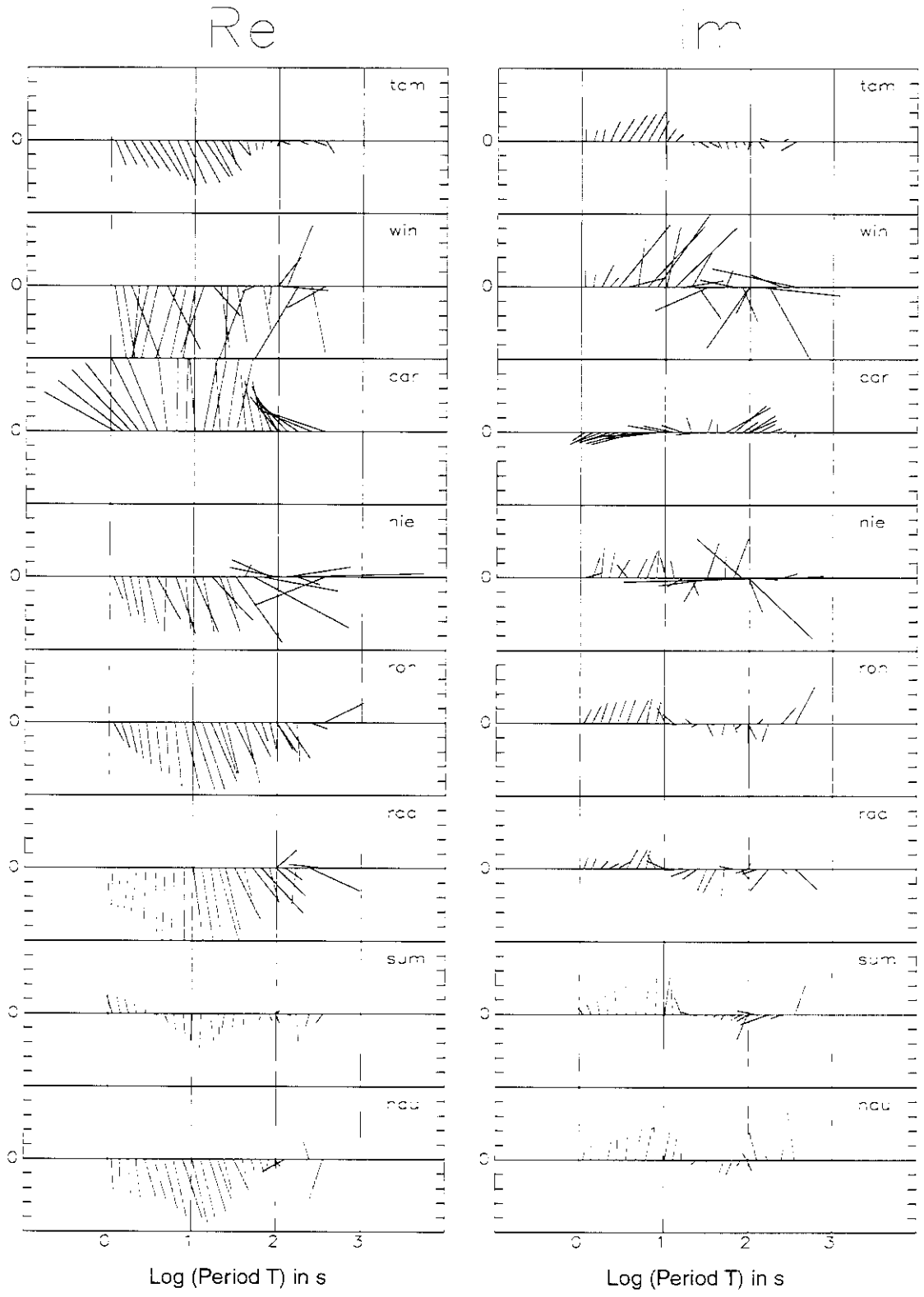

Fig. 3.5 (cont.): Measured induction arrows vs. signal period

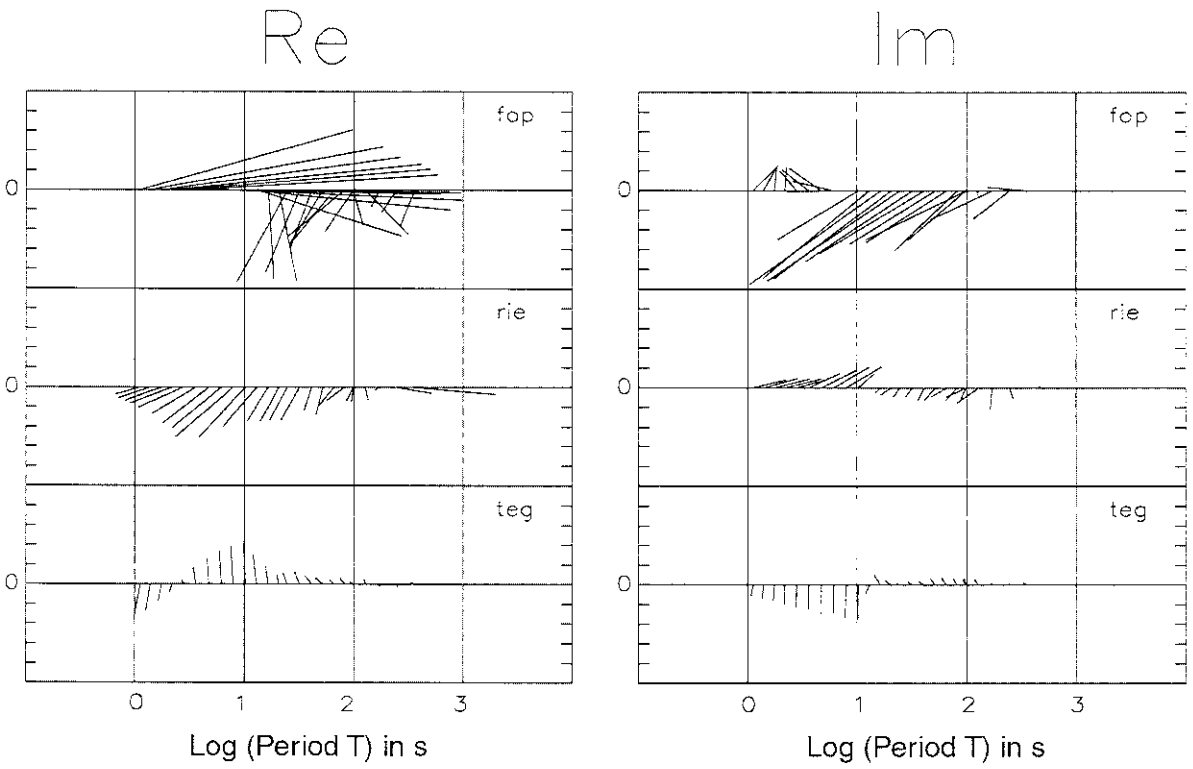

Fig. 3.5 (end): Measured induction arrows vs. signal period

3.3 MT transfer functions

Plots of apparent resistivity and phase for the Z_{xy} and Z_{yx} components of the non-rotated impedance tensor are shown in Fig. 3.7. Some sites (BAE, RUB, PAL, MUR) point to a characteristic feature in the MT sounding curves: they show an extreme splitting of the two components, as one would expect from the "coastal effect". Such effects are caused by the contrast in conductivity between seawater and high resistivity onshore rocks. Thus, similar contrasts in conductivity must be expected in the survey area. This renders the treatment of MT soundings and their modelling much more difficult.

Compared to GDS transfer functions, their period dependence is less smooth and at some periods there is even data loss. Quite generally, the estimated MT transfer functions are of minor quality, are more affected by small-scale inhomogeneities and topographic effects, and are at present not extensively used for studying the conductivity distribution in Graubünden. Decomposition methods, for each single site did not permit to recover a trustworthy regional strike and the galvanic distortion model also failed. We therefore confine ourselves in what follows on the joint treatment of the magnetic transfer functions arranged in a coarse data array.

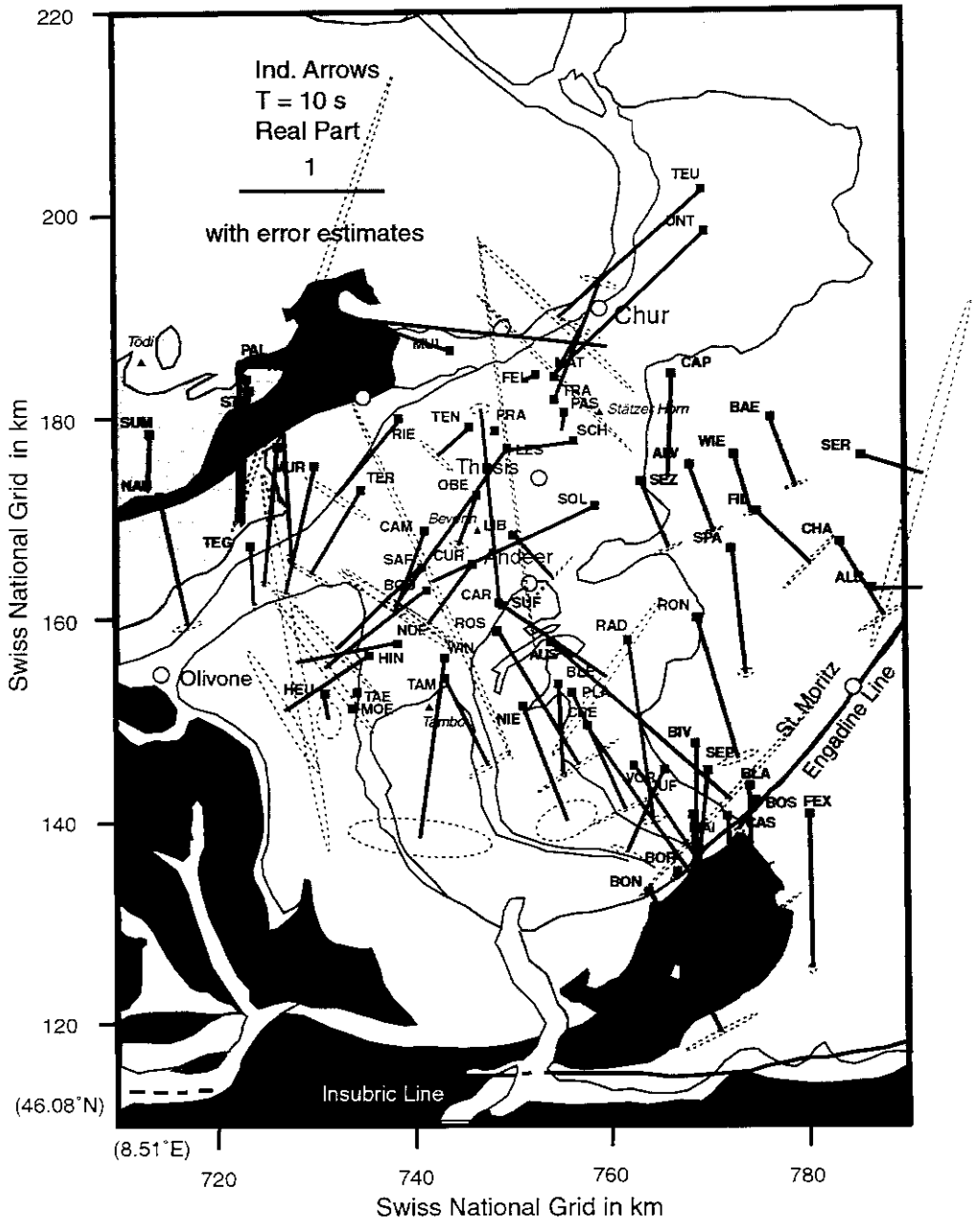

Fig. 3.6: Real induction arrows for the period T= 10 s.

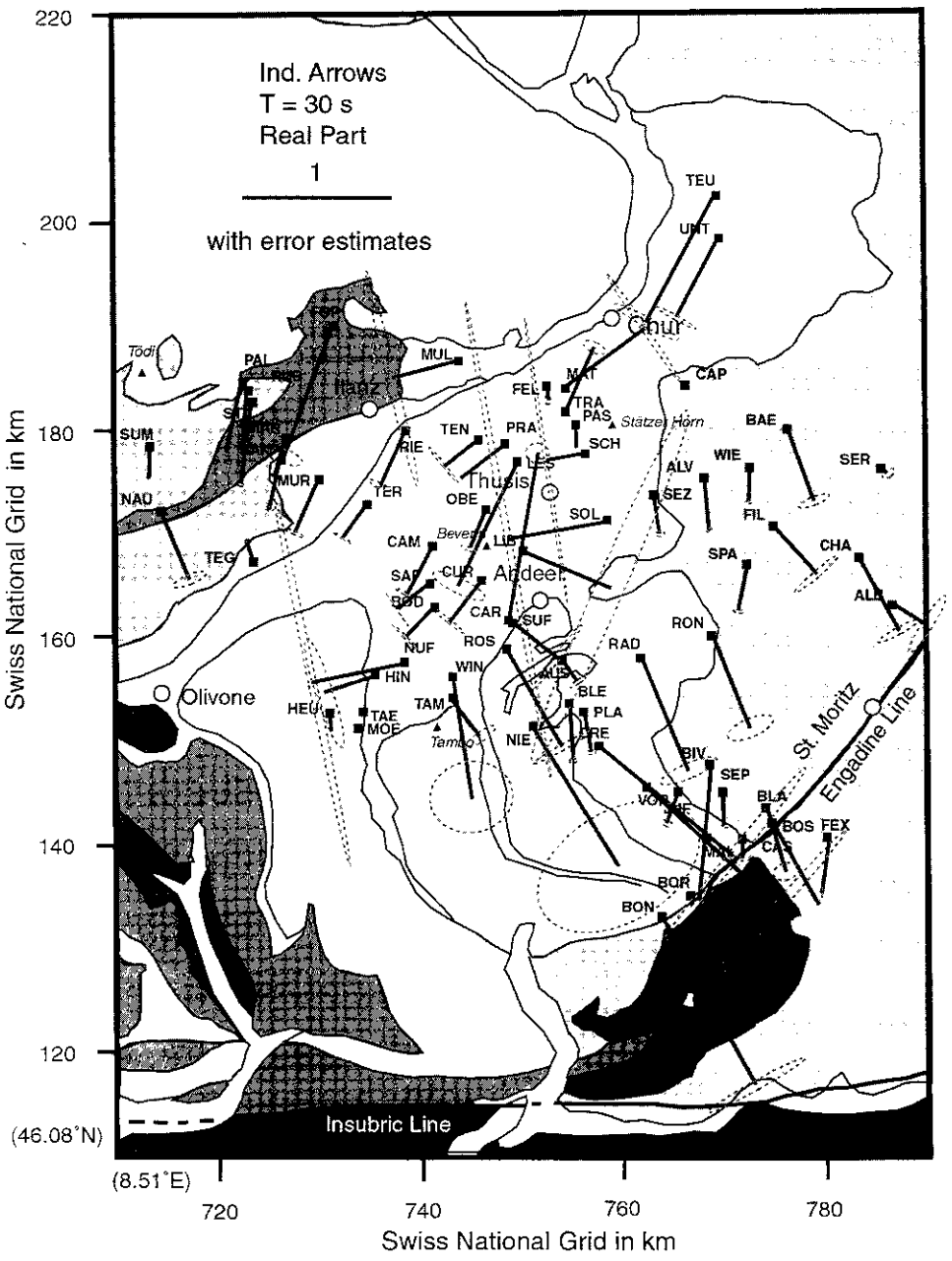

Fig 3.6 (cont.): Real induction arrows for the period T= 30 s.

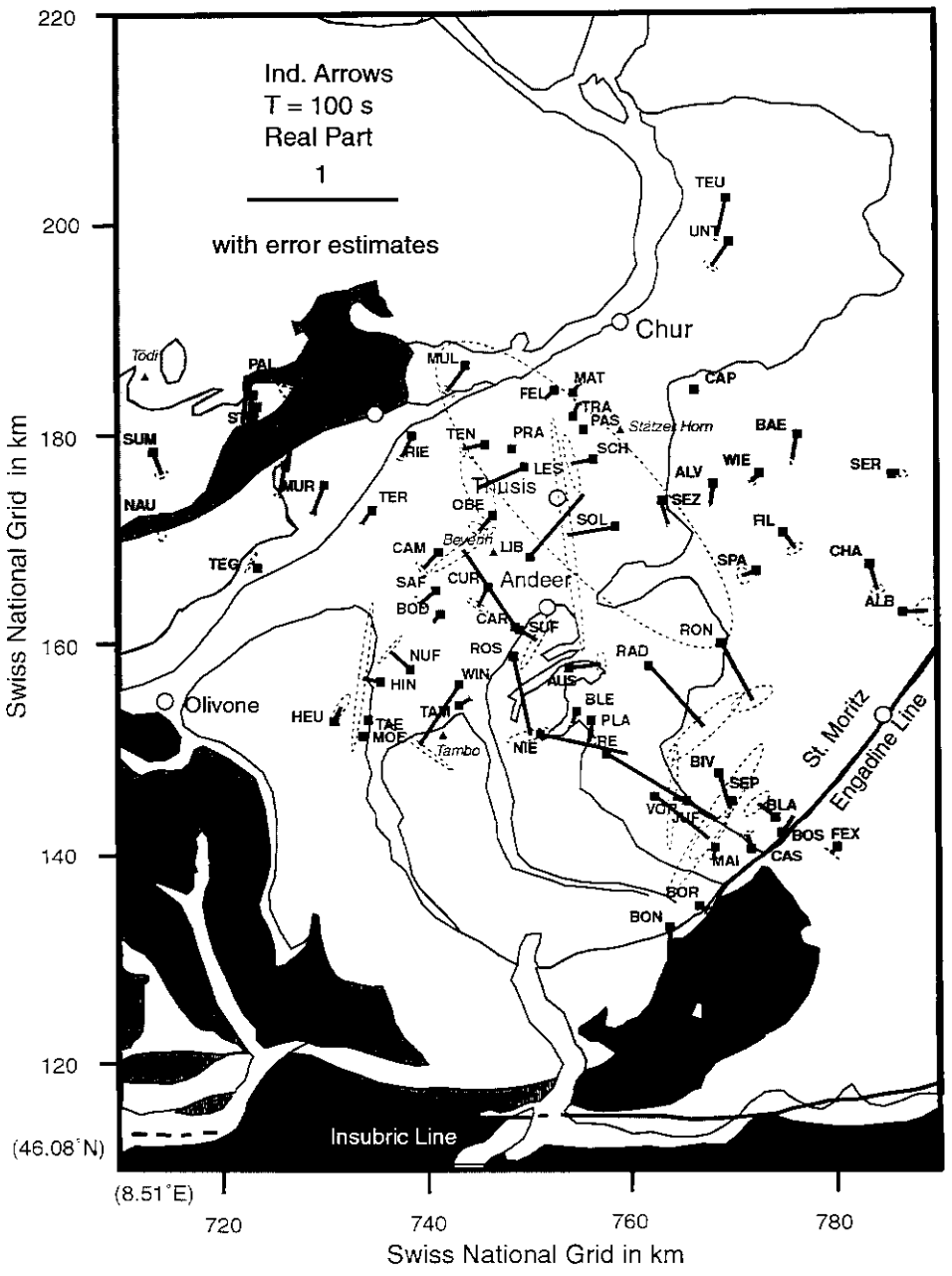

Fig. 3.6 (end): Real induction arrows for the period T= 100 s.

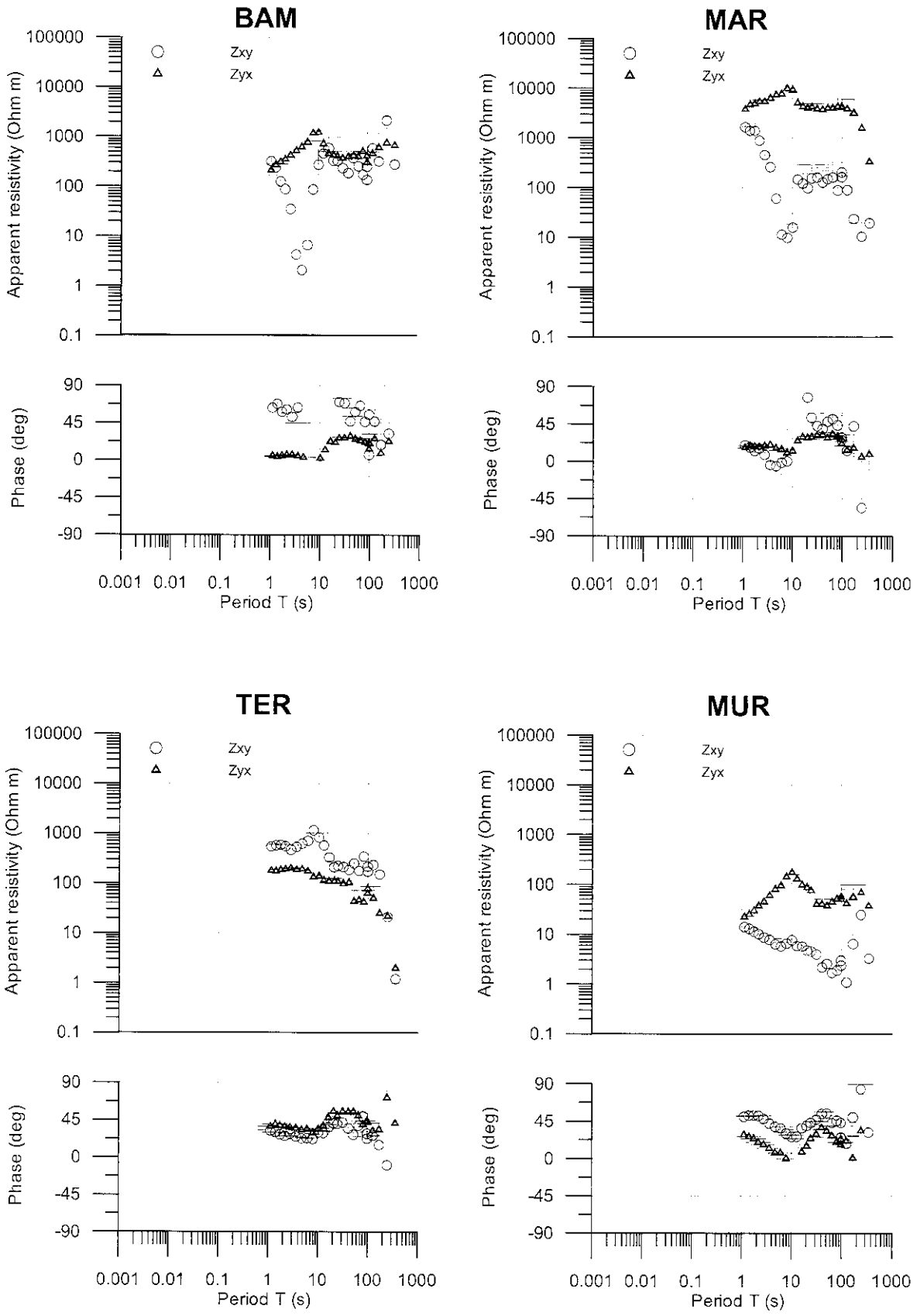

Fig. 3.7: MT transfer function vs. signal period

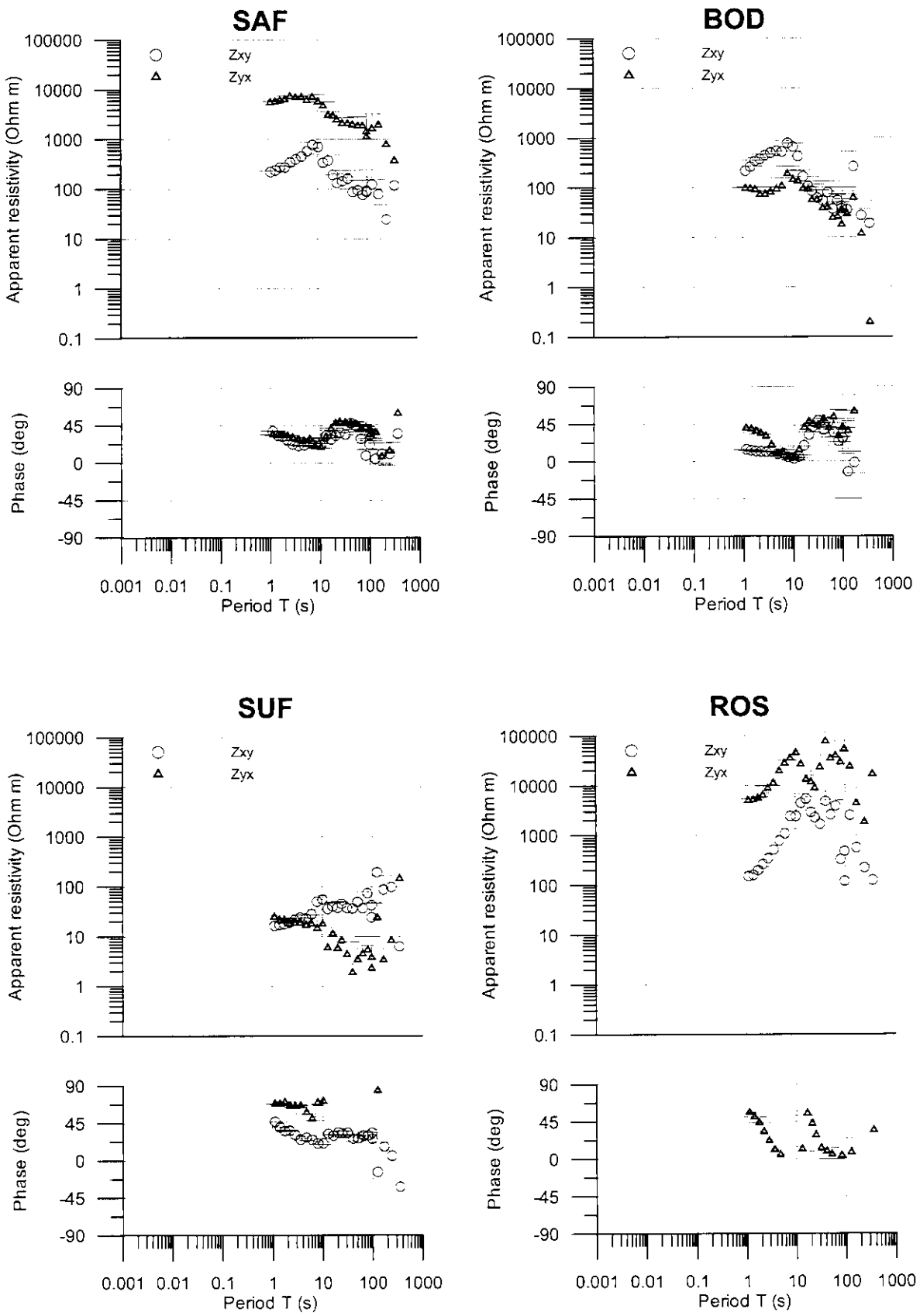

Fig. 3.7 (cont.): MT transfer function vs. signal period

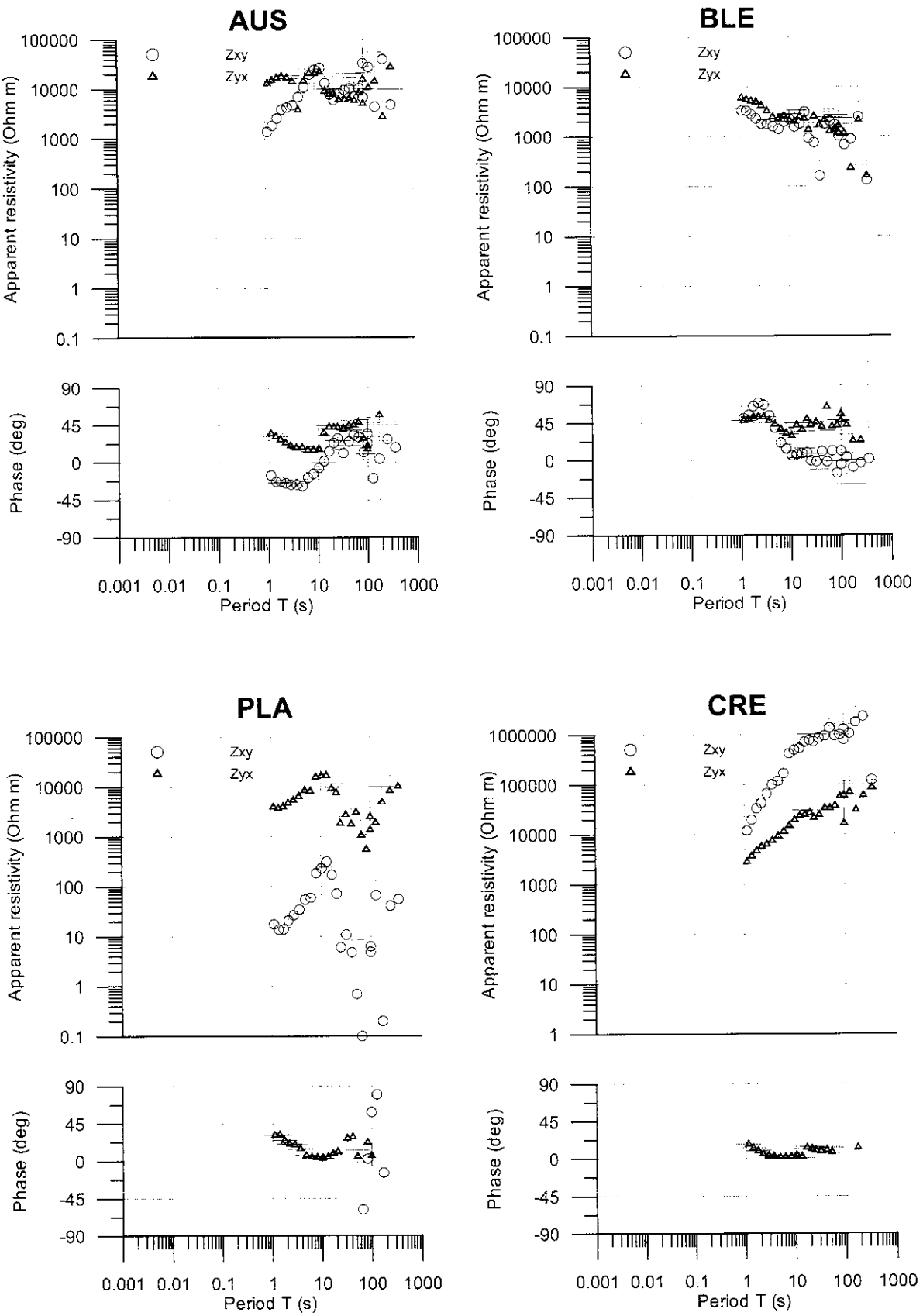

Fig. 3.7 (cont.): MT transfer function vs. signal period

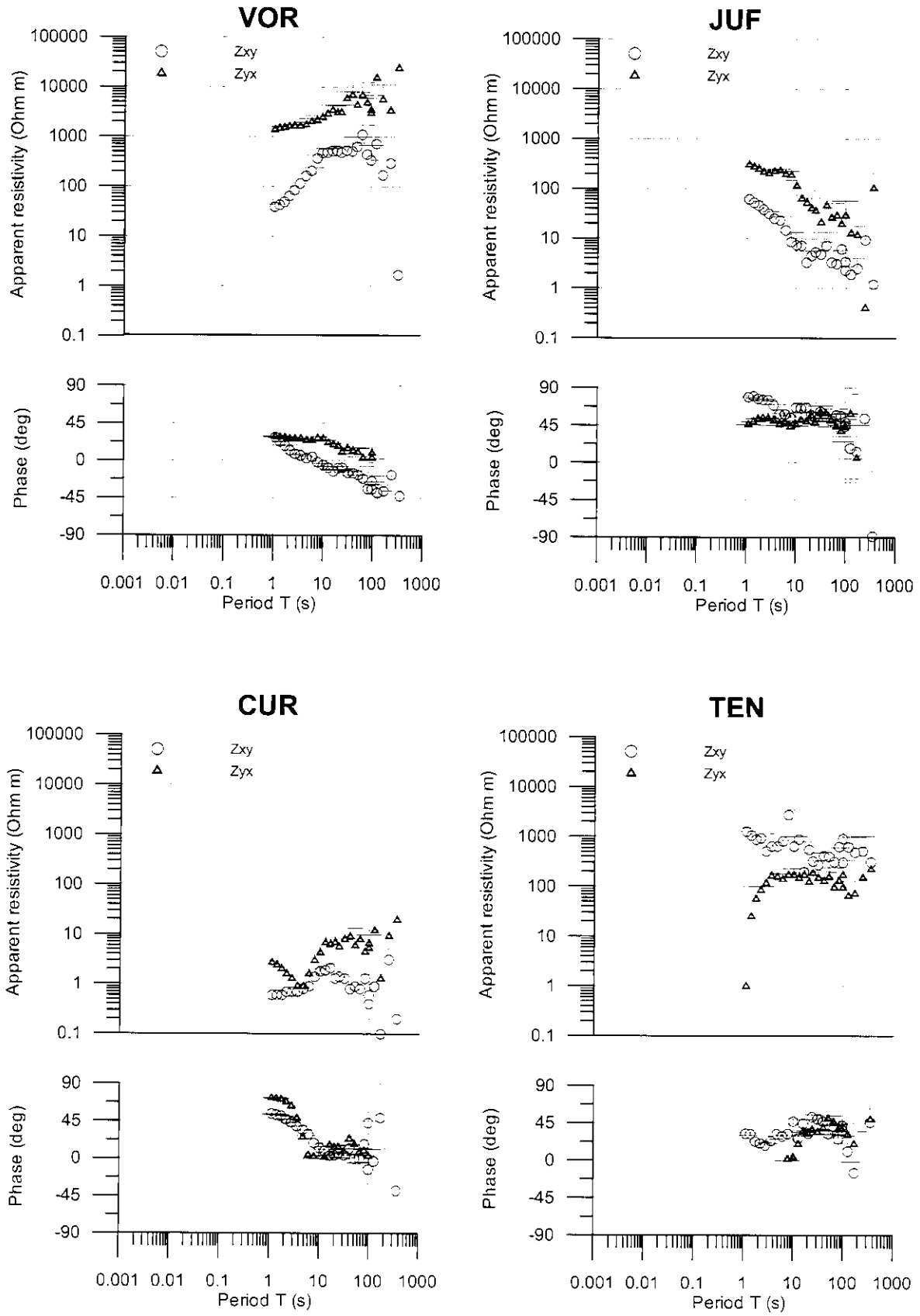

Fig. 3.7 (cont.): MT transfer function vs. signal period

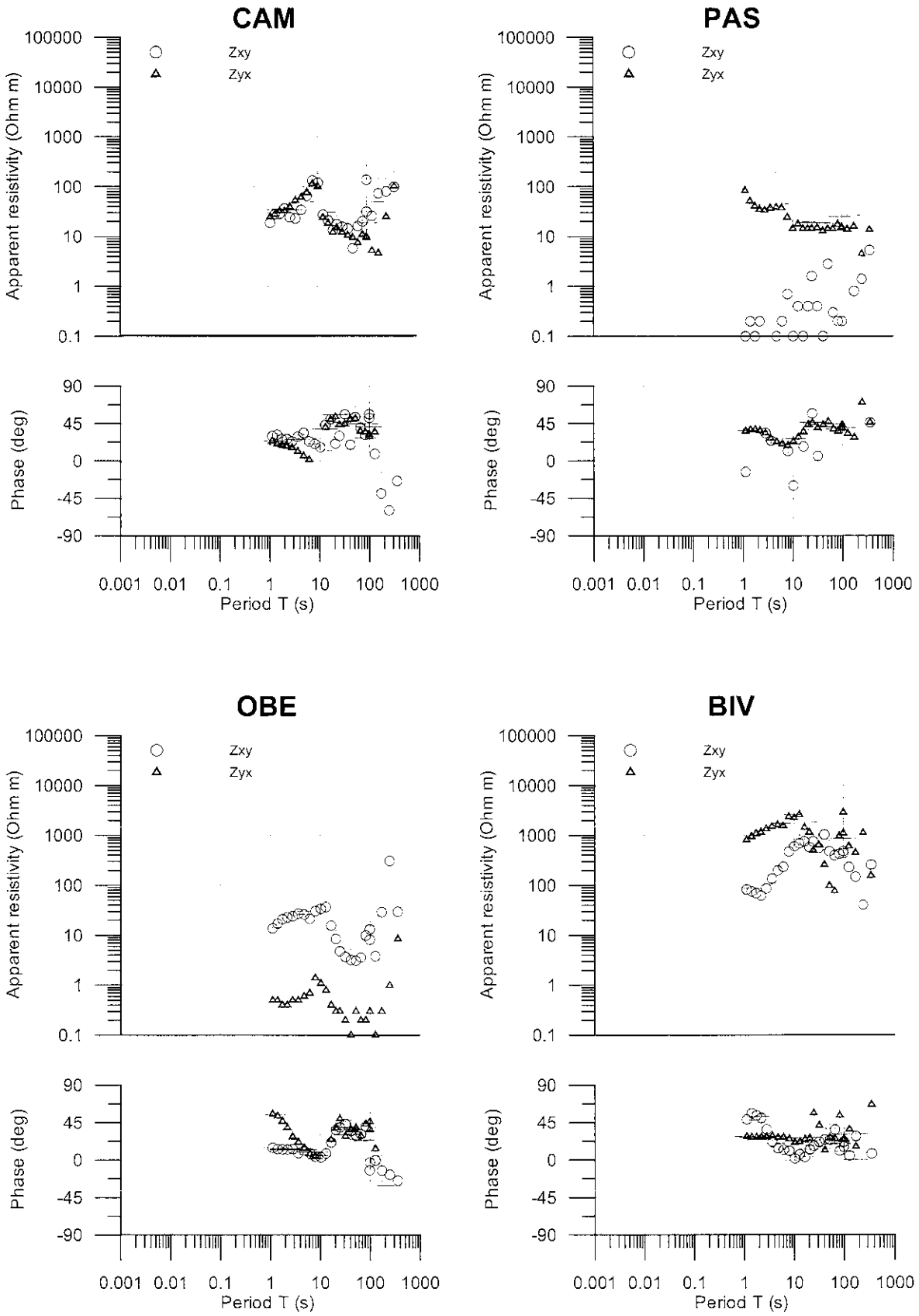

Fig. 3.7 (cont.): MT transfer function vs. signal period

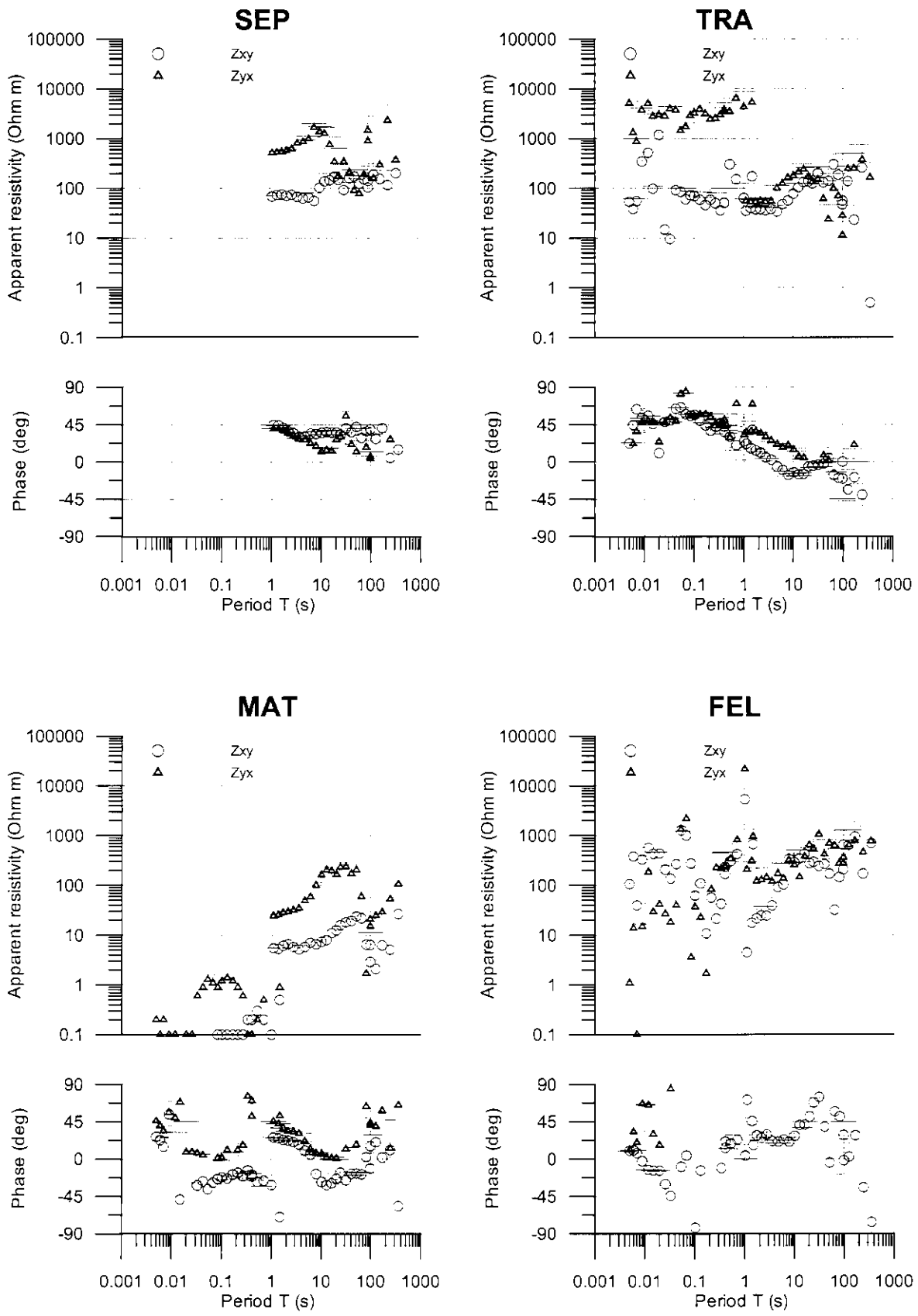

Fig. 3.7 (cont.): MT transfer function vs. signal period

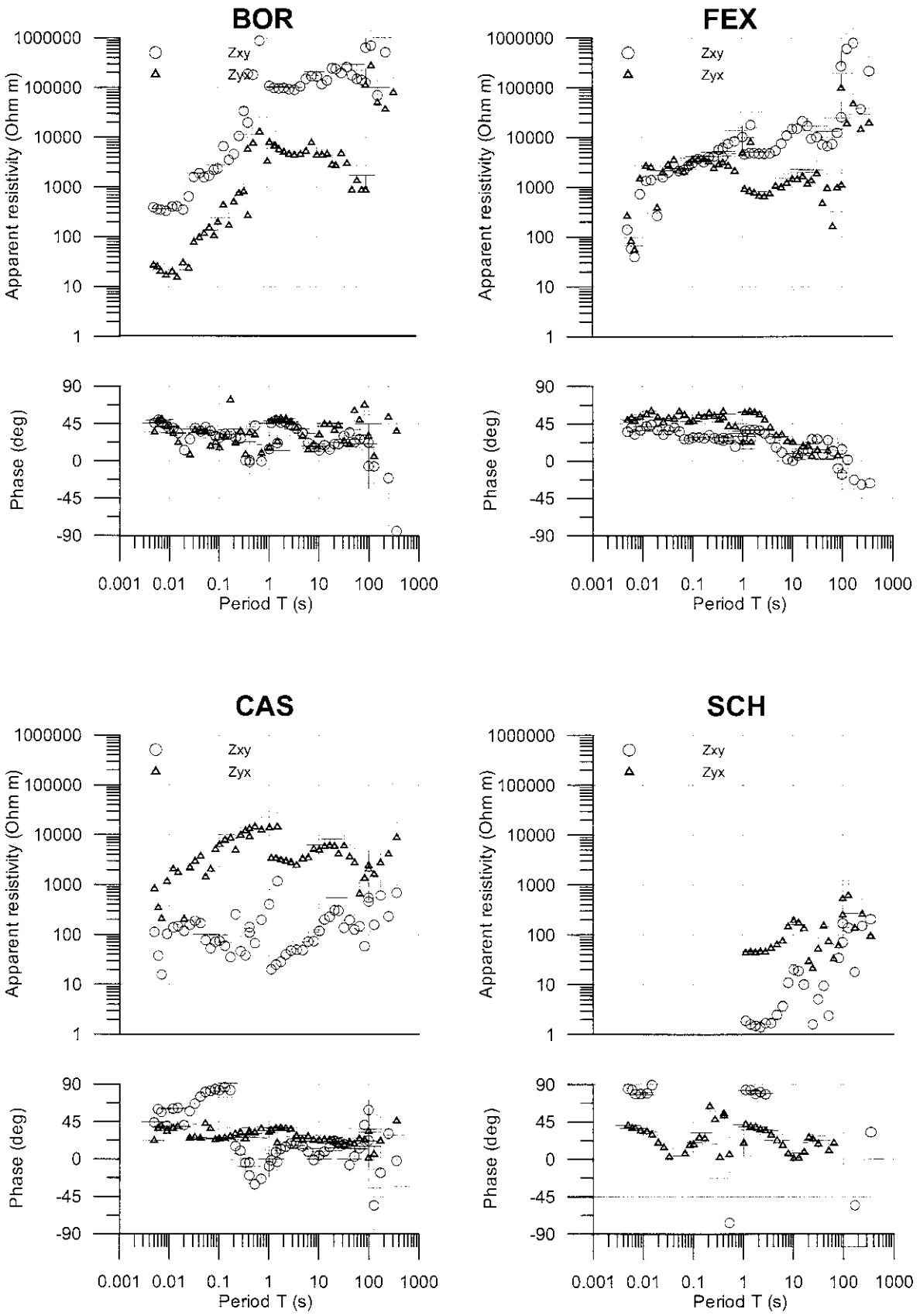

Fig. 3.7 (cont.): MT transfer function vs. signal period

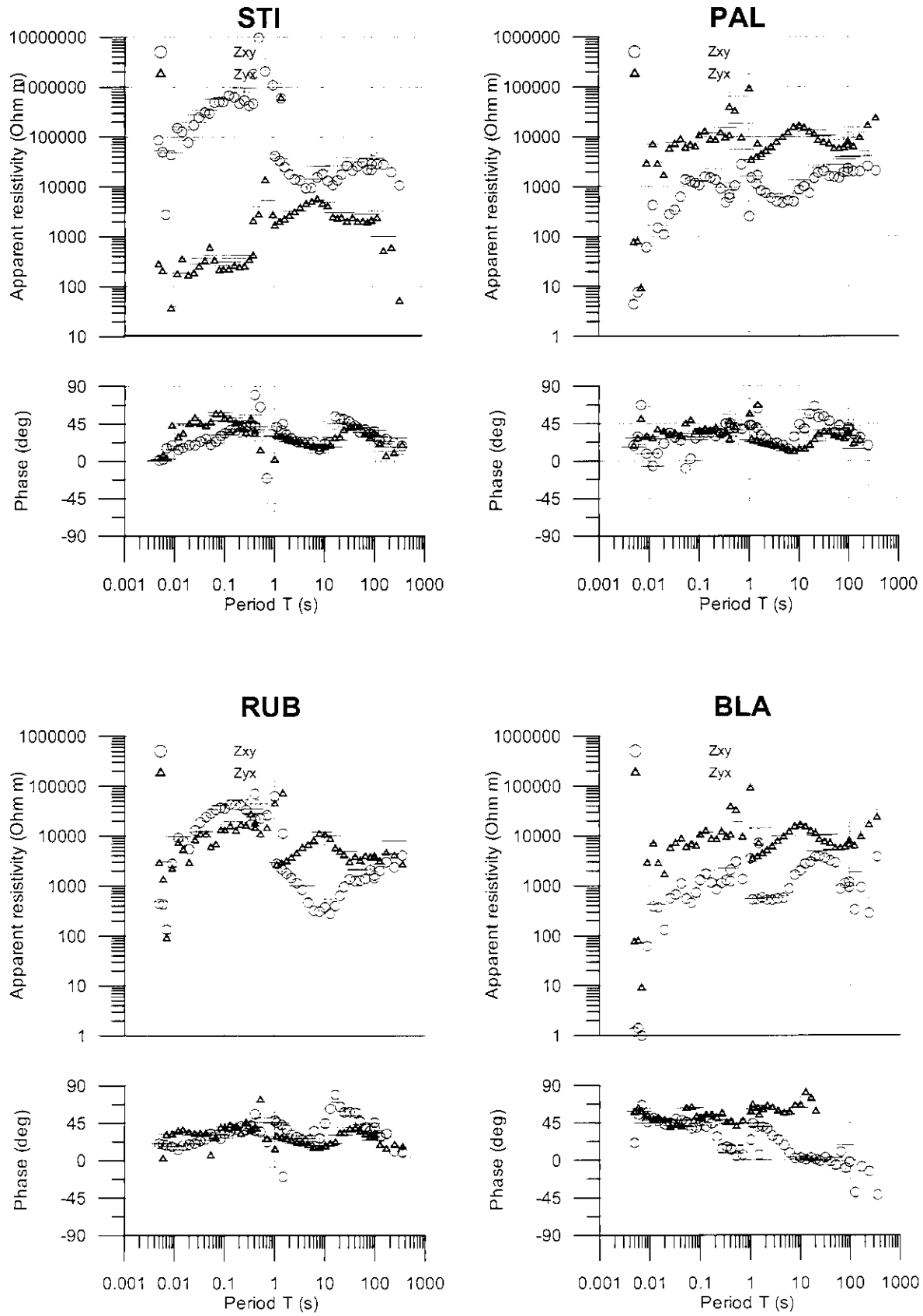

Fig. 3.7 (cont.): MT transfer function vs. signal period

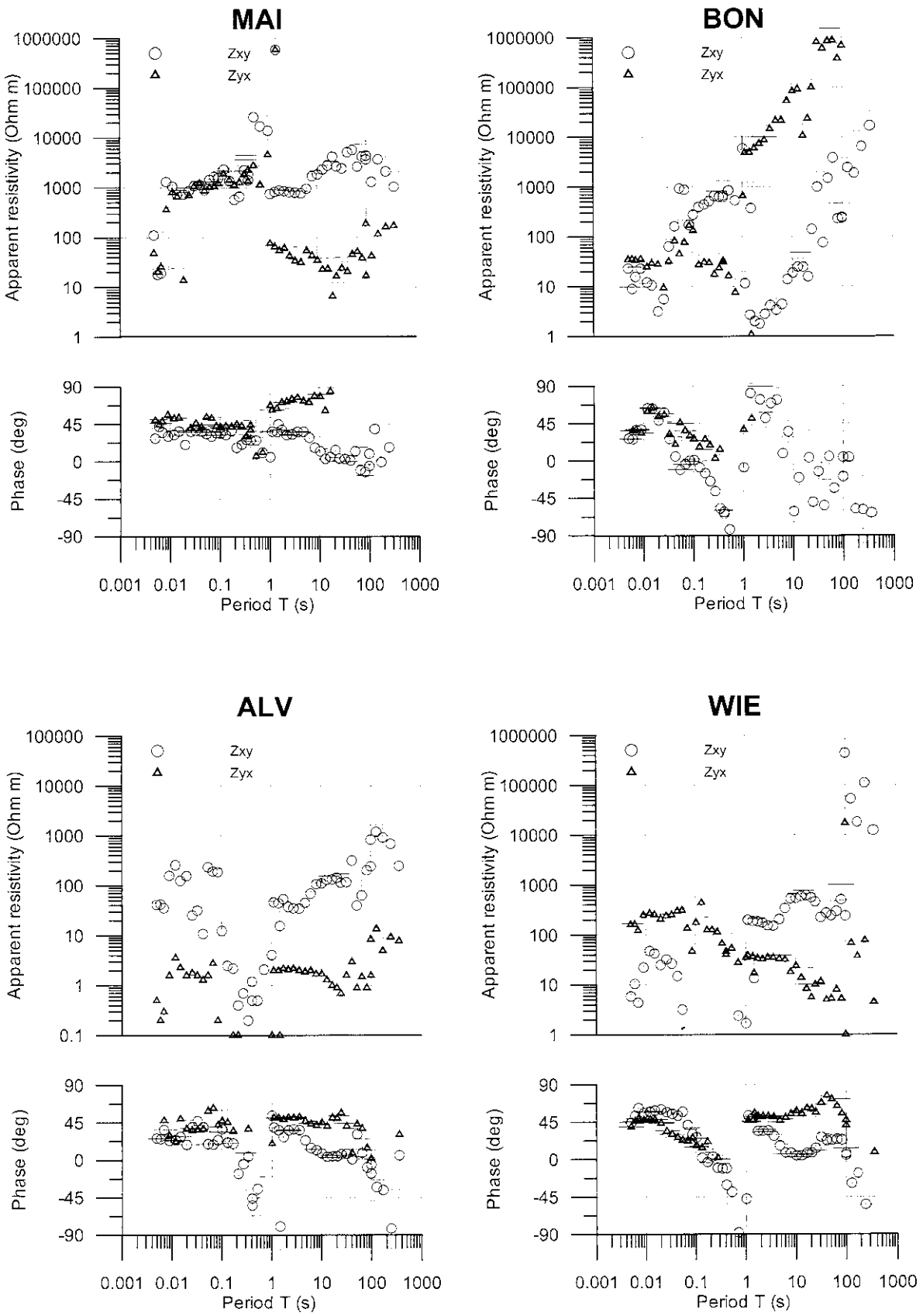

Fig. 3.7 (cont.): MT transfer function vs. signal period

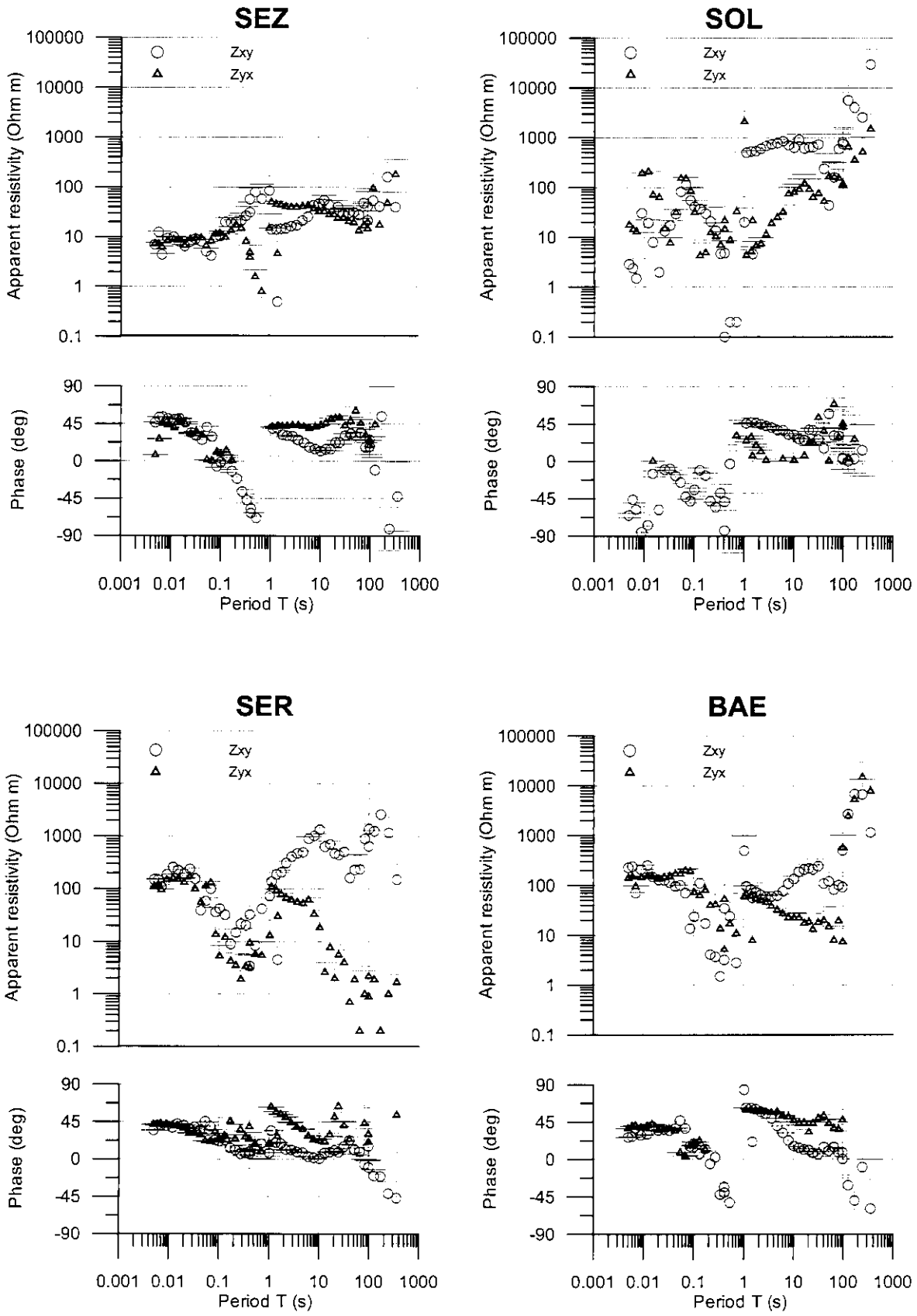

Fig. 3.7 (cont.): MT transfer function vs. signal period

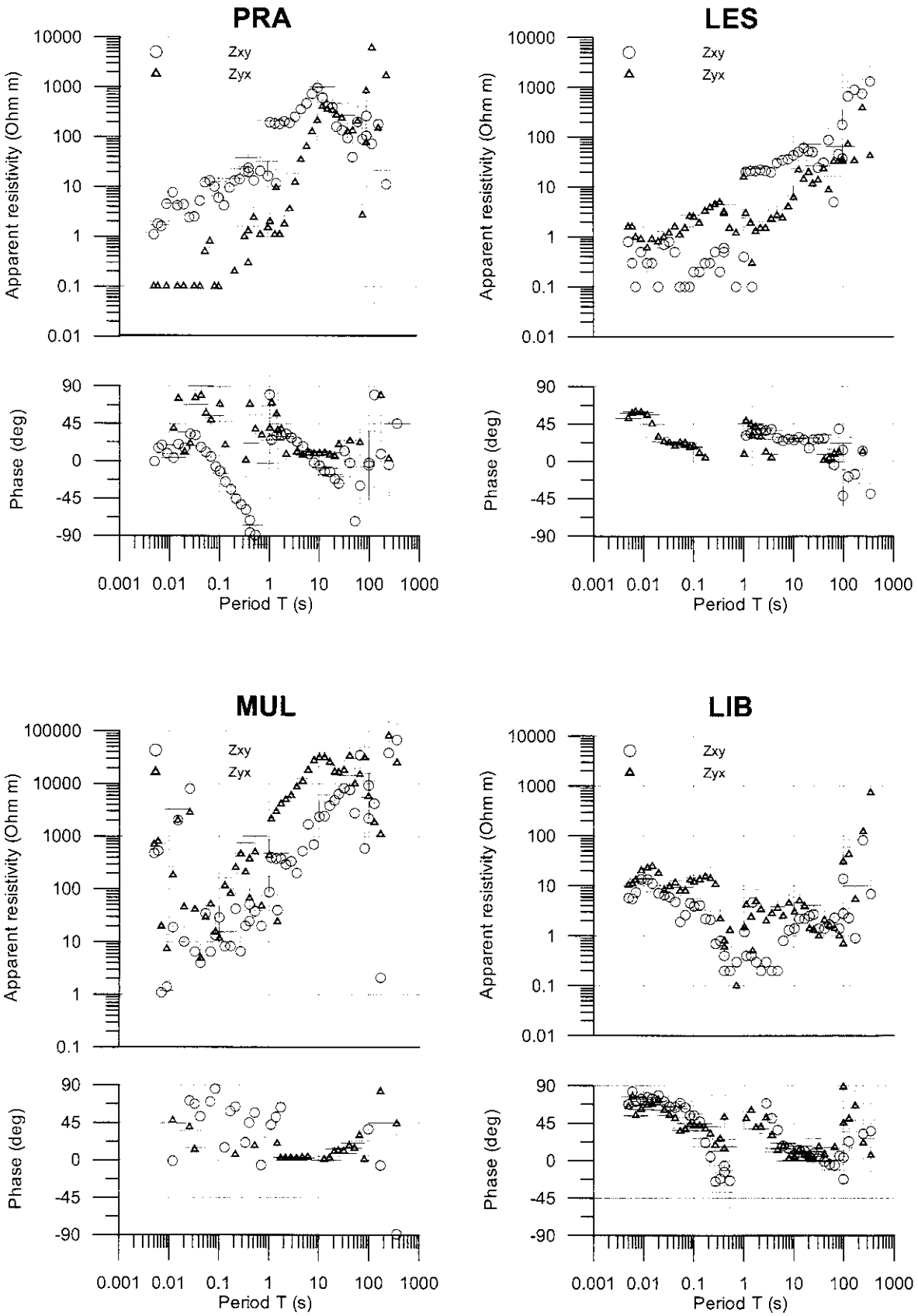

Fig. 3.7 (cont.): MT transfer function vs. signal period

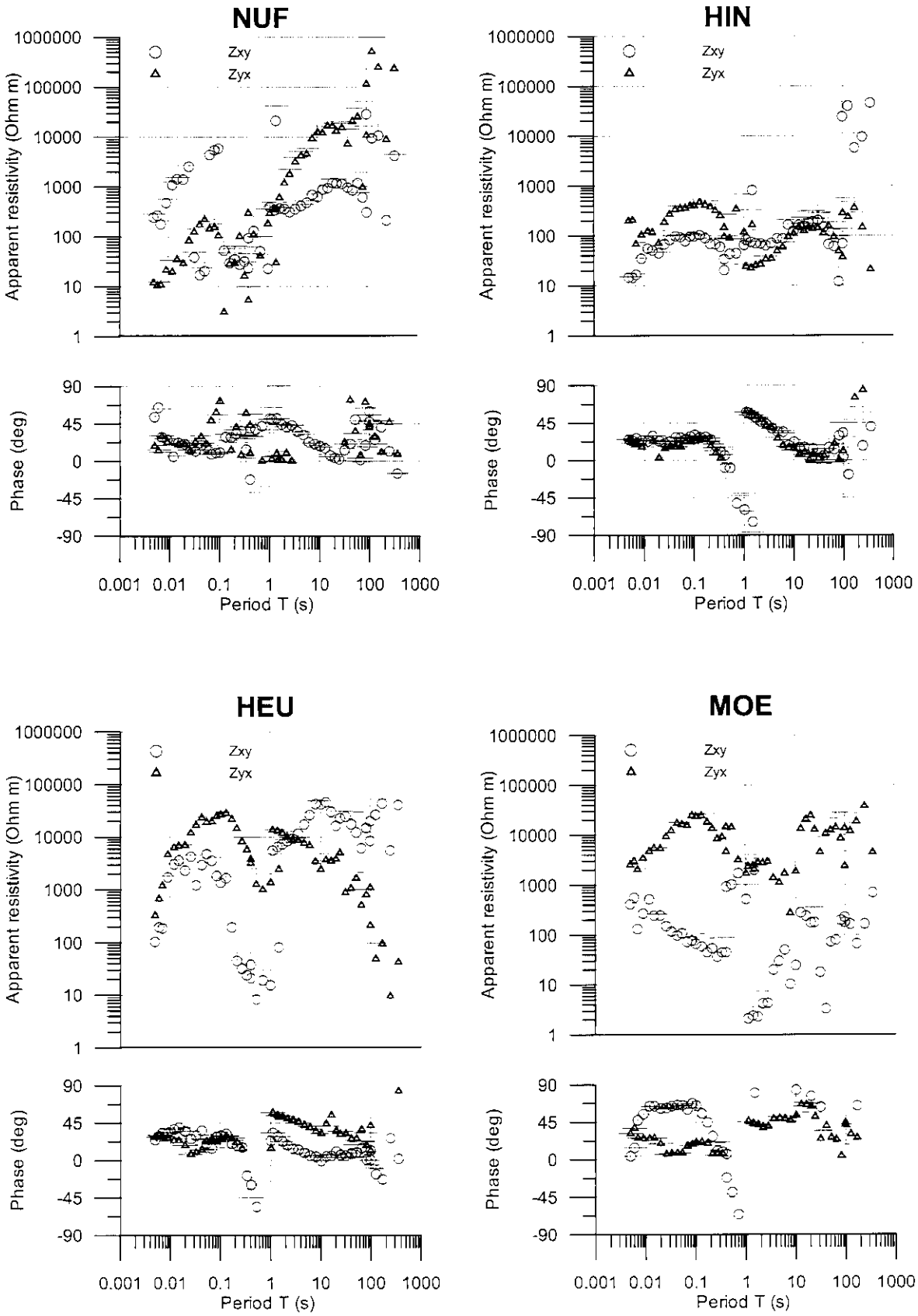

Fig. 3.7 (cont.): MT transfer function vs. signal period

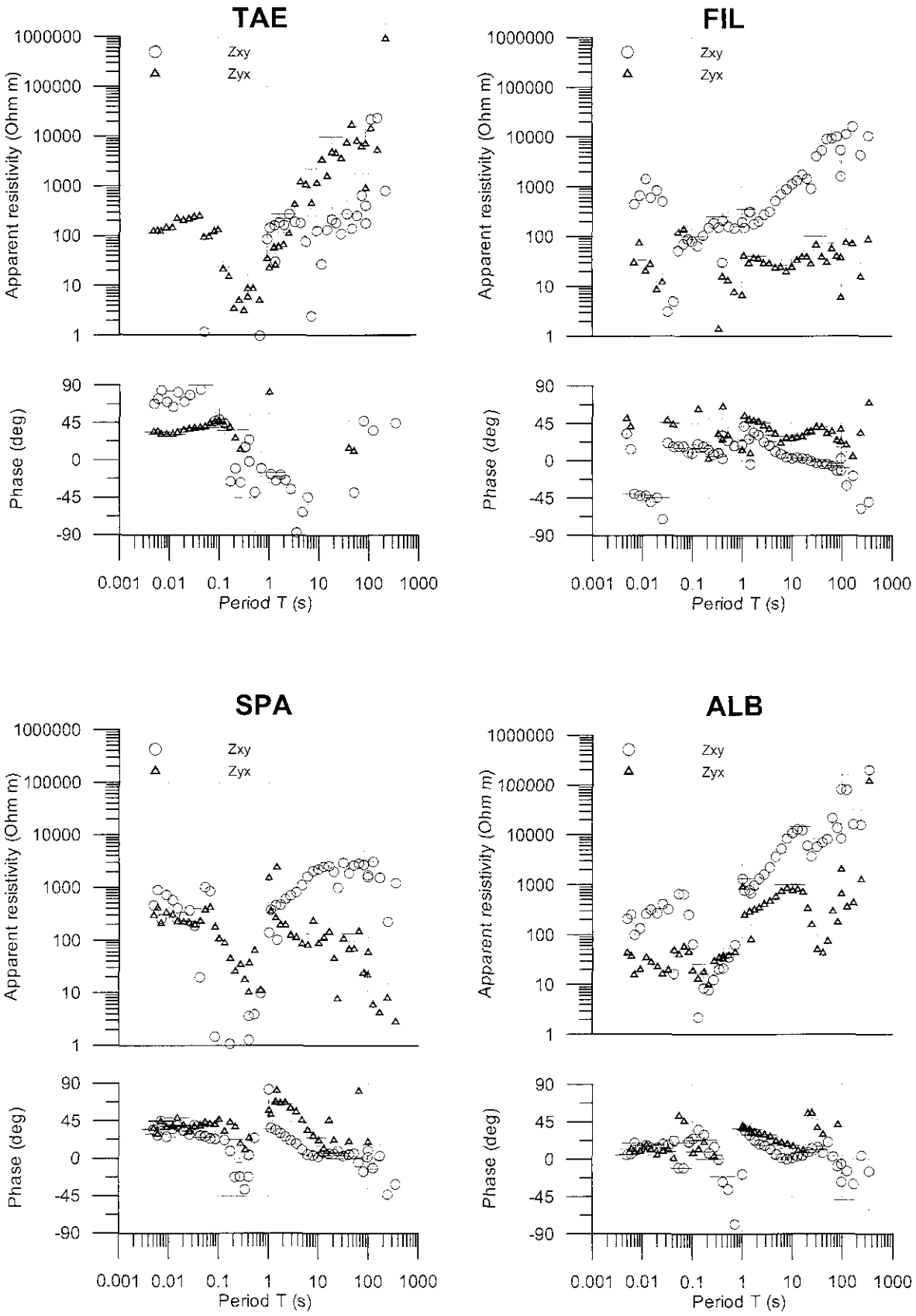

Fig. 3.7 (cont.): MT transfer function vs. signal period

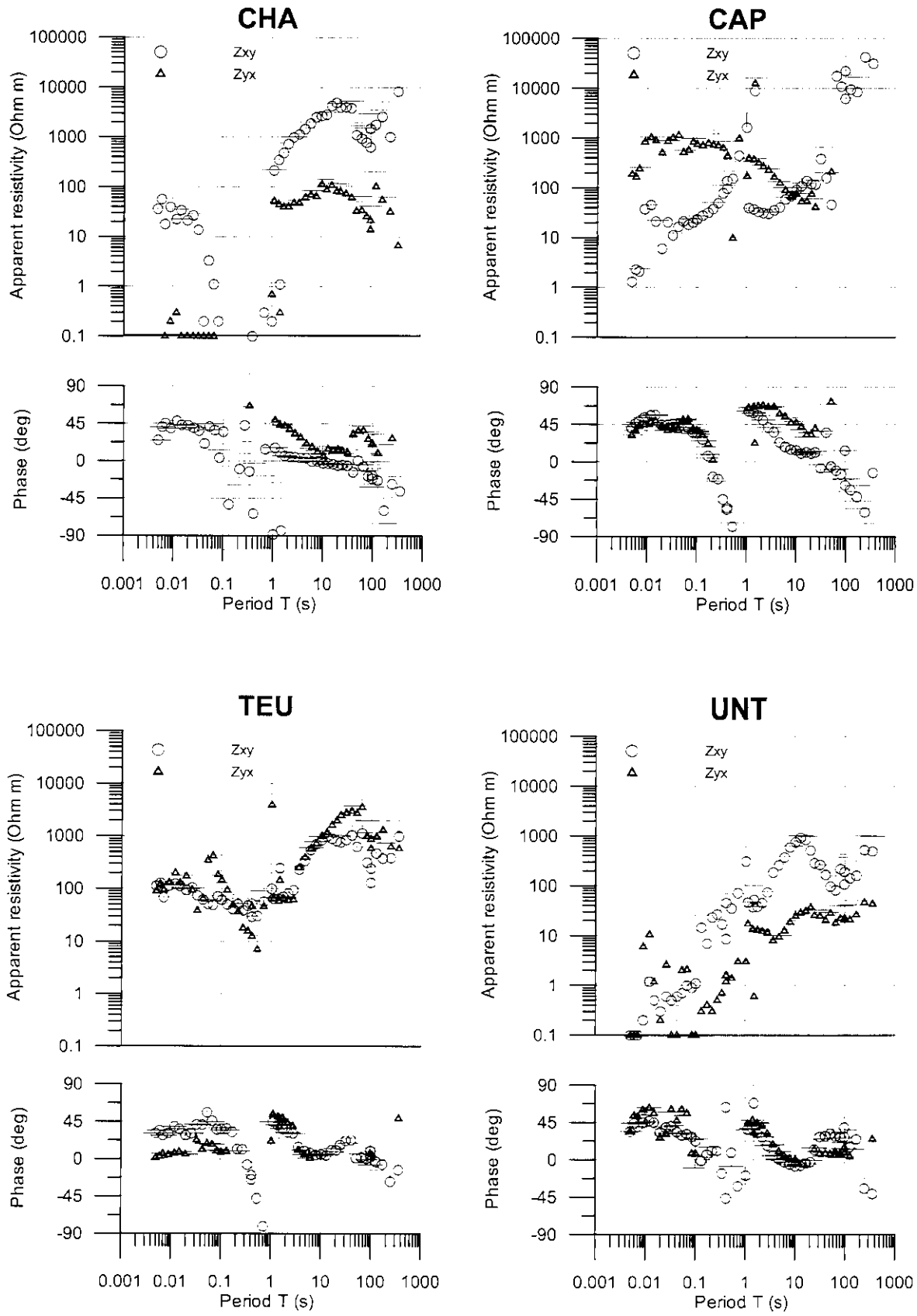

Fig. 3.7 (cont.): MT transfer function vs. signal period

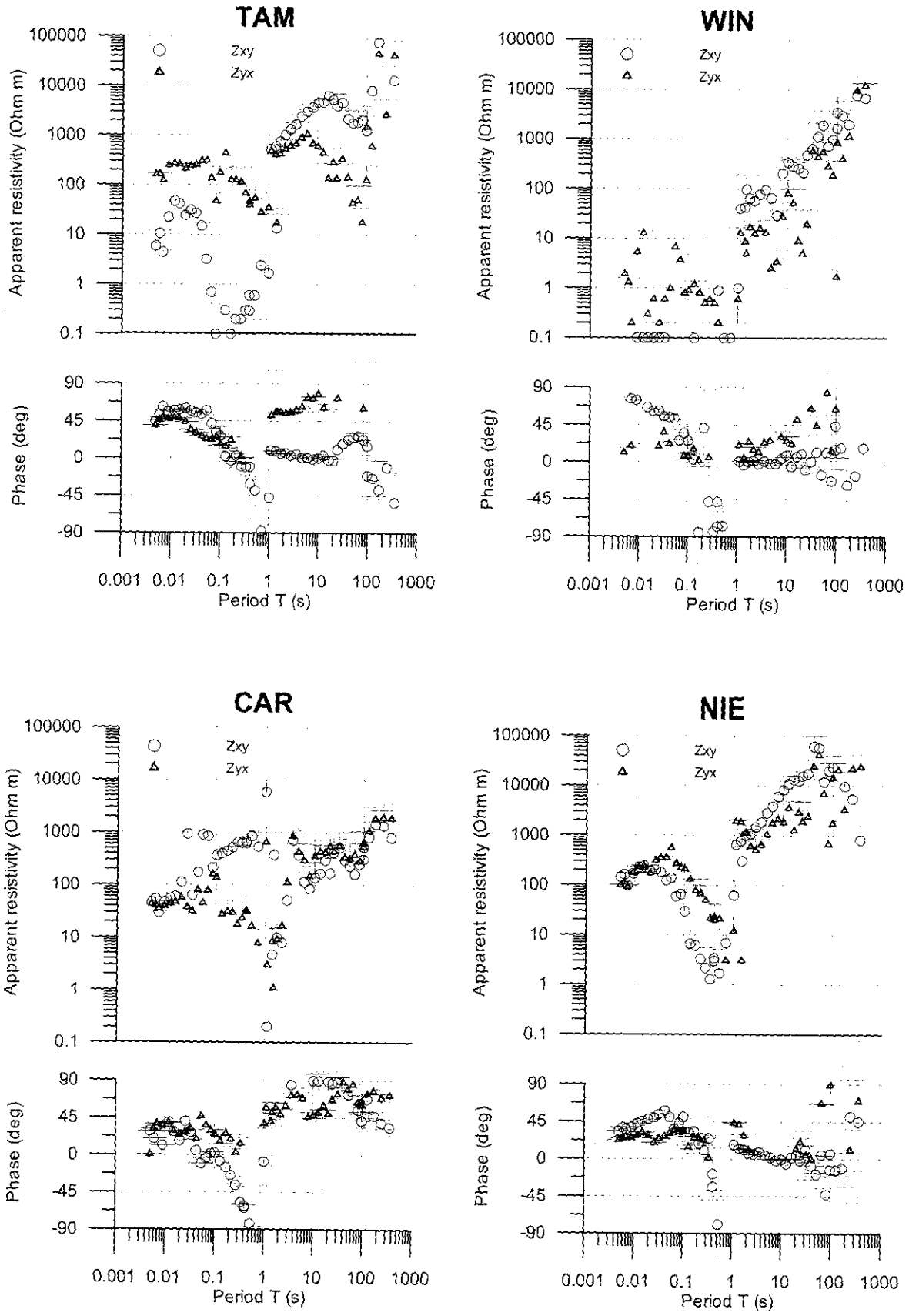

Fig. 3.7 (cont.): MT transfer function vs. signal period

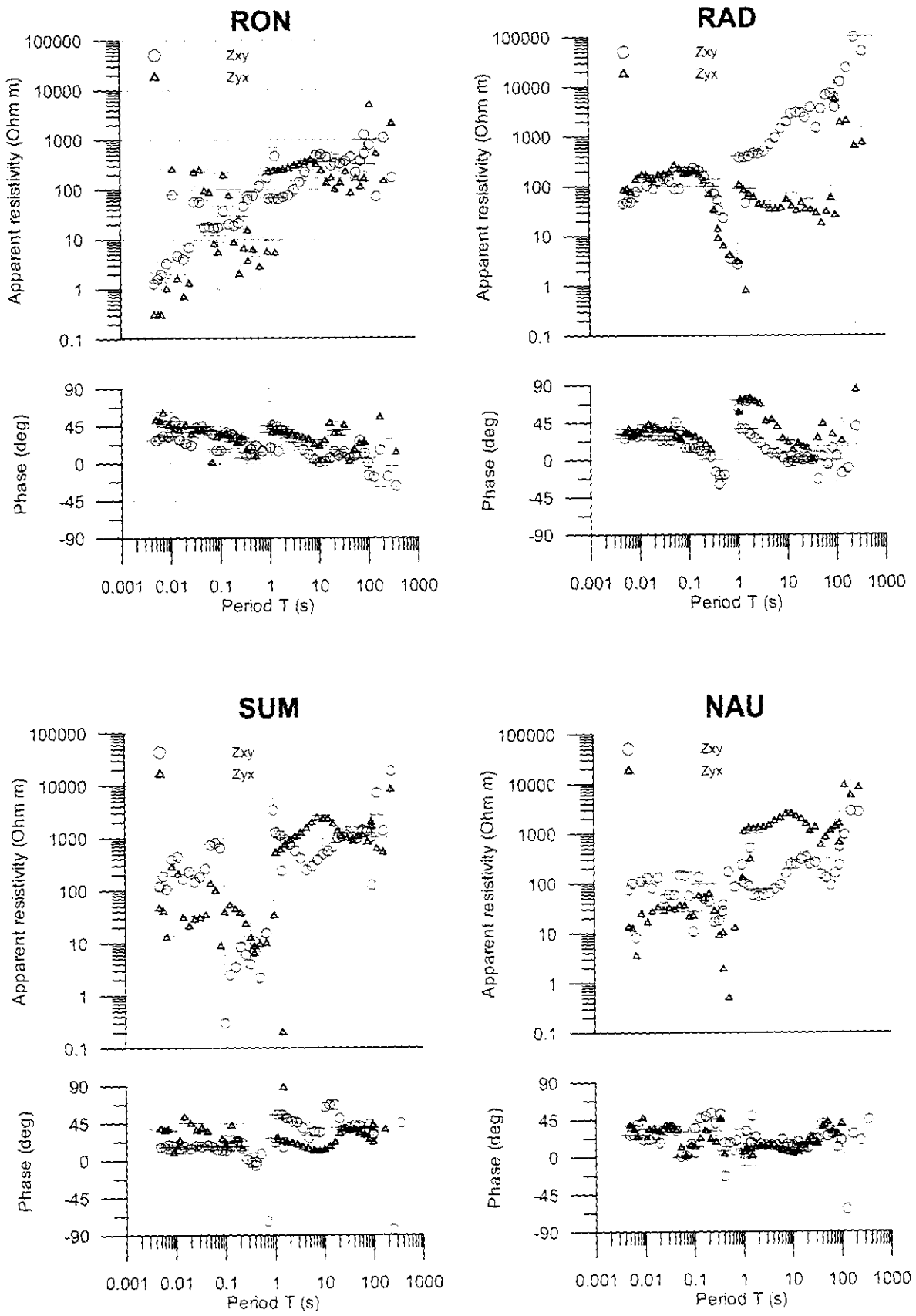

Fig. 3.7 (cont.): MT transfer function vs. signal period

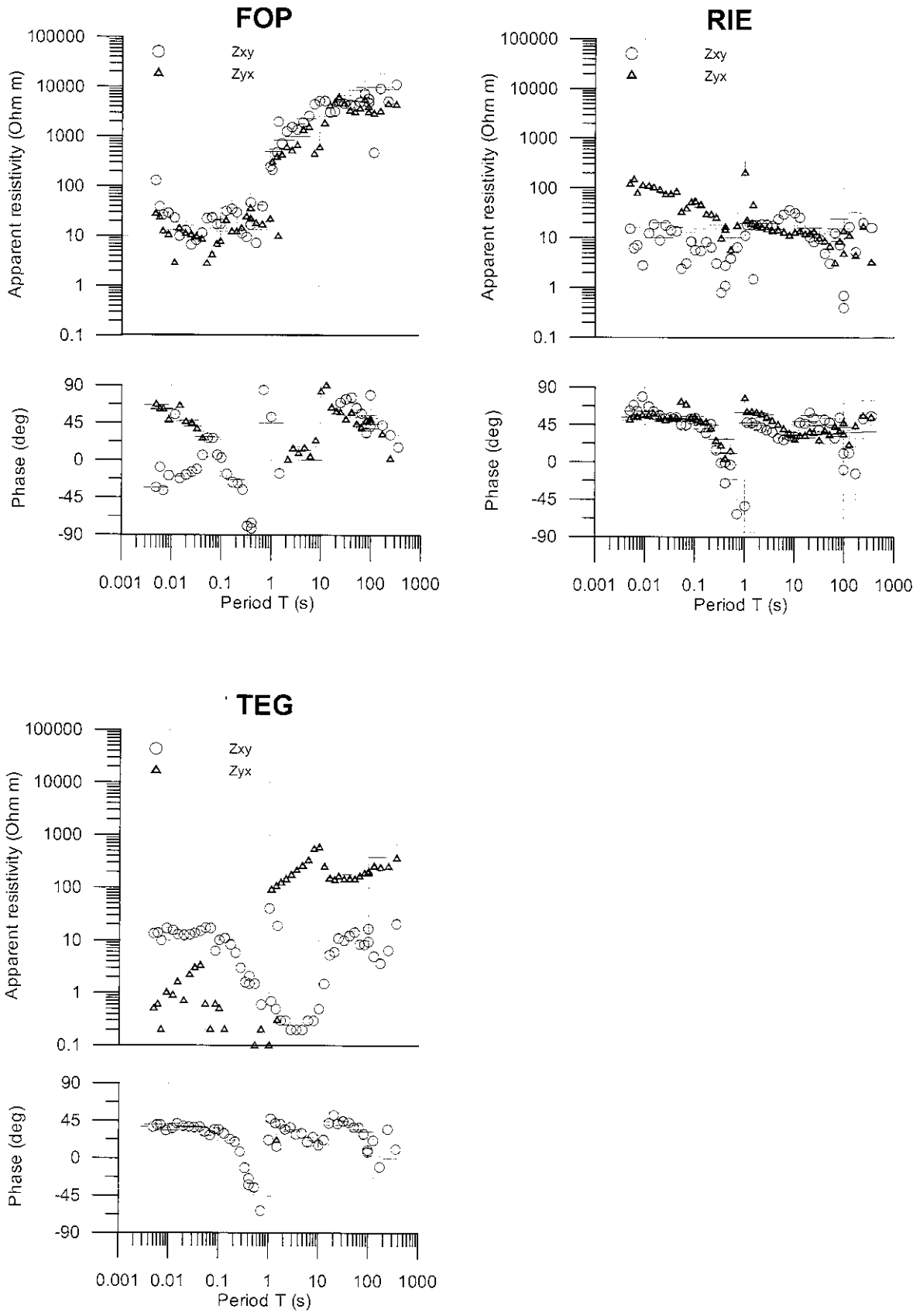

Fig. 3.7 (end): MT transfer function vs. signal period

4 Analysing GDS transfer functions

4.1 The pattern of the induction arrows

The inclusion of the imaginary induction arrows in the examination gives a quantitative measure for the influence of a three-dimensional conductivity distribution in the investigation area:
In the period range where no distortion takes place we expect the imaginary arrows to be opposed to the direction of the real arrows. At the periods of maximum induction, indicated by the maximum amplitude of the real induction arrows, the imaginary arrows change their direction by 180°. Generally, the measured induction arrows in Fig. 3.5 do not significantly show different behaviour to what would be expected for a two-dimensional structure. Except for a few sites, they do not indicate any influence of other conductors nearby.
From other induction studies in the Penninic Alps of western Switzerland (Fig. 4.2) (Schnegg, 1998), the Jura Mountains and the area between the Rhinegraben, the Bohemian Massive and the Central Alps (Berktold, 1978), we know that the predominant direction for real induction arrows is south-eastwards. Induction studies (Tab. 4.1) conducted by Bahr (pers. comm.) in the Western Alps (Fig. 4.1) confirm this observation also to longer periods, whereas his study (Bahr, 1992) in the Grossvenediger Massiv (Eastern Alps) shows induction arrows pointing south-west (Fig. 4.1).
The Molasse foredeep contributes to the direction south-east (Richards et al., 1982). This sediment basin (1-30 Ωm) extends over 800 km from Vienna to Geneva, and is partly overridden and incorporated into the orogenic wedge of the northerly propagating Alpine front (Schlunegger et al., 1997). Geological and geophysical observations confirm that the Bündnerschiefer in the investigation area is situated between the Penninic basement slices and the Helvetic massif. The Bündnerschiefer forms an elongated eastward plunging ramp with a considerable extension beneath the Austroalpine Units. The general eastwards plunging feature of the structures is confirmed by the shift of the maximum inductive response of the real parts of the induction arrows to longer periods towards the East. The maximum inductive response at ca. T= 10 s also indicates the top-of-basement. We consider the Bündnerschiefer's resistivities comparable with flysch sediments (20-100 Ωm), or lower, due to high organic carbon content ($\geq$ 1 wt %) (Steinmann, 1994).
Since the Bündnerschiefer can be regarded as a quasi two-dimensional structure, the azimuth of the induction arrows should be perpendicular to the strike of the inhomogeneity and point south-east or north-west. However, a rather different behaviour can be observed in the data. Apart from the expected predominant south-eastward direction of the real induction arrows, we also find real induction arrows (Fig. 3.6) on the Bündnerschiefer and in adjacent areas of the Helvetic Mesozoic cover sediments orientated in the main Swiss alpine strike direction (N65°E -N70°E). The particular geometry of the tectonic setting suggests that a flow of telluric currents around the surface boundary of the Bündnerschiefer might be responsible for this anomalous directional behaviour of the induction arrows. The very long induction arrows for the period T= 10 s together with their directional behaviour, indicate that a major lateral contrast in conductivity and geometry is present between the Mesozoic sediments and the resistive crystalline nappes.

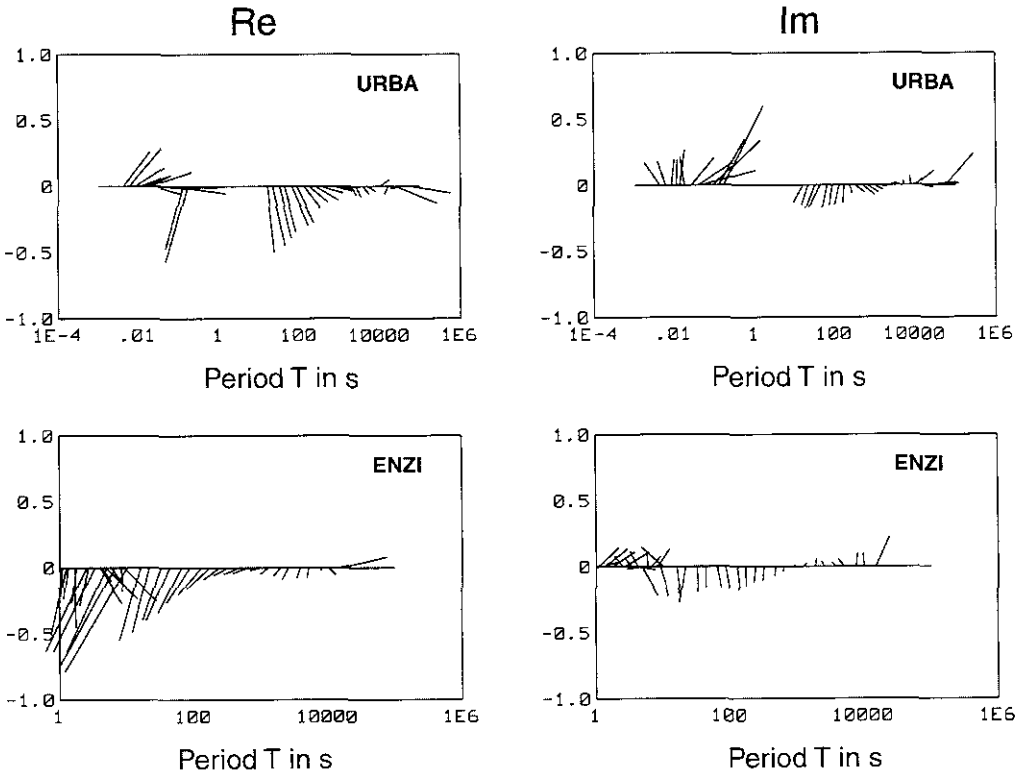

Fig. 4.1: Long period real and imaginary induction arrows vs. signal period in the Western and Eastern Alps. For location see Tab. 4.1, Bahr (1992).

site	X	Y	latitude	Longitude	alt. (m)	map no.	date	location
ENZI	236.507	995.81	47°09.729N	12°39.68E	1400			Gross Venediger (A)
URBA	168.75	658.55	46°40.122N	8° 12.290E	925	1230		Urbachtal (CH)

Tab. 4.1: Long period MT/GDS site locations in the Western and Eastern Alps by Bahr (1992). **X, Y** are the metric coordinates in the Swiss system CH1903. The **map no.** give the number of the "Landeskarte der Schweiz, 1:25 000", the period range covered is: T= 1-4096 s.

In particular, the change of direction next to the site SUF marks the direct and steep contact of both structures as illustrated in Fig. 4.4.

Induced polarisation measurements near the site RON (Suana, 1984) provides surface resistivities for crystalline rocks of the Penninic domain of about 8000 Ωm. Deep geoelectric surveys in the Southern Alps of Orobie revealed the existence of a substratum with high resistivity values of 15000-40000 Ωm (Alfano et al., 1994). Similar values are found by this method and seem to be typical for the exposed mantle rocks of the Ivrea Zone (Blohm, 1977). These values strongly suggest the existence of lateral conductivity contrasts between 10^0 and 10^3 and deep penetration depths for the electromagnetic field in the host medium from the Mesozoic sediments.

4.2 Local and regional conductive structures in Graubünden

Bündnerschiefer - Avers-Schiefer – Molasse foredeep

The induction arrow map (Fig. 3.6) suggests magnetic distortions of GDS data due to a possible current channelling or deflection effect. The Bündnerschiefer and Avers-Schiefer may be local conductive structures embedded between crystalline rocks, while the Molasse foredeep has to be considered as the dominant regional structure with a possible conductive link to the Bündnerschiefer. The minimum length of the prismatic ramp formed by the Bündnerschiefer is about 80 km, whereas the Avers-Schiefer is 30 km. The lengths of these structures, compared with the estimated skin depth in their host media shown in Tab. 2.2, are small for periods longer than T = 10 s and resistivity values of the host rocks greater than 1000 Ωm. This indicates that if magnetic distortion is present in the data, the magnetic transfer functions are mostly affected for periods longer than T= 10 s. Furthermore, even the whole data set can be distorted if the host rocks reach resistivities of 10 000 Ωm.

Basal Penninic Thrust

Schnegg (1998) found a highly conductive slab (0.2 Ωm) in the western Swiss Alps at the base of the Penninic nappes. This slab (Fig. 4.3) assumes the shape of the alpine arc. In analogy, we expect a similar or possibly the same structure related to the Penninic basement in eastern Switzerland. In this context, the outcrop of the basal Penninic thrust (Fig. 1.4) represents the shape of a possible regional conductive structure into which currents might be induced and finally injected into the Bündnerschiefer.

The Helvetic units in eastern Switzerland

Erdelbrock (1994) studied the area situated between Appenzell and Chur for its diagenetic or metamorphic grade, using vitrinite reflectance and illite "crystallinity". The area comprises the complete tectonic sequence of the Helvetic nappe stack and Penninic relicts which are partially preserved in the uppermost parts. The nappe stack just against the Subalpine Molasse in the North – in the South it is separated by the Main Helvetic Thrust from underlying allochtonous Ultrahelvetic to Penninic and parautochtonous Helvetic units.
The overall metamorphic grade shows little variation along the strike, but increases strongly from North to South with only a minor influence from tectonic limits. Between the Helvetic-Penninic nappe stack and the Infrahelvetic, as well as between the uppermost Helvetic Säntis nappe and the Subalpine Molasse, sudden changes in the diagenetic or metamorphic grade (Fig. 4.5) were observed (Erdelbrock, 1994). A ca. 3 km broad zone containing semi graphite tends from Bad Ragaz along the alpine strike towards the Plattenspitz (Erdelbrock, 1994). If the graphite minerals form interconnected phases, which is a necessary condition for electrical current flow, remains uncertain

The Turba Mylonite Zone

The Turba Mylonite Zone (TMZ) defines the Penninic-Austroalpine boundary in eastern Switzerland. It separates upper and lower stacks of nappes with contrasting tectonic history (Nievergelt et al., 1996). The lower nappes comprise the Suretta nappe, Schams nappe, Avers-Schiefer, and Oberhalbstein flysch, conatin Tertiary sediments. The upper stacks consist out of the Austroalpine Platta ophiolites and Malenco-Forno-Lizun ophiolites. The zone itself shows a top to West directed movement and is interpreted as an east dipping, low angle normal fault (45 – 30 Ma), more precisely as an extensional shear zone. The Engadine Line accommodates an oblique sinistral slip and block rotation (Schmid & Froitzheim, 1993) and causes a sinistral offset of the Turba Mylonite Zone in the map view of Fig. 1.4.
Vitrinite reflectance and illite "crystallinity" data (Mählmann, 1995) in shaly sediments above and below the TMZ coincides with a drop in peak metamorphic temperatures from 350°C in the top of the footwall to about 280°C at the base of the hangingwall (Nievergelt et al., 1996). The data in Fig. 4.6 indicate for the base of the hangingwall a peak metamorphic temperature of about 280°C. The TMZ represents a marked discontinuity of the vitrinite reflectance profile normal to the vertical nappe boundaries. Organic matter (syngenetic?) was almost exclusively converted into graphite, indicating a temperature of more than 350° C (Nievergelt et al., 1996). Thus, the TMZ might create an effective conductivity anomaly for the shallow upper crust.

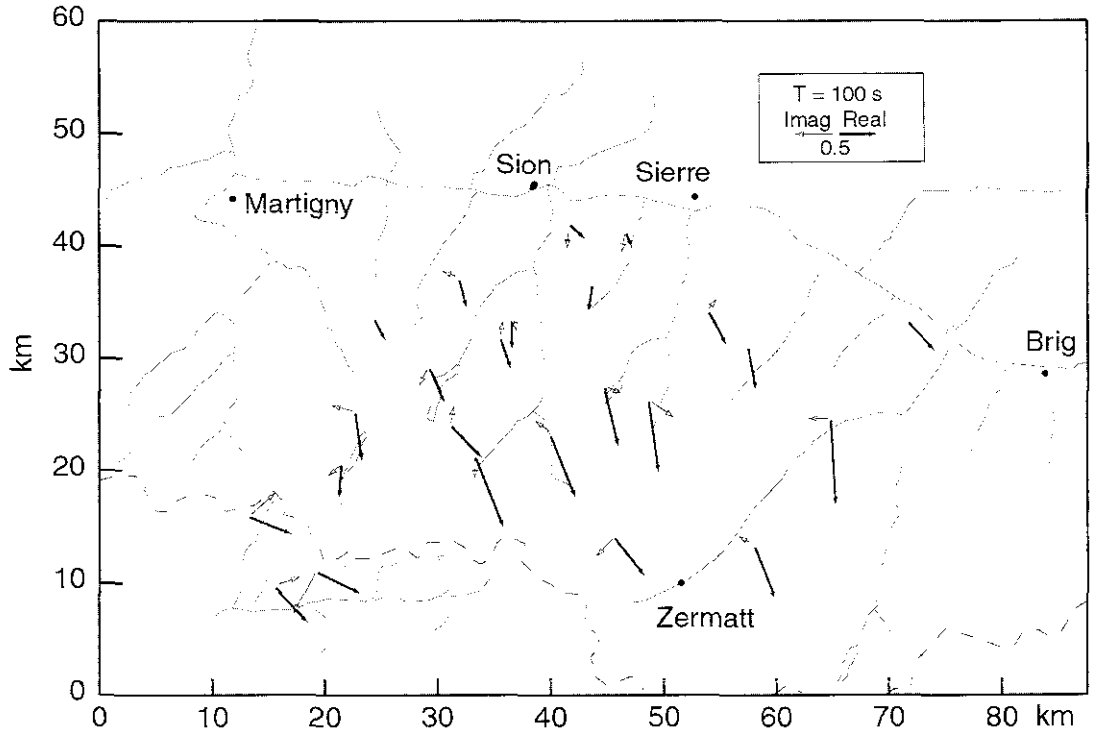

Fig 4.2 Measured real and imaginary induction arrows in the western Swiss Alps. Frame rotated N30°E (Schnegg,1998).

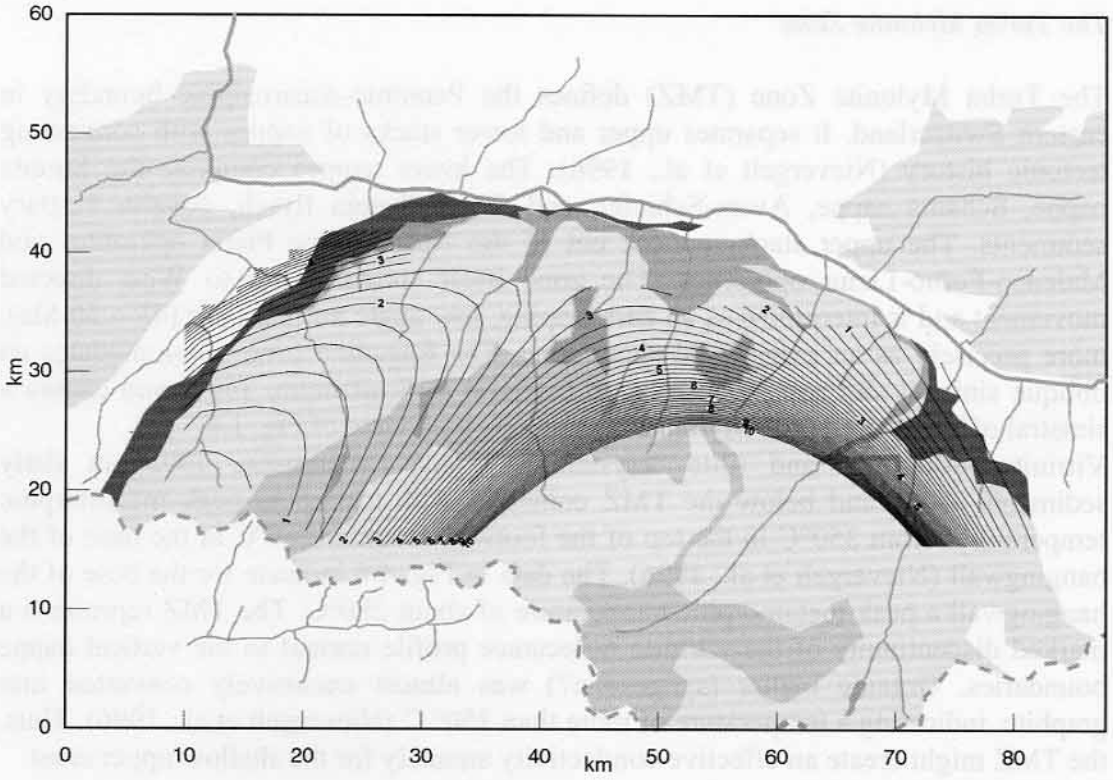

Fig. 4.3: 3-D final model of the MT/GDS survey of the Penninic Alps of Valais (Schnegg, 1998) showing isolines of the depth to the 0.2 Ωm body (km). Frame rotated N30°E.

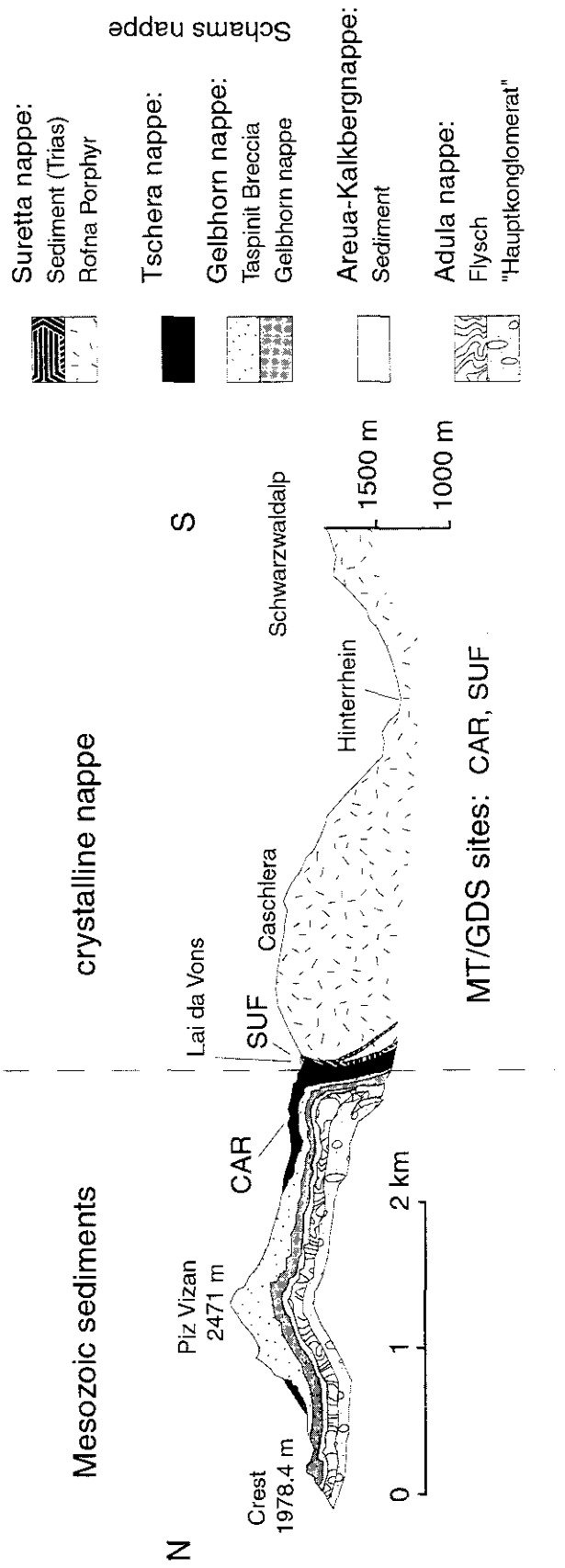

Fig. 4.4: Cross-section through the investigation area showing the steep sedimentary bands of the Schams unit in front of the hangingwall of the Suretta nappe . After J. Neher in: (Streiff et al., 1976).

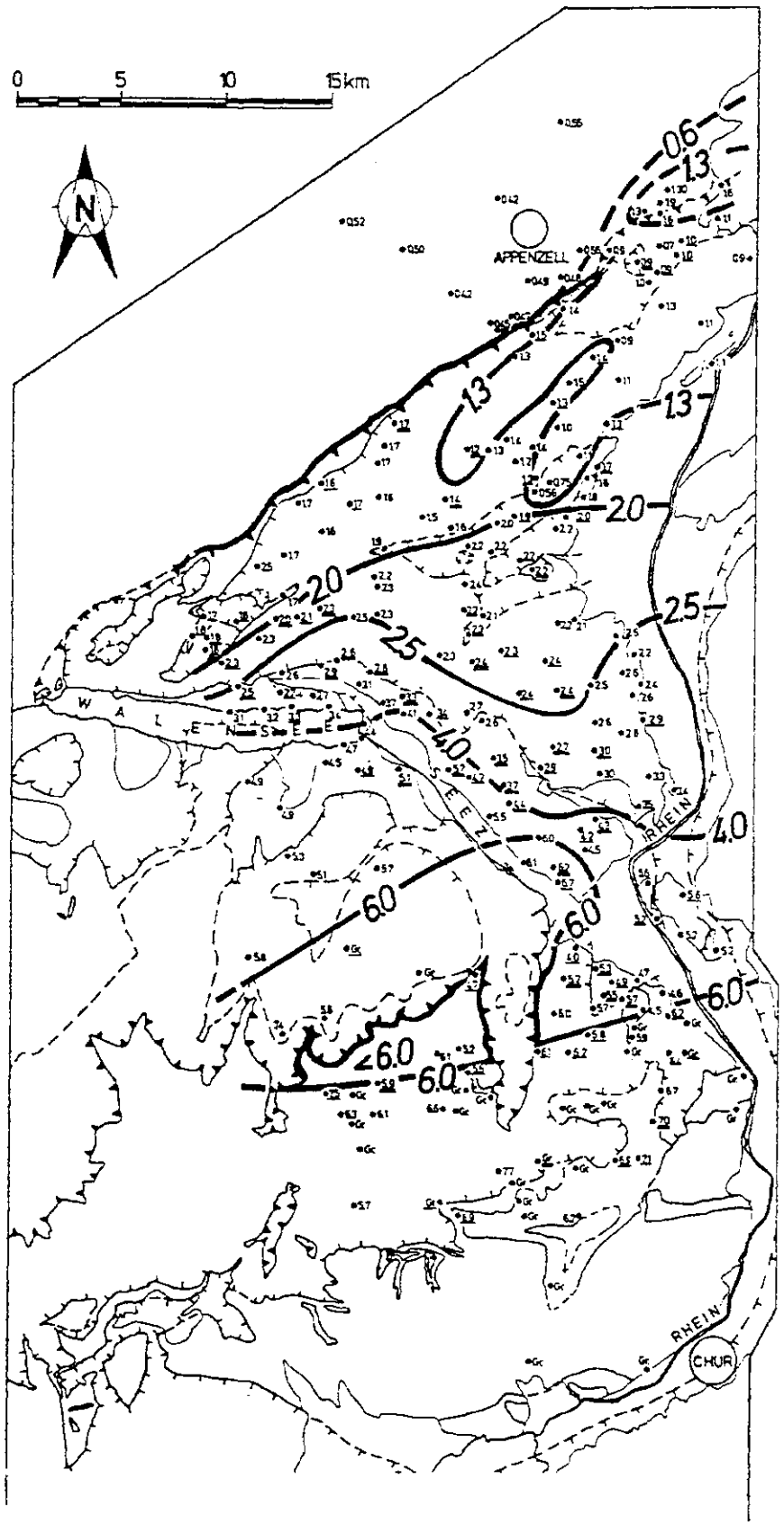

Fig. 4.5: Coal rank development (isoapostilben) in the Helvetic units of eastern Switzerland. Values of R max vitrinite reflectance. Gr = graphite. (Erdelbrock, 1994).

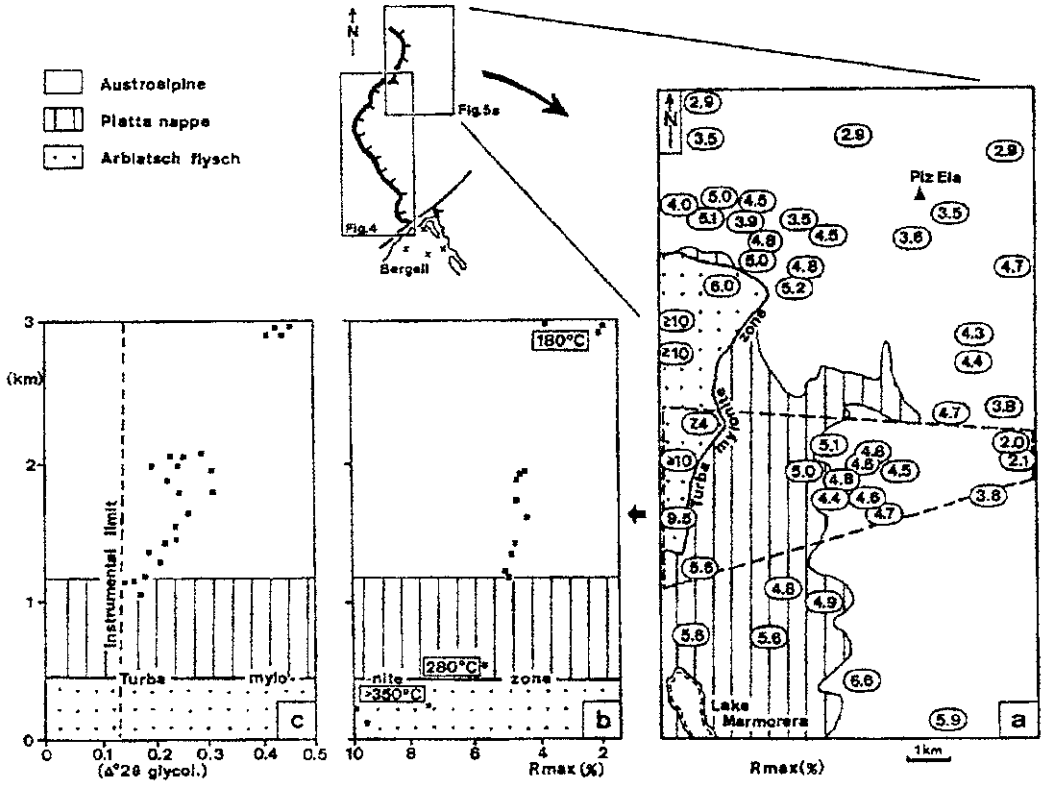

Fig. 4.6: Vitrinite reflectance and illite "crystallinity" data from the northern part of the Turba Mylonite Zone. (a) Map showing sample location and measured maximum reflectance (R max) values. (b) Vertical distribution of R max values from area outlined by dashed line in Fig. (a). The vertical axis gives the position in the nappe pile measured perpendicularly to the gently east dipping nappe boundaries. Numbers in boxes are peak temperatures derived from various vitrinite parameters and illite "crystallinity". Note the linear increase of R max in hanging wall and the abrupt change toward higher values across the Turba Mylonite Zone. (c) Illite "crystallinity"; data from the same profile. (Nievergelt et al., 1996).

4.3 Structural discontinuities – a case study of the Tschera nappe

The change of direction of the real induction arrows occurs between the two MT/GDS sites SUF and CAR over a 400 m distance on the Tschera/Gelbhorn nappe. This implies that a major contrast in the conductivity with considerable lateral and vertical extension is present in this contact zone.
A combined survey using the self-potential (SP), magnetic profiling and continuously measuring Radio-Frequency Electro-Magnetic (RF-EM) method was undertaken to study the fold geometry and the lithostratigraphy of the Tschera nappe (Fig. 4.7). Originally, the measurements were initiated to give evidence for the existence or the absence of a presumed electrical high conductivity zone of large lateral extent within this major contact. If the conductivity anomaly really exists, the zone could contribute to the directional dualism of the real parts of the induction arrows observed in the MT/GDS survey of Graubünden. The absence of such a highly conductive zone would, on the contrary, supports the magnetic distortion hypothesis for the magnetic transfer function in the Graubünden. This major contact is therefore an important key for the understanding of electromagnetic induction processes in the Central Alps.

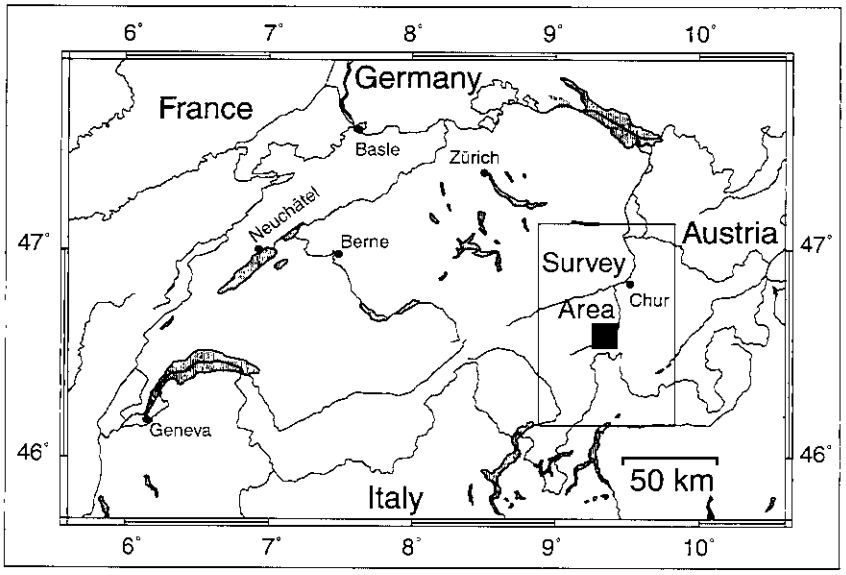

Fig. 4.7: Location of the combined geophysical survey over the Tschera nappe (black box).

The Tschera and Gelbhorn nappe (Fig. 4.4) are sub-units of the Schams nappe, which is the allochthonous part of the Mesozoic sedimentary cover of the imbricated Tambo/Suretta basement slices. The structural contact of the Bündnerschiefer further to the North and the crystalline Suretta nappe to the South is characterised by the presence of various sediments. The series include Plattensandstein, anoxic black shales and various Triassic carbonates. The rocks form a compressed series of steep and deep reaching (detached) sedimentary bands divided by thrusts. The black shales exhibit a high content of organic carbon (Schmid et al., 1990). The alteration of competent and incompetent layers creates an eroded, smoothly varying morphology without any remarkable outcrops (see also Fig. 4.16a).
Structural discontinuities are promising candidates for the creation of conductive zones. Besides highly conductive structures caused by partial melt (Shankland & Waff, 1977), (Schmeling, 1986), there are two other principal conductivity

mechanisms producing low resistivity zones. Increased conductivities can result from electronically conducting ores, such as interconnected graphite or pyrite minerals, or arise from an ionic current flow caused by fluids (Jödicke, 1992). Graphite as a conductive solid phase is another reasonable candidate able to cause enhanced conductivity zones (ELKTB-Group, 1994). The role of interconnected graphite and electrolytic fluids to increase the electrical conductivity in the Preadriatic-Lineament in South Austria is discussed in several MT studies (Adam et al., 1986; Adam et al., 1992; Adam, 1995). Apart from the non-linear induced polarisation method (Bigalke & Junge, 1999), standard resistivity field surveys do not allow to distinguish between these two conductance mechanisms. However, SP-anomalies with magnitudes of several hundreds of millivolts are an important argument for the existence of electronically conducting minerals (Sato & Mooney, 1960).

A general hydrological model for fluid transport and escape of brines in the Western Alps is given in Fig. 4.8 (Arthaud & Dazy, 1989). This model reflects the tectonic setting of the stacked Penninic basement slices either in a N-S or in an E-W cross-section. The expected enhanced conductivity along deep reaching thrusts in the studied contact zone can then be caused by migrated brines from the lower crust.

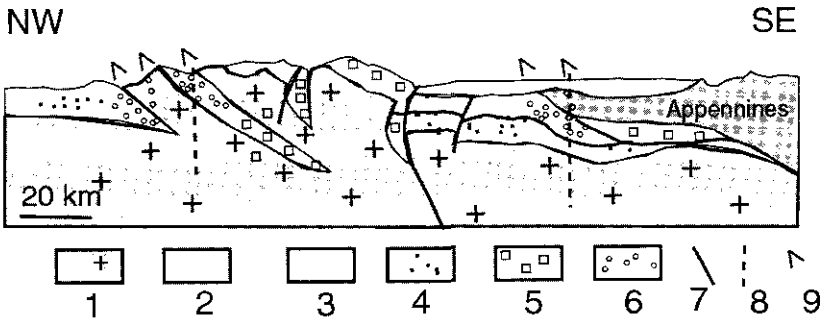

1 crystalline basement, 2 sediments, 3 Po basin, 4 non migrated brines,5 brines fixed by metamorphism, 6 brines migrated and/ or concentrated,7 major faults, 8 seismic fault, 9 source.

Fig. 4.8: Simplified tectonic section through the western alpine arc showing a general model of fluid traps and fluid escape along deep reaching thrusts. Redrawn from Arthaud & Dazy (1989).

In Fig. 4.9, we see that both conductivity mechanisms are, at first sight, possible in the area of interest: several sources and sinks are arranged along the major thrusts. However, the water in these sources reach conductivity values of about 200 µS/cm (T= 26°C). They stand in contrast (Fig. 4.10) with the extremely high conductivities in excess of 15000 µS/cm at T= 5.6°C (ca. 0.65 Ωm) measured in the mineral springs of Scuol-Tarasp/Inn valley, 50 km to the East (Bissig, 1997). Their isotopic CO_2 significance is typical for thermo-metamorphic reactions in carbonates from the crust (Wexsteen et al., 1988).
On the other hand, metamorphic organic matter up to a coal rank of semi-graphite is present in Graubünden (Erdelbrock, 1994; Mählmann, 1995; Mählmann, 1996). Weh et al. (1996) state that in many cases, structural and metamorphic discontinuities coincide.

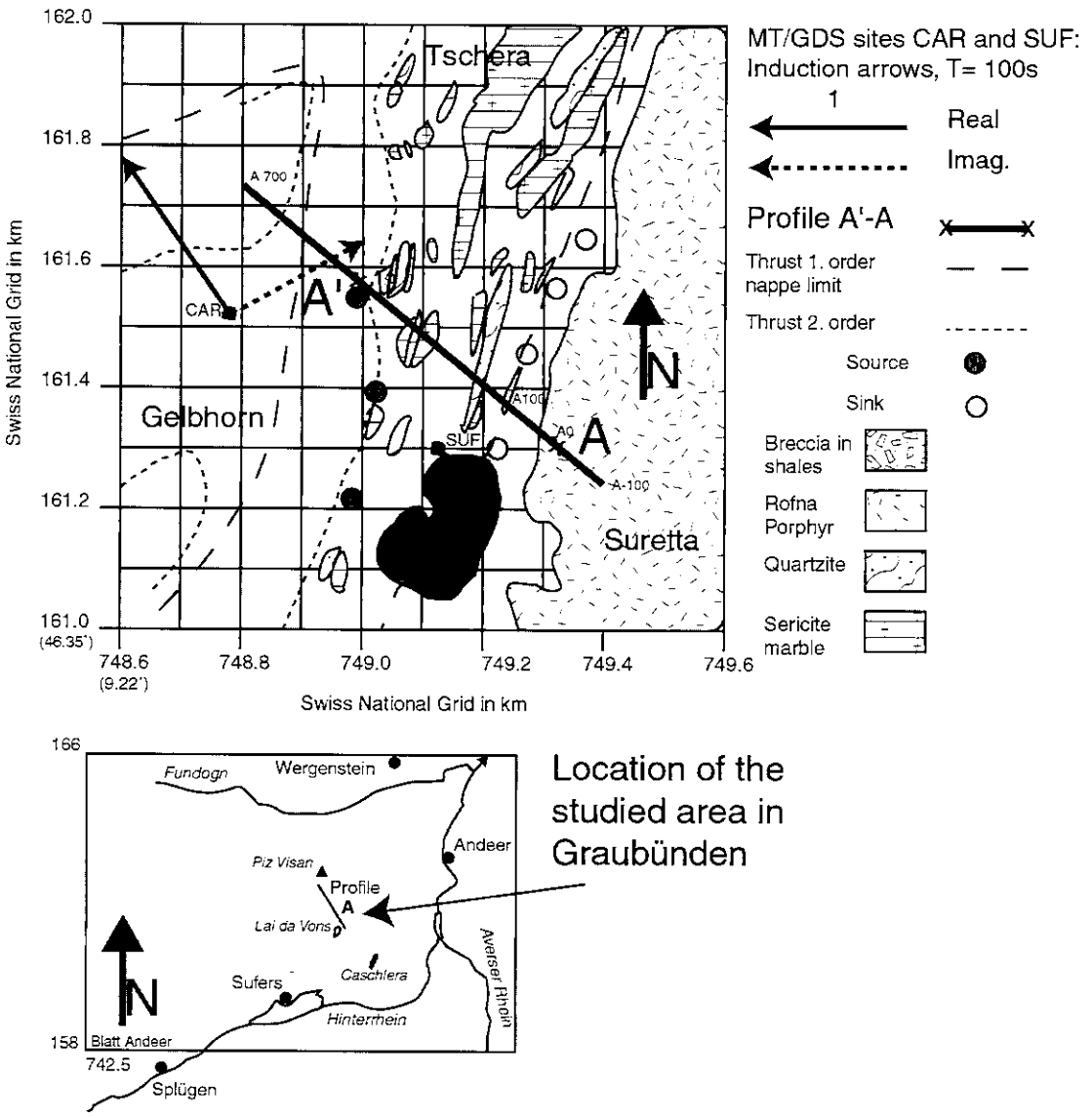

Fig. 4.9: Map of the studied area showing the main tectonic/geologic features and the profile A on wich the geopysical measurements were conducted. Adapted from Streiff (Streiff et al., 1971).

In conclusion it can be said that because of the enhanced organic carbon content of the black shales in the Tschera unit one expects in analogous to what was found in the MT/GDS survey in the Alps of Valais (Schnegg, 1998), to find a graphite conductivity anomaly.

Fig. 4.9 (see also Fig. 4.16) shows profile A (length: 800 m, orientation: N309°E). It lies almost at right angle to the Suretta nappe and to the Gelbhorn which extend to the Tschera nappe. Also shown are the induction arrows (pointing away from a good conductor) for the period T= 100 s of the two MT/GDS sites CAR and SUF. Since the change of direction of the induction arrows in Graubünden is almost independent of the signal period (Gurk, 1999), this supports our initial hypothesis that a major lateral change in conductivity might exist over these narrow sequences.

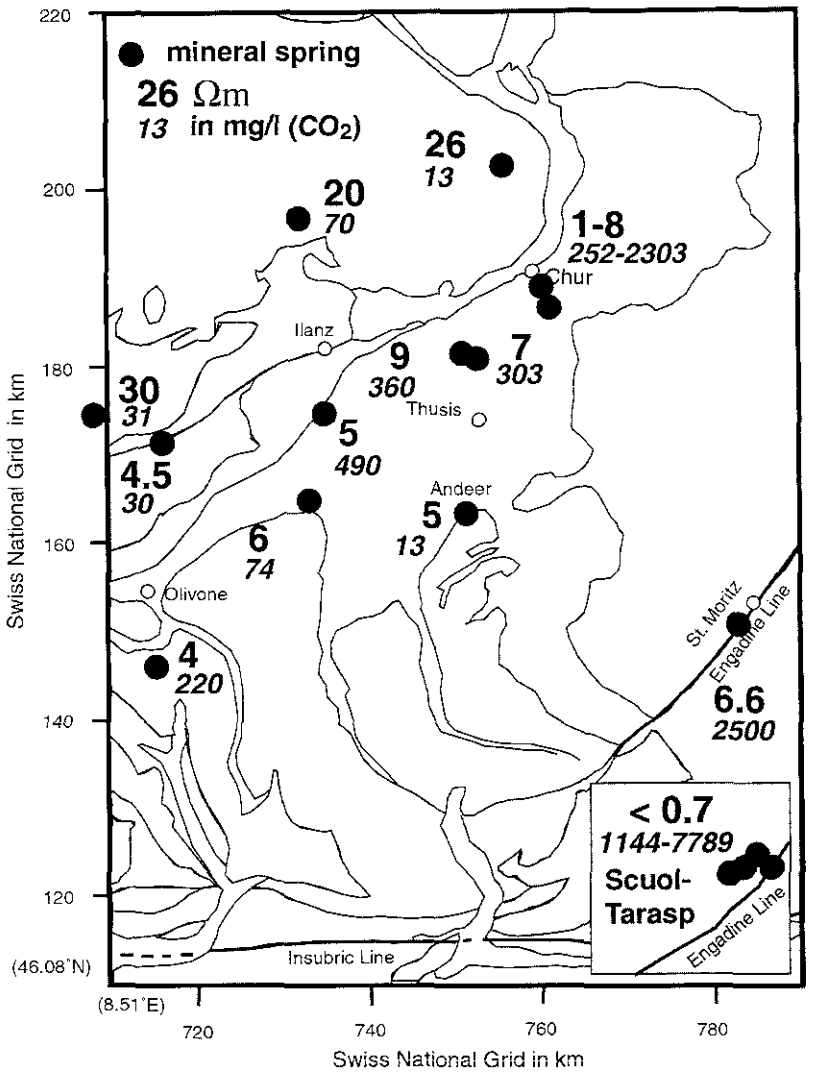

Fig. 4.10: Electrical resisitivities and CO_2 content of some mineral waters in Graubünden. Adapted from Vuataz (1998).

4.3.1 Data acquisition

Self-potential

Following the procedure of the SP technique described in section 2.5, the field is sampled every 20 m. On the anomalies the step size is reduced to 1.0 m or less.

Geoelectric

Schlumberger profiling along profile A of Fig. 4.9(100-200 m) and two Schlumberger deep soundings (L/2= 100 m, not shown in this paper) at 200 m and 160 m are carried out with an equipment developed at the Centre d'Hydrogéologie of the University of Neuchâtel (CHYN).

Magnetic field

Measurement of the total magnetic field was performed with a Geometrics G 816 proton precession magnetometer. We started with a sampling interval of 10 m to find the main anomalies and to document the magnetic background. On the anomalies the measuring interval was reduced to 1.0 or 0.2 m. All values were corrected for time variations using data of the Neuchâtel Geomagnetic Observatory.

RF-EM

The method is an enhancement of the traditional VLF-EM (Very–Low Frequency Electromagnetic) method. It uses electromagnetic signals of remote sources in the extended frequency range of 15-300 kHz.
The instrumentation we used was developed at the CHYN (Turberg & Müller, 1992). It continuously measures the local horizontal and vertical magnetic fields with two orthogonal induction coils. For a chosen frequency the device directly determines the "in-phase" and "out-of-phase" components of the secondary to primary magnetic field ratio, i.e. the real and imaginary part of the magnetic transfer function. Datalogging with 1 Hz or 4 Hz sampling rates can be chosen. Data obtained on a profile yield resistivity contrasts in the subsurface that directly reflect geological features such as fractures, faults or lateral facies/permeability variations.
The measuring system can be adapted in different configurations:

- self orientating antenna used with a vehicle,
- handheld antenna for use in difficult terrain.

In this survey we worked in the handheld mode. Compared to the imaginary parts, the real parts of the transfer function are affected much more by shaking the antenna while walking. In the handheld mode, these real parts are generally of minor quality and have not been used in this study.
The frequencies we used were 216 kHz with 4 Hz sampling rate and 20.3 kHz with 1 Hz sampling rate. With the subsurface apparent resistivities of about 1000-3000 Ωm obtained in previous geoelectric mapping (Fig. 4.12) and soundings along the profile, these frequencies provide the estimated penetration depths δ shown in Tab. 4.2.

	ρ_a = 1000 Ωm	ρ_a = 3000 Ωm
f=216 kHz, N221°E	δ= 30 m	δ= 60 m
f=20.3 kHz, N144°E	δ= 110 m	δ= 192 m

Tab. 4.2: Estimated skin–depths against apparent resistivities of the subsoil and signal frequencies of the RF-EM technique. These data were obtained with two transmitters in a northern azimuth.

4.3.2 Observations

A preliminary survey showed that all kinds of magnetic and SP anomalies are found with stable background values in the profile interval 0-320 m (A'-A, in Fig. 4.9).

Therefore we restrict our presentation to this 320 m part of the profile. The results of the three methods just discussed are presented in Fig. 4.11. The most striking anomalies are found with the self-potential and the magnetic method, whereas the RF-EM method shows a complex series of responses.

The magnetic and SP values create an ordered series of anomalies:
Starting from SE, the series begins with magnetic anomaly **M1** at 143 m immediately followed by a broad self-potential anomaly **SP1** with a minimum of about –270 mV at 149 m.
The series continues with the sharp magnetic anomaly **M2** at 181 m and self-potential anomaly **SP2** of about –300 mV at 229 m. An intermediate self-potential anomaly **SPi** (190 m) between **SP1** and **SP2** reaches only -150 mV. Beyond 200 m, the magnetic data show a smooth trend to higher values and ends with a sudden step (**M3**) to lower magnitudes at 250-260 m, followed by two small anomalies **M4** and **M5** (274 m, 300 m) at the left side of the profile. If we focus on the magnitudes of the magnetic anomaly pairs (**M1/M2**), (**M4/M5**), we state that this series starts with a low amplitude anomaly (**M1**) followed by the high amplitude **M2** anomaly. The pair on the left side of the profile shows the inverse order.

The shape of the self-potential anomalies

The dip of a buried conductor, or ideally a dyke with infinite lateral extension, can be estimated from the shape of the anomaly. A vertical dyke, as shown in Fig. 2.7, produces a symmetric SP anomaly, whereas a dyke with a certain dip distorts the anomaly shape. Anomaly **SP2** is in such a way distorted, that the NW shoulder is lower than the SE one. This behaviour corresponds to the model of a right dipping dyke (Telford et al., 1990). It is difficult to draw the same conclusion for **SP1**. This anomaly cannot be described by a simple dyke model. Nevertheless, a predominant right dipping feature seems to be present in the data.
The **SPi** anomaly shows an effect of a NW dipping structure.

The shape of the magnetic anomalies

Similar estimation about the dip of a buried dyke can be made for magnetic anomalies (Telford et al., 1990). But unfortunately, both magnetic anomaly pairs (**M1/M2**) and (**M4/M5**) are too close to each other. Therefore, no magnetic background values can be found between the anomalies and the analysis of their shape will be misleading. However, the sudden step (**M3**) to lower magnetic values, as mentioned above, is typical for a contact between two blocks of different susceptibilities.

Schlumberger profiling

The results of the Schlumberger-Profiling are shown in Fig. 4.12. The estimates of the integrated conductivities over the profile sequence (100-200 m) do not point to a high conductive zone. Nevertheless, the distinct repetition of some integrated conductivities implies to find a repetition of the lithology.

RF-EM sounding curves

Before analysing the RF-EM data, some aspects of the method should be considered:

The RF-EM technique is a true 2-D method for vertical structures. It obtains the magnetic transfer functions over a profile assuming E-polarisation.
Therefore, the instrument actually yields the magnetic field components: $B_z/B_{y'}$, with y' normal to the strike of the structure.
As listed in Tab. 4.2, the directions of the transmitter do not allow the precise E-polarisation case. Consequently a mixture of polarisation results in a distorted sounding curve. Additionally, the dip of a buried conductor will deform the RF-EM response (Neill & Labson, 1991-1993). This fact will severely impede the RF-EM interpretation.

a) 216 kHz RF-EM:

This sounding curve shows two branches of similar slope divided by a steep gradient in the middle of the profile. From the right to the left, the transfer functions of the first branch (110-180 m) decrease from values of about 10 % down to –5 %. The strong gradient in the uppermost right values results from an electric power line crosscutting the profile at zero metre. The second branch (220-300 m) shows signals decreasing from 10 % to 0 %. This branch is, compared to the first one, shifted (by a constant factor) to slightly higher values. Both branches show an anomaly pattern that can be correlated to those (**SP1**, **SP2**) of the self-potential survey, whereas only the inflection point at 260 m directly coincides with the sudden step (**M3**) in the magnetic data. The biggest change of the amplitudes is shown in the middle of the profile. At this position we also find the broad **SPi** anomaly in the self-potential data. The change rises from ca. 2 % at 180 m to ca. 9 % at 220 m and looks like the superposition of two signals yet far away enough from each other to be separated. Inflection points are found at 186 m and 210 m, giving a hint for a thrust and/or a major change in the lithology between these positions.

b) 20.3 kHz RF-EM:

This sounding curve is less smooth because of the decreased sampling rate. We find the signals less affected by the power line. Generally, compared to the 216 kHz band, information obtained by this frequency shows conductive features over the profile that are related to deeper structures:
From profile 0-50 m, the influence of the electric powerline in visible. The curve (50-95 m) reaches a plateau with values of about 0 % followed by a gradient with an inflection point at ca. 102 m. From 116-170 m, the "out-of-phase" signal decreases (-5% to -13%). The conductive structure that produces the **SP1** anomaly is in the RF-EM curve (145 m) also detectable.
From 170-255 m we find a constant increase of the sounding curve up to values of ca. –5 %.
Towards the end of the profile (255-300 m), the curve is disturbed. Nevertheless, it might show a gradient with inflection point at 260 m (**M3**).
The 20.3 kHz curve shows the same trend as the 216 kHz one, but the presence of a steep gradient at ca.180-220 m and an effect due to the **SP2** anomaly can not be confirmed.

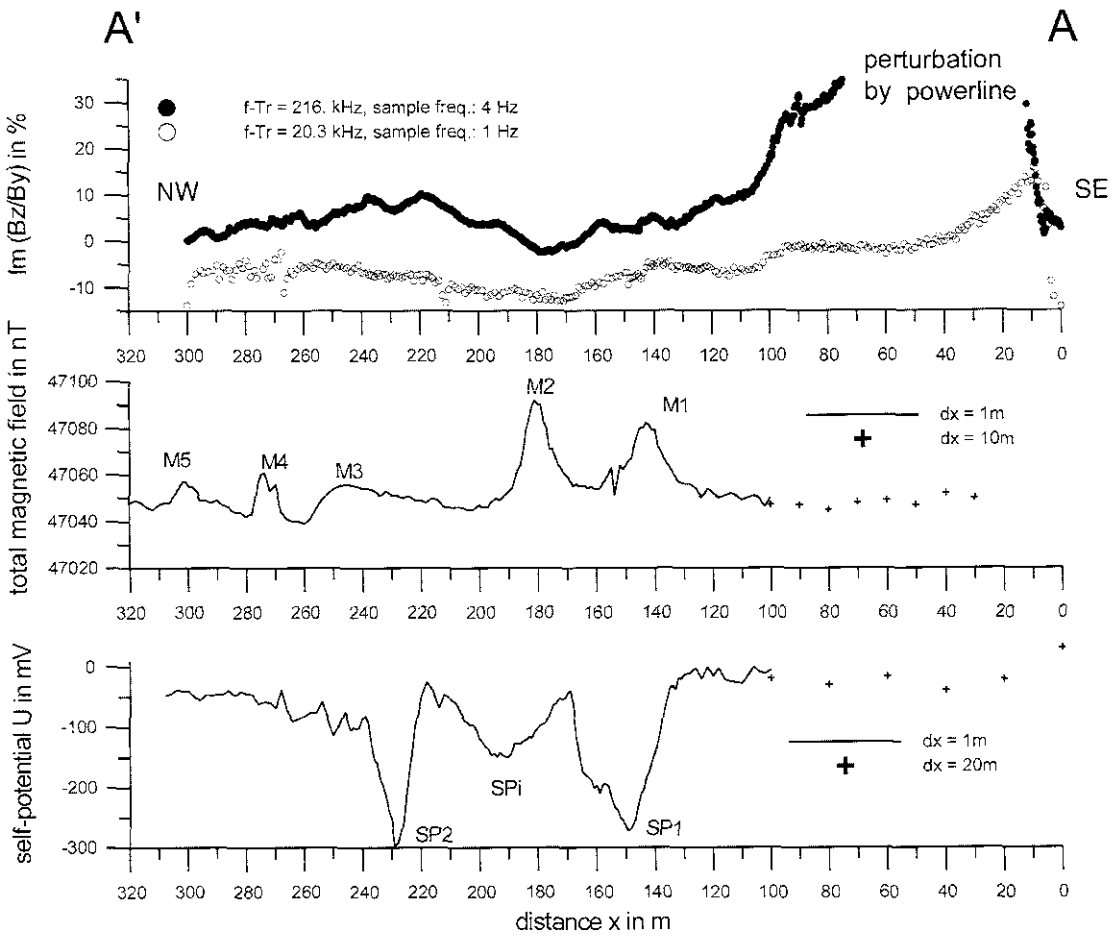

Fig. 4.11: RF-EM, total intensity of the magnetic field, and self-potential measurements along profile section A'-A.

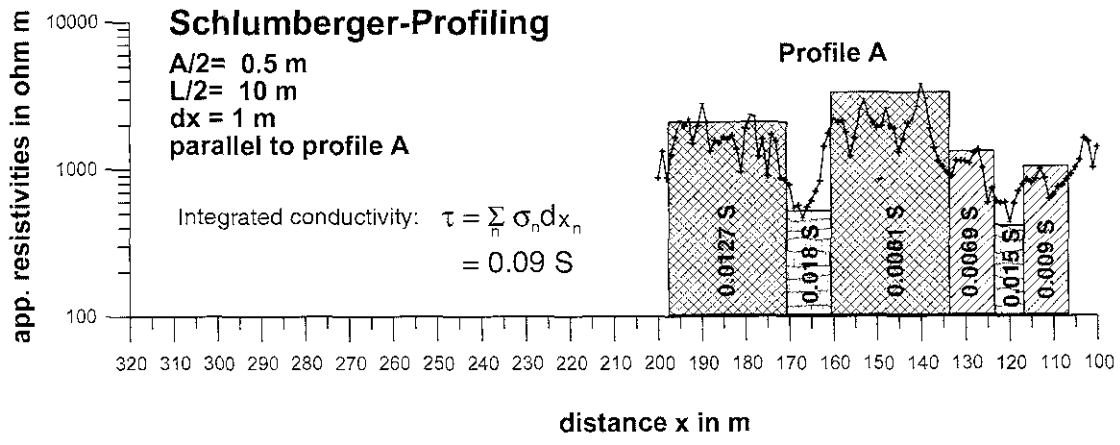

Fig. 4.12: Apparent resistivities and estimates of the integrated conductivity along a section of profile A.

4.3.3 Interpretation

The sequence of magnetic and SP anomalies:

SP2-M2-SP1-M1

may be interpreted in stratigraphical and tectonic terms. According to the geological map (Fig. 4.9, Streiff, 1971) we can assume that both types of anomalies of this series are caused by the same lithology. Fig.4.13 shows that this series can then be interpreted as tight folds, which are dipping either NW or SE.

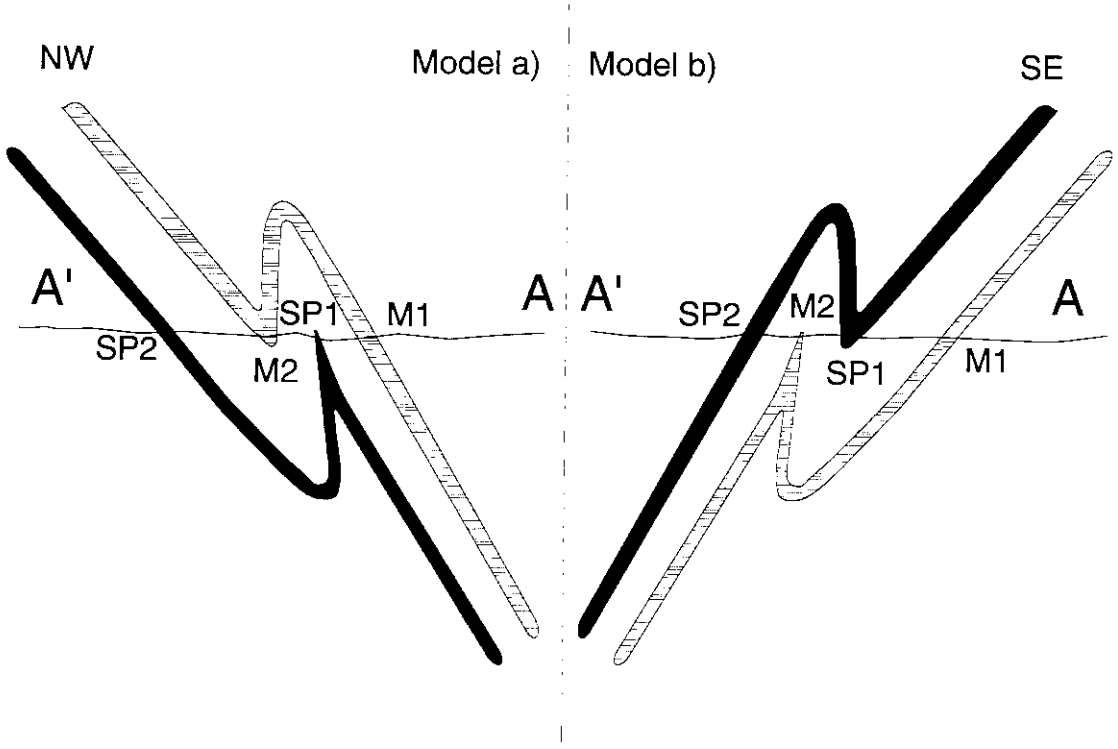

Fig. 4.13: Two equivalent explanation for the observed series of magnetic and self-potential anomalies.

The first case is less probable since the analysis of the shape of anomaly **SP2** already points towards a south dipping structure. However, the dip angle and the extension with depth of the strata remain uncertain. The SP data may be modelled to delineate the most realistic fold geometry (Fig. 4.14).

Self-Potential Model

The modelling has been performed at the University of Frankfurt/Main using a routine by Bigalke (Bigalke & Grabner, 1997) which includes an electrochemical model of the redox potential distribution. It was necessary to split the self-potential data into two branches and to limit the sample interval to 3.5 m. The intermediate anomaly **SPi** was excluded from the modelling. Each branch has been treated separately.
The most striking feature is the good match of both models. The first conductor, responsible for anomaly **SP2**, plunges southwards down to a depth of 40 m and with a dip of about 45°. If extrapolated, the conductor finds its continuation in the 80°

northwards and 62° southwards dipping limbs of the anticline structure of the second conductor. Although we did not take the **SPi** anomaly into account, the model fits the field data sufficiently well. Generally, the model confirms our former analysis of the ordered anomaly series. Yet, the origin of the **SPi** anomaly, respectively the structure referring to the strong gradient in the 216 kHz RF-EM data between 180 m and 220 m is still unknown.

Interpretation of the RF-EM data

We can extract the following information out of the RF-EM survey:
The inflection point in the 20.3 kHz curve at 102 m indicates the structural contact (thrust) between the Rofna Porphyr (Fig. 4.9) and the Tschera nappe. Another thrust is shown by the inflection points in both frequencies and by the magnetic anomaly **M3** at 260 m.
The **SP1** anomaly is detected in both frequencies at slightly different position (ca.148 m). Hence this anomaly extends almost vertically. The **SP2** anomaly is only visible in the 216 kHz band. Therefore, it extends only to a depth of about 30-110 m, which is in good agreement with the SP model. The same conclusion can be drawn for the structure corresponding to the steep gradient in the middle of the 216 kHz curve.
A line current approximation on the base of the SP model allows studying the contribution of the SP model to the RF-EM sounding. The approximation is shown in Fig. 4.15. Generally, the RF-EM data are sufficiently explained by the SP model, except for one inflection point in the middle of the profile. From this comparison we may conclude, that the RF-EM curve is at this point created by a different tectonic feature and not caused by the lithology that forms the **SP1** and **SP2** anomalies.

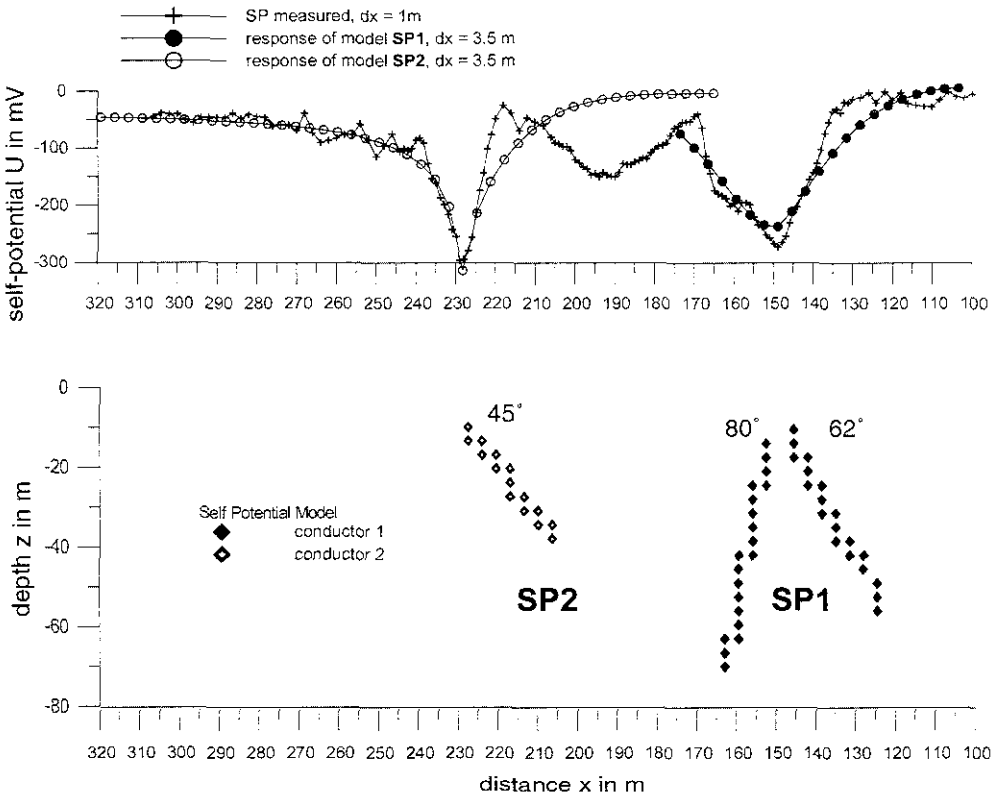

Fig. 4.14: Model of the self-potential data and its response.

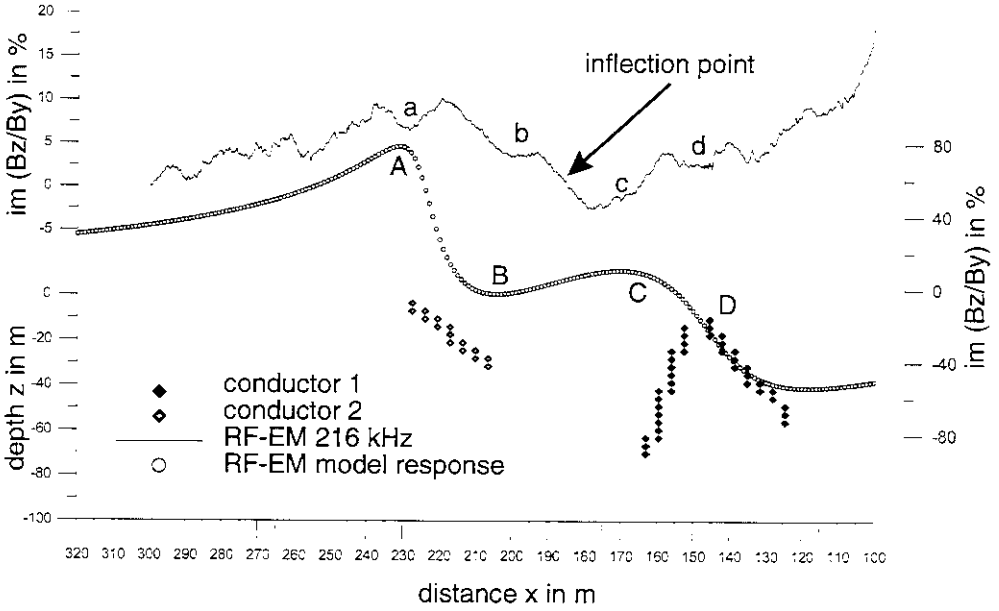

Fig. 4.15: Synthetic RF-EM sounding curve (RF-EM model response) calculated on the base of the SP model (conductor 1 and 2) compared with the measured RF-EM sounding curve (216 kHz).

4.3.4 Conclusion

In order to confirm our interpretation, we investigated the anomalies along the profile A'-A by coring and rock sampling. The main findings are listed in Table 4.3. The magnetic anomalies (**M1**, **M2**) and (**M4**, **M5**) are generated by (exposed) magnetite bearing Plattensandstein. Black shale with a high graphite content can be addressed to the **SP1** and **SP2** anomaly, whereas at the place of the **SPi** anomaly only strongly weathered gneiss was found. From this observation and from the findings of the previous section, we conclude that the **SPi** anomaly and the strong gradient in the 216 kHz RF-EM data are caused by a thrust. It extends, slightly dipping to the NW, down to a maximum depth of 30-110 m. This conclusion leads to the synoptic model presented in Fig. 4.16a. Compression of the isoclinal folds (see Fig. 4.16b) leads to a detachment along the most incompetent series (black shale) of the folded Tschera nappe. The projected effective direction of the magnetisation in the Plattensandstein onto the profile will then create the observed change in the amplitudes of the magnetic anomaly pairs (**M1**/**M2**) and (**M4**/**M5**).

The geophysical findings and the modelling of the SP data are in good agreement with the geological analysis of the sequence. Moreover, the survey was able to confirm the known geology at this place and could detect two additional thrust faults in the Tschera unit. The presence of interconnected graphite is confirmed by the SP method.

On a more regional scale, the electrical properties offered by the Tschera nappe are not sufficient to create a large conductive zone, which can be responsible for the directional dualism of the GDS real induction arrows observed in Graubünden at long periods ($T > 10$ s). Consequently, the directional change of the real part of the induction arrows is more likely the result of magnetic distortion of the magnetic transfer function (Gurk, 1999).

x in m	Anomaly	Lithology
100	RF-EM	thrust (structural contact Tschera/Rofna porphyr)
143	**M1**	exposed Plattensandstein ("Gault") with magnetite (N285°E / 68°)
149	RF-EM/ **SP1**	exposed graphitic blackshale (N285°E / 79°)
179		exposed sericite marble (N302°E / 67°)
181	**M2**	Plattensandstein ("Gault") with magnetite
190	RF-EM **SPi**	strongly weathered gneiss, dip to NW, thrust
229	RF-EM/ **SP2**	graphitic blackshale (ca. 2 m overburden by strongly weathered gneiss)
260	RF-EM/ **M3**	thrust, contact between two units of different susceptibility
287	**M4**	(N123°E / 69°) Plattensandstein ("Gault")
290	**M5**	(N123°E / 78°) Plattensandstein ("Gault")

Tab. 4.3: Type of geophysical anomaly, lithology after Streiff (1971) and strike and dip values along the profile section A'-A.

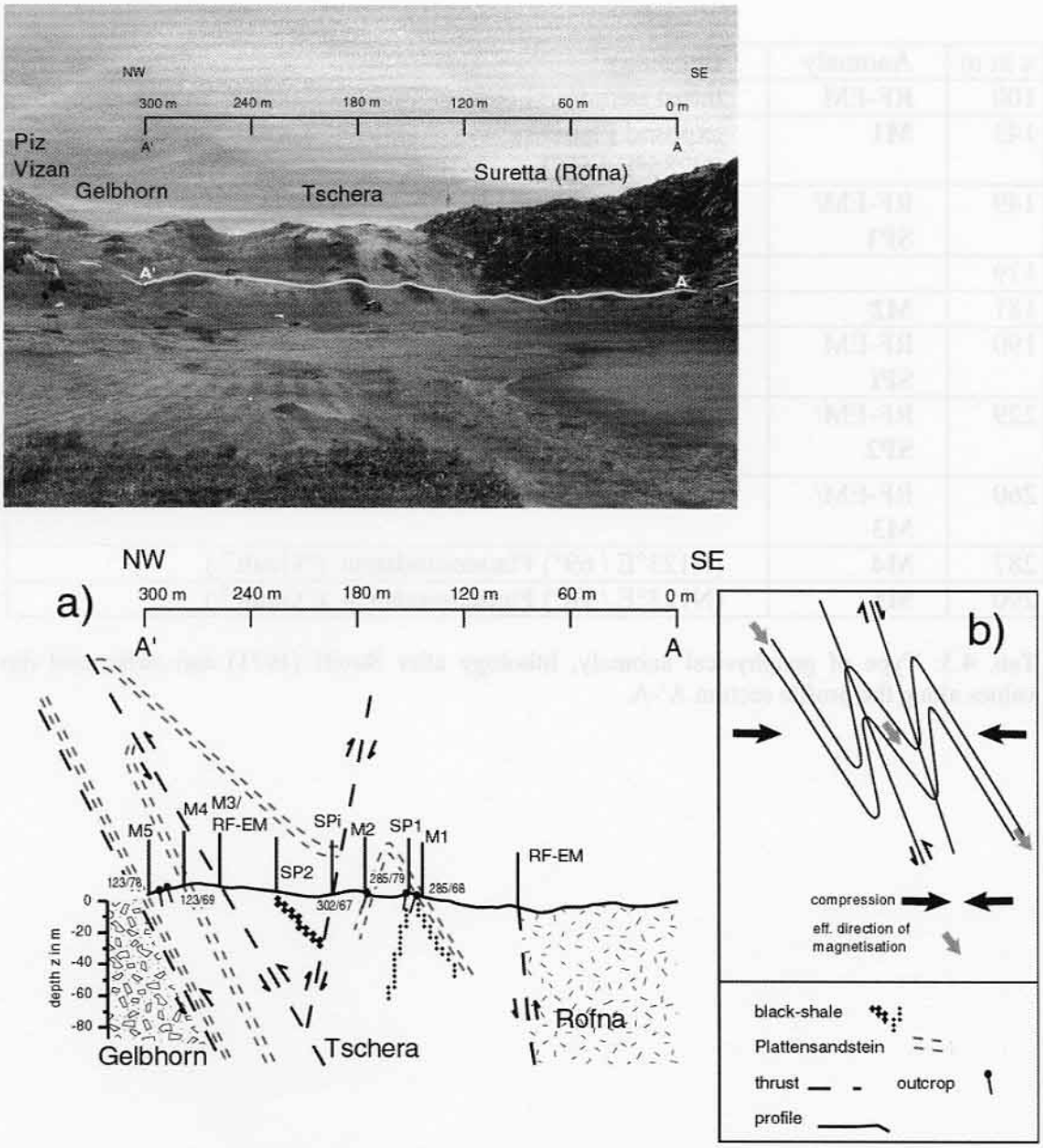

Fig. 4.16: Photography (upper part) of the structural contact between mesozoic sediments and Penninic basement at Sufers; a): Synoptic model of the fold geometry and lithostratigraphy of the Tschera nappe along the profile section A'-A; b): Kinetic explanation for the observed detachement faults.

4.4 Separation of Local and Regional conductive structures

The previous paragraph has shown that the induction arrow pattern in Graubünden is more likely caused by magnetic distortion. Under this condition, we will now focus on the components A and B of the magnetic transfer function so that we can use their significance to delineate the channel geometry and to separate local and regional geological structures. To do so, the magnetic transfer functions of each site of the entire data set are grouped according to their behaviour over period, tectonic setting and their amplitudes into five groups shown in Fig. 4.17.

1) Group **A**: Helvetic sediments and basement
2) Group **B**: Bündnerschiefer, Mesozoic sediments
3) Group **C1**: Austroalpine
4) Group **C2**: Austroalpine
5) Group **D**: Avers-Schiefer, Mesozoic sediments

Figure 4.18 shows plots of the real (RE) and imaginary (IM) components of the magnetic transfer functions for each site j of a group. In the period band T= 10 s the minimum of the Re Aj curves of group **A** and **C1** show strong evidence for a current flow in East-West direction. This effect is smaller in group **C2**. The minimum in RE Aj from group **A** to **C1** and further to **C2** are shifted to longer periods. This is the consequence of the eastwards dipping tectonic units. However, a maximum of the RE Bj values for the most eastern sites SER, CHA, ALB and BAE of the **C2** group are now influenced by a North-South trend of the electrical current. Overall, real and imaginary parts in groups **A**, **C1** and **C2** show a smoother behaviour over period and comparable amplitudes. In contrast, the magnetic transfer functions of group **B** and **D** show different behaviour. In Fig. 4.18 we find the real parts of both components of group **B** similar in amplitude and over period, whereas in group **D** they show inverse sign. The relationship between the magnetic data of group **B** and of group **D** can be explained in terms of the magnetic distortion theory for two-dimensional structures:

If magnetic distortion is present in the data of one of the groups, the components of the local transfer function are given by (see paragraph 2.4.2):

$$A^l = D''_{zx} \cdot \left(-Z_E \cdot \sin\theta_r \cdot \cos\alpha + Z_B \cdot \cos\theta_r \cdot \sin\alpha\right)$$
$$B^l = D''_{zx} \cdot \left(+Z_E \cdot \cos\theta_r \cdot \cos\alpha + Z_B \cdot \sin\theta_r \cdot \sin\alpha\right).$$

This leads to special cases due to the geometric configuration of local and regional conductive structures and their spatial constellation as shown in Tab. 4.4 and in the simple model of Fig. 4.19. The components A^l and B^l of the local transfer function depend only on the regional impedances Z_E, Z_B, the strike of the local inhomogeneity θ_l, the strike of the regional structure θ_r, and their difference $\alpha = \theta_l - \theta_r$, and a real and frequency independent distortion parameter D''_{zx}.

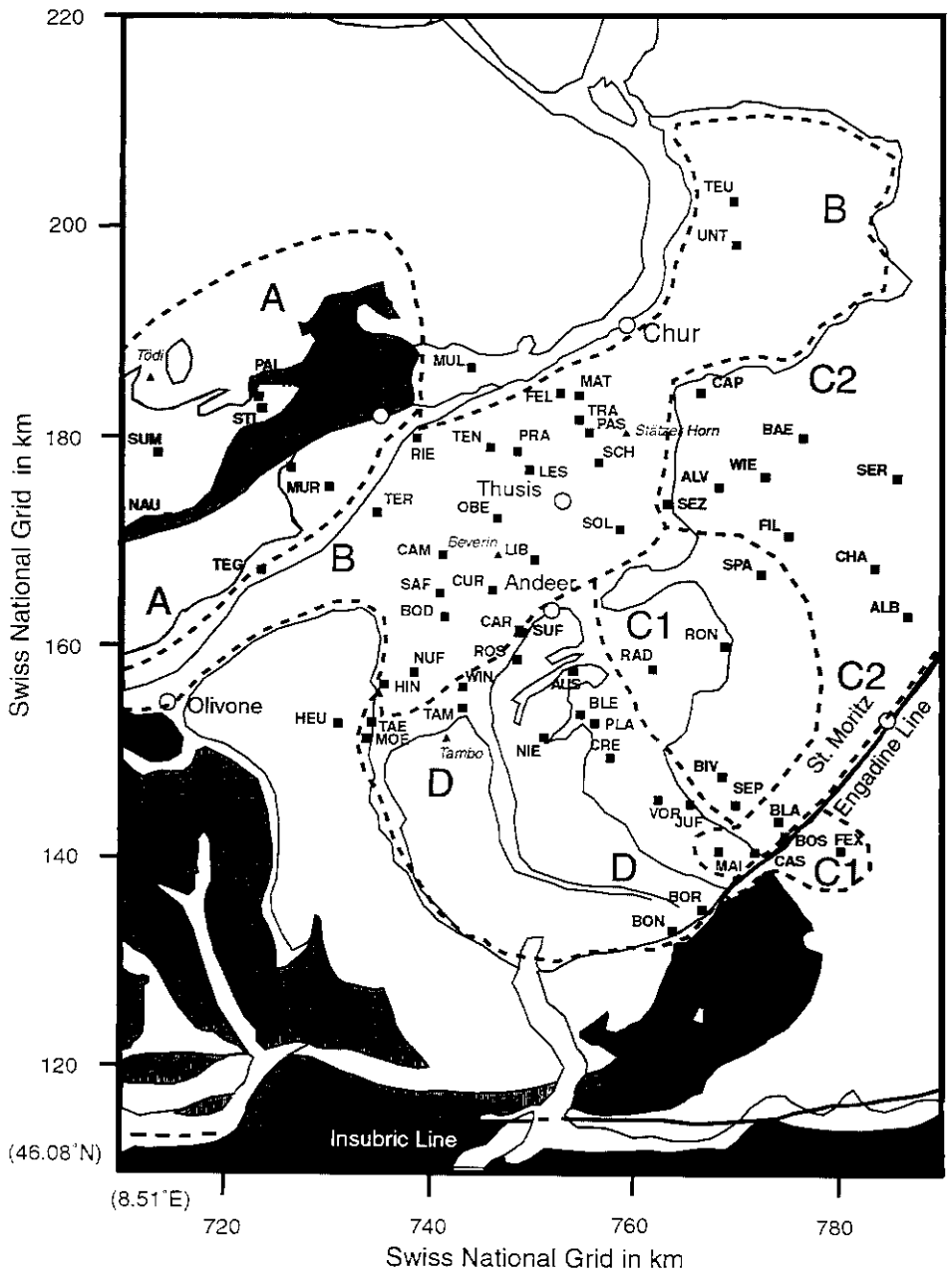

Fig. 4.17: Simplified tectonic map of the Graubünden with 5 different groups (**A-D**, dashed lines) of magnetic transfer functions.

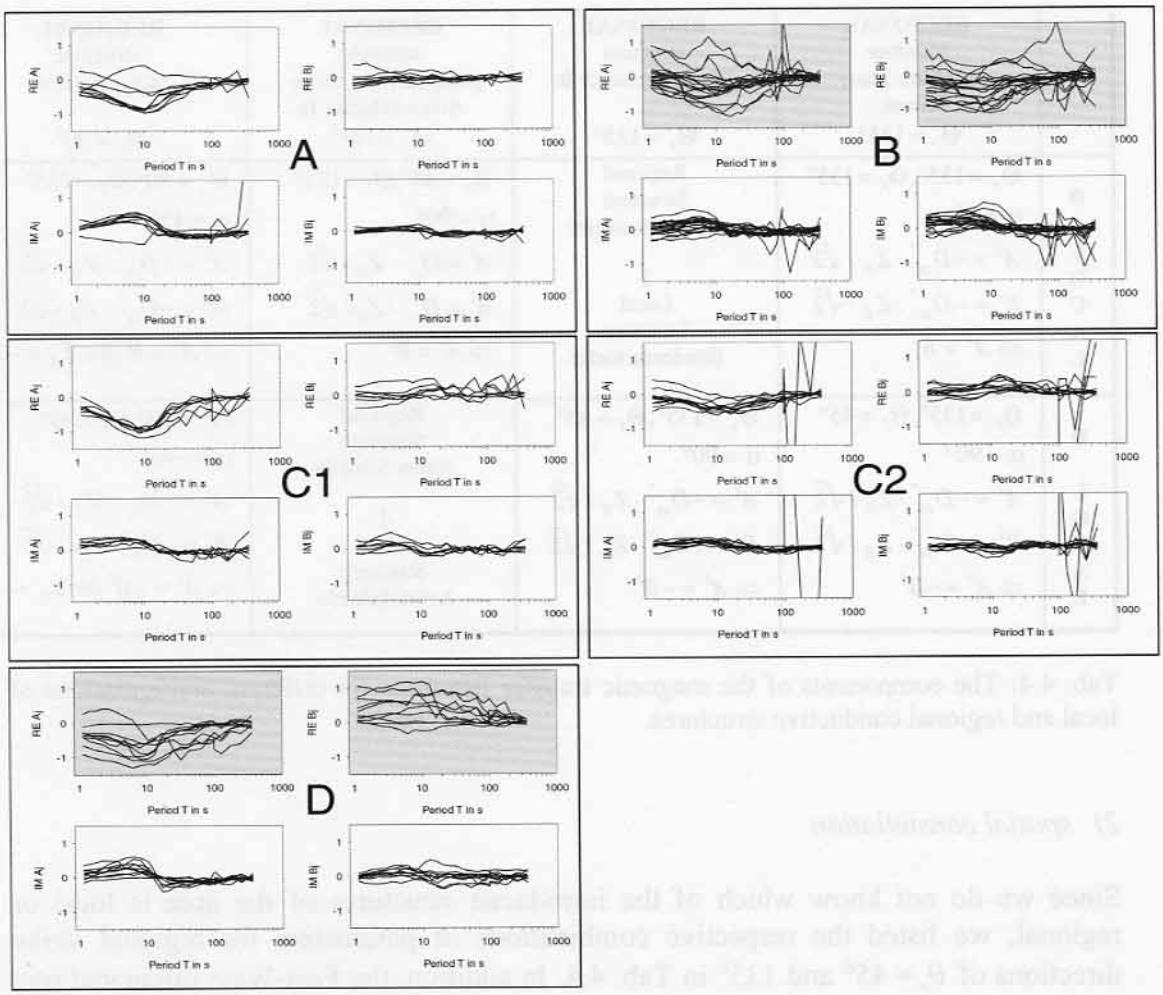

Fig. 4.18: Real and imaginary parts of the GDS transfer functions (rotation: N0°E) for groups **A-D**.

1) geometric configuration

Regional strike parallel or perpendicular to local strike:

$\underline{\alpha = 0°}$:

$$A^{l} = D''_{zx} \cdot \left(-Z_E \cdot \sin\theta_r\right)$$
$$B^{l} = D''_{zx} \cdot \left(+Z_E \cdot \cos\theta_r\right) \qquad (55)$$

$\underline{\alpha = 90°}$:

$$A^{l} = D''_{zx} \cdot \left(+Z_B \cdot \cos\theta_r\right)$$
$$B^{l} = D''_{zx} \cdot \left(+Z_B \cdot \sin\theta_r\right) \qquad (56)$$

	REGIONAL structure penninic basal thrust: $\Theta_r = 135°$	**REGIONAL** structure Bündnerschiefer **B**: $\Theta_r = 135°$	**REGIONAL** structure penninic basal thrust ; Avers-Schiefer **D**: $\Theta_r = 135°$	**REGIONAL** structure Molasse basin: $\Theta_r = 90°$
B **L O C A L**	$\Theta_r = 135°, \Theta_l = 135°$ $\alpha = 0°$ $A^l = -D_{zx}^{"} \cdot Z_E / \sqrt{2}$ $B^l = -D_{zx}^{"} \cdot Z_E / \sqrt{2}$ $\Rightarrow A^l = B^l$	Regional Structure Bündnerschiefer ↕ Local Structure Bündnerschiefer	$\Theta_r = 45°, \Theta_l = 135°$ $\alpha = 90°$ $A^l = D_{zx}^{"} \cdot Z_B / \sqrt{2}$ $B^l = D_{zx}^{"} \cdot Z_B / \sqrt{2}$ $\Rightarrow A^l = B^l$	$\Theta_r = 90°, \Theta_l = 135°$ $\alpha = 45°$ $A^l = -D_{zx}^{"} \cdot Z_E / \sqrt{2}$ $B^l = +D_{zx}^{"} \cdot Z_B / \sqrt{2}$ $\Rightarrow A^l = B^l$ *for* $Z_E = -Z_B$
D **L O C A L**	$\Theta_r = 135°, \Theta_l = 45°$ $\alpha = 90°$ $A^l = -D_{zx}^{"} \cdot Z_B / \sqrt{2}$ $B^l = +D_{zx}^{"} \cdot Z_B / \sqrt{2}$ $\Rightarrow A^l = -B^l$	$\Theta_r = 135°, \Theta_l = 45°$ $\alpha = 90°$ $A^l = -D_{zx}^{"} \cdot Z_B / \sqrt{2}$ $B^l = +D_{zx}^{"} \cdot Z_B / \sqrt{2}$ $\Rightarrow A^l = -B^l$	Regional Structure Avers-Schiefer ↕ Local Structure Avers-Schiefer	$\Theta_r = 90°, \Theta_l = 45°$ $\alpha = -45°$ $A^l = -D_{zx}^{"} \cdot Z_E / \sqrt{2}$ $B^l = -D_{zx}^{"} \cdot Z_B / \sqrt{2}$ $\Rightarrow A^l = -B^l$ *for* $Z_E = -Z_B$

Tab. 4.4: The components of the magnetic transfer functions for different configurations of local and regional conductive structures.

2) spatial constellation

Since we do not know which of the introduced structures of the area is local or regional, we listed the respective combinations of parameters for regional strike directions of $\theta_r = 45°$ and 135° in Tab. 4.4. In addition, the East-West orientated (α= 45°) Molasse basin is also shown. The Table provides a series or permutation, which combines regional and local conductive structures to generate the observed relationship between the real transfer functions of group **B** and **D**.

The Molasse basin is the only case which depends on both principal impedances Z_E and Z_B. This structure can be responsible for the anomalous direction of the real induction arrows on the Bündnerschiefer only if the regional conductivity distribution is one-dimensional ($Z_E = -Z_B$). However, we can not exclude this basin to be the origin of currents injected into the Mesozoic sediments. Furthermore, it is curious that the sediment filling of the Po basin do not show any (visible) influence on the GDS data.

If the Penninic basal thrust represents an L shaped regional conductive structure as shown in Fig. 4.19, it has the ability to cause the observed effects upon the magnetic transfer functions of group **B** as well as for group **D**. If we regard the Bündnerschiefer as regional conductive structure and the Avers-Schiefer as a local conductive structure, we can explain the effect on the magnetic field in group **D** but not in group **B**, and vice versa. But we have to point out, that the Avers structure does not exceed the required longitudinal extension to allow currents to be induced in the observed period range and presumably for much longer periods. The continuation of the Bündnerschiefer beneath the Middle Penninic, South Penninic and Austroalpine units

to the East is generally considered. From these observations following conclusions can be made:

- Any superposition of conductive structures of regional extension with an azimuth of a multiple of N45°E can cause magnetic distortion in GDS data in the investigation area.
- Structures with a strike of N0°E (i.e. Molasse) and/or N90°E can cause the observed effect upon the induction arrows on the Bündnerschiefer, provided the conductivity distribution in these structures is one-dimensional.
- The superposition of point 1 and point 2 can cause the observed induction arrow pattern.
- The Avers-Schiefer is a local, whereas the Bündnerschiefer is a regional structure.

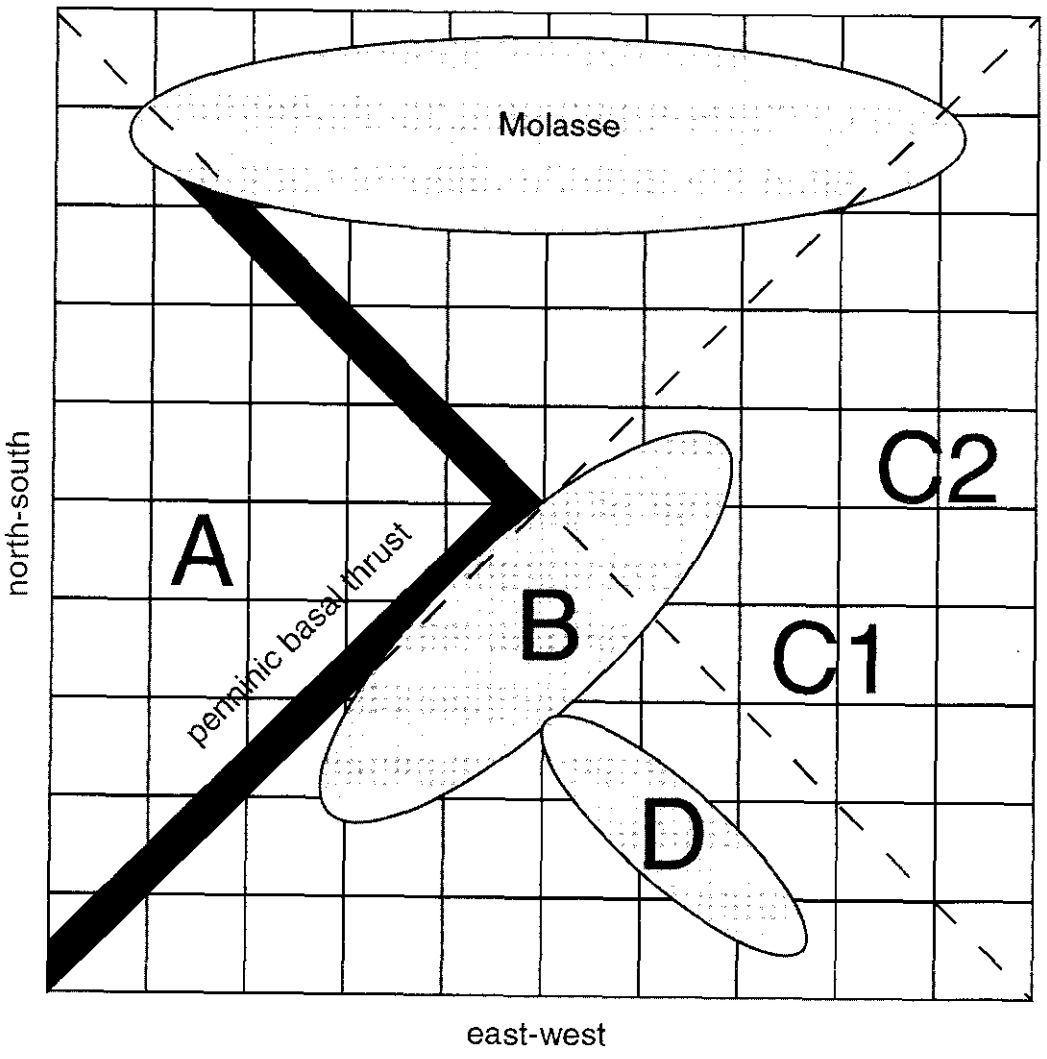

Fig. 4.19: Possible configuration of local and regional conductive structures in the eastern Swiss Alps. **A-D** are groups of magnetic transfer functions. Not to scale !

4.5 Hypothetical Event Analysis

To verify the validity of the model obtained in the previous section, the method of the Hypothetical Event Analysis (HEA) has been applied to the measured data set. This method uses a hypothetical uniform external horizontal field $\mathbf{B}_h^*$ of specific polarisation ϑ^* (angle North over East) to calculate a predicted vertical magnetic field B_z^p for all stations in a data array. All variations in the generated predicted map are of internal origin and are caused by channelling effects or induction (Bailey et al., 1974). From a calculated predicted map of B_z^* for each period T and different polarisation ϑ^*, we try to infer the anomalous current distribution and therefore to analyse the three-dimensional conductivity structure with depth:

$$B_z^p = A \cdot B_x^* + B \cdot B_y^*. \tag{57}$$

In practice, a horizontal field of 1 nT amplitude is chosen to generate maps of the anomalous field (Bailey, 1974).

$$B_z^p = (A,B) \cdot \begin{pmatrix} 1 \cdot \cos\vartheta^* \\ 1 \cdot \sin\vartheta^* \end{pmatrix}. \tag{58}$$

Consequently, if the hypothetical event is polarised in the East or North direction relative to the magnetic North with zero phase, the predicted value B_z^p reduces to one of the principal magnetic transfer functions:

$$B_z^p = A \text{ for } \vartheta^* = 0°$$
$$B_z^p = B \text{ for } \vartheta^* = 90°. \tag{59}$$

This technique is similar to the VLF technique, where only one transmitter produces a horizontal magnetic field of unique polarisation. The transmitter will be then virtually rotated around the investigation area to find the position that coincides with the strike direction of the E-Polarisation of the transfer functions. Other polarisation azimuths are blanked-out and the magnetic transfer functions are decomposed into E- and B-polarisation.

A virtual transmitter situated in the East produces a magnetic field polarised in the North direction that should drive a telluric current in East-West direction, whereas an eastwards polarised magnetic field drives currents in the North-South direction through the area of interest (Tab. 4.5).

Transmitter	0°	22.5°	45°	67.5°	90°	112.5°	135°	157.5°
ϑ^*	90°	112.5°	135°	157.5°	0°	22.5°	45°	67.5°

Tab. 4.5: Transmitter positions (North over East) and corresponding polarisation azimuths ϑ^* of the Hypothetical Event.

4.5.1 HEA maps derived from the real parts of the magnetic transfer functions

The analysis of the magnetic transfer function in the previous section already implied main regional strike direction for the structures to be either N90°E, N45°E or N135°E. In Fig.4.20 – Fig. 4.23 we virtually rotated a transmitter stepwise (22.5°) from North over East to South. This rotation produces polarisation azimuths as listed in Tab. 4.5 and are used to generate HEA maps of the real part of the vertical magnetic field for the period T= 4.7 s and T= 126 s.
If one of the presumed current channelling effect related to the specific strike direction (given by the position of the transmitter) is inside the survey area, the current concentration are indicated by the spatial gradients (± 1 nT) in the vertical magnetic field.

Regardless of the polarisation angle, we find, for the short periods, a complex pattern of anomalies mainly generated on the Mesozoic sediments. On the other hand, the Helvetic Domain, the Penninic basement slices and the Austroalpine units are almost free from current channelling effects. Significantly, the HEA maps for T= 126 s contrasts with the previous cases and show a dominating anomaly under the Austroalpine Units. The anomaly forms a corner and is strongly associated with the strike of the Engadine Line, whereas the anomalies for the shorter periods on the Penninic domain have virtually disappeared.

From the model of Fig. 4.19, we would expect an anomaly pattern, that is correlated with the basal Penninic thrust and the Mesozoic sediments Bündnerschiefer and Avers-Schiefer. In fact, the HEA maps for a magnetic field with an azimuth of N67.5°E-N157.5°E and T= 4.7 s produces a straight forward current channelling system. Among these, the polarisation angle of ϑ^{*}=N67.5°E shows the strongest current concentration. This polarisation direction corresponds to a strike direction of N157.5°E. Here, we find a strong anomaly in front of the Tambo and Suretta nappes which deviates into the Avers-Schiefer and stops at the end of the Engadine Line. The latter system seems to be controlled by the Turba Mylonite Zone. Another branch of this current system flows around internal inhomgeneities in the region of Thusis. A current channelling effect might be associated with the Verrucano, which separates the Aar- and Gotthard massives, and finally injects into the Helvetic units. The overall impression is that the predominating strike direction for this period range coincides with the strike of the interception of the Mesozoic cover sediments with the surface that separates the Penninic basement slices. However, the current system in this pattern moderately reflects the boundaries of the magnetic transfer functions found for the groups **A-D**.

Conclusions:
The HEA maps of the real parts of the induction arrows show a spatial decoupling of induction processes with depth. For short periods (T= 1-10 s), induction and/or current channelling is related to the Mesozoic sediments and their internal inhomogeneities. For periods longer than T= 126 s, induction and/or current channelling is almost limited to the Austroalpine and Penninic basement.

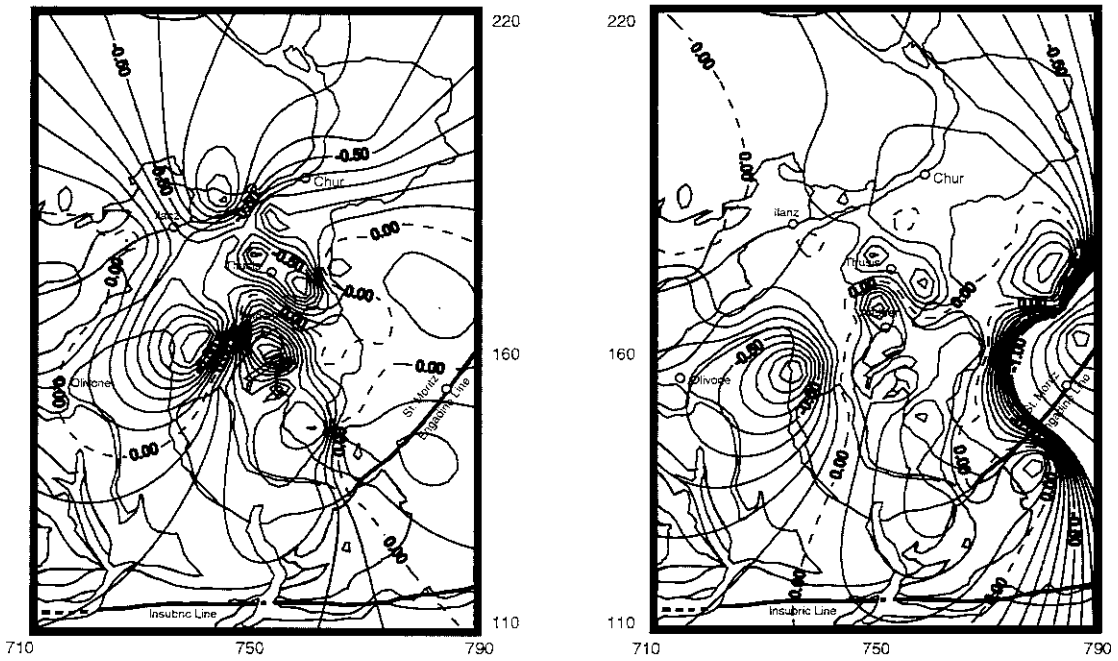

Hypothetical event map of the anomalous vertical magnetic field: real part, azimuth of regional field relative to magnetic North: 90°, period T= 4.7 s (left), period T= 126 s (right). Amplitude of horizontal field: 1 nT, phase of the horizontal field: 0°.

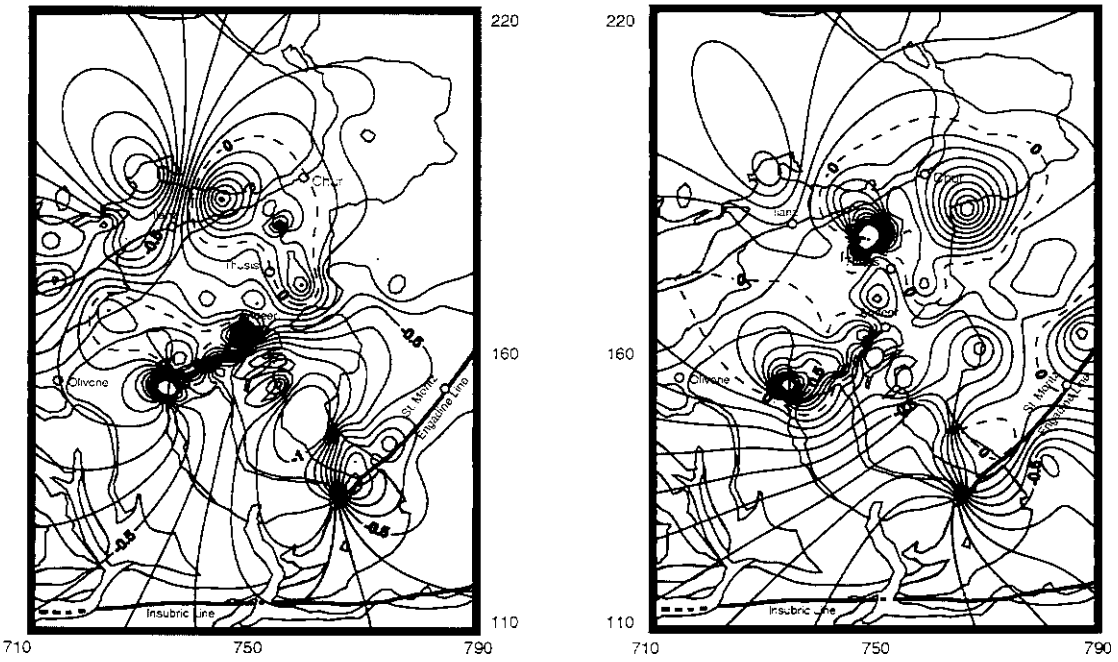

Hypothetical event map of the anomalous vertical magnetic field: real part, azimuth of regional field relative to magnetic North: 112.5°, period T= 4.7 s (left), period T= 126 s (right). Amplitude of horizontal field: 1 nT, phase of the horizontal field: 0°.

Fig. 4.20: HEA maps, transmitter at N0°E and N22.5°E

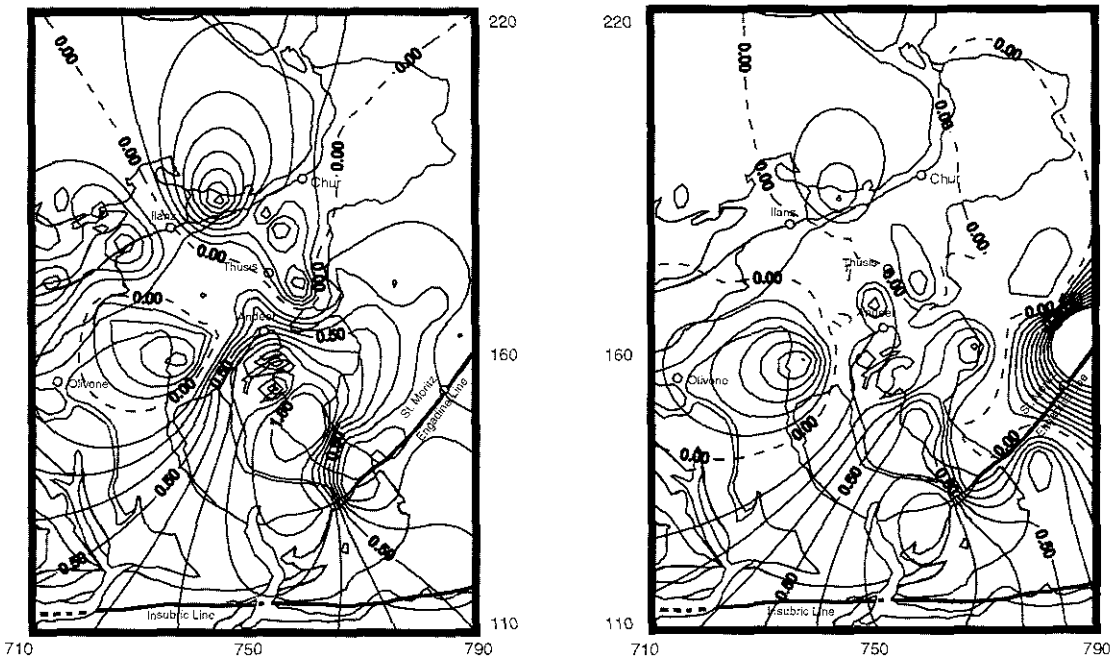

Hypothetical event map of the anomalous vertical magnetic field: real part, azimuth of regional field relative to magnetic North: 135°, period T= 4.7 s (left), period T= 126 s (right). Amplitude of horizontal field: 1 nT, phase of the horizontal field: 0°.

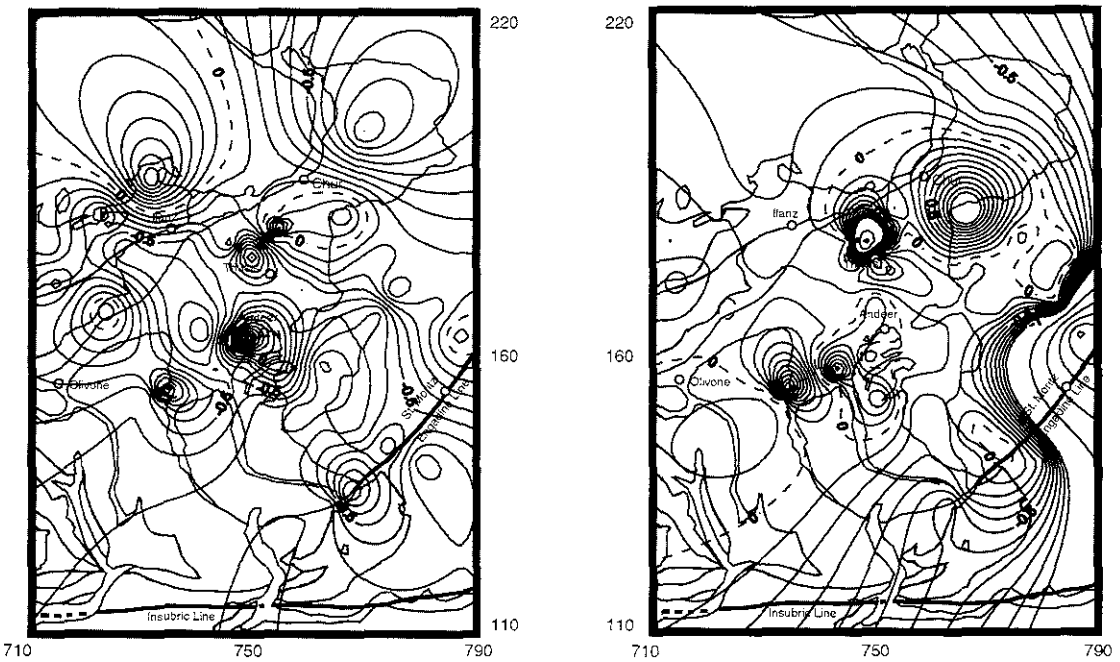

Hypothetical event map of the anomalous vertical magnetic field: real part, azimuth of regional field relative to magnetic North: 157.5°, period T= 4.7 s (left), period T= 126 s (right). Amplitude of horizontal field: 1 nT, phase of the horizontal field: 0°.

Fig. 4.21: HEA maps, transmitter at N45°E and N67.5°E

Hypothetical event map of the anomalous vertical magnetic field: real part, azimuth of regional field relative to magnetic North: 0°, period T= 4.7 s (left), period T= 126 s (right). Amplitude of horizontal field: 1 nT, phase of the horizontal field: 0°.

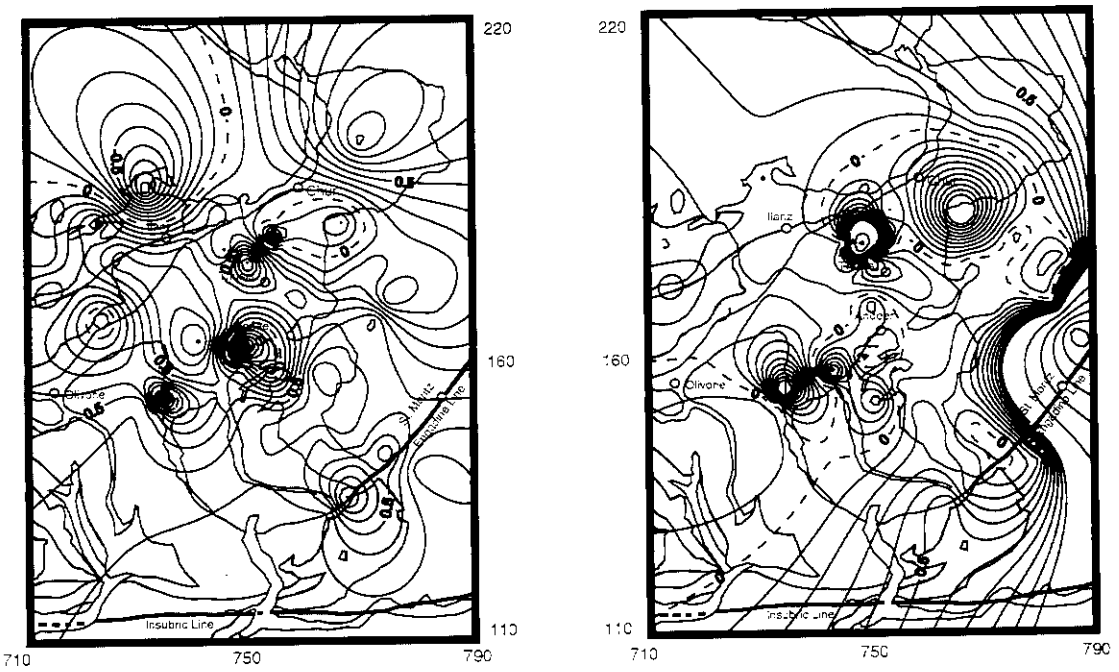

Hypothetical event map of the anomalous vertical magnetic field: real part, azimuth of regional field relative to magnetic North: 22.5°, period T= 4.7 s (left), period T= 126 s (right). Amplitude of horizontal field: 1 nT, phase of the horizontal field: 0°.

Fig. 4.22: HEA maps, transmitter at N90°E and N112.5°E

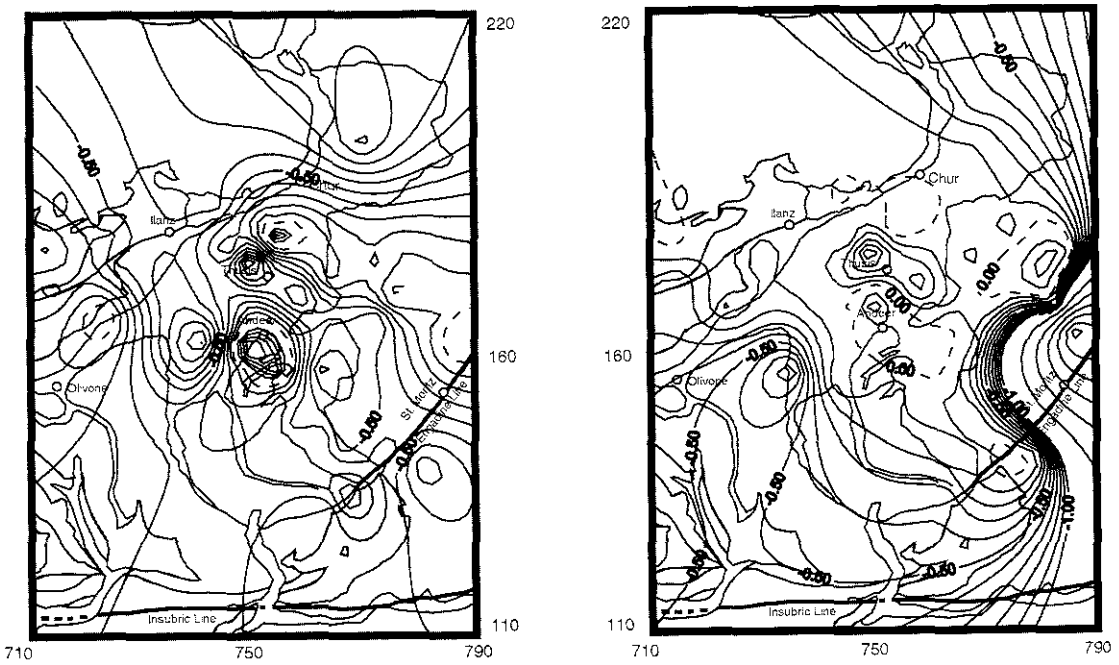

Hypothetical event map of the anomalous vertical magnetic field: real part, azimuth of regional field relative to magnetic North: 45°, period T= 4.7 s (left), period T= 126 s (right). Amplitude of horizontal field: 1 nT, phase of the horizontal field: 0°.

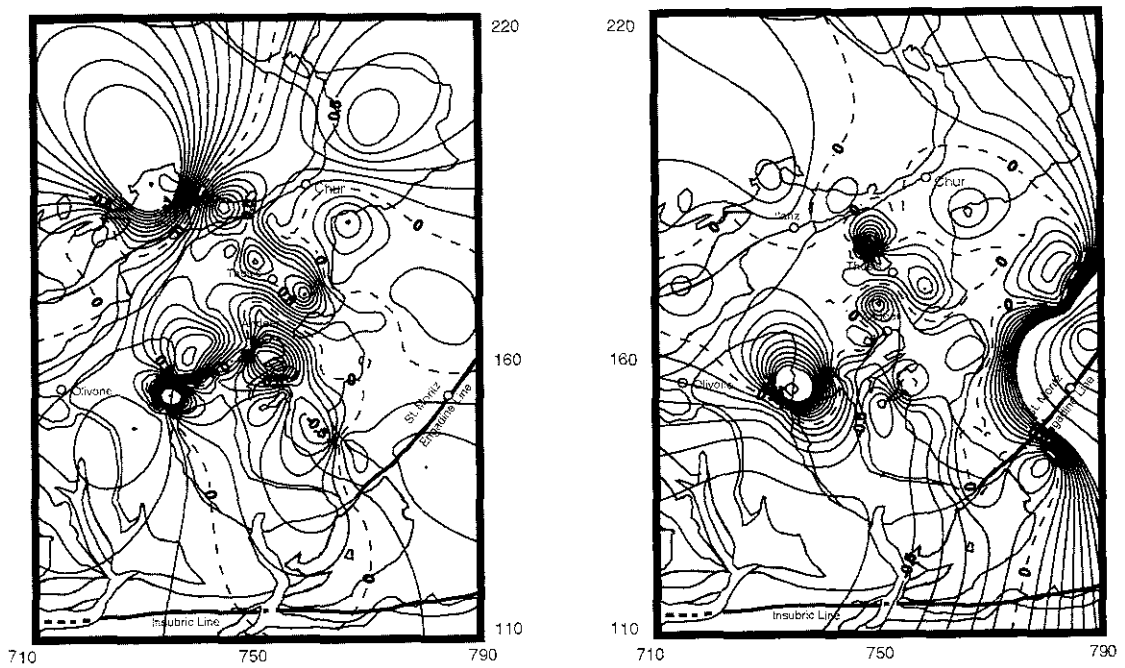

Hypothetical event map of the anomalous vertical magnetic field: real part, azimuth of regional field relative to magnetic North: 67.5°, period T= 4.7 s (left), period T= 126 s (right). Amplitude of horizontal field: 1 nT, phase of the horizontal field: 0°.

Fig. 4.23: HEA maps, transmitter at N135°E and N157.5°E

The model of an L shaped structure associated with the Penninic basal thrust cannot be confirmed. But a structural conductivity anomaly with the same geometric properties (strike N45°E respectively N135°E) is found at depth, confirming in an excellent manner the conclusions made in the previous section. Obviously, the size of investigation area accounts for the regional induction and/or current channelling effect on the data. Therefore, we were able to visualise a small portion of a presumably super-regional current system in the lower crust. Thus the conductivity distribution in this part of the Alps is strongly three-dimensional and contrasts with the more simple cylindrical conductivity distribution in the Penninic Alps of Valais (Schnegg, 1998). The correlation of the deep conductor with the Engadine Line implies that this strike slip fault is of lower crustal origin. The continuation of the current system over the Engadine Line towards south-east is not proved but likely.

4.5.2 HEA for a regional 2-D conductivity distribution

At this stage of investigation, we do not know if magnetic distortion affects all data of the survey. Moreover, we did not take the imaginary parts of the magnetic transfer function into account.
If magnetic distortion is present, Ritter (1996) gives the information content of the predicted vertical magnetic field of hypothetical event related to a supposed regional 2-D conductivity distribution in measurement coordinates by:

$$B_z^p = \left[\left(0, B^{0'}\right)\cdot \underline{\mathbf{R}}_{\theta_r}^{\mathrm{T}} + \left(A', B'\right)\cdot \underline{\mathbf{R}}_{\theta_r}^{\mathrm{T}}\right]\cdot \mathbf{B}_{\mathrm{h}}^{*} \qquad \textbf{(60)}$$

$$= \left[\left(0, B^{0'}\right)\cdot \underline{\mathbf{R}}_{\theta_r}^{\mathrm{T}} + \left(D_{zx}, D_{zy}\right)\cdot \underline{\mathbf{R}}_{\theta_r}\cdot \underline{\mathbf{Z}}^{0}\cdot \underline{\mathbf{R}}_{\theta_r}^{\mathrm{T}}\right]\cdot \begin{pmatrix} 1\cdot cos\,\vartheta^{*} \\ 1\cdot sin\,\vartheta^{*} \end{pmatrix}. \qquad \textbf{(61)}$$

Explicitly, we yield:

$$\begin{aligned} B_z^p\left(\vartheta^{*}\right) = {} & D_{zx}\cdot\left[Z_E\cos\theta_r\sin\left(\vartheta^{*}-\theta_r\right) - Z_B\sin\theta_r\cos\left(\vartheta^{*}-\theta_r\right)\right] \\ & + D_{zy}\cdot\left[Z_E\,sin\,\theta_r\,sin\left(\vartheta^{*}-\theta_r\right) + Z_B\,cos\,\theta_r\,cos\left(\vartheta^{*}-\theta_r\right)\right] \\ & + B^{0'}\,sin\left(\vartheta^{*}-\theta_r\right). \end{aligned} \qquad (62)$$

For a polarisation azimuth ϑ^{*} of the hypothetical event in line or normal to the regional strike, B_z^p is decomposed into the B-polarisation and E-polarisation case:

$$\vartheta^{*} = \theta_r: \qquad B_z^p = Z_B\left[D_{zx}\,sin\,\theta_r + D_{zy}\,cos\,\theta_r\right] \qquad (63)$$

$$\vartheta^{*} = \theta_r + 90°: \qquad B_z^p = Z_E\left[D_{zx}\,cos\,\theta_r + D_{zy}\,sin\,\theta_r\right] + B^{0'}. \qquad (64)$$

Substituting with $\alpha = \theta_t - \theta_r$, former equations are determining the magnetic transfer functions in the coordinates of the regional strike (Ritter, 1996):

$$\vartheta^{*} = \theta_r: \qquad B_z^p = D_{zx}''\cdot Z_B\cdot sin\,\alpha \qquad = A' \qquad (65)$$

$$\vartheta^* = \theta_r + 90°: \qquad B_z^{p} = D''_{zx} \cdot Z_E \cdot \cos\alpha + B^{0'} \qquad = B'. \tag{66}$$

The expressions are indicating *lines*: $y = a + m \cdot x$

$$A' = \sin\alpha \cdot (D''_{zx} \cdot Z_B) \Rightarrow y = m \cdot x \tag{67}$$

$$B' = B^{0'} + \cos\alpha \cdot (D''_{zx} \cdot Z_E) \Rightarrow y = a + m \cdot x, \tag{68}$$

with $a = B^{0'}$, $m = \sin\alpha$ and $x = (D''_{zx} \cdot Z_B)$.

Furthermore, these equations show that magnetic and telluric fields are in-phase. Hence, this fact offers an improved technique to infer the regional strike out of the combined analysis of real and imaginary parts of the magnetic transfer functions in the complex plane:
By gradually varying the polarisation azimuth ϑ^* and monitoring the predicted vertical magnetic field B_z^{p} of all sites simultaneously at one given period in an Argand diagram, the regional strike direction is found, when the data points fall on a line through the origin. The line can be observed when the hypothetical event is polarised in the strike of the regional 2-D structure. Besides this, the slope of this line indicates the phase angle of one of the regional impedances (Ritter, 1996).

Contrarily, for a polarisation azimuth of the hypothetical event normal to the strike of the 2-D structure, the values will scatter along the phase line of the orthogonal principal impedance. This phase line may be shifted by a factor $B^{0'}$ of the uniform regional vertical magnetic component.

In order to confirm these analytical results, Ritter (1996) analysed the behaviour of the regional magnetic transfer function in the frame of a 3-D modelling study with a special emphasis on the magnetic phases.
The results in dependency of the (increasing) investigated periods for a regional 2-D conductivity distribution are cited as follows:

i) The local distortion of regional currents begins to affect the magnetic transfer function at a period for which the skin-depth of the host rocks is of the same size as the local body.

ii) If the period investigated with HEA is not in the period range in which distortion processes influence the magnetic transfer functions, the magnetic phases found in the Argand diagram are *negative*. They indicate a phase difference between the anomalous magnetic field and the regional electric field due to induction inside the local anomaly. In this case, a regional strike direction of a larger scale structure can still be detected if its influence can be minimised clearly for a certain polarisation azimuth, and the predicted vertical fields collapse on a line through the origin with a *negative* gradient.

iii) The magnetic phase is zero at the period T_0 of maximum induction because here, the phase shifts of primary and secondary induction are compensated. This period also marks the onset of distortion processes.

iv) In the *intermediate* period range of *transition*, where both processes affect the data, the magnetic phase is *positive* and *approaches* the regional impedance phase.

v) In the period range of pure *distortion*, the magnetic phase is *positive* and *indicates* the regional impedance phase.

4.5.3 Argand diagrams for selected periods

The next figures (4.24 – 4.26) illustrate the Hypothetical Event Analysis for all the groups of magnetic transfer functions using Argand diagrams. The polarisation azimuth varies stepwise (20°) form 0° to 160 ° from North over East. The periods shown in the diagrams represents an example where the predicted vertical fields collapse best on a line, preferably through the. The results are listed in Tab. 4.6:

To start with the whole data set (Fig. 4.24), the corresponding figure shows for the period T= 41 s the collapse of the fields on a line through the origin at a given azimuth of 100°-120°. Despite of the misleading regression line computed by the plot program, the gradient of the data cloud is positive, indicating for this period either pure distortion or the intermediate period range of transition.
The predicted fields of group **A** (T= 41 s) fall best on a line through the origin for $\vartheta^* = 40°$-$60°$, its gradient is positive (Fig. 4.24).
At T= 171 s, the data of group **B** fall best on a positive line through the origin at an azimuth of 80°-100° (Fig. 4.25).
The best collapsed fields of group **C1** (T= 6 s) show negative gradient and positive line offset at an azimuth of 120°-140° (Fig. 4.25). Hence, the shown period range is not the period range in which magnetic distortion affects the magnetic transfer functions. The same conclusion can be drawn for group **C2** (T= 13 s). These data (Fig. 4.26) fall best on a line at an azimuth of 100°-120°. The offset of the regression lines shown for group **C1** points to the presence of a strong regional vertical magnetic field component $B^{0'}$.
The predicted fields for the long period T= 246 s of group **D** (Fig. 4.26) fall best on a positive line through the origin at $\vartheta^* = 40°$-$60°$.

The results from this section prove the presence of magnetic distortion and pure induction in Gaubünden.

	T in s	$\vartheta^* = \Theta_r$	Period range of distortion	$B^{0'}$ present
All Sites	41	N100°E-N120E°	yes	no
A	41	N40°E-N60°E	yes	no
B	171	N80°E-N100°E	yes	no
C1	6	N120°E-N140°E	no	yes
C2	13	N120°E-N140°E	no	no
D	246	N40°E-N60°E	yes	no

Tab. 4.6: Results of the analysis of the Argand diagrams.

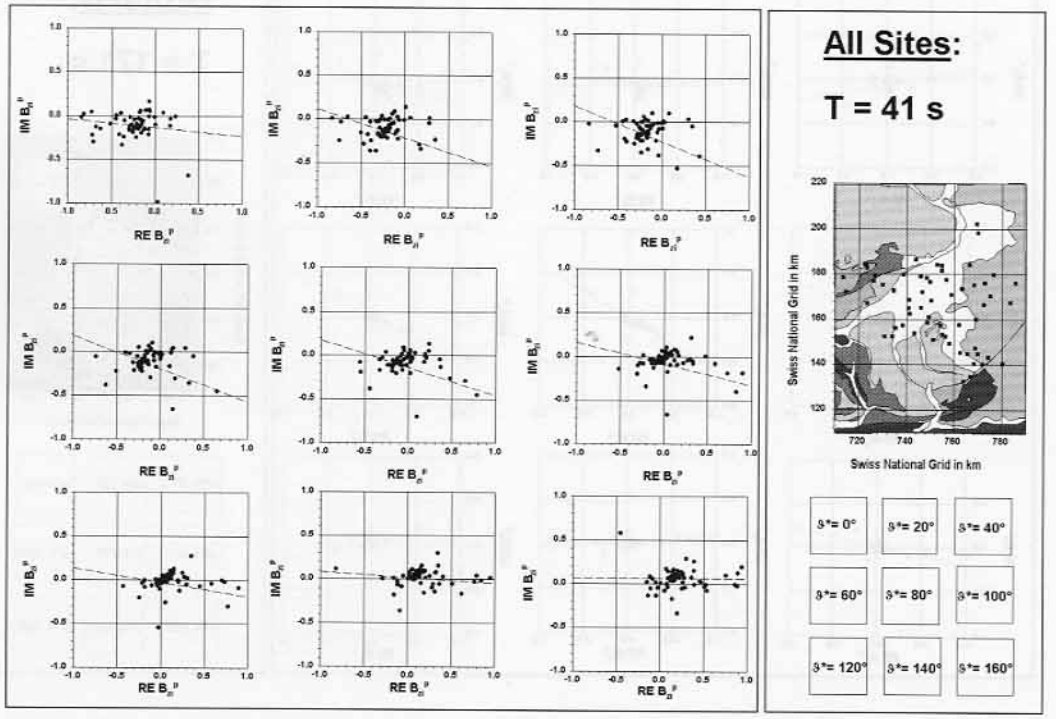

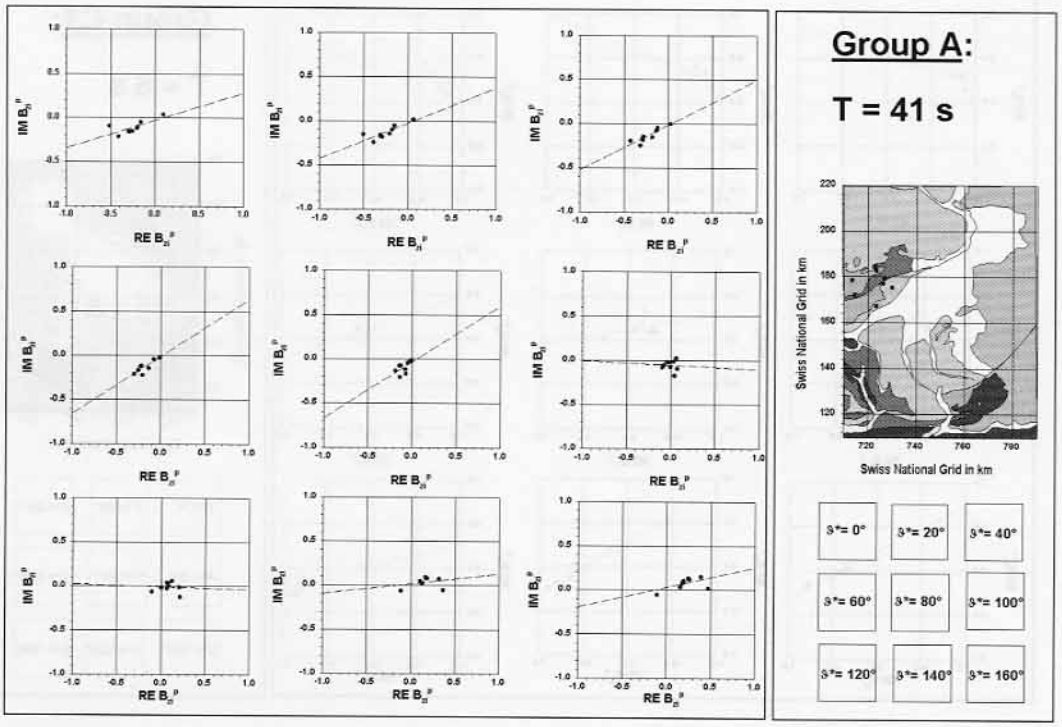

Fig. 4.24: Argand diagrams for **All Sites** (T= 41 s) and group **A** (T= 41 s).

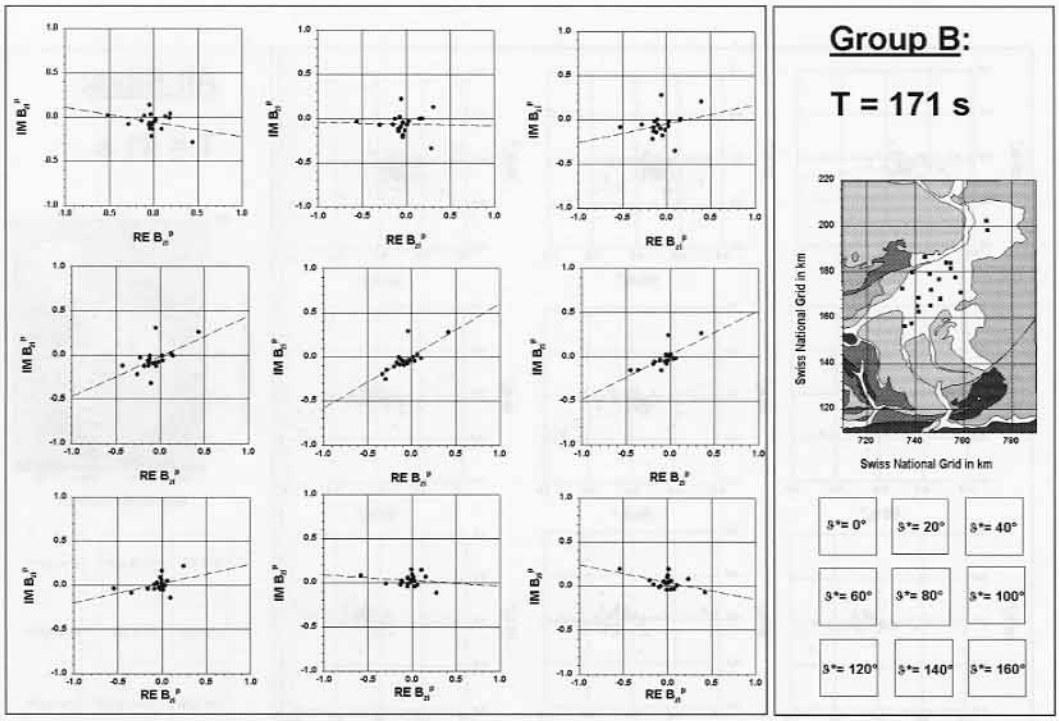

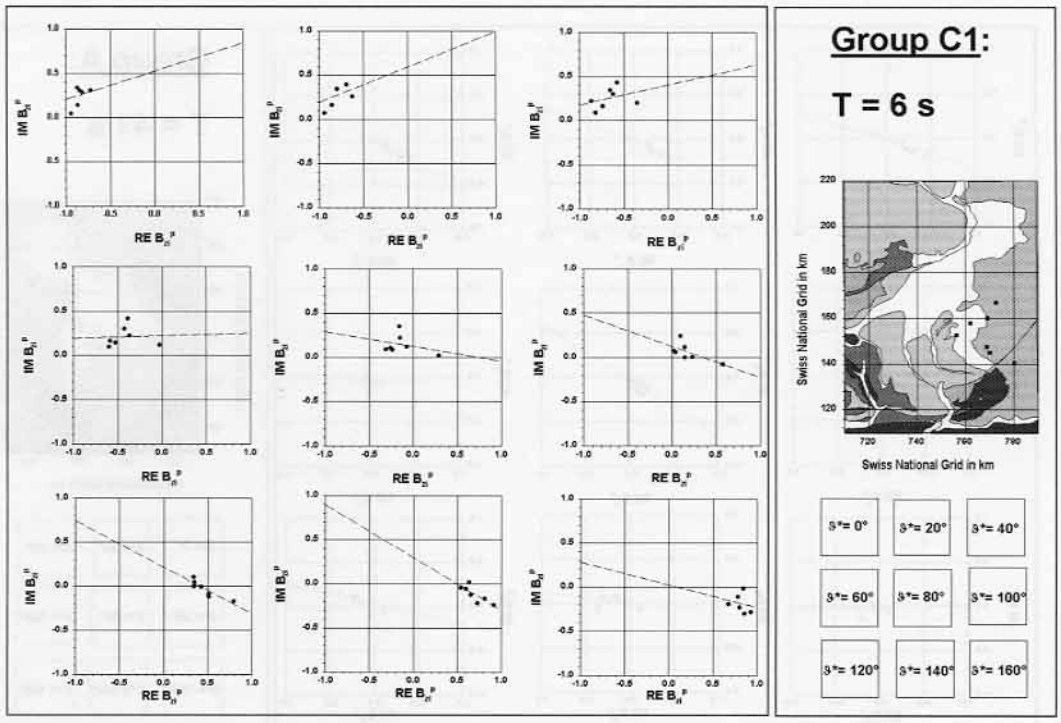

Fig. 4.25: Argand diagrams for group **B** (T= 171 s) and **C1** (T= 6 s).

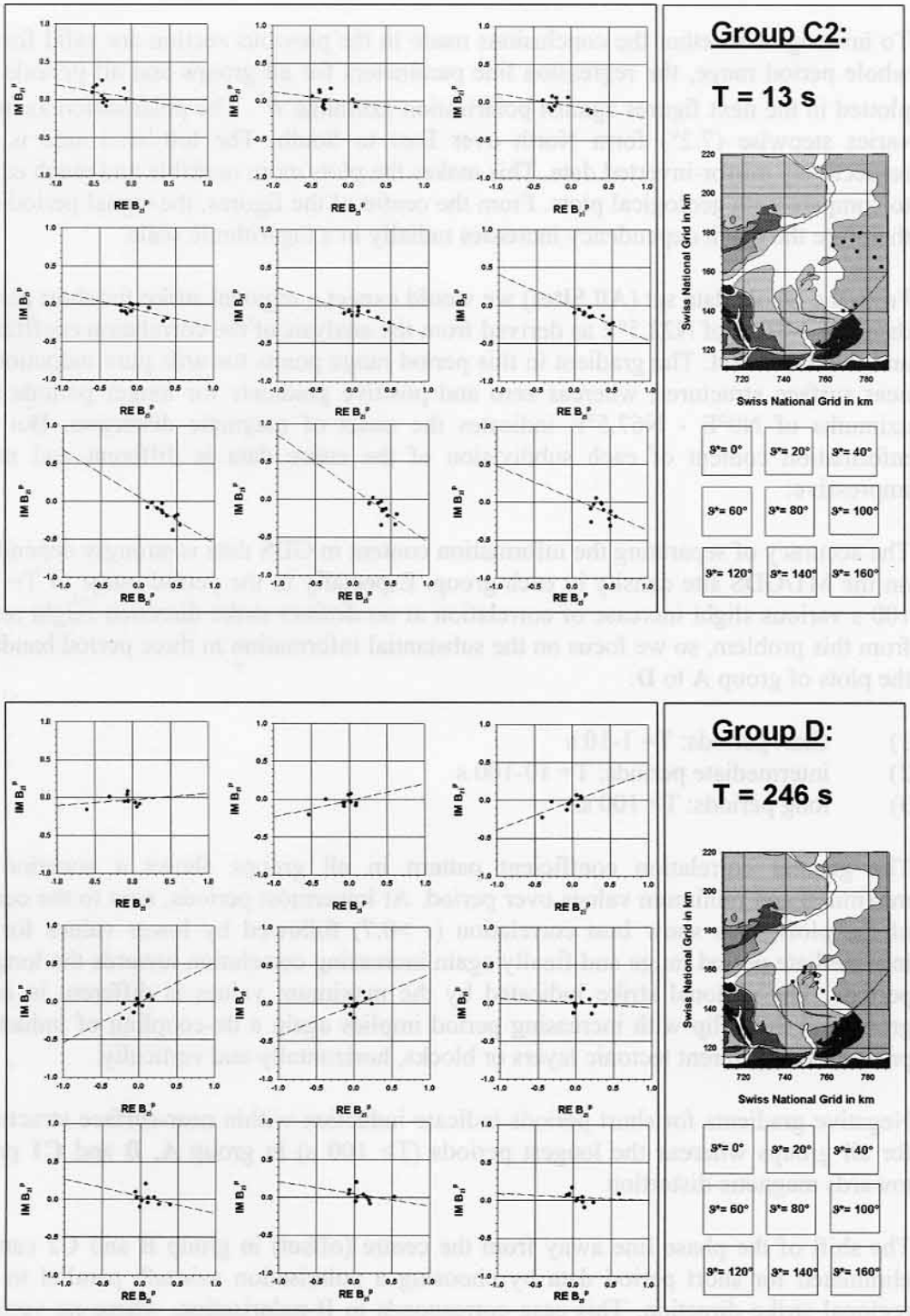

Fig. 4.26: Argand diagrams for group **C2** (T= 13 s) and **D** (T= 246 s).

4.5.4 Investigation over the entire period range

To investigate whether the conclusions made in the previous section are valid for the whole period range, the regression line parameters for all groups and all periods are plotted in the next figures against polarisation azimuths ϑ^*. The polarisation azimuth varies stepwise (7.2°) form North over East to South. The left-hand side is the respectively mirror-inverted data. This makes the plots more readable and much easier to compare with geological plots. From the centre of the figures, the signal period and therefore the depth dependency increases radially in a logarithmic scale.

From the whole data set (**All Sites**) we would expect a regional strike for short period data (T= 1-10 s) of N22.5°E as derived from the analysis of the correlation coefficient and the line offset. The gradient in this period range points towards pure induction in near surface structures, whereas zero and positive gradients for longer periods and azimuths of N0°E - N67.5°E indicates the onset of magnetic distortion. But the information content of each subdivision of the entire data is different and more impressive:

The accuracy of separating the information content in GDS data is strongly depending on the MT/GDS site density in each group. Especially in the period range of T= 10-100 s various slight increase of correlation at no distinct strike direction might result from this problem, so we focus on the substantial information in three period bands in the plots of group **A** to **D**:

1) short periods: T= 1-10 s
2) intermediate periods: T= 10-100 s
3) long periods: T> 100 s.

The general correlation coefficient pattern in all groups shows a zonation of maximum and minimum values over period. At lowermost periods, next to the centre of the plots, data show best correlation (r >0.7) followed by lower values for an intermediate period range and finally again increasing correlation towards the longest periods. The regional strike indicated by the maximum values is different in each group and their flip with increasing period implies again a de-coupling of induction processes in different tectonic layers or blocks, horizontally and vertically.

Negative gradients for short periods indicate induction within near-surface structures for all groups whereas the longest periods (T> 100 s) in group **A**, **B** and **C1** point towards magnetic distortion.

The shift of the phase line away from the centre (offset) in group **B** and **C2** can be eliminated for short period data by choosing a polarisation azimuth parallel to the regional strike direction. This case corresponds to B-polarisation, where no vertical magnetic component is generated. The feasibility of removing this offset indicates regional two-dimensionality of the data (Ritter, 1996). Hence, the combined interpretation of offset and correlation coefficient allows finding a trustworthy regional strike, provided the regional conductivity distribution is 2-D.
The short period data of group **C1** and **D** show different behaviour. The shift away from the origin for short period data of group **C1** and **D** for a polarisation normal and parallel to the strike results from the presence of a significant vertical conductivity

boundary nearby. This presumably superficial body produces a uniform regional vertical magnetic field component in these groups.

We can give estimates of the complex regional vertical magnetic field component in group **C1** and **D** for a given period out of single site measurements by calculating the differences of the predicted vertical field parallel to the regional strike and normal to it (Ritter, 1996):

$$B_z^0 = \frac{1}{N}\sum B_z^p(parallel) - B_z^p(normal)\,. \qquad (69)$$

We yield for T= 10 s:

a) group **C1**, reg. strike = N135°E $\quad B_z^0 \approx$(-1.375. –0.281)

b) group **D**, reg. strike = N112.5°E $\quad B_z^0 \approx$(-1.482. –0.008).

The estimates point to a rather unique vertical component of high amplitudes for the two neighbouring groups, which is likely to be of the same internal origin of a conductive body nearby. This body might be genetically the same structure, which is responsible for the magnetic anomalies (Fig. 4.30) cited in the geomagnetic survey of Switzerland (Fischer & Schnegg, 1994). Similar conclusion can be made for short period data of group **A**. In this case, no uniform horizontal magnetic field or impedance can be expected and the magnetic distortion model inappropriate (Ritter, 1996).

The joint analysis of the regression parameters is listed in Tab. 4.7 and provides to separate at least three distinct strike directions in the investigation area at depth (Fig. 4.31) that are in agreement with the preliminary results from section 4.4. If we assume host rock resistivities of about 2000-8000 Ωm, the overall length of a structure in East-West direction may reach values of 250-500 km at T= 126 s.

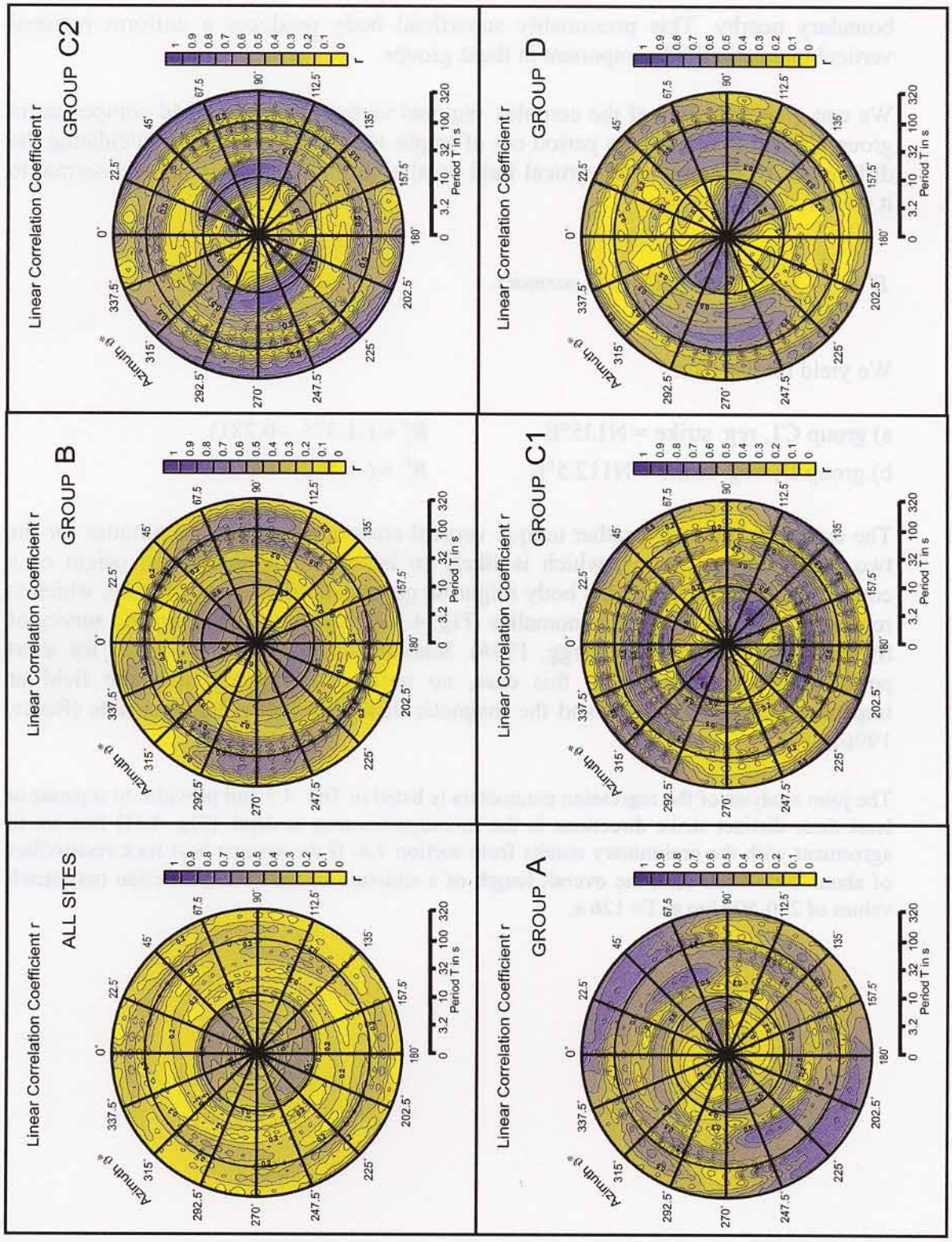

Fig. 4.27: HEA for all groups, all periods, polarisation azimuths 0°-180°, **correlation**.

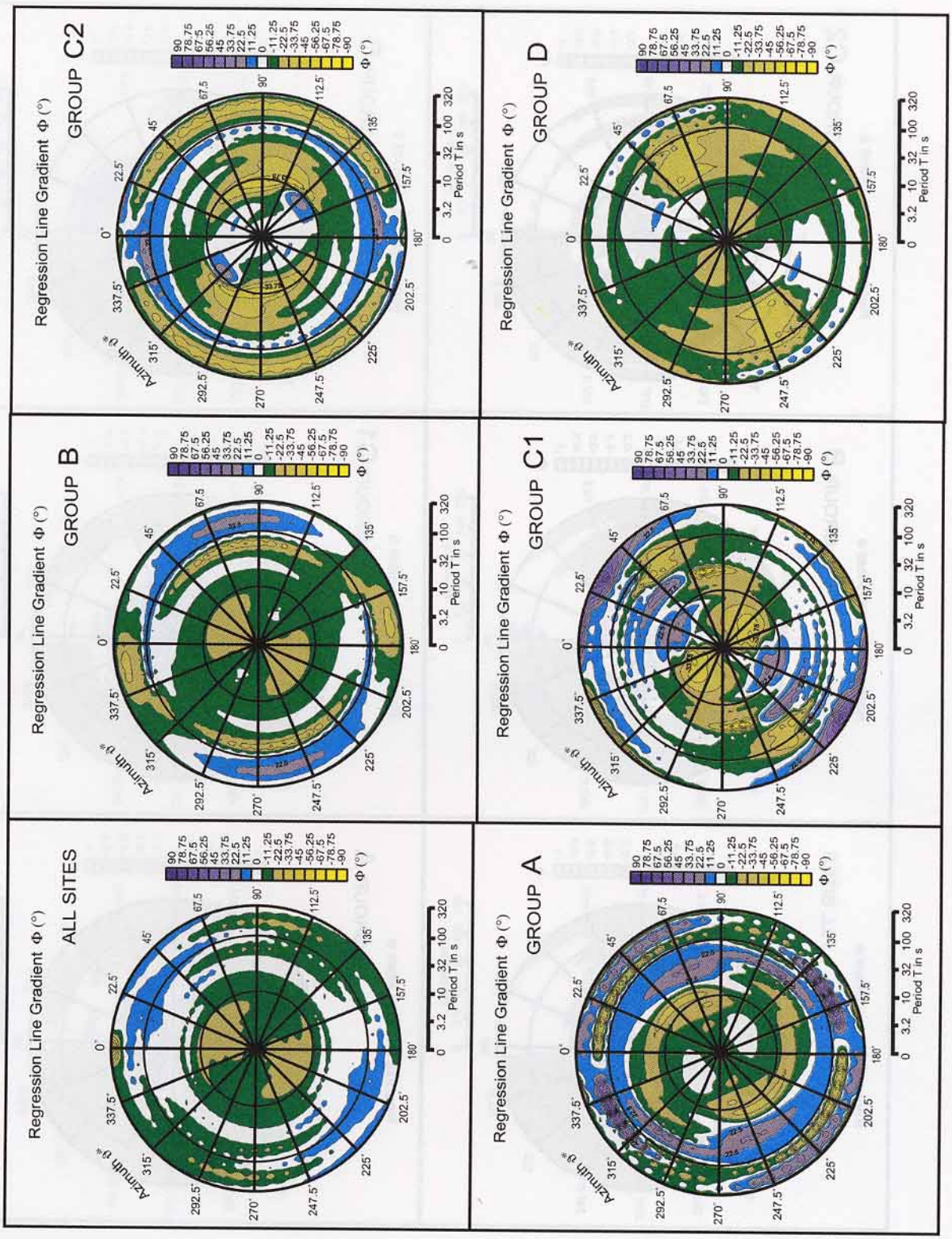

Fig. 4.28: HEA for all groups, all periods, polarisation azimuths 0°-180°, **gradient**.

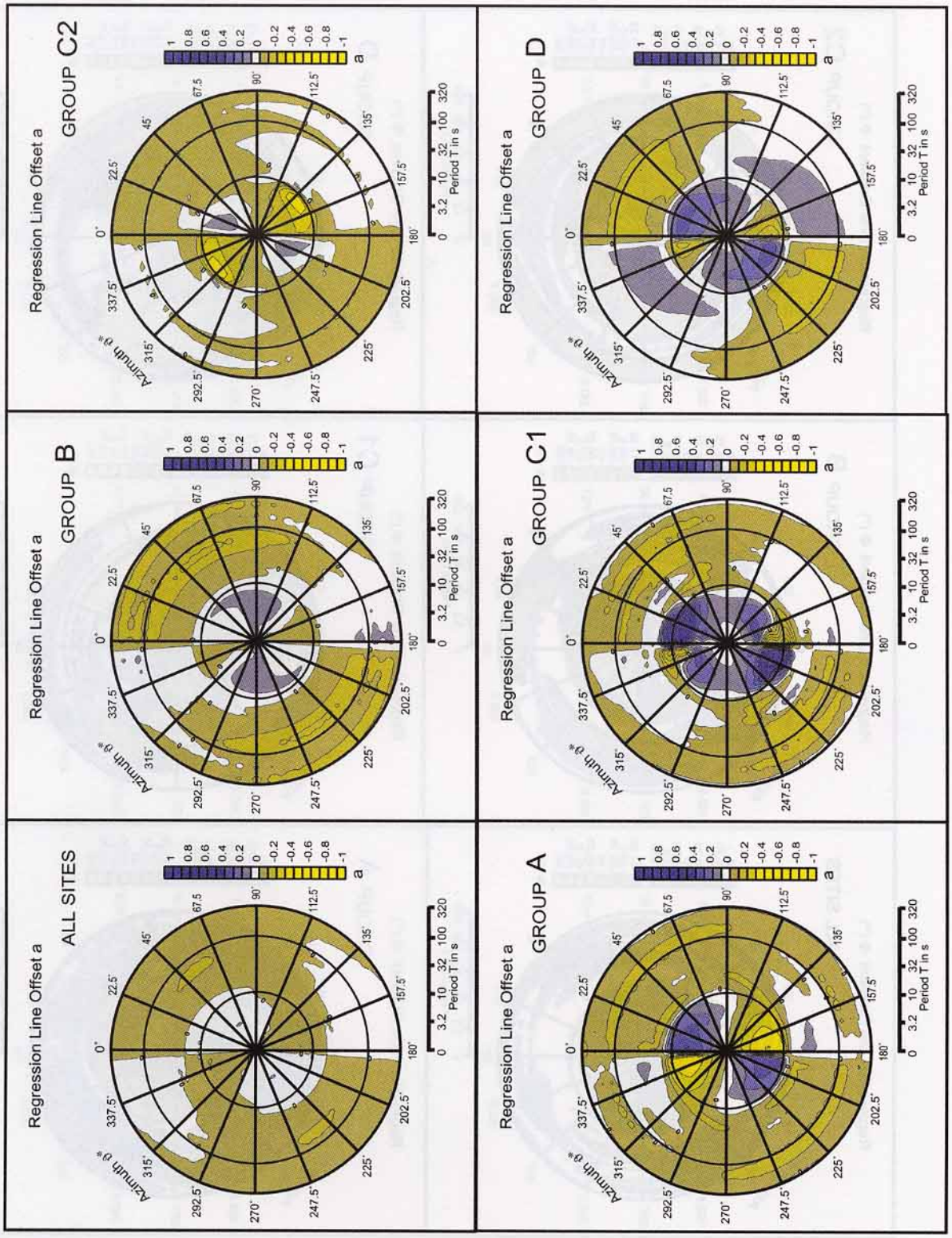

Fig. 4.29: HEA for all groups, all periods, polarisation azimuths 0°-180°, **offset**.

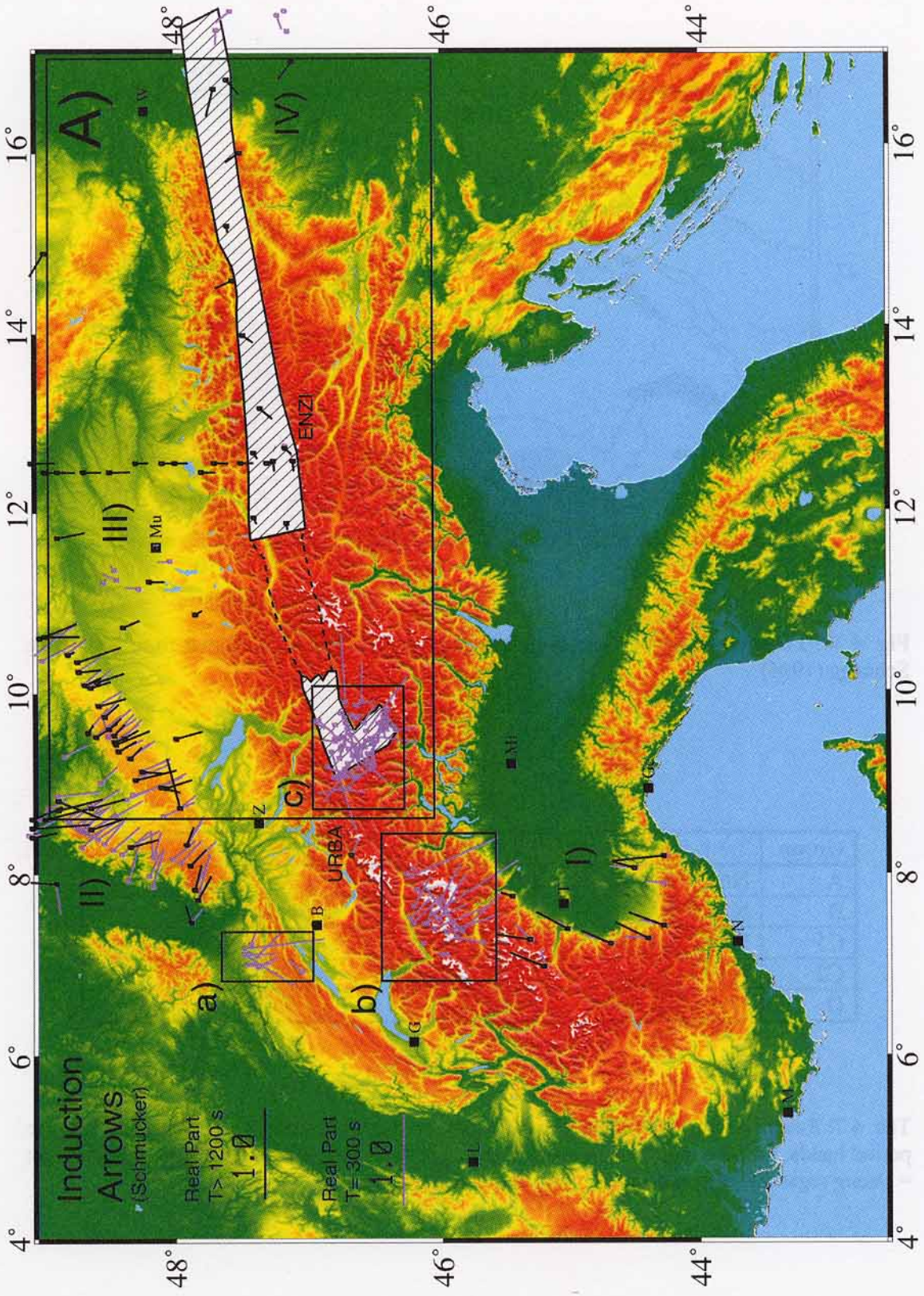

Fig. 5.2: Compilation of real part induction arrows (T= 300 s and T>1200) from the Alps. The data refer to several European Research Groups (listed in Tab. 5.1). Striped area marks zone of anomalous directional behaviour (and anomalous amplitude) of real induction arrows. Dotted line marks the area of presumed anomalous directional behaviour of real induction arrows. Mi: Milan, T: Turin, Ge: Genova, L: Lyon, N: Nice, M: Marseille, G: Geneva, B: Bern, Z: Zürich, Mu: München, W: Wien.

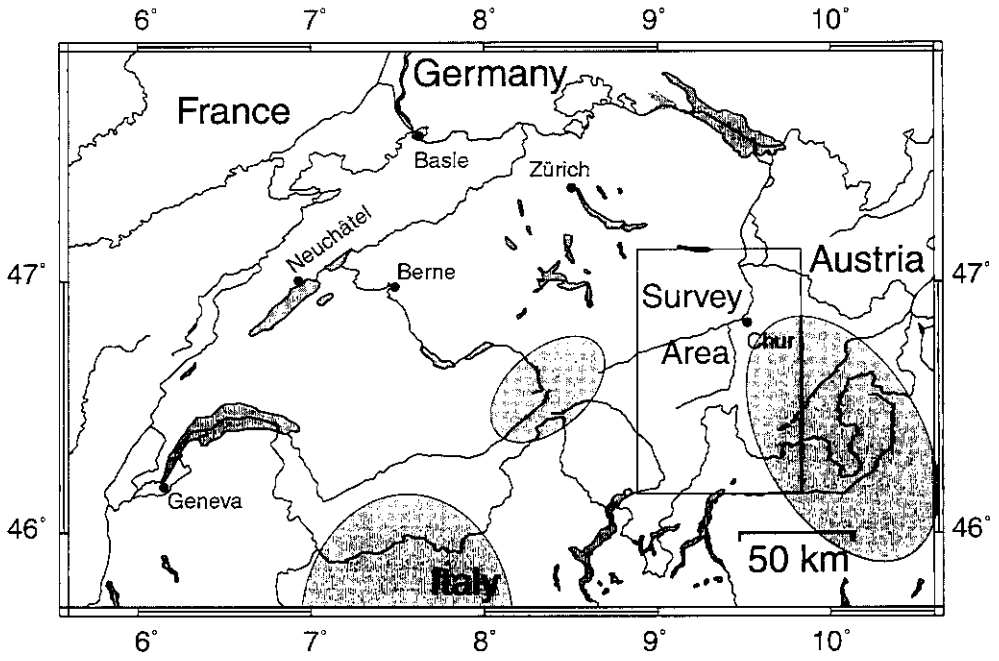

Fig. 4.30: Location of major magnetic anomalies in Switzerland. Redrawn from Fischer & Schnegg (1994).

Group	T= 1-10 s	T= 10-100 s	T> 100 s
A	N67,5°E, **i, bz**	N56°E	N45°E, **d**
B	N22.5°E, **i**		N90°E, **d**
C1	N135°E, **i, bz**	N11.5°E	N135°E, **o, d**
C2	N34°E, **o, d**	N80°E-N90°E	N90°E, **i**
D	N112.5°E, **i, bz**	N56°E	N45°E, **d**

Tab. 4.7: Results of the Hypothetical Event Analysis. Regional strikes for groups **A-D** in three period bands; **i** = pure induction, **o** = onset of magnetic distortion, **d** = magnetic distortion, **bz** = strong regional vertical magnetic field component present.

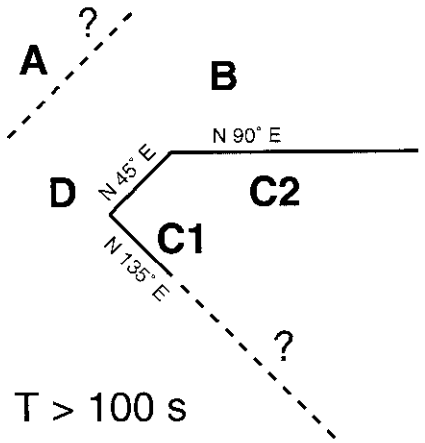

Fig. 4.31: Most likely geometric configurations of strike directions at depth (T> 100 s) in Graubünden as derived from the Hypothetical Event Analysis. **A-D** are groups of magnetic transfer functions. Not to scale!

4.6 Summary

The results from this chapter show, that EM induction processes in eastern Switzerland are dominated by the superposition of at least two distinct conductive structures, – the Bündnerschiefer in the uppermost crust and a super-regional conductivity anomaly at depth (Gurk, 1999). The deeper anomaly forms an edge in which eddy currents are concentrated. Studying GDS transfer function with the Hypothetical Event Analysis (Banks & Beamish, 1984; Ritter & Banks, 1998), the 3-D current concentration in the investigation area is found to be characteristic in distinct period bands and tectonic regions. The displayed current concentration shows a spatial de-coupling of induction processes, almost independent form the chosen direction of the hypothetical event. For short periods (T= 1-10 s) induction is related to Mesozoic sediments and their internal inhomogeneities. For periods longer than T= 100 s, current channelling and/or induction is limited to the Austroalpine and Penninic basement. An East-West striking structure at depth is found where pure induction takes place, hence this structure should be regarded as the super-regional structure that evokes magnetic distortion in the Bündnerschiefer facies.
The particular geometric constellation of both structures evokes magnetic distortion (independent of signal period!) in Graubünden: real induction arrows on the Bündnerschiefer point SW in (anomalous) strike direction, whereas outside the Bündnerschiefer, the real parts of induction arrows point towards SE. Locally, magnetic distortion and/or a superficial magnetic body increases the amplitude of real induction arrows on the Mesozoic Avers- Schiefer sediments.
The concept of magnetic distortion expects to find anomalous directional behaviour of real parts of the induction arrows on the *continuation* of the Mesozoic Bündnerschiefer as long as the geometric relation between local and regional conductive structures are valid (Gurk, 1999). Since the MT/GDS survey of the Penninic Alps of Valais (Schnegg, 1998) (western Switzerland) do not show magnetic distortion, the prolongation of the Bündnerschiefer facies should be found towards east. Hence, anomalous direction of induction arrows in the Eastern Alps is a tool to map this distinct facies beneath Austroalpine and South Penninic units. This hypothesis will be treated in the following chapter.

5 Anomalous directional behaviour of real induction arrows in the Central and Eastern Alps

The results presented in this chapter are mainly based on GDS data from the Penninic Alps of Switzerland (Schnegg, 1998; Gurk, 1999), the Eastern Alps (Berktold et al., 1976; Berktold, 1978; Bahr, 1992) and from the Transdanubian conductivity anomaly in west Hungary (Adam, et al., 1972; Adam, et al., 1990). This compilation uses available geomagnetic observations from various research groups and the more recent studies from Switzerland. Generally, Swiss data comprises the entire magnetic and magnetotelluric transfer function set covering a period range from T= 1-300 s. This period range was thought to be sufficient with respect to induction processes in many of the typical rocks of the Penninic Alps. Contrarily, data from other parts of the Alps are (with exception) solely accessible as real induction arrows covering a standard period range of $T \geq 1200$ s. Thus, imaginary parts of the magnetic transfer function are not subject of this chapter. Most of the conclusions drawn in this chapter are based on the magnetic distortion hypothesis for two-dimensional conductive structures. Since this distortion model is independent of the signal period, the maps displaying real induction arrows of different period ranges are justified. All presented real induction arrows are pointing towards more resistive regions. A list of the data used for the compilation is given in Tab. 5.1.

Key	**Region**	**Reference**
I)	Northwest Italy I	(Bozzo & Meloni, 1989) (Meloni et al., 1989) (Di Mauro et al., 1998)
II)	Rhinegraben and Jura of Swabia D, F	(Richards et al., 1980) (Richards et al., 1982) (Tezkan, 1986) (Menvielle & Tarits, 1986) (Blundell et al., 1992)
III)	Molasse D	(Berktold, 1974) (Blundell et al., 1992)
IV)	Eastern Alps and West Hungary D, A, H	(Berktold et al.,1976) (Wallner, 1977) (Adam et al., 1972) (Adam et al., 1992) (Adam, 1995) (Blundell et al., 1992) (Bahr, 1992) Bahr, pers. comm.
a)	Jura Mountain (Ajoie), CH	Gurk, pers. comm.
b)	Penninic Alps of Valais, CH, I	(Schnegg, 1998)
c)	Penninic Alps of Graubünden CH	(Gurk, 1999)

Tab. 5.1: List of data used for the compilation of induction arrows in the Alps

5.1 Electromagnetic induction pattern in the Alps

In the past 20-30 years, several geomagnetic deep soundings and MT studies have been carried out to investigate the electrical conductivity distribution in the transition zone Molasse Basin/ Calcareous Alps and below the Hohen Tauern and Zillertaler Alps (Teufel, 1983; Beblo, 1974; Berktold, 1974; Duma, 1980; Kemmerle, 1974). Only a small increase of electrical conductivity, however was found below the Hohen Tauern and below the upper valleys of the rivers Drau and Rienz. Nevertheless, Berktold (1978) already marked this region from the Zillertaler Alps to the Hungarian border that delineates a portion of the large structure (Fig. 5.1) on which we focus in this chapter. As the number of stations was too small, no detailed information could be given about the extension and the depth range of these local conductivity anomalies.

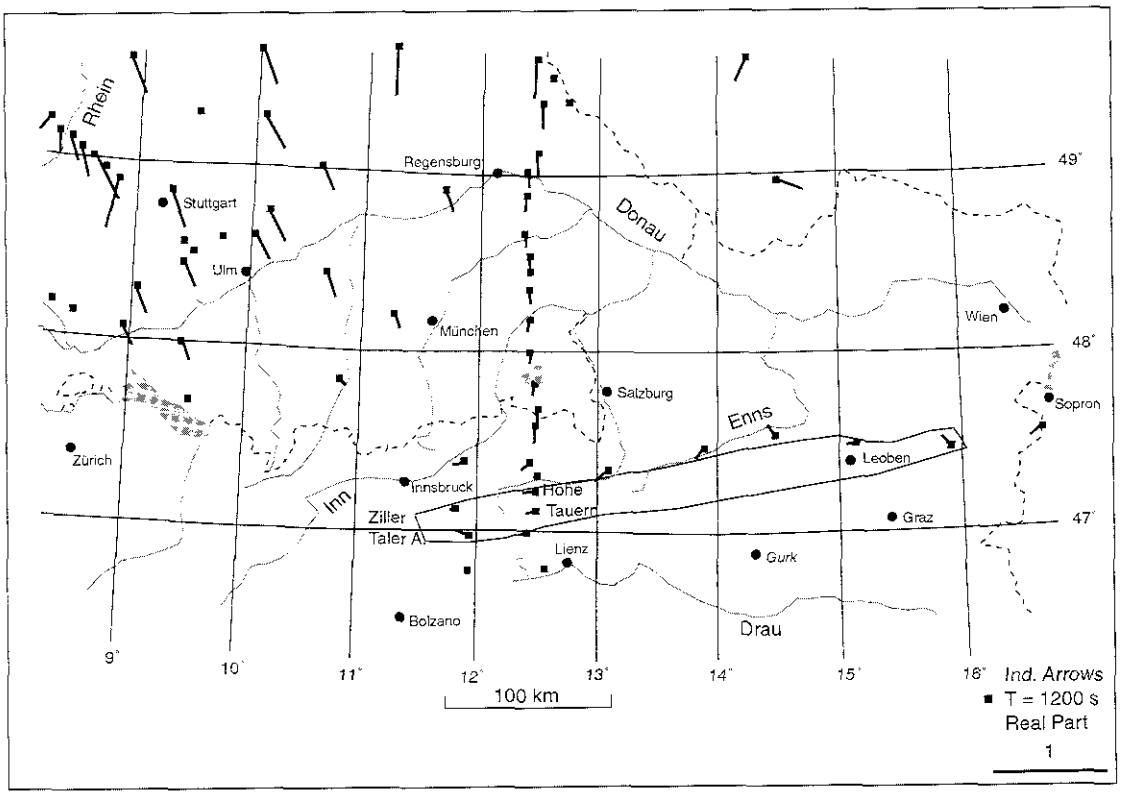

Fig. 5.1: Real part induction arrow distribution in the area between the Rhinegraben, the Bohemeian Massif and the Central Alps. Marked area indicates presumed anomalous current distribution. Redrawn from Berktold (1978).

The strike, or more generally, the lineament indicating feature of the real induction arrows is well illustrated in Fig. 5.2 (see also Tab. 5.1). In the Western Alps, their directions assume the alpine arc (Tab. 5.1, b). In the Upper Rhinegraben area (Tab.5.1, II) they are influenced by a current channelling effect caused by high resistive Variscan basement rocks of the Vosges and Black Forest at both sides of the graben driving an electric current flow in the sediments of the Rhinegraben to the South. Consequently, the induction arrows are tending to point away from the centre of the current system. At the southern end of the Rhinegraben (Tab. 5.1, a), the

induction arrow pattern shows that the current flow tends to leak into the Bressegraben rather than into the Swiss Molasse. Another important effect on induction arrows is presented at the southernmost sites in Northwest Italy (Tab. 5.1, I). The very large amplitude of these induction arrows is caused by the "coastal effect" – due to a high lateral conductivity contrast between the extreme low resistive seawater and the high resistive onshore rocks. Large contrasts in conductivity between the Mesozoic Sediments and crystalline rocks are present in the western and eastern Penninic Alps (see paragraph 4.3) of Switzerland (Tab.5.1, b and c). Similar to the "coastal effect", this contrast increases real induction arrow amplitudes locally up to $L_P > 1$.

Contrarily, the electromagnetic induction pattern in the Central and Eastern Alps is dominated by a large-scale zone on the Penninic domain, shaped as an almost horizontal strip, where real induction arrows are in strike with the structure, pointing SW (Fig. 5.1, Fig. 5.2). This directional behaviour is anomalous since we generally expect real induction arrows on this strip to be normal to the strike of this structure.

5.2 Similarities between the induction pattern and magnetic signature in the Eastern Alps

Striking similarities between the elongated zone of anomalous directional behaviour of real part induction arrows and the magnetic signature of the Eastern Alps are present.

Heinz reports three main types of magnetic anomalies in the Eastern Alps (Heinz, 1989; Heinz and Seiberl, 1990):

- "marginal" types of short wavelength and high amplitudes connecting the Penninic system of the Engadin window to the Rechnitz-Bernstein, situated along the northern margin of the Austroalpine thrust sheet;
- "large scale structures" extending from the Engadin window into the Carphatian ranges;
- anomalies associated with basement structures north of the Alps.

The "marginal" types (Fig. 5.3) are addressed to ophiolithic remnants of the South Penninic ocean whereas "large scale structures" are associated with remnants of a North Penninic ocean domain (Heinz & Seiberl, 1990). Arrangement and position of the induction anomaly corresponds with the "marginal" type and "large scale structure" anomalies of the total magnetic field. The former anomaly is restricted to the North Penninic Bündnerschiefer facies and is not caused by ophiolithic rocks but by the paired anomaly of Bündnerschiefer facies and a crustal conductor at depth. Obviously, all anomaly types are connected via the geodynamic history of the Eastern Alps (Fig. 1.1b):

After initial rifting during Triassic time, oceanic crust was developed in the south Penninic ocean since the early Jurassic. These events were largely controlled by the opening of the Central Atlantic (Laubscher & Bernoulli, 1977). The actual arrangement of the paired anomalies is the result of later tectonic activities. The opening period of the South Penninic basin was followed by the development of a southward dipping subduction zone on its southern margin, implying the almost simultaneous opening of a North Penninic ocean and southward motion of the Middle

Penninic High (Briançonnais) (Ratschbacher & Frisch, 1988). The consumption of the southern Penninic oceanic crust and the subsequent first "continent-continent" collision completed this period (Middle Cretaceous to early Upper Cretaceous). A second "continent-continent" collision took place as the consequence of the subduction and consumption of the northern Penninic basin which was presumably completed in the late Eocene (Frisch, 1981). The southern rim of stable Europe collided with the welded Middle-Penninic-Southern Penninic-Austroalpine complex. During this event, the Bündnerschiefer facies in Graubünden was 30 km subducted and finally uplifted and exposed. Remnants of the South Penninic were tilted, uplifted and partly exposed by erosion (Heinz, 1989), forming the sources of the "marginal" anomaly signature.

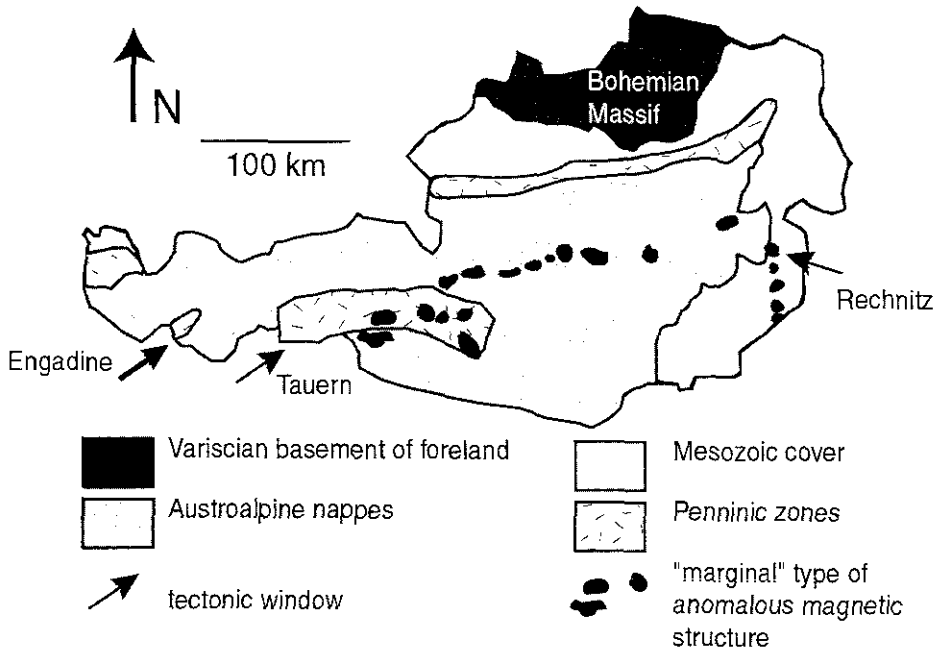

Fig. 5.3: Simplified tectonic map of Austria with magnetic anomaly pattern (black dots) of marginal type (high gradient, short wavelength). Modified fromr Heinz (1989).

5.3 Tectonic and palaeogeographic implications

"Large scale" magnetic anomalies and the elongated zone of anomalous directional behaviour of the induction arrows are of North Penninic origin. Both structures are terminated at west (Graubünden) and extend towards east (Bernstein/Rechnitz) (Heinz, 1989).

From this reason we confirm the conclusion drawn by Heinz that the North Penninic basin is terminated at west and is opened at east (Heinz, 1989; Heinz & Seiberl, 1990). Consequently, the northern Penninic ocean was not directly dependent on the history of the Central Atlantic. Several studies support this model (Frisch, 1977; Frisch, 1979; Schmid, et al., 1990).

Furthermore, the continuation of the North Penninic Bünderschiefer-facies beneath Austroalpine and South Penninic units at least to the Rechnitz window can be deduced from the joint GDS observation.

6 Conclusions

Little is known about the deep structure of the transition zone from the Central to the Eastern Alps. Recent seismic refraction studies, however, revealed a region partially lacking of lower crustal reflectivity that coincides in position with the observed anomalous current distribution at depth. The lacking of reflectivity is probably related to strong energy scattering along complex deformation structures (Pfiffner et al., 1997). Figure 5.4 shows depth contour lines of the Moho boundary derived from seismic and gravity data together with our investigation area (box). Line (4) represents a strip of a Moho offset (< 10 km) due to a possible Adriatic indenter or terrane which forms in its western part a wedge bearing the geometric properties necessary to justify the observed deep conductivity anomaly. Since their data resolution is quite poor, we may shift this structure some kilometers to the West. In our model shown in Fig. 5.5, this Moho offset is caused by a strip of peeled Adriatic lower crust/mantle overlaying the European lower crust. This arrangement creates a stacked lithosphere that begins in the eastern Central Alps of Graubünden and stretches (N90°E) to the East. As a fact of this offset, good conductive Adriatic lower crust lies side by side with resistive European upper crust, creating a sharp lateral contrast in conductivity. Additionally, we suspect the presence of brines generated by dehydration at depth to be tectonically trapped (Arthaud & Dazy, 1989) along the northern limitation of the stacked lithosphere system, created by the indentation of the northern Adriatic promontory or terrane. Hence the current concentration at depth could delineate the transition between European and Adriatic lithosphere. From a speculative point of view, the stacked lithosphere might also result from the remnant of the Middle Penninic High.

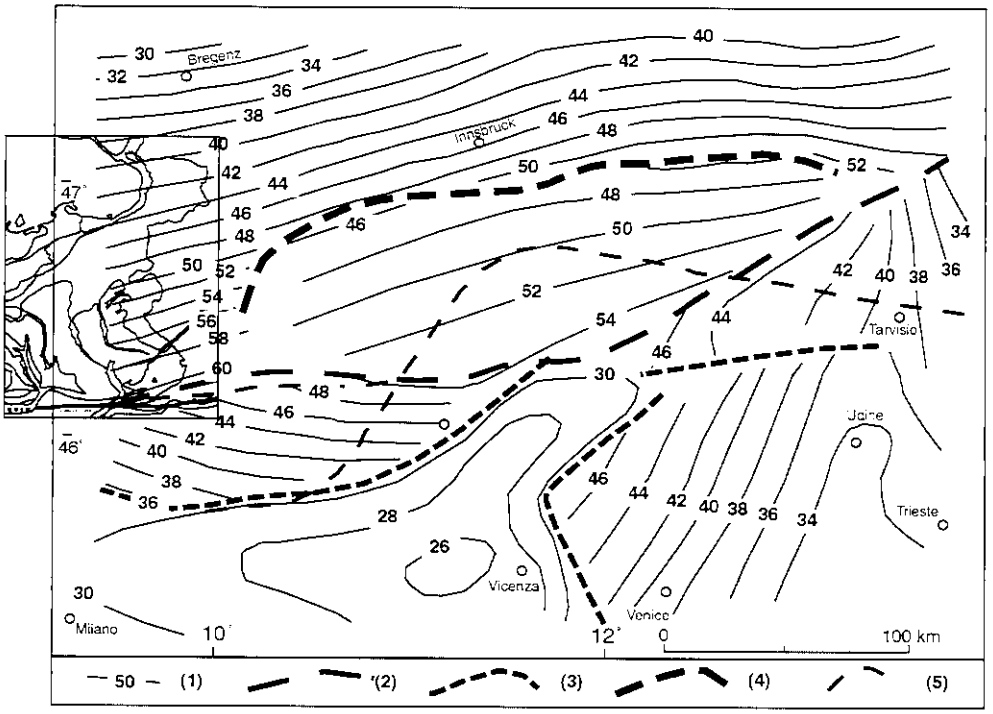

Fig. 5.4: Depth contour lines 1) of the Moho boundary (km) inclusive the location of the Graubünden investigation area. The major near vertical offsets and overriding fronts are plotted; 2) Moho overriding front; 3) offset > 10 km; 4) offset < 10 km; 5) Insubric Line. Modified from Cassinis (Cassinis et al., 1997).

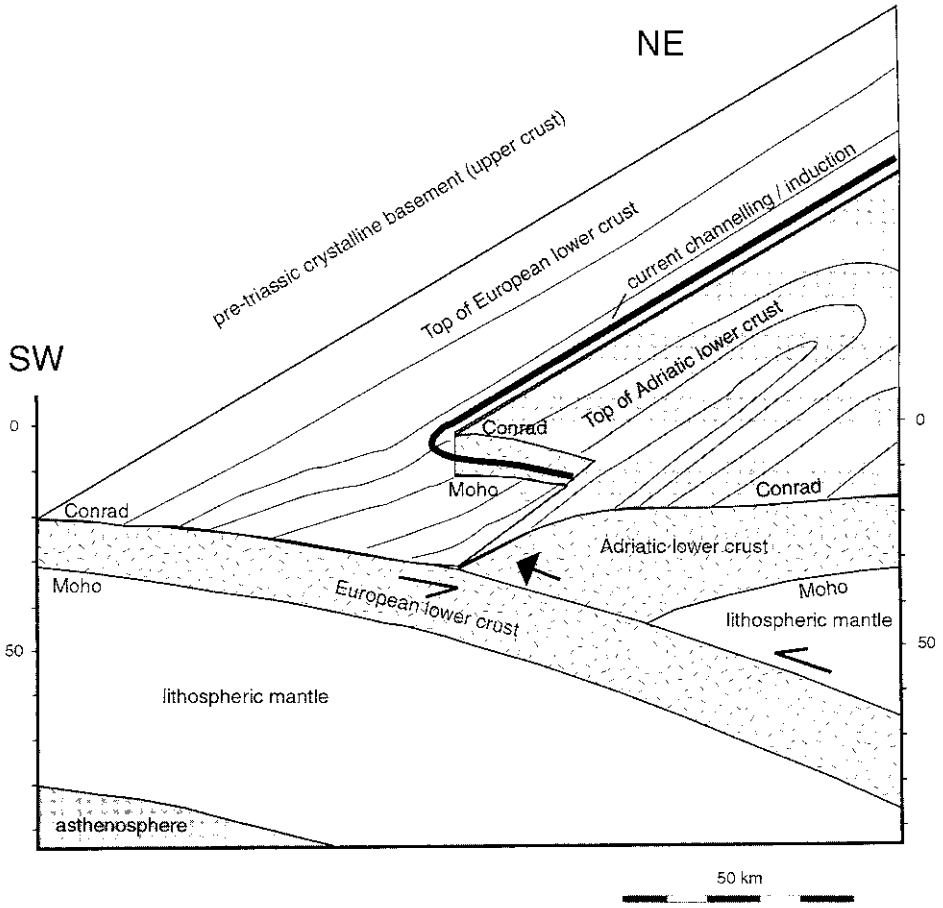

Fig. 5.5: Simplified model of the top of lower crust from the trace of the Eastern Traverse to the North-East (Austroalpine) showing the indentation by the Adriatic plate and the presumed induction/ current channelling. The upper crust is stripped off. Adapted from Pfiffner (Pfiffner et al., 1997) and Cassinis (Cassinis et al., 1997).

7 Summary

Two predominant anomalies are present in Central Europe: The North German anomaly (Untiedt, 1970) that roughly extends East-West and a conductivity anomaly that assumes the arc of the Carpathian Ranges. The North German anomaly is the largest in extent, and most extensively investigated. On the other hand, the electromagnetic induction pattern in the Central Alps remains almost unknown. Besides two long periodic (T> 1000 s) induction studies in the Western and Eastern Alps (Bahr, 1992) and the MT/GDS survey in the western Swiss Alps (Schnegg, 1998), no further modern studies have been conducted in the Central Alps so far.

Although far away from the influence of the North German anomaly, the characteristic South direction of the real part of the induction arrow does not generally change towards and within (Schnegg, 1998) the Western/Central Alps. This observation is not well understood at present. It might result from a gradual decrease of the subsurface conductivity towards the South or result from a more complex structure of the external field (Schmucker, 1999). In southern Germany, a predominant Southeast direction of the real part induction arrows can be observed. Berktold (pers. comm.) suspects an additional conductivity anomaly (900-9000 S)

within the Northern Phyllite Zone of the Post Variscian cover in front of the Mid-German Crystalline High (Blundell et al., 1992) superimposed on the North German anomaly to cause the Southeast direction of induction arrows in southern Germany. Real part induction arrows that exhibit this general direction north of the Central Alps are well documented by several MT and GDS studies (Richards et al., 1980; Tezkan, 1988; Berktold, 1977).

The present publication reports a conductivity anomaly found in the transition zone between the Central and the Eastern Alps. In contrasts to the findings in the western Swiss Alps (Schnegg, 1998), the MT[1]/GDS (magnetotelluric/geomagnetic deep sounding) survey in Graubünden (eastern Switzerland) revealed a change of direction of the real parts of the induction arrows over the entire period range (T=1-300 s) on the Mesozoic Bündnerschiefer facies. This facies is formed by series of low-grade metamorphic, shaly-calcereous-terrigenous sediments (Steinmann, 1994). The change in direction of the induction arrows coincides in Graubünden with the structural contact (SW-NE) between the Bündnerschiefer and the middle Penninic basement slices Adula, Tambo and Suretta. It occurs between two MT/GDS sites over a 400m distance on the Tschera nappe. In consideration of the model for 2-D conductivity anomalies and the local tectonic setting, we expect to find an almost vertical highly conductive zone of large lateral extent in this major structural contact - more precisely, at the observation point within the lithology of the Tschera nappe. If the presumed conductivity anomaly exists, the zone can contribute to the directional dualism of the observed real parts of the induction arrows in Graubünden. However, the absence of such a high conductive zone supports the magnetic distortion hypothesis for magnetic transfer functions.

A local survey on the Tschera nappe deals with the above hypothesis. The results obtained by the integrated local study do not confirm a conductivity zone with the required electromagnetic properties related to this structural contact but reveals precise information about the inner structure of the Tschera fold. Hence, anomalous directional behaviour of the real part of the induction arrows in Graubünden is more likely the result of magnetic distortion of the GDS transfer functions.

Using the Hypothetical Event Analysis (HEA) for 2-D conductivity distribution (Ritter & Banks 1998), the characteristics of the real and imaginary parts of the magnetic transfer functions in Graubünden can be analytically explained by the superposition of local and regional conductive structures that are separated vertically and horizontally. The study considers electric currents induced in these structures and leaking into the Bündnerschiefer as possible causes for the observed magnetic distortion effect upon the electromagnetic field. Only distinct geometric configurations and spatial constellations of local and regional conductive structures are able to explain the measured data:

- Any superposition of conductive structures of regional extension with an azimuth of a multiple of N45°E.

[1] Compared to the GDS data, the estimated MT transfer functions are of minor quality and are at present not extensively used for studying the conductivity distribution in Graubünden.

- Structures with a strike of N0°E and/or N90°E can cause the observed effect on the Bündnerschiefer, provided that the magnetotelluric (MT) transfer function is 1-D.

In order to verify this analytical model, the anomalous current distribution in the survey area is displayed by HEA-maps. The analysis shows that induction processes in the Central Alps (Graubünden) are predominated by the superposition of two distinct conductive structures – the (local) Bündnerschiefer in the uppermost crust and a super-regional conductivity anomaly at depth. The deeper anomaly forms in the investigation area an edge in which telluric currents are concentrated or even induced. The geometric configuration of the deeper anomaly is in good agreement with the previous analytical model. Induction processes are found to be de-coupled, horizontally and vertically. The chosen extension of the investigation area and the period range (T= 1-300 s) were able to display parts the anomalous current distribution. However, with regard to further electromagnetic investigations in the Alps, the period range should be extended towards longer periods.

The particular geometric arrangement of the Bündnerschiefer in the upper crust and the lower conductive structure evokes anomalous directional behaviour of the real parts of the induction arrows on the Bündnerschiefer. The concept of magnetic distortion expects to find anomalous directional behaviour of induction arrows on the *continuation* of the Bündnerschiefer as long as the geometric properties of local and regional structures are valid. Hence, anomalous directional behaviour is a tool to map the Bündnerschiefer facies beneath Austroalpine and Southalpine units.

In the final chapter of this publication this hypothesis was applied on a review of former geomagnetic data. The analysis reveals an elongated zone of large extension toward the East on which induction arrows show anomalous behaviour. Striking similarities in position and arrangement between this zone and the magnetic signature in the Eastern Alps were found. From this observation, the following main tectonic and palaeogeographic implications are deduced:

i) A lower crustal conductor caused by the indentation of the northern Adriatic promontory or terrane
ii) A stacked lithosphere beneath the Eastern Alps
iii) The eastward continuation of the Bündnerschiefe-facies at least to the tectonic window of Rechnitz
iv) The northern Penninic Ocean was not directly dependent on the history of the Central Atlantic.

Bündnerschiefer and lower crustal conductor are creating a "paired anomaly". Therefore, the extension of the zone of anomalous directional behaviour of the real parts of induction arrows towards the East gives also indication of the extension of the lower crustal anomaly. A connection of the latter with the Carpathian anomaly can be considered. However, the nature of the deep conductor remains unknown. Most promising candidate is a stacked (double) lithosphere originated by a peeled strip of lower crust that has been created during the indentation of the northern Adriatic promontory or terrane. The stacked lithosphere might also be produced by crustal remnants of the middle Penninic High. The author suspects that the enhanced conductivity is caused by fluids, created by the dehydration processes within the

stacked lithosphere. The fluids finally become trapped or have migrated along the northern boundary of the stacked system.

References

Adam, A., 1995, New AMT Data of the Gailtaler Alps: Acta Geod. geoph. Hung., v. 30, p. 227-239.

Adam, A., Duma, G., Berger, J., and Horvath, J., 1992, Tectonic and Geoelectrical Features of the Periadriatic-Lineament (S-Austria) with a Generalization: Acta Geod. Geoph. Mont. Hung., v. 27, p. 47-64.

Adam, A., Duma, G., Gutdeutsch, R., Verö, J., and Wallner, A., 1986, Preadriadict lineament in the Alps studied by magnetotellurics: J. Geophys., v. 59, p. 103-111.

Adam, A., Duma, G., and Horvath, J., 1990, A new approach to the electrical conductivity anomalies in the Drauzug-Bakony geological unit: Physics of the Earth and Planetary Interiors, v. 60, p. 15-162.

Adam, A., Verö, J., and Wallner, A., 1972, Regional properties of geomagnetic induction arrows in Europe: Acta Geodaet., Geophys. et Montanist. Acad. Sci. Hung., Tomus, v. 7, p. 251-287.

Alfano, L., Lorenzoni, G., Melandri, C., Mocchi, M., Nuttini, G., Pirera, F., and Soffientini, M. E., 1994, A deep geoelectrical survey in the Southern Central Alps: Annali di geofisica, v. XXXVII, p. 1185-1198.

Andrieux, P., Clerc, G., and Tort, P., 1974, Capteur magnétométrique triaxial pour la prospection magnétotelluric artificielle entre 4Hz et 4 kHz: Physique Appliquée, v. 9, p. 757-759.

Arora, B. R., and Adam, A., 1992, Anomalous directional behaviour of induction arrows above elongated conductive structures and its possible causes: Physics of the Earth and Planetary Interiors, v. 74, p. 183-190.

Arthaud, F., and Dazy, J., 1989, Migration des saumures au front des chevauchements de l'arc alpin occidental: C. R. Acad. Sci. Paris., v. 309, p. 1425-1430.

Bahr, B., 1992, Erste Ergebnisse der langperiodischen Magnetotellurik in den Alpen: Eine 200 km mächtige Lithosphäre?: 14. Kolloquium "Elektromagnetische Tiefenforschung", p. 229-234.

Bahr, K., 1985, Magnetotellurische Messungen des Elektrischen Widerstandes der Erdkruste und des oberen Mantels in Gebieten mit Lokalen und Regionalen Leitfähigkeitsanomalien: Unpub. PhD thesis, August Univ. Göttingen.

Bahr, K., 1988, Interpretation of the magnetotelluric impedance tensor: regional induction and local telluric distortion: Journal of Geophysics, v. 62, p. 119-127.

Bahr, K., 1991, Geological noise in magnetotelluric data: a classification of distortion types: Physics of the Earth and Planetary Interiors, v. 66, p. 24-38.

Bailey, R. C., Edwards, R. N., Garland, G. D., Kurtz, R., and Pitcher, D., 1974, Electrical Conductivity Studies over a Tectonically Active Area in Eastern Canada: J. Geomag. Geoelectr., v. 26, p. 125-146.

Banks, R. J. and Beamish, D., 1984, Local and regional induction in the British Isles: Geophys. J. R. astr. Soc., 79, p. 539-553.

Beblo, M., 1974, Magnetotellurik-Messungen in den Ostalpen: Probleme der Auswertung und Interpretation durch Topographie und Geologie der oberen Kruste: Erdmagnetische Tiefensondierung, p. 201-220.

Beniof, H., 1960, Observation of Geomagnetic Fluctuations in the Period Range 0.3 to 120 seconds: J. Geophys. Res., v. 65, p. 1413-1422.

Berktold, A., 1974, Erdmagnetische Tiefensondierung in Süddeutschland und in den Alpen: Erdmagnetische Tiefensondierung, p. 58-71.

Berktold, A., 1978, On the distribution of the electrical conductivity in the area between the Rheingraben, the Bohemian Massif and the Central Alps: Acta Geodaet. et Montanist. Acad. Sci. Hung. Tomus, v. 13, p. 437-440.

Berktold, A., M.Beblo, and Kemmerle, K., 1976, On the distribution of the electrical conductivity below the Eastern Alps: Geol. Rundschau, v. 65, p. 715-732.

Bigalke, J., and Grabner, E. W., 1997, The Geobattery Model: A contribution to large scale Electrochemistry: Electrochimica Acta, v. 42, p. 3443-3452.

Bigalke, J., and Junge, A., 1999, Using evidence of non-linear induced polarization for detecting extended ore mineralisations: Geophys. J. Int., v. 137, p. 516-520.

Bissig, P., 1997, Hydrogeologische Untersuchung der CO2-reichen Mineralquellen von Scoul-Tarasp (GR, Schweiz): Unpub. Diploma Thesis, Neuchâtel, 91 p.

Blohm, E.-K., 1977, Ultrabasisches Mantelgestein (Tiefengeoelektrik beim Ultramafitit- Körper von Finero 1976), Hannover, BGR.

Blundell, D., Freemann, R., and Mueller, S., 1992, A continent revealed. The European Geotraverse: Cambridge, Cambridge University Press, 275 p.

Bozzo, E., and Meloni, A., 1989, Geomagnetic variation anomalies in north-western Italy: Physics of the Earth and Planetary Interiors, v. 53, p. 255-260.

Campbell, W., Wallace, H., and Matsushita, S., 1967, Physics of Geomagnetic Phenomena: IV a Geomagnetic Pulsations: Int. Geophysics Series V. II. London (Academic Press).

Cassinis, R., Federici, F., Galmozzi, A., and Scarascia, S., 1997, A 3D gravity model of crustal structure in the Central-Eastern Alpine sector: Annali Di Geofisica, v. XL, p. 1095-1107.

Chave, A. D., and Smith, J. T., 1994, On electric and magnetic distortion tensor decompositions: Journal of Geophysical Research, v. 99, p. 4669-4682.

Coward, M., and Dietrich, D., 1989, Alpine tectonics-an overview, Alpine tectonics, London, Geol. Soc. London Spec. Publ., p. 1-29.

Di Mauro, D., Armadillo, E., Bozzo, E., Cerv, V., Gambetta, A. D. S. M., and Meloni, A., 1998, GDS (Geomagnetic Depth Sounding) in Italy: application and perspectives: ANNALI DI GEOFISICA, v. 41, p. 477-490.

Duma, G., 1980, Magnetotellurik vom Grazer Becken in die Ostalpen: Elektromagnetische Tiefenforschung, p. 47-53.

Egbert, G., and Booker, J. R., 1986, Robust estimation of geomagnetic transfer function: Geophys. J. R. Astron. Soc, v. 87, p. 173-194.

Eisel, M., 1995, Interpretation magnetotellurischer Messungen im Umfeld der kontinentalen Tiefbohrung unter besonderer Berücksichtigung lateraler anisotroper Leitfähigkeitsstrukturen: Unpub. PhD thesis, Freie Universität Berlin.

Eisel, M., and Haak, V., 1999, Macro-anisotropy of the electrical conductivity of the crust: a magnetotelluric study of the German Continental Deep drilling site (KTB): Geophys. J. Int., v. 136, p. 109-122.

ELKTB-Gruppe, Bahr, K., Bigalke, J., Eisel, M., Haak, V., Harms, U., Hirschmann, G., Huenges, F., Jödicke, H., Kontny, A., Kücke, J., Nover, G., Rauen, A., Stoll, J., Walther, J., Winter, H., and Zulauf, G., 1994, Untersuchungen zur elektrischen Leitfähigkeit in der Kontinentalen Tiefbohrung und ihrem Umfeld - was bringt sie uns Neues: Mitteilungen der Deutschen Geophysikalischen Gesellschaft, v. 4, p. 2.

Erdelbrock, K., 1994, Diagenese und schwache Metamorphose im Helvetikum der Ostschweiz (Inkohlung und Illit-"Kristallinität"): Unpub. PhD thesis, Rheinisch-Westfälische Technische Hochschule Aachen 220 p.

Filloux, J., 1973, Techniques and instrumentation for study of natural electromagnetic induction at sea: Phys. Earth Planet. Inter., 7, p. 323-338.

Fischer, G., 1984, The North Pyrenean magnetic anomaly re-examined: Annales Geophysicae, v. 2, p. 181-186.

Fischer, G., and Schnegg, P.-A., 1994, Updating the geomagnetic survey of Switzerland, Matériaux pour la Géologie de la Suisse, Bern, Swiss Geophysical Commission.

Fischer, G., and Masero, W., 1994, Rotational properties of the magnetotelluric impedance tensor: the example of the Araguainha impact crater, Brazil: Geophys. J. Int., 119,p. 548-560.

Fittermann, D. V., 1979, Calculation of self-potential anomalies near vertical contacts: Geophysics, v. 44, p. 195-205.

Frisch, W., 1979, Tectonic progradation and plate tectonic evolution of the Alps: Tectonophysics, v. 60, p. 121-139.

Frisch, W., 1981, Plate motions in the Alpine region and their correlation to the opening of the Atlantic ocean: Geologische Rundschau, v. 70, p. 402-411.

Gamble, T. D., Goubau, W. M., and Clarke, J., 1979, Magnetotellurics with a remote magnetic reference: Geophysics, v. 44, p. 53-68.

Gay, S. P., 1967, A 1800 Millivolt Self-Potential Anomaly near Hualgayoc, Peru: Geophys. Prosp., v. 15, p. 236-245.

Gharibi, M., and Pedersen, L. B., 1999, Transformation of VLF data into apparent resistivities and phases: Geophysics, v. 64, p. 1393-1402.

Goffe, B., and Oberhänsli, R., 1992, Ferro-magnesiocarpholite in the "Bündnerschiefer" of the eastern Central Alps (Grisons and Engandine window): Eur. J. Mineral, v. 4, p. 835-838.

Gold, B., and Rader, C., 1969, Digital processing of signals: New York, McGraw-Hill.

Groom, R. W., 1988, The effects of inhomogeneities on magnetotellurics, Univerisity Toronto.
Groom, R. W., and Bahr, K., 1991, Correction for near surface effects: decomposition of the magnetotelluric impedance tensor and scaling corrections for regional resistivities: a tutorial: Surveys in Geophysics, v. 13, p. 341-379.
Groom, R. W., and Bailey, R. C., 1989, Decomposition of Magnetotelluric Impedance Tensors in Presence of Local Three-Dimensional Galvanic Distortion: Journal of Geophysical Research, v. 94, p. 1913-1925.
Gurk, M., 1999, Magnetic Distortion of GDS Transfer Functions: An Example from the Penninic Alps of Eastern Switzerland Revealing a Crustal Conductor: Earth Planets Space, v. 51, p. 1023-1034.
Heinz, H., 1989, Aeromagnetic measurements in the eastern Alps: the area east of the Tauern Window: Tectonophysics, v. 163, p. 25-33.
Heinz, H., and Seiberl, W., 1990, Magnetic structures of the eastern Alps west of the Tauern window, *in* Roure, F., Heitzmann, P., and Polini, R., eds., Deep Structures of the Alps, Paris, Zürich, Roma, Mém. Soc. géol. Fr.; Mém. Soc. géol. suisse; Vol. spec. Soc. Geol. It., p. 123-128.
Hermance, J. F., 1973, Processing of magnetotelluric data: Phys. Earth Planet. Int., v. 7, p. 349-364.
Ishido, T., and Pritchett, J. W., 1999, Numerical simulation of electrokinetic potentials associated with subsurface fluid flow: Journal of Geophysical Research, v. 104, p. 15247-15259.
Jenkins, G. M., and Watts, D. G., 1968, Spectral analysis and its application: San Francisco, Holden Day.
Jiracek, G. R., 1990, Near-Surface And Topographic Distortions In Electromagnetic Induction: Surveys in Geophysics, v. 11, p. 163-203.
Jödicke, H., 1992, Water and graphite in the earth's crust - an approach to the interpretation of conductivity models: Surveys in Geophysics, v. 13, p. 381-407.
Jones, A. G., and Groom, R. W., 1993, Strike-angle determination from the magnetotelluric impedance tensor in the presence of noise and local distortion: rotate at your peril !: Geophys J. Int., v. 113, p. 524-534.
Junge, A., 1990, A new telluric KCl probe using Filloux's AgAgCl electrode: Pageoph., v. 134, p. 589-598.
Kemmerle, K., 1974, Magnetotellurik am Alpen-Nordrand: Erdmagnetische Tiefensondierung, p. 220-240.
Lange, J., 1985, Audiomagnetotellurische Messungen in verschiedenen Messgebieten unter besonderer Berücksichtigung von Störeinflüssen: Unpub. Diploma thesis, Westfälische Wilhelms-Universität Münster.
Larsen, J. C., 1977, Removal of local surface conductivity effects from low frequency mantle response curves: Acta geodaet. geophys. Montanist. Acad. Sci. Hung., v. 12, p. 183-186.
Laubscher, H. P., and Bernoulli, D., 1977, Mediterranean and Thethys, *in* Narin, E. M., Laubscher, W. H., and Stehli, F. G., eds., The ocean basins and margins, New York, London, Plenum Press, p. 1-28.
Lilley, F. E. M., 1993, Magnetotelluric analysis using Mohr circles: Geophysics, v. 58, p. 1498-1506.
Lüke, H. D., 1991, Signalübertragung: Berlin Heidelberg New York, Springer Verlag, 301 p.
Mählmann, R. F., 1995, Das Diagenese-Metamorphose-Muster von Vitrinitreflexion und Illit-"Kristallinität" in Mittelbünden und im Oberhalbstein. Teil 1: Bezüge zur Stockwerkstektonik: Schweiz. Mineral. Petrogr. Mitt. v. 75, p. 85-122.
Mählmann, R. F., 1996, Das Diagenese-Metamorphose-Muster von Vitrinitreflexion und Illit-"Kristallinität" in Mittelbünden und im Oberhalbstein. Teil 2: Korrelation kohlenpetrographischer und mineralogischer Parameter: Schweiz. Mineral. Petrogr. Mitt., v. 76, p. 23-46.
Manatschal, G., Marquer, D., and Früh-Green, G. L., 2000, Channellized fluid flow and mass transfer along rift-related detachement fault (Eastern Alps, southeast Switzerland): GSA Bulletin, v. 1, p. 21-33.
Meloni, A., Santis, A. D., Magno, L., Bozzo, E., Cantaneo, M., and Foggioni, O., 1989, A Magnetovariational Study in the SW Alpine Arc: A Short Report: Il Nuovo Cimento, v. 12 C, p. 567-574.
Menvielle, M., and Tarits, P., 1986, 2-D or 3-D interpretation of conductivity anomalies: example of the Rhine-Graben conductivity anomaly: Geophys. J. R. astr. Soc., v. 84, p. 213-226.
Michel, S., and Zlotnicki, J., 1998, Self-Potential and magnetic surveying of la Fournaise volcano (Réunion Island) : Correlation with faulting, fluid circulation and eruption: J. of Geophys. Res., v. 103, p. 17845-17857.

Milligan, P. R., 1999, A Geomagnetic induction study across the east coast of Australia, and its relevance to high-resolution aeromagnetic surveys: IUGG, p. A.304.

Nabighian M. N., 1984, Toward a three-dimensional automatic interpretation of potential field data via generalized Hilbert transforms: Fundamental relations: Geophysics, v.49 (6), p. 780-786.

Neill, J. D. M., and Labson, V. F., 1991-1993, Geological mapping using VLF radio fields.: Investigation in Geophysics - Electromagnetic methods in Applied Geophysics, v. 3, Society of Exploration Geophysicists, 551-640 p.

Nievergelt, P., and Liniger, M., 1996, Early to mid Tertiary crustal extension in the Central Alps: The Turba Mylonite Zone (Eastern Switzerland): Tectonics, v. 15, p. 329-340.

Parasnis, D. S., 1986, Principles of Applied Geophysics: London, Chapman and Hall.

Perrier, F., Petiau, G., Clerc, G., Bogorodsky, V., Erkul, E., Jouniaux, L., D.Lesmes, Macnae, J., Meunier, J., Nascimaento, D., Oettinger, G., Schwarz, G., Toh, H., Vailant, M., Vozoff, K., and Yazici-Cakin, O., 1997, One year systematic study of electrodes for long period measurement of the electric field in geophysical environments: J. Geomag. Geoelec., v. 49.

Petiau, G., and Dupis, A., 1980, Noise, temperature coefficient, and long time stability of electrodes for telluric observations: Geophys. Prospect., v. 28, p. 792-804.

Pfiffner, O. A., and Hitz, L., 1997, Geologic interpretation of the seismic profiles of the Eastern Traverse (lines E1-E3, E7-E9): eastern Swiss Alps, *in* Heitzmann, P., ed., Results of NRP 20: Deep Structures of the Swiss Alps, Basel, Birkhäuser Verlag, p. 73-100.

Pfiffner, O. A., Lehner, P., Heitzmann, P., Mueller, S., and Steck, A., 1997, Results of NRP 20: Deep Structure of the Swiss Alps: Results of NRP 20: Basel, Birkhäuser Verlag, 380 p.

Poll, H. E., Weaver, J. T., and Jones, A. G., 1989, Calculations of voltages for magnetotelluric modelling of a region with near-surface inhomogeneities: Physics of the Earth and Planetary Interiors, v. 53, p. 287-297.

Radic, T., and Aschmann, L., 1998, Messungen von magnetischen Übertragungsfunktionen im Radiofrequenzbereich (10kHz bis 1 MHz).: Protokoll über das Kolloquium "Elektromagnetische Tiefenforschung" in Neustadt an der Weinstrasse, p. 65-72.

Ratschbacher, L., and Frisch, W., 1988, Transpressive Tektonik in den Ostalpen: II Symposium Tektonik - Strukturgeologie, p. 81.

Revil, A., Pezard, P. A., and Glover, P. W. J., 1999a, Streaming potential in porous media. 1: Theory of the zeta potential: Journal of Geophysical Research, v. 104, p. 20021-20031.

Revil, A., Schwaeger, H., III, L. M. C., and Manhardt, P. D., 1999b, Streaming potential in porous media. 2. Theory and application to geothermal systems: Journal of Geophysical Research, v. 104, p. 20033-20048.

Richards, M. L., Schmucker, U., and Steveling, E., 1980a, Erdmagnetische Tiefensondierung und Magnetotellurik mit Pulsationen im Bereich der Uracher Wärmeanomalie: Elektromagnetische Tiefenforschung, p. 13-21.

Richards, M. L., Schmucker, U., and Steveling, E., 1980b, Magnetic variations and magnetotelluric studies in Rheingraben and Schwarzwald: "Erdmagnetische Tiefenforschung", p. 22-35.

Richards, M. L., Schmucker, U., and Steveling, E., 1982, Electrical conductivity in the Urach geothermal area, a geomagnetic induction study using pulsations, *in* Ralph, H., ed., The Urach Geothermal project (Swabian Alb Germany), Stuttgart, Schweizerbart'sche Verlagsbuchhandlung, p. 301-311.

Ritter, P., 1996, Seperation of Local and Regional Information in Geomagnetic Response Functions using Hypothetical Event Analysis: Unpub. PhD thesis, University of Edinburgh 168 p.

Ritter, P., and Banks, R., 1998, Seperation of local and regional information in distorted GDS response functions by hypothetical event analysis: Geophys J. Int., v. 135, p. 932-942.

Robinson, P. T., Lewis, B. T. R., Flower, M. F. J., Salisbury, M. H. & Schmincke, H.-U., 1983. Crustal accretion in the Gulf of California: an intermediate-rate spreading axis. Init Rep DSP 65. B. T. R. Lewis and P. Robinson. Washington DC, US Government Printing Office: 739-752.

Rokityansky, I., 1982, Geoelectromagnetic Investigation of the Earth's Crust and Mantle: Berlin, Heidelberg, New York, Springer-Verlag, 381 p.

Sato, M., and Mooney, H. M., 1960, The Electrochemical Mechanism of Sulfide Self-Potentials: Geophysics, v. XXV, p. 226-249.

Scheelke, I., 1972, Magnetotellurische Messungen im Rheingraben und ihre Deutung mit zweidimensionalen Modellen, *in* Braunschweig, I. f. G. u. M. d. T. U., ed., Geophysikalische Arbeiten sowie Mitteilungen aus Meteorologie und Astrophysik (GAMMA), Braunschweig, Institut für Geophysik und Meteorologie der Technischen Universität Braunschweig, p. 199.

Schlunegger, F., Matter, A., Burbank, D. W., and Klapper, E. M., 1997, Magnetostratigraphic constraints on relationships between evolution of the central Swiss Molasse basin and Alpine orogenic events: Bull geol. Soc. Am., v. 109, p. 225-241.

Schmeling, H., 1986, Numerical models on the influence of partial melt on elastic, anelastic and electrical properties of rocks. Part II, electrical conductivity: Phys. Earth Planet. Inter., v. 43, p. 123-135.

Schmid, S. M., and Froitzheim, N., 1993, Oblique slip and block rotation along the Engadine line: Eclogae. geol. Helv., v. 86, p. 569-593.

Schmid, S. M., Pfiffner, O. A., Froitzheim, N., Schönborn, G., and Kissling, E., 1996, Geophysical-geological transect and tectonic evolution of the Swiss-Italian Alps: Tectonics, v. 15, p. 1036-1064.

Schmid, S. M., Rück, P., and Schreurs, G., 1990, The significance of the Schams nappes for the reconstruction of the paleotectonic and orogenic evolution of the Penninic zone along the NFP-20 East traverse (Grisons, eastern Switzerland): Mém. Soc. géol. Fr., v. 156, p. 263-287.

Schmucker, U., 1970, Anomalies of geomagnetic variations in the southwestern United States: Bull. Scripps Inst. Oceanograph. Univ. Calif., v. 13.

Schmucker, U., 1999, Von Induktionskurven und Induktionsparametern - ein Rückblick auf die Anfänge der erdmagnetischen Tiefensondierung und ein Ausblick auf neue Möglichkeiten: Mitteilungen der Deutschen Geophysikalischen Gesellschaft e. V., v. 3, p. 22-38.

Schnegg, P.-A., 1998, The magnetotelluric survey of the Penninic Alps of Valais. Bern. Swiss Geophysical Commission, p. 76.

Schnegg, P.-A., and Fischer, G., 1986, The effect of D.C. Railways on MT measurements in northern Italy: 8th Electromagnetic Induction Workshop Neuchatel.

Schwartz, M., and Shaw, L., 1975, Signal Processing: New York, McGraw-Hill.

Shankland, T. J., and Waff, H. S., 1977, Partial melting and conductivity anomalies in the upper mantle: J. Geophys. Res., v. 82, p. 5409-5417.

Sivenas, P., and Beales, F. W., 1982, Natural geobatteries associated with sulphide ore deposits. I. Theoretical Studies: Journal of Geochemical Exploration, v. 17, p. 123-144.

Stämpfli, G., and Marchant, R., 1997, Geodynamic Evolution of the Thetian margins of the Western Alps, *in* Pfiffner, O. A., Lehner, P., Heitzmann, P., Müller, S., and Steck, A., eds., Deep structures of the Swiss Alps: Results of NRP20, Basel, Birkhäuser, p. 223-239.

Steinmann, M., 1994, Ein Beckenmodell für das Nordpenninikum der Ostschweiz: Jb. Geol. B. -A. v. 137, p. 675-721.

Steinmann, M., and Stille, P., 1999, Geochemical evidence for the nature of the crust beneath the eastern North Penninic basin of the Mesozoic Thethys ocean: Geol. Rundsch., v. 87, p. 6333-643.

Stoll, J., Bigalke, J., and Grabner, E. W., 1995, Electrochemical Modelling of Self-Potential Anomalies: Surveys in Geophysics, v. 16, p. 107-120.

Streiff, V., Jäckli, H., and Neher, J., 1971, Geologischer Atlas der Schweiz, Blatt: 1235 Andeer: Kommissionsverlag: Kümmerly & Frey AG Geographischer Verlag Bern.

Streiff, V., Jäckli, H., and Neher, J., 1976, Erläuterungen zu Blatt: 1235 Andeer: Bern. Kommissionsverlag: Kümmerly & Frey AG. Geographischer Verlag Bern. 106 p.

Suana, M., 1984, Die Manganerzlagerstätten von Tinizong (Oberhalbstein, Graubünden): Beiträge zur Geologie der Schweiz, v. 64: Bern, Schweizerische Geotechnische Kommission, 92 p.

Swift, C. M., 1967, A magnetotelluric investigation of an electrical conductivity anomaly in the southwestern United States: Unpub. PhD thesis, Cambridge Masse.

Telford, W. M., Geldart, L. P., and sheriff, R. E., 1990, Applied Geophysics: Cambridge, Cambridge University Press, 770 p.

Teufel, U., 1983, Erdmagnetische Tiefensondierung am Alpennordrand: Unpub. PhD thesis, Ludwig-Maximillians-Universität, München, 97 p.

Tezkan, B., 1986, Erdmagnetische und Magnetotellurische Untersuchungen auf den hochohmigen Kristallinstrukturen des Hochschwarzwaldes und des Bayerischen Waldes bei Passau: Unpub. PhD thesis, Georg-August-Universität, 117 p.

Tezkan, B., 1988, Electromagnetic sounding experiments in the Schwarzwald central gneiss massif: J. Geophys, v. 62, p. 109-118.

Tezkan, B., Veeser, N., and Müller, M., 1996, Ueber die Modellierung der Induktionspfeile: Anisotropie - oder 3D-Modelle: Protokoll über das Kolloquium:" Erdmagnetische Tiefenforschung", p. 80-88.

Trümpy, R., 1988, A possible Jurassic-Cretaceous transform system in the Alps and the Carpathians: Geological Society of America Special Paper, v. 218, p. 93-109.

Turberg, P., and Müller, I., 1992, La méthode inductive VLF-EM pour la prospection en continue de milieu fissuré: Cinquiéme Coll. d'Hydrol. en Pays calcaire, p. 207-214.

Untiedt, J., 1970, Conductivity Anomalies in Central and Southern Europe: J. Geomag. Geol., v. 22, p. 131-149.

Volland, H., 1984, Atmospheric Electrodynamics, Springer Verlag, Berlin-Heidelberg-New York-Tokyo.

Vozoff, K., 1972, The Magnetotelluric Method in the Exploration of Sedimentary Basins: Geophysics, v. 37, p. 98-141.

Vuataz, F.-D., 1998, Hydrogéologie, Géochimie et Géothermie des Eaux Thermales de Suisse et des Régions Alpines Limithrophes, *in* Naturelles, C. d. H. o. d. l. S. H. d. S., ed., Matériaux pour la Géologie de la Suisse - Hydrogéologie, Bern, Kümmerly & Frey, p. 174.

Wallner, A., 1977, The main features of the induction arrows on the area of the transdanubian conductivity anomaly: Acta Geodaet., Geophys. et Montanist. Acad. Sci. Hung. Tomus, v. 12, p. 145-150.

Weh, M., Mählmann, R. F., and Froitzheim, N., 1996, Strukturelle und metamorphe Diskontinuitäten im Penninikum am Westrand der Ostalpen: TSK 96.

Weissert, H. J., and Bernoulli, D., 1985, A transform margin in the Mesozoic Thetys: evidence from the Swiss Alps: Geol. Rundschau, v. 74, p. 665-679.

Wexsteen, P., Jaffé, F. C., and Mazor, E., 1988, Geochemistry of cold CO2 -rich springs of the Scuol-Tarasp region, Lower Engadine, Swiss Alps: Journal of Hydrology, v. 104, p. 77-92.

Wiese, H., 1962, Geomagnetische Tiefentellurik Teil II: Die Streichrichtung der Untergrundsstrukturen des elektrischen Widerstandes, erschlossen aus geomagnetischen Variationen: Geofis pura Appl., v. 52, p. 83-102.

Wybraniec, S., Jankowski, J., Ernst, T., Pecova, J., and Praus, O., 1999, A new method for presentation of induction vector distribution in Europe: Acta Geophysica Polonica, v. XLVII, p. 323-334.

Wybraniec, S., 1997, Vectorial images - a new method of presentation of 2-D dat (in Polish): Posiedz Nauk. PIG, v. 53 (5), p. 42.

Zhang, P., Pedersen, L. B., Mareschal, M., and Chouteau, M., 1993, Channelling contribution to tipper vectors: a magnetic equivalent to electric distortion: Geophys. J. Int., v. 113, p. 693-700.

Zhang, P., Roberts, R. G., and Pedersen, L. B., 1987, Magnetotelluric strike rules: Geophysics, v. 52, p. 267-278.

Beiträge zur Geologie der Schweiz | **Contributi alla Geologia Svizzera**
Matériaux pour la Géologie de la Suisse | **Contributions to the Geology of Switzerland**

Geophysik - Géophysique - Geophysics - Geofisica

No.		Fr.
1	**H. Röthlisberger.** Zur seismischen und petrographischen Charakterisierung einiger Molassegesteine, einschliesslich der Beschreibung von Methoden der Korngrössenbestimmung in Festmaterial, 91 Seiten, 31 Figuren. 1957	20.-
2	**O. Friedenreich.** Eine grossräumige Widerstandskartierung nordwestlich von Zürich und ihre geologische Deutung. 47 Seiten, 22 Texftiguren, 9 Karten. 1959.	24.-
3	**F. Gassmann.** Schweremessungen in der Umgebung von Zürich. 70 Seiten, 24 Texftiguren, 2 Tafeln. 1962.	30.-
4	**E. Poldini.** Les Anomalies Gravifiques du Canton de Genève. Avec 63 pages, 25 figures et 3 planches. 1963.	30.-
5	**L. Rybach.** Refraktionsseismische Untersuchungen im Raum Aare-, Limmat- und Surbtal. 49 Seiten, 42 Figuren. 1962	20.-
6	**O. Gonet.** Etude gravimétrique de la plaine du Rhône. Région St Maurice - Lac Léman. 50 pages, 30 figures, 2 planches. 1965.	20.-
7	**C. Meyer de Stadelhofen.** Carte des résistivités de la Plaine du Rhône. 8 pages, 2 figures, 2 planches. 1966	10.-
8	**O. Gonet.** Etude gravimétrique du Lac Léman à bord du mésoscaphe *Auguste Piccard.* 50 pages, 8 figures, 1 planche. 1969	10.-
9	**J. -J. Wagner.** Elaboration d'une carte d'anomalie de Bouguer. Etude de la vallée du Rhône de St Maurice à Saxon (Suisse). 91 pages, 32 figures, 2 planches. 1970	27.-
10	**H. Lazreg.** Etude géophysique, géologique et hydrogéologique de la région de Concise à Pompaples (Pied du Jura vaudois). 51 pages, 16 figures, 2 planches. 1971.	27.-
11	**M. Petch.** Contribution à l'étude hydrogéologique de la plaine de l'Orbe. 95 pages, 23 figures, 15 planches. 1970.	27.-
12	**P.-A. Gilliand.** Etude Géoélectrique du Klettgau (Suisse), Canton de Schaffhouse. 85 pages, 47 figures, 10 annexes, 5 planches.1970.	27-
13	**P. Corniche.** Application des méthodes géophysiques à la recherche hydrogéologique. 65 pages, 25 figures. 1973.	27.-
14	**F. Heller.** Magnetische und petrographische Eigenschaften der granitischen Gesteine des Albignagebietes (Nördliches Bergeller Massiv). 66 Seiten, 24 Textfiguren. 1972.	27.-
15	**E. Klingelé.** Contribution à l'étude gravimétrique de la Suisse romande et des régions avoisinantes. 94 pages, 6 figures, 35 planches. 1972.	27.-
16	**W. Sigrist.** Contribution à l'étude géophysique des fonds du Lac Léman. 56 pages, 28 figures, 1 planche. 1974.	27.-
17	**R. Olivier.** Elaboration d'un système de traitement gravimétrique géré par l'ordinateur. Etude gravimétrique du plateau romand de Versoix (GE) à Concise (VD). 56 pages, 21 figures, 10 planches. 1974.	27.-
18	**H. Buchli, R. Paquin, A. Donzé.** Etude géoélectrique et gravimétrique du Chablais entre Anières et Evian. 170 pages, 81 figures, 4 planches. 1976.	38.-
19	**G. Fischer, P.-A. Schnegg, J. Sesiano.** A new geomagnetic survey of Switzerland. 44 pages, 15 figures, 8 tables, 10 cartes. 1979.	34.-
20	**E. Klingelé, R. Olivier.** La nouvelle carte gravimétrique de la Suisse (Anomalies de Bouguer). 96 pages, 9 figures, 4 tables, 1 carte. 1980.	34.-
21	**J.-J. Wagner, St. Müller.** Geomagnetic and gravimetric studies of the Ivrea zone. 64 pages, 44 figures. 1984.	32.-
22	**Ph. Bodmer, L. Rybach.** Geothermal map of Switzerland (Heat flow density). 48 pages, 21 figures, 6 tables. 1984.	42.-
23	**G. Schwarz.** Methodische Entwicklungen zur Aerogammaspektrometrie. 160 Seiten, 56 figuren. 1991.	42.-
24	**U. Schärli, L. Rybach.** Geothermische Detailkartierung der zentralen Nordschweiz (1:100'000). 59 Seiten, 13 Figuren, 2 Karten. 1991.	48.-
25	**G. Schwarz, E. Klingelé, L. Rybach.** Airborne radiometric mapping in Switzerland. 74 pages, 12 figures, 17 tables, 14 maps, 1992.	48.-
26	**K. Risnes, B. Dumont, R. Olivier & J.-J. Wagner.** Etude des anomalies magnétique et gravimétrique de la région du Chasseral. 42 pages,14 figures et 3 tables.1993.	26.-
27	**G. Fischer, P.-A. Schnegg.** Up-dating the geomagnetic survey of Switzerland. 8 pages, 5 figures, 3 tables, 6 maps. 1994.	30.-
28	**S. Sellami.** Propriétés physiques de roches des Alpes suisses et leur utilisation à l' analyse de la réflectivité de la croûte alpine. 160 pages, 59 figures, 16 tables. 1994.	45.-
29	**E. Rüttener.** Earthquake hazard evaluation for Switzerland. 150 pages, 88 figures. 12 tables, 1995.	45.-
30	**F. Medici, L. Rybach.** Geothermal map of Switzerland 1995 (Heat flow density). 36 pages, 11 figures, 1 table, 1 carte.	55.-
31	**E. Klingelé, M. Cocard, M. Halliday, H.-G. Kahle.** The airborne gravimetric survey of Switzerland. 104 pages, 66 figures, 10 tables, 1996.	55.-
32	**P.-A. Schnegg.** The magnetotelluric survey of the Penninic Alps of Valais. 75 pages, 38 figures, 5 tables, 1998.	45.-
33	**J.J. Wagner, G. Gong, M. Sartori and St. Jordi.** A catalogue of physical properties of rocks from the Swiss Alps and nearby areas. 80 pages, 14 figures, 5 appendices, 2 diskettes , 1999.	55.-
34	**A. Rosselli, R. Olivier, Ph. Logean, B. Dumont.** Les anomalies gravifiques de la vallée du Rhône entre Villeneuve et Brigue. 64 pages, 14 figures, 2 tables, 16 cartes, 1999.	45.-

Imprimeries Centrales Neuchâtel S.A. - CH-2001 Neuchâtel, 2000